

Thermal Evolution and Small Scale Structure of Sommerfeld Enhanced Dark Matter

Dissertation

zur Erlangung des Doktorgrades

des Fachbereichs Physik

der Universität Hamburg

vorgelegt von

Laura Gusta van den Aarssen MSc

aus Bergen op Zoom, Niederlande

Hamburg

2013

Gutachter der Dissertation:	Dr. T. Bringmann Prof. Dr. R. Banerjee
Gutachter der Disputation:	Dr. T. Bringmann Prof. Dr. Buchmüller
Datum der Disputation:	1.2.2013
Vorsitzender des Prüfungsausschusses:	Dr. G. Steinbrück
Vorsitzender des Promotionsausschusses:	Prof. Dr. P. Hauschildt
Dekan des Fachbereichs Physik:	Prof. Dr. H. Graener

Zusammenfassung

Obwohl die Existenz der Dunklen Materie (DM) durch zahlreiche unabhängige Beobachtungen auf verschiedenen Skalen bestätigt worden ist, bleibt ihre Natur ein Rätsel. Die aussichtsreichsten Kandidaten für die kalte nichtbaryonische DM sind die schwach wechselwirkenden massiven Teilchen (Weakly Interacting Massive Particles - WIMPs), die durch Ergebnisse aus der Teilchenphysik wohlmotiviert sind und für die es mit dem thermischen Produktionsmechanismus eine natürliche Art und Weise gibt, die beobachtete Reliktdichte zu erklären.

In dieser Arbeit betrachten wir insbesondere diejenige Klasse von WIMP-Modellen, für die es notwendig ist, den Sommerfeld-Effekt miteinzubeziehen. Dabei handelt es sich um ein quantenmechanisches Phänomen welches den Wirkungsquerschnitt der Paarvernichtung im nichtrelativistischen Grenzfall signifikant erhöhen kann. Dieser nichtperturbative Effekt kann im Rahmen einer nichtrelativistischen effektiven Feldtheorie beschrieben werden, die aus der vollständigen Quantenfeldtheorie abgeleitet werden kann. Wir diskutieren ausführlich die Berechnungen für das rechtshändige Sneutrino, welches der Superpartner des Neutrinos und zudem ein plausibler Kandidat für DM ist.

Wie wir zeigen werden, kann die Sommerfeld-Verstärkung einen tiefgreifenden Einfluss auf die thermische Entwicklung der DM haben, welche nicht länger durch ein herkömmliches Szenario beschrieben werden kann. Wir stellen ein Konzept vor, welches diesen Effekt korrekt berücksichtigt und wenden es auf ein einfaches leptophiles DM-Modell an. Ein neues Zeitalter der Paarvernichtung kann die Dichte der Dunklen Materie sogar noch nach dem herkömmlichen Ausfrieren senken und, für den Fall, dass die Sommerfeld-Verstärkung besonders groß ist, selbst bis nach dem Zeitpunkt des Gleichgewichts zwischen Materie und Strahlung andauern. Der Einfluss auf die asymptotische WIMP-Temperatur, welche direkt zu dem bei kleinen Skalen eingeführten Cutoff der Fluktuationen der Materiedichte in Beziehung gesetzt werden kann, bewirkt, dass die Masse der kleinsten gravitativ gebundenen Objekte größer ist als die, die aus herkömmlichen Berechnungen zu erwarten wäre.

Weiterhin untersuchen wir den Effekt der geschwindigkeitsabhängigen DM-Selbststreuung in Bezug auf die Strukturbildung auf kleinen Skalen. Numerische Simulationen der Λ CDM zeigen eine bemerkenswerte Übereinstimmung mit der Struktur des Universums auf großen Skalen. Allerdings sind die Simulationen nicht vollständig im Einklang mit den beobachteten Häufigkeiten, inneren Dichten und Geschwindigkeitsprofilen von Zwerggalaxien. Wir führen ein einfaches phänomenologisches Modell ein, welches in der Lage ist, sämtliche Probleme auf kleinen Skalen gleichzeitig zu lösen. Wichtige Bestandteile sind hierbei eine durch einen leichten Vektorboson vermittelte Sommerfeld-Verstärkung und eine viel später als im Normalfall stattfindende kinetische Entkopplung.

Abstract

Although the existence of Dark Matter (DM) has been confirmed by many independent observations on various scales, its nature still remains a mystery. Leading candidates for the cold, non-baryonic DM are Weakly Interacting Massive Particles (WIMPs), that are well motivated from particle physics and naturally explain the observed relic density by their thermal production mechanism.

In this thesis we focus on a particular class of WIMP models in which the Sommerfeld effect has to be taken into account. This is a quantum mechanical phenomenon that can significantly enhance the annihilation cross section in the non-relativistic limit. To describe the non-perturbative effect, we use a non-relativistic effective field theory derived from the full quantum field theory. We include a detailed discussion of the calculation for the right-handed sneutrino, which is the superpartner of the neutrino and a viable DM candidate.

As we will show, the Sommerfeld enhancement can have a profound influence on the thermal evolution of the DM, which can no longer be described by the standard scenario. We introduce a framework to correctly take this effect into account and apply it to a simple leptophilic DM model. A new era of annihilations can decrease the DM density even after usual freeze-out, and in some cases where the Sommerfeld enhancement is especially large, even continue until after matter-radiation equality. The effect on the asymptotic WIMP temperature, which can be directly related to a small scale cutoff in the matter density fluctuations, causes the mass of the smallest gravitationally bound objects to be larger than expected from standard calculations.

Furthermore we study the effect of velocity dependent DM self-scattering in relation to the small scale structure formation. Numerical simulations of Λ CDM have shown a remarkable agreement with the large scale structure of the Universe. However, the simulations are in tension with observed abundances, inner densities and velocity profiles of dwarf galaxies. We introduce a simple phenomenological model that is able to solve all small scale problems simultaneously. The important ingredients are a Sommerfeld enhancement mediated by a light vector boson, and much later kinetic decoupling than in the standard case.

Table of Contents

List of Publications	ix
List of Figures	xi
List of Tables	xvii
1 Introduction	1
2 Dark Matter	3
2.1 Introduction to Cosmology	3
2.2 Evidence for Dark Matter	7
2.3 Dark Matter properties and candidates	10
3 Weakly Interacting Massive Particles	13
3.1 Motivation and Dark Matter candidates	13
3.2 Basics of the Minimal Super Symmetric Model	15
3.3 Chemical decoupling	18
3.4 Kinetic decoupling	20
3.5 Detectional prospects	23
4 Structure formation in the Universe	27
4.1 Theory of structure formation	27
4.1.1 A cutoff in the power spectrum	32
4.1.2 The first protohalos	33
4.2 Numerical simulations of Λ CDM	35
4.3 Small-scale problems	40
4.3.1 Missing satellites problem	40
4.3.2 Cusps vs. Cores	43
4.3.3 ‘Too big to fail’-problem	45
5 Sommerfeld Enhancement	49
5.1 Introduction	49
5.2 Resummation of ladder diagrams	52
5.2.1 Preliminaries	52
5.2.2 Deriving the non-relativistic effective action	55
5.2.3 Two-body effective action	61
5.3 Annihilation and the enhancement factor	63

Table of Contents

5.4	Self-Scattering	69
6	Right-handed sneutrino Dark Matter	73
6.1	Introduction	73
6.2	A scalar toy model	76
6.3	Sommerfeld effect for right-handed sneutrino Dark Matter	79
6.3.1	Potential term	79
6.3.2	Annihilation term	82
6.4	Conclusions and discussion	88
7	Thermal decoupling of Sommerfeld enhanced Dark Matter	91
7.1	Interplay between chemical and kinetic decoupling	91
7.2	Leptophilic Dark Matter	95
7.2.1	Annihilation and the Sommerfeld enhancement	96
7.2.2	Dark Matter scattering off heat bath particles	96
7.2.3	Dark Matter self-scattering	97
7.2.4	Model constraints	98
7.2.5	Thermal evolution on and off resonance	99
7.2.6	Off resonance analysis	102
7.2.7	Resonance analysis	106
7.3	Conclusions and discussion	109
8	Sommerfeld enhanced Dark Matter and the small-scale problems of ΛCDM	111
8.1	Self-scattering Dark Matter with late kinetic decoupling	111
8.2	Model setup and results	114
8.3	Model building and particle physics bounds	118
8.4	Conclusions and discussion	119
9	Conclusions and outlook	121
A	Calculation of Sommerfeld effect	125
A.1	Quantum electrodynamics	125
A.1.1	Derivation of the non-relativistic effective action	125
A.1.2	Two-body effective action	131
A.2	Scalar toy model	134
A.3	Right-handed sneutrino Dark Matter	140
A.3.1	Box diagram with Z-boson intermediate states	140
A.3.2	Annihilation matrix	142
	Bibliography	145
	Acknowledgements	167
	Selbstständigkeitserklärung	169

List of Publications

[1] L. G. van den Aarssen, T. Bringmann, and Y. C. Goedecke, “Thermal decoupling and the smallest subhalo mass in dark matter models with Sommerfeld-enhanced annihilation rates,” *Phys.Rev.* **D85** (2012) 123512, arXiv:1202.5456 [hep-ph].

[2] L. G. van den Aarssen, T. Bringmann, and C. Pfrommer, “Is Dark Matter with Long-Range Interactions a Solution to All Small-Scale Problems of Λ Cold Dark Matter Cosmology?,” *Phys. Rev. Lett.* **109** (2012) 231301, arXiv:1205.5809 [astro-ph.CO].

List of Figures

2.1	Left: the circular velocities of the spiral galaxy Ngc-3198 flatten out at larger radii instead of decreasing like expected from the visible disk, implying the presence of an invisible halo component (taken from [3]). Right: this image of the Bullet cluster shows the hot baryonic gas (color) that got dragged behind in the collision of the two clusters, which is displaced with respect to the peaks in the mass distribution (green lines), indicating that the majority of the mass is collisionless. [4]	7
2.2	On the right-hand side the power spectrum of the anisotropies in the CMB is shown, which has a peak around $l \approx 200$, corresponding to angular scales of $\sim 1^\circ$ in the all-sky map (left) (source: NASA / WMAP)	10
3.1	Field content of the MSSM: for each SM particle there is a superpartner, plus an additional Higgs doublet and its superpartner. Table taken from [5].	15
3.2	The DM number density closely follows the equilibrium distribution until the annihilation rate can no longer compete with the expansion of the Universe. The value of $\langle \sigma v_{\text{rel}} \rangle$ around chemical decoupling determines the final relic abundance.	18
3.3	The standard evolution of T_χ as a function of x is shown for a typical DM particle with $m_\chi = 1$ TeV. The WIMP temperature closely follows the heat bath temperature until kinetic decoupling, which happens long after chemical decoupling ($x_{\text{kd}} \gg 25$) and on a rather short timescale. Afterwards, the WIMP temperature expands with the Universe, i.e., $T_\chi \propto a^{-2}$	22
3.4	Schematic overview of the mechanism behind three different kinds of WIMP detection. Indirect detection (orange) depends on the DM annihilation cross section, which also governs the chemical decoupling. The reverse process of WIMP production is considered in collider searches (green). WIMP scattering (blue) is the interaction that is responsible for kinetic decoupling and provides the basis for direct detection experiments.	24
4.1	The evolution of a large halo in the Millennium-II simulation is shown at three different length scales (indicated in top panels) at four different redshifts (indicated in first column) [6]. The cosmic structure on larger scales looks like a web, consisting of voids, filaments, and nodes. The hierarchical formation of structure is obvious; smaller structures form first and later collapse and merge into a larger halo.	37

List of Figures

4.2	Cumulative circular velocity function $N(> V_{\max})$ of subhalos for a host halo with $V_{\max} = 160$, and 208 km s^{-1} (solid, black). Circular velocities of MW satellites (pink stars) have been estimated from line-of-sight velocity dispersions (see text). Predicted subhalos at small V_{circ} are much more abundant than the observed MW dwarfs. Taken from [7]	41
4.3	Low surface brightness galaxies seem to agree better with pseudo-isothermal profiles (dotted lines) than with a NFW profile (solid line) or with an even cusper profile $\rho^{-1.5}$ (dashed). The data-points are taken from various studies. For more details, see [8], where this figure originates from.	44
4.4	The brightest dSphs in the MW (squares) all have a maximal circular velocity that is less than 24 km s^{-1} . The shaded bands indicate the rotation curves for the subhalos (assuming a NFW profile) with a 1σ deviation. Each of the simulated halos in the Aquarius simulation contains at least 10 subhalos that are much denser than the MW satellites, i.e., $V_{\max} > 24 \text{ km s}^{-1}$ [9].	46
4.5	Each panel shows the subhalo rotation curves with $V_{\text{infall}} > 30 \text{ km s}^{-1}$ and $V_{\max} > 10 \text{ km s}^{-1}$ for one simulated MW halo (mass indicated in upper left corner) in comparison with the observed dSphs (squares). No assumptions about the simulated DM density profiles were made, and subhalos comparable to the Magellanic clouds were excluded. Subhalos denser than the dwarfs by more than 2σ (solid lines) are much too dense to host any of the bright satellites. Among the remaining subhalos (dotted lines) there are also subhalos that do not correspond to any of the bright dwarfs. [9]	47
5.1	The white blob includes all short-range interactions, whereas the exchange of a mediator particle is a long-range effect. The grey blob includes all interactions with the Sommerfeld effect taken into account, which is obtained by performing a resummation over all possible ladder diagrams, where the mediator particles represent the rungs on the ladder.	49
5.2	The optical theorem relates the imaginary part of the forward scattering matrix element to the squared modulus of the matrix element that describes annihilation into all possible final states.	53
5.3	Tree level diagrams on the left correspond to kinematically allowed terms in S_{int} in Eq. (5.27) and cannot correctly be described by our non-relativistic theory due to their relativistic initial or final states. Combining them as indicated, we obtain a higher order diagram (right) with only non-relativistic initial and final states and relativistic virtual states that can be integrated out. The box diagram (top right) can be related to the annihilation diagram into two photons by cutting the diagram in half over the dashed line by using the optical theorem. The other two diagrams on the right correspond to interactions we are not interested in, and will therefore not be considered in our further discussion.	58
5.4	The different box diagrams that are described by the four-point correlation function: the t-channel diagrams (left) actually contribute the same amount to the four-point correlation function Eq. (5.29). The same is true for the u-channel diagrams on the right. For more information, see Appendix section A.1.	59

5.5	Left: Full numerical Sommerfeld factor as a function of ϵ_ϕ for different values ϵ_ν . It can be seen that the enhancement factor increases for smaller values of ϵ_ν and ϵ_ϕ . Resonances appear for specific values of ϵ_ϕ and sufficiently small values of ϵ_ν . Right: Plotting the Sommerfeld factor as a function of ϵ_ν one can clearly see the saturation of the factor for small enough values of ϵ_ν , in contrast to the analytical solution for the Coulomb potential (black, dashed). For large enough values of ϵ_ν the numerical solution is well approximated by the Coulomb enhancement. Off resonance (blue, yellow) the enhancement factor grows like $1/v$ for $v \rightarrow 0$, whereas on a resonance (green) it follows a $1/v^2$ behavior. When the configuration is near, but not precisely on resonance, there is a transition from $1/v$ to $1/v^2$ behavior when ϵ_ν decreases (red).	67
5.6	An overview of different approximations to the transfer cross section as a function of v for a model with DM mass $m_\chi = 1$ TeV, mediator mass $m_\phi = 1$ MeV, and coupling $\alpha = 0.028$. The min (blue, dashed) and max (red, dotted) approximations from [10] are in good agreement with the approximation σ_{tr} (black) from [11, 12] in the intermediate regime $10^{-7} \lesssim v \lesssim 10^{-1}$. The full cross section becomes independent of v for values $v \lesssim 10^{-6}$ and approaches the asymptotic value of σ^{pot} (purple, dashed), such that the other approximations become invalid in this region. The conservative approach described in the text corresponds to taking $\sigma^{\text{pot}}(v \rightarrow 0)$ in the low velocity regime, and σ_{min} for higher velocities, where the transition is defined by the intersection point between these two curves. For completeness the transfer cross section for a resonance is shown in green.	72
6.1	All possible couplings between the two sneutrino species and the h and Z boson. For clarity shorthand notations for the couplings c.f. Eq. (6.13) - (6.17) are included.	76
6.2	On the left, the potential diagram with light scalar (red) exchange between the heavy scalars (blue) in the t-channel. On the right, the box diagram is shown that relates to the annihilation of two h into two l by cutting the diagram along the black dashed line. The arrows denote the direction of momentum.	78
6.3	Diagrams that contribute to the potential matrix for h (left) and Z (right). Note that the Higgs boson does not mediate $\tilde{\nu}_2 \tilde{\nu}_2^* \rightarrow \tilde{\nu}_2 \tilde{\nu}_2^*$ scattering (see Eqs. (6.13) - (6.17)), such that the diagram corresponding to V_{22}^h does not exist.	81
6.4	Box diagram for higgs (left) and Z -boson (right) intermediate states. All initial, final and relativistic states are indicated with corresponding subscripts, and the direction of the momenta are indicated with arrows. The box diagrams are cut along the dashed line.	82
6.5	All box diagrams that correspond to annihilation to hh , ordered according to the matrix element to which they belong. The fact that $A_{22} = 0$ restricts the total number of box diagrams to nine.	84
6.6	All sixteen box diagrams that correspond to annihilation to ZZ . Each matrix element Γ_{ij}^Z contains the sum of four possible diagrams which differ by the virtual sneutrino states l, k exchanged in the t-channel.	85

List of Figures

6.7	Full solutions for the hh annihilation matrix elements as a function of the lightest sneutrino mass \tilde{v}_1 and the mass difference between the two sneutrino generations δm . Values of $A_{\tilde{\nu}} = 100$ and $m_{\tilde{L}} = 1$ TeV were used throughout the calculation. It can be seen that all box diagrams give rather similar contributions for small mass differences.	86
6.8	Contour plots showing full solutions for the ZZ annihilation matrix elements as a function of the lightest sneutrino mass \tilde{v}_1 and the mass difference between the two sneutrino generations δm . A mixing angle $\theta_{\tilde{\nu}}$ was used with $m_{\tilde{L}} = 1$ TeV and $A_{\tilde{\nu}} = 100$. Γ_{22}^Z is dominant since no electroweak symmetry breaking effects are necessary for this process to occur.	87
7.1	The Hubble rate (black) is shown in comparison to the effective DM self-scattering rate from Eq. (7.20) as a function of temperature. The minimal (red) and maximal (blue) possible self-scattering rates for the leptophilic model are plotted for the on- and off-resonant case as dashed and dotted lines, respectively. Once the self-scattering rate becomes comparable to the Hubble rate, i.e. $\Gamma_s(T_{\text{nt}}) \sim H(T_{\text{nt}})$ the DM velocity distribution starts to deviate from a Maxwellian form. For resonant Sommerfeld enhancements this occurs even after matter-radiation domination, which is indicated by a dash-dotted line [1].	97
7.2	The full numerical solution for the Sommerfeld factor (solid) and two analytic approximations (dotted, dashed) are shown for $m_\chi = 1$ TeV, $m_\phi = 5$ GeV and $\alpha = 0.03$ [1].	100
7.3	For a parameter set where the Sommerfeld enhancement is not near a resonance ($m_\chi = 1$ TeV, $m_\phi = 5$ GeV, $\alpha = 0.03$, and $g_\ell = 10^{-7}$), we show the evolution of the relic density Y (as defined in Eq. (3.17)), and the WIMP temperature y (as defined in Eq. (3.23)). The solution to the full set of coupled Boltzmann equations (black) is shown in comparison to the solution to the standard, uncoupled equations (blue). As a further approximation we show results for assuming sudden kinetic decoupling (red; not visible in left-hand plot). Different approximations to the Sommerfeld enhancement are shown according to Fig. 7.2 by dotted, dashed, or solid lines. Additionally, the solution without Sommerfeld enhancement is shown in the left-hand panel (green, dash-dotted) [1].	101
7.4	We show the same results as in Fig. 7.3, but now for a parameter set where the Sommerfeld enhancement is resonant ($m_\chi = 1$ TeV, $m_\phi = 1$ GeV, $\alpha = 0.00168$ and $g_\ell = 4.6 \times 10^{-5}$). The full solutions show a significant difference with the standard calculation for $x \geq 10^7$; after kinetic decoupling a new era of annihilations takes place and simultaneously the WIMP temperature increases again. Annihilations even continue until after matter-radiation equality (denoted as a gray, dash-dotted line). In the right-hand panel, the intersection of the asymptotic WIMP temperature (green, dash-dotted) with the temperature of the heat bath (red, dotted) denotes T_{dec}^∞ as defined in Eq. (7.15) [1].	101

7.5 For models where the Sommerfeld enhancement is not on a resonance, the kinetic decoupling temperature is shown as a function of the mediator particle coupling to leptons, for $m_\phi = 100$ MeV (black, full), 500 MeV (blue, dashed), 1 GeV (red, dotted), and 5 GeV (green, dash-dotted). From bottom to top, the lines correspond in each case to a DM mass of $m_\chi = 100, 500, 1000, 5000$ GeV [1]. 103

7.6 For off resonance models, the ratio of the uncoupled solution for the relic DM abundance is shown w. r. t. the coupled solution as a function of the kinetic decoupling temperature. Each panel shows the results for one particular mediator mass m_ϕ (indicated in panel, color coding matches that of Fig. 7.5). The ratio increases for earlier kinetic decoupling, since the restarted annihilations can then continue for a longer time before the Sommerfeld enhancement saturates. The maximal (minimal) ratio is obtained for the highest (lowest) DM mass m_χ (see legend). The dependence of the ratio on x_{kd} , however, depends highly on the DM coupling and thus the magnitude of the Sommerfeld enhancement; for a fixed m_ϕ and m_χ , each ‘chain’ of markers is defined by a particular value of α . See text for more details. 103

7.7 Same as Fig. 7.6, but here the saturation temperature as a function of kinetic decoupling is shown for the off resonance models. As expected, the saturation happens later for earlier decoupling, since the era of annihilations will be more pronounced. Since large Sommerfeld enhancements are obtained for small values of $m_\phi/(\alpha m_\chi)$, the saturation temperature increases for smaller mediator masses and large DM masses. 104

7.8 For models where the Sommerfeld enhancement is not on a resonance, the cutoff mass is shown as a function of the lepton coupling, for $m_\phi = 100$ MeV (black, full), 500 MeV (blue, dashed), 1 GeV (red, dotted), and 5 GeV (green, dash-dotted). From top to bottom, the lines correspond in each case to a DM mass of $m_\chi = 100, 500, 1000, 5000$ GeV [1]. 105

7.9 For models where the Sommerfeld enhancement is resonant, the kinetic decoupling temperature T_{kd} (filled) in comparison to the effective asymptotic decoupling temperature T_{dec}^∞ (empty) is shown. Again $m_\phi = 100$ MeV (black, squares), 500 MeV (blue, circles), 1 GeV (red, diamonds), and 5 GeV (green, triangles). Comparing this figure to Fig. 7.5, we see that here T_{kd} is a little bit higher, however T_{dec}^∞ , which determines the mass of the first protohalos, is in general lower. For more details, see text. 106

7.10 Same as Fig. 7.6, but now for models where the Sommerfeld enhancement is on a resonance and the correct relic density is obtained. As expected, there is a vast difference between the coupled and uncoupled solutions for the relic density, with ratios ranging from ~ 2 up to almost $\sim 10^3$. Again, smaller relic densities are obtained in models where kinetic decoupling happens earlier. 107

List of Figures

7.11	The cutoff mass M_{cut} as a function of the lepton coupling for models where the Sommerfeld enhancement is resonant, for $m_\phi = 100$ MeV (black, squares), 500 MeV (blue, circles), 1 GeV (red, diamonds), and 5 GeV (green, triangles). The values of M_{cut} are in general higher than in the off resonance case shown in Fig. 7.8 due to the lower values of asymptotic decoupling temperatures.	107
8.1	Cutoff mass M_{cut} as a function of the lepton coupling g_ℓ for Sommerfeld enhanced models where the mediator is a vector boson with a mass $m_V = 10$ keV (green), 100 keV (blue), or 1 MeV (purple). When the DM only couples to electrons, the cutoff mass reaches an asymptotic value of $\sim 10^5 M_\odot$ due to the Boltzmann suppression of the electron number density. However, when neutrino scatterings are taken into account, the cutoff scale grows steadily with larger values of g_ℓ and can reach values up to order $\sim 10^{16} M_\odot$. Different values of DM mass, $m_\chi = 3$ TeV (solid) and 10 TeV (dashed), hardly make any difference. . .	113
8.2	The relic density is set by the Sommerfeld enhanced annihilation of DM into vector bosons, which eventually decay into neutrinos (left). The properties of dwarf halos are affected by the induced DM self-scattering, which changes inner velocity and density profiles (middle), and DM scattering off neutrinos, which suppresses the formation of small subhalos (right). [2]	114
8.3	Models with DM and mediator masses that lie in the white area may be able to solve the ‘cusp vs. core’ problem without being ruled out by astrophysical bounds. The two crosses denote benchmark models from [13] for which detailed simulations have shown that they additionally solve the ‘too big to fail’ problem. Dashed and solid lines show contours of the astrophysical relevant quantities σ_{max}^T and v_{max} . Figure taken from [2].	115
8.4	Contour lines of different values of M_{cut} are shown as a function of mediator mass m_V and coupling strength g_V . Large values of g_V and small values of m_V lead to late kinetic decoupling and thus a large mass M_{cut} of the smallest protohalos. Lyman- α data excludes $M_{\text{cut}} \gtrsim 5 \times 10^{10} M_\odot$, while $M_{\text{cut}} \gtrsim 10^9 M_\odot$ may solve the small-scale abundance problems of Λ CDM cosmology [2].	117

List of Tables

7.1 For the leptophilic model and parameter ranges considered here, we show an overview of the resulting ranges of the decoupling temperatures, change in relic density with respect to the standard calculation, and the smallest subhalo masses, where we considered non-resonant and resonant Sommerfeld enhancements separately [1]. 108

1 Introduction

Probably one of the most interesting puzzles of modern science is the existence of Dark Matter (DM) in our Universe. Since the DM is non-luminous – hence the name *dark* – its presence is only revealed by the gravitational interaction it exerts. There is an overwhelming amount of observational evidence taken over a wide range of distance scales (to be discussed in chapter 2) that have confirmed $\sim 23\%$ of the Universe to be in the form of this cold, non-baryonic DM. Although we quite accurately know the present abundance of DM, we hardly know anything about its Nature. One of the most attractive theories is to assume the DM consists of Weakly Interacting Massive Particles (WIMPs) that are very heavy and barely interact with ordinary matter.

Interestingly, WIMPs quite naturally explain the observed DM abundance by their thermal production mechanism. Shortly after the Big Bang, WIMPs are in chemical equilibrium with the Universe and their density decreases as the DM is annihilated into other particles. At some point, however, the annihilation rate falls behind the Hubble expansion rate and the abundance ‘freezes out’, i.e., it remains fixed for the rest of time. After this *chemical* decoupling, the DM still frequently scatters off heat bath particles, which keeps them in local thermal equilibrium. Only after a very long time these reactions also fail to be effective and the DM *kinetically* decouples from the heat bath. The temperature at which this happens is directly related to a small scale cutoff in the matter density fluctuations, from which the mass of the first gravitationally bound objects can be determined. In chapter 3, we will make the reader familiar with WIMPs and their standard, thermal evolution.

Since the amount of DM is so large compared to the ordinary matter, it plays an important role in the formation of structure. Numerical simulations that include the observed amount of DM and a cosmological constant Λ have shown to be very successful: besides recreating the large scale structure, they can explain many other important cosmological observations, such as the existence and structure of the cosmic microwave background, the abundance of light elements, and the accelerating expansion of the Universe. This so-called Λ CDM or ‘cosmological concordance’ model is therefore viewed as a cornerstone of modern science.

Lately, however, it has been shown that the Λ CDM is in tension with observations on smaller scales. Simulations predict a larger abundance of DM satellites than the observed dwarf galaxies to which they should correspond. In addition, the inner density of these small satellites follow a cuspy profile, which seems to be in tension with observed density cores in dwarfs. Recently it was realized that the most massive satellites in the simulations are far too dense to correspond to the brightest dwarf galaxies in our Milky Way, i.e., their velocity profiles do not match. These small scale problems pose a serious threat to the otherwise so successful Λ CDM model. We will discuss the formation of structure and the small scales problems in chapter 4.

In this thesis, we focus on a particular class of WIMP models that feature a quantum mechanical effect named after its discoverer Arnold Sommerfeld, and study its influence on the above

1 Introduction

mentioned cosmological processes. In these models, the DM is able to interact through a light force carrier, which increases the probability for the WIMPs to undergo a short range interaction. This non-relativistic effect causes the DM annihilation rate to be increased by a velocity dependent enhancement factor, which can become incredibly large in the special case that the two DM particles form a quasi bound state. Since the DM annihilation rate is important for the calculation of the relic abundance and indirect detection of DM, the Sommerfeld effect can thus have a profound effect on the phenomenology of the DM model. We will therefore spend chapter 5 on explaining this effect in detail.

The Sommerfeld effect is caused by the multiple exchange of mediator particles between the DM and is often visualized in so-called ladder diagrams. Since this is a non-perturbative effect, one has to perform a resummation over all possible ladder diagrams in order to correctly describe the effect. We will show it is equivalent to use a renormalized non-relativistic effective theory derived from the full quantum field theory. In chapter 6 we will perform this calculation for a particular WIMP, namely the right-handed sneutrino, the superpartner of the neutrino, which arises in certain supersymmetric theories.

Since the thermal history of the DM depends greatly on the particle physics details, it is expected that the Sommerfeld effect can influence the relic DM density and the formation of the smallest DM objects. When the DM annihilation rate depends on the velocity of the WIMPs, it generates a complicated feedback between the DM abundance and its temperature. In chapter 7 we discuss the non-standard thermal decoupling in Sommerfeld enhanced DM models and introduce a new set of equations that takes the interplay between chemical and kinetic decoupling correctly into account. To illustrate our treatment, we use it on a simple Sommerfeld enhanced DM model and show that the thermal evolution is very different from the standard scenario. We find that in models with a velocity enhanced annihilation rate, a new era of annihilations occurs after regular freeze-out that can decrease the relic density by a significant amount. This correspondingly influences the asymptotic WIMP temperature in such a way, that the mass of the first DM halos can be larger than expected.

Furthermore, the Sommerfeld effect induces velocity dependent DM self-scattering that alters small scale structure formation in numerical simulations of Λ CDM. As a result, the velocity and inner density profiles of small subhalos are in better agreement the observed dwarf properties. In chapter 8 we will investigate the particle physics parameter space for which Sommerfeld enhanced DM can solve these two internal density problems effectively. Moreover, we present a simple, phenomenological model that is able to additionally solve the satellite abundance problem. We find that the key ingredients are velocity dependent self-interactions mediated by a light vector boson and very late kinetic decoupling. The latter is needed to suppress the formation of small subhalos such that they do not exceed the observed abundance of dwarf galaxies. In this way, we are able to solve all small scale problems for the first time by a single model, which might help to save the Λ CDM from its downfall.

Finally, we summarize our findings and give an outlook in chapter 9. Detailed calculations of the Sommerfeld enhancement for various models discussed in this work can be found in Appendix A. Note that in this study we work in units where $c = \hbar = k_B = 1$. The results presented in this thesis are based on two papers, which I co-authored and have been published in refereed journals [1, 2].

2 Dark Matter

By now, the existence of Dark Matter (DM) has been established on many different scales in our Universe. After giving a short introduction to cosmology, we will briefly review the most important evidence, and discuss the DM properties we can infer from them in this chapter. An excellent book on cosmology is, e.g., [14]. For more information on the current status of DM evidence, candidates and constraints see [15, 16], and [17] for observational constraints and detection methods.

2.1 Introduction to Cosmology

Our picture of the Universe is based on the *cosmological principle*, which states that it is homogeneous and isotropic on large scales. The isotropy can be inferred from various observations of e.g. large scale structure [18] and the cosmic microwave background (CMB) radiation [19]. The latter consists of photons that last scattered off electrons some 380.000 years ago, and traveled through space ever since. Measurements show that the CMB has an (almost) perfect thermal black body spectrum with a temperature of 2.75K. The high degree of isotropy of the CMB reflects the homogeneity and isotropy of the Universe at the time of last scattering (see also section 2.2)). Homogeneity follows from the assumption that the earth is not in a particular special place, such that the Universe is the same from whatever place you look at it.

The geometry of spacetime in such a Universe is well described by the *Friedmann-Robertson-Walker* (FRW) metric

$$ds^2 = g_{\mu\nu}dx^\mu dx^\nu = -dt^2 + a^2(t) \left[\frac{dr^2}{1 - kr^2} + r^2 d\Omega^2 \right], \quad (2.1)$$

with $d\Omega^2 \equiv d\theta^2 + \sin^2 \theta d\phi^2$. The coordinates t, r, θ, ϕ are co-moving, which means they do not change during the evolution of the Universe. The scale factor $a(t)$ is a measurement of the size of the Universe at t , and the curvature constant k reflects the geometry of the Universe, i.e., $k = -1, 0, 1$ for an open, flat and closed Universe.

The physical distance between an observer at the origin and an object at a distance r is then given by

$$d_{\text{phys}}(r, t) = a(t) \int_0^r \frac{dr}{\sqrt{1 - kr^2}}. \quad (2.2)$$

Since the origin is no special place, all physical distances between co-moving objects are proportional to $a(t)$, and their rate of change is given by $\dot{d}_{\text{phys}} = d_{\text{phys}}\dot{a}/a$, where a dot denotes the derivative d/dt .

The evolution of the of the scale factor can be derived by assuming the Universe consists of a perfect fluid. The energy momentum tensor $T^{\mu\nu}$ is then completely determined by the energy

2 Dark Matter

density ρ and pressure p of the fluid. Imposing energy conservation, we obtain

$$\dot{\rho} + 3\frac{\dot{a}}{a}(p + \rho) = 0, \quad (2.3)$$

where the equation of state has to obey

$$p = w\rho. \quad (2.4)$$

With these two equations one can derive that the density evolves as

$$\rho \propto a^{-3(1+w)}. \quad (2.5)$$

In our Universe we distinguish between three different components that each evolves in its own way. Cold matter (e.g., dust) has zero pressure, $p_m = w_m = 0$, and therefore evolves like $\rho_m \propto a^{-3}$. Radiation is a form of hot matter, defined by the equation of state $p_r = \rho_r/3$, and correspondingly evolves as $\rho_r \propto a^{-4}$. Furthermore, there exists a component for which $w_\Lambda = -1$, such that ρ_Λ is constant. This is referred to as vacuum energy.

Whether the scale factor increases, decreases, or stays constant with t , can be inferred from observations of the light from distant galaxies. The frequency ν_1 of this light emitted at time t_1 will be affected by the change in the scale factor, such that the frequency ν_0 at which it is observed at t_0 is given by

$$\frac{\nu_0}{\nu_1} = \frac{a(t_1)}{a(t_0)} \equiv 1 + z. \quad (2.6)$$

If $a(t)$ increases (decreases) with time, this quantity is positive (negative) and the the frequency is redshifted (blueshifted). Since we observe the light at present, the scale factor today is usually denoted by $a(t_0) = a_0 \equiv 1$.

For nearby sources we can Taylor expand the scale factor, such that we obtain the relation

$$z = H_0 d_{\text{phys}} + \dots, \quad (2.7)$$

where H_0 is the *Hubble parameter* today

$$H_0 \equiv \frac{\dot{a}(t_0)}{a(t_0)} = 100 h \text{ km s}^{-1} \text{ Mpc}^{-1}. \quad (2.8)$$

Observations show that spectral lines of galaxies are redshifted; the quantity z is thus positive [20, 21]. Objects in space are receding from us and from each other, which means that our Universe is actually expanding, i.e. $\dot{a} > 0$.

If we reverse this argument, it would suggest that our Universe started out in a much denser state with $a \rightarrow 0$, more generally known as the *Big Bang*. Light that has propagated towards us since the Big Bang characterizes the maximal length that any information in the Universe could have traveled. This is also known as the *particle horizon*

$$d_H(t) = a(t) \int_0^t \frac{dt'}{a(t')} = d_{\text{phys}}(r(t), t), \quad (2.9)$$

where $d_{\text{phys}}(r_{1,t})$ is given by Eq. (2.2), and the light was emitted at a distance $r(t)$.

In order to determine the dynamics of the expansion of the Universe, we need to include Einstein's theory of gravity, which is described by

$$R_{\mu\nu} - \frac{1}{2}Rg_{\mu\nu} + \Lambda g_{\mu\nu} = 8\pi G_N T_{\mu\nu}, \quad (2.10)$$

where $R_{\mu\nu}(R)$ is the Ricci tensor (scalar) and G_N is the gravitational constant. The cosmological constant Λ was first introduced in 1917 by Einstein in order to obtain a static solution for the Universe. The observation of the Hubble redshift of galaxies few years later led Einstein to abandon his idea of a static Universe and famously call the cosmological constant the ‘‘biggest blunder’’ of his life. It was only after measuring the distance-redshift relation of Type Ia supernovae that it became clear that the expansion of our Universe is actually accelerating [22, 23], implying a non-zero cosmological constant after all.

After substituting Eq. (2.1) into Eq. (2.10), we arrive at the *Friedmann equations* [24]

$$\left(\frac{\dot{a}}{a}\right)^2 = H^2(t) = \frac{8\pi G_N}{3}\rho(t) + \frac{\Lambda}{3} - \frac{k}{a^2}, \quad (2.11)$$

$$\frac{\ddot{a}}{a} = -\frac{4\pi G_N}{3}(\rho + 3p) + \frac{\Lambda}{3}, \quad (2.12)$$

which describe the evolution of the scale factor. The cosmological constant is usually expressed in terms of the vacuum energy with $\rho_\Lambda = -p_\Lambda = \Lambda/(8\pi G_N)$ as discussed above. It is useful to define the critical density today as $\rho_c \equiv 3H_0^2/(8\pi G_N)$ such that Eq. (2.11) transforms into

$$\Omega + \Omega_\Lambda = 1 + \frac{k}{\dot{a}^2}, \quad (2.13)$$

where all energy densities are expressed in terms of the critical density, i.e. $\Omega \equiv \rho/\rho_c$ and $\Omega_\Lambda = \rho_\Lambda/\rho_c$. Measurements show that the density of our Universe is actually very close to the critical density such that all contributions add up to one: $\Omega_M + \Omega_r + \Omega_\Lambda = 1$ [19]. This means the Universe is very close to being spatially flat, i.e. $k = 0$. Moreover, it is comprised of roughly $\sim 25\%$ matter and $\sim 75\%$ vacuum density at present. Cosmological models with this set of parameters have shown to give results that in very good agreement with the Universe as we observe it. The Λ CDM *model* of cosmology is therefore viewed as the standard model of the Universe.

Looking at the different scaling with a of the various components of the Universe, we can infer that the curvature and vacuum density can be neglected for small enough a . From Eq. (2.11) we thus infer that at early times the density was very close to the critical density. The fact that this has not changed in the course of the history of the Universe until today is puzzling, and also referred to as the flatness problem [25]. Inserting then the scaling behavior from Eq. (2.5) into the first Friedmann equation, we find that

$$a(t) \propto t^{\frac{2}{3(1+w)}}, \quad (2.14)$$

for a matter or radiation dominated era. In this case, Eq. (2.9) can be approximated by the

2 Dark Matter

Hubble radius $d_H \approx H^{-1}$, since the scale factor follows a power law. Assuming a vacuum energy dominated era, however, the scaling factor is given by $a(t) \propto \exp Ht$ with H a constant, such that it corresponds to an accelerated expansion of the Universe.

A period of accelerated expansion before the Big Bang, also known as *inflation*, could explain why the Universe is so flat and isotropic today [25]. It also predicts that quantum fluctuations that were present before inflation are the origin of tiny temperature anisotropies ($\delta T/T \sim 10^{-5}$) in the CMB. These correspond to density fluctuations in the cosmic fluid at the time of recombination, and serve as initial conditions for the evolution of structure and anisotropy in the Universe. The formation of structure will be further discussed in chapter 4.

Right after the Big Bang, radiation dominated the energy budget, and the entropy density was given by

$$s(T) = \frac{2\pi^2}{45} g_{*S}(T) T^3. \quad (2.15)$$

where g_{*S} are the entropy degrees of freedom. Using the fact that in thermal equilibrium the entropy in a co-moving volume is conserved, i.e. $\partial_t (sa^3) = 0$, we can derive that

$$T \propto g_{*S}^{-1/3} a^{-1}. \quad (2.16)$$

Thus, the temperature of the Universe increases for earlier times, which corresponds to the picture of a *hot* Big Bang. Together with entropy conservation, the first Friedmann equation can be integrated to give

$$t = - \int \frac{s'(T) dT}{s(T) \sqrt{24\pi G_N \rho_r T}}, \quad (2.17)$$

where the radiation energy density is given by

$$\rho_r = \frac{\pi^2}{30} g_{\text{eff}} T^4. \quad (2.18)$$

The effective degrees of freedom $g_{\text{eff}}(T)$ are calculated from all particle species that contribute to the radiation density at T . Assuming it to be constant, which is a reasonable approximation as long as no radiative particle species become non-relativistic, one can start to unravel the thermal history of the Universe.

A very important result is Big Bang Nucleosynthesis (BBN), which correctly predicts the abundance of light elements [26]. In the beginning the Universe was so hot and dense, that neutral atoms or bound states would immediately be destroyed by the radiation. As the Universe expanded and cooled down below the binding energy of nuclei, light elements such as Deuterium (D or ^2H), Helium (^3He and ^4He) and Lithium (^7Li) started to form. The predictions from BBN, which strongly depend on the baryon-to-photon ratio $\eta \equiv n_B/n_\gamma$, are in very good agreement with the observed elements in the Universe. In addition, it gives a very accurate prediction for the baryon density.

In the rest of this chapter we will focus on the matter component on the Universe. In section 2.2 we will see that there is overwhelming evidence for a large *invisible* matter component, which will be quantified in section 2.3.

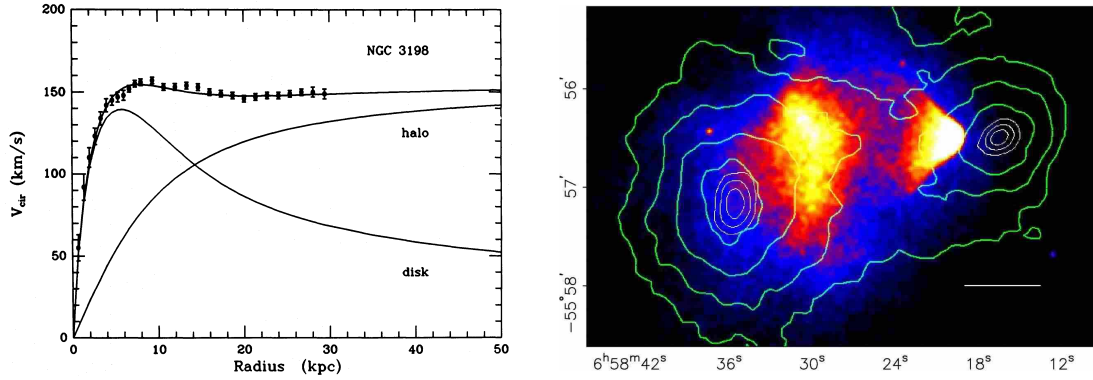


Figure 2.1: Left: the circular velocities of the spiral galaxy NGC-3198 flatten out at larger radii instead of decreasing like expected from the visible disk, implying the presence of an invisible halo component (taken from [3]). Right: this image of the Bullet cluster shows the hot baryonic gas (color) that got dragged behind in the collision of the two clusters, which is displaced with respect to the peaks in the mass distribution (green lines), indicating that the majority of the mass is collisionless. [4]

2.2 Evidence for Dark Matter

Perhaps the most compelling evidence for DM, at least on galactic scales, can be found in observations of galaxy rotation curves. Newtonian dynamics predicts that the circular velocity of stars in a galaxy behave like

$$v_c = \sqrt{\frac{G_N M(r)}{r}}, \quad (2.19)$$

as a function of their distance r to the galactic center and $M(r) \equiv 4\pi \int_0^r d\tilde{r} \rho(\tilde{r}) \tilde{r}^2$ is the total mass of the system inside the radius r . Assuming that the visible matter comprises all of the matter in the galaxy, the circular velocity should scale like $v_c \propto 1/\sqrt{r}$ beyond the visible disc. However, as it was first observed by Vera Rubin and coworkers [27] in 1980, the circular velocity profiles of many galaxies instead show a different behavior. At larger radial distances the circular velocities become independent of r instead of decreasing with it (see Fig. 2.1), implying the presence of more matter than what is optically observed. This much larger, invisible halo must have a mass that scales like $M(r) \propto r$ (or a density profile $\rho \propto r^{-2}$)¹.

Although the DM density profiles on large distances from the center are quite well known, the inner density profile is prone to larger uncertainties. In this region, the density is often dominated by baryons, making it more difficult to extract information on the behavior of DM. Even for Low Surface Brightness (LSB) galaxies that are among the most DM dominated objects in the Universe, it is still not possible to resolve the inner DM structure. In subsection 4.3.2 this issue will be discussed in more detail.

The first evidence of DM, however, was obtained on scales of galaxy clusters. In 1933, Fritz Zwicky estimated the mass of the Coma cluster by making use of the virial theorem [28]. The

¹At even larger distances the profile should be steeper than $\rho \propto r^{-3}$ in order to prevent a divergent total halo mass.

2 Dark Matter

average kinetic energy of the galaxies in the cluster

$$\langle T \rangle \approx \frac{3}{2} m \sigma^2, \quad (2.20)$$

can be obtained by observing the radial velocity distribution $v_{\text{obs}} = v_0 \pm \sigma$ of individual galaxies with an average mass m . From the virial theorem, $\langle T \rangle = -\langle V \rangle/2$, one can then infer the total mass of the galaxy cluster M , since the average gravitational potential is well approximated by

$$\langle V \rangle \approx -\frac{GmM}{R/2}, \quad (2.21)$$

where R is the radius of the cluster. The resulting estimation for the cluster mass is then independent of the average mass of the member galaxies,

$$M \approx \frac{3R\sigma^2}{2G}. \quad (2.22)$$

Using this method, Zwicky derived a mass-to-light ratio for the Coma cluster that was two orders of magnitude larger than that of the solar neighborhood: $M/L \sim 400 M_\odot/L_\odot$. Even though more recent analyses are consistent with values of $M/L \sim 200 - 300 M_\odot/L_\odot$, this still hints towards the presence of a large quantity of invisible matter in the Coma cluster (see e.g. [15] and references therein).

Another way to estimate the mass of a galaxy cluster is to study the X-ray emission of the hot gas in the system. Considering an ideal gas with pressure $p = nT$ and density $\rho(r)$, it should obey

$$p' = -\rho(r)\Phi' = -\rho(r)\frac{GM_b(r)}{r^2}, \quad (2.23)$$

in hydrostatic equilibrium, where $M_b(r)$ is the mass of the (baryonic) gas in the cluster. We can express the density of the gas (which we assume to be fully ionized) in terms of the average molecular weight $\mu \equiv \rho/(m_p n)$, where m_p is the proton mass and n is the number density of all charged particles in the gas. Eq. (2.23) then becomes:

$$\frac{T'}{T} + \frac{\rho'}{\rho} = -\frac{\mu m_p}{T} \frac{GM_b(r)}{r^2}. \quad (2.24)$$

Observations show that the gas-density scales like $\rho \propto r^{-n}$, with $n \approx 1.5 - 2$ at large radii, and that the temperature becomes independent of r outside the core. Assuming that the gas consists of 25% helium and 75% hydrogen, we can use $\mu \approx 0.6$. Inserting these numbers in the above equation, one obtains

$$T \approx (1.3 - 1.8) \text{ keV} \left(\frac{M_b(r)}{10^{14} M_\odot} \right) \left(\frac{\text{Mpc}}{r} \right), \quad (2.25)$$

which we can compare to temperature measurements of clusters. These are however much larger, and typically of the order $T \approx 10$ keV. Again, the only explanation for this temperature difference is that a considerable amount of mass must be present in addition to the baryonic gas,

in order to keep it contained in the cluster.

The two methods described above are complemented by weak gravitational lensing measurements, where the mass is inferred from distortions of background images that are caused by the gravitational potential of the cluster. Unsurprisingly, these results also show a large discrepancy between the total and visible mass on cluster scales.

The cluster merging system 1E0657-558 – more commonly known as the ‘Bullet Cluster’ – is a very striking evidence of DM and its collisionless property [29, 4]. It consists of 2 gravitationally bound clusters, of which the smaller one fell into the larger one some $\sim 10^8$ years ago and subsequently passed through it. Optical and X-ray images of the system tracing the gas in the two clusters indeed show deformations of the plasma that were created by the collision. The characteristic cone-like shape of the hot gas from the smaller cluster – reminiscent of the shock wave created by bullet – gave the system its popular name. Measurements of the mass peaks of the merger system, however, reveal a totally different behavior. Gravitational lensing images show that the center of mass of the two clusters are significantly displaced with respect to the hot gas (Fig. 2.1), indicating that the dominant component of the mass is not made up by the baryonic plasma and has only very weak interactions with it.

Although all observations described above strongly support the existence of DM, they cannot quantify the total amount of DM in our Universe. Fortunately, this information can be inferred from the analysis of the CMB. Discovered by Arno Penzias and Robert Wilson in 1965 [30], the background radiation originates from the time shortly after recombination ($z_r = 1090$), when the Universe became transparent for the first time. Before recombination, the photons and baryons were tightly coupled such that temperature fluctuations in the plasma oscillated with the speed of sound. At recombination, the photons decoupled from the baryons and the acoustic oscillations left their imprint on both the the CMB and the structure of the Universe.

The latter appears as Baryon Acoustic Oscillations (BAO) in the matter power spectrum, which is derived from the distribution of galaxies across the Universe and provides insight on the cosmic structure [31]. An initial spherical density perturbation in the cosmic fluid is subject to acoustic oscillations generated by the interplay of gravity and radiative pressure. Before recombination, the latter causes the baryon-photon density fluctuation to move outwards in a spherical shell, leaving the DM perturbation mostly intact. This movement continues until recombination removes the driving force behind the baryons, leaving a shell of baryons at a characteristic radius. The result is a slight increase of structure at a distance scale of ~ 150 Mpc, which is visible in the matter power spectrum [32].

In 1992 the Cosmic Background Explorer (COBE) measured temperature fluctuations of order $\delta T/T \sim 10^{-5}$ in the CMB [33, 34]. The observed anisotropies can be expanded in spherical harmonics

$$\frac{\delta T(\theta, \phi)}{T} = \sum_{l,m} a_{lm} Y_{lm}(\theta, \phi), \quad (2.26)$$

where the coefficients a_{lm} seem to follow a Gaussian distribution, and the variance C_l is given by

$$\langle a_{lm} a_{l'm'}^* \rangle = C_l \delta_{ll'} \delta_{mm'}. \quad (2.27)$$

All the information that the CMB contains can then be expressed by the power spectrum of the temperature fluctuations, i.e., C_l as a function of the multipole number l , as shown in Fig. 2.2 on

2 Dark Matter

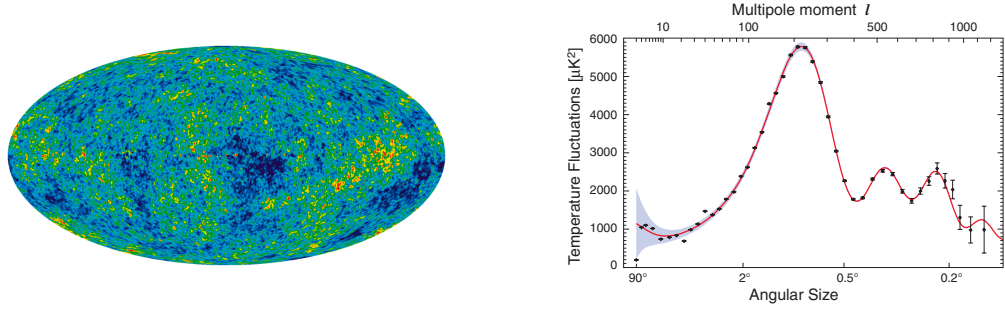


Figure 2.2: On the right-hand side the power spectrum of the anisotropies in the CMB is shown, which has a peak around $l \approx 200$, corresponding to angular scales of $\sim 1^\circ$ in the all-sky map (left) (source: NASA / WMAP)

the right.

The details of our cosmology can be inferred from the shape and height of the peaks in the power spectrum. Baryons have the effect of increasing the odd peaks with respect to the even ones, whereas the total amount of matter (mainly consisting of DM) determines the overall amplitude of the peaks. This is explained by the fact that density fluctuations can only start to grow during the matter dominated epoch, the beginning of which is determined by the matter to radiation density ratio. Nowadays, the best fit to the CMB power spectrum is obtained with the Λ CDM model (see also 4.2), which yields very accurate estimations on e.g. the total matter density Ω_m , the baryonic matter density Ω_b , and the dark energy density Ω_Λ . Again, the results show that the DM component is about 5 times as abundant as baryonic matter.

2.3 Dark Matter properties and candidates

As already discussed at the end of section 2.2, the CMB tells us exactly how much DM there is in our Universe. Combining the 7-year data from the Wilkinson Microwave Anisotropy Probe (WMAP), with data from BAO, and Hubble parameter measurements, the most recent estimation for the DM and baryon density (as of this writing) is [19]

$$\Omega_{\text{DM}}h^2 = 0.1126 \pm 0.0036, \quad 100\Omega_b h^2 = 2.255 \pm 0.0054, \quad (2.28)$$

where $h = 0.702 \pm 0.014$ gives the Hubble rate today that was introduced in Eq. (2.8). This gives a DM-to-baryon-ratio of ~ 5 on average cosmological scales; note that locally this value can differ significantly.

That we know Ω_{DM} with high precision is quite remarkable, especially since we hardly know anything about the nature of DM. From indirect observations we can, however, derive a few properties of DM that we will shortly list here below (for a good review on the properties of DM see [35]):

- *Electrically neutral:* Since the DM is invisible to us, we know that the DM does not interact electromagnetically. Otherwise, the DM would emit or absorb some form of radiation that would be detectable and it would not categorize as ‘dark’ matter.

2.3 Dark Matter properties and candidates

- *Non-baryonic*: As already mentioned, the CMB is consistent with a $\sim 5\%$ and $\sim 23\%$ cosmological abundance of baryonic and dark matter, respectively. A deviation from these ratios would give a worse fit to the peaks in the power spectrum. Furthermore, BBN correctly predicts the abundances of light elements that are observed today. A too large fraction of DM in the form of baryonic objects such as Massive Compact Halo Objects (MACHOs) would spoil this prediction. Analyses of microlensing observations, which can identify both baryonic and non-baryonic small objects in the Milky Way, rule out a large MACHOs fraction of our halo[36].
- *Color neutral*: If the DM would be charged under $SU(3)$, these ‘heavy partons’ would be confined in color neutral hadrons, which in turn would interact too strongly with baryons. This would consequently affect BBN by dissociating light elements, distort the temperature fluctuations in the CMB, and cause disruptions in disks of spiral galaxies. Furthermore, the self-interactions induced by the color charge would be in conflict with the Bullet cluster (see also the last point).
- *Stable on cosmological timescales*: Another piece of information that can be derived from the CMB (complemented with data from type Ia supernovae, Lyman- α forest, large scale structure and weak lensing), are lower limits on the decay rate of DM. In order for the DM abundance to be significant today, the particle needs to be stable on longer timescales. One can assume that the lifetime of DM must exceed the Hubble time H_0^{-1} .
- *Non-relativistic*: To be consistent with the observed large scale structure in the Universe, the DM must be non-relativistic. Relativistic or *hot* DM has a large free streaming length, which would wash out structure such that, for instance, our galaxy would not have been able to form. For instance, if all the DM would be in the form of neutrinos², the structure formation would have occurred top-down, meaning that larger structures form first, which is in contradiction with what is observed. In this way, the observed structure places a limit on the ‘temperature’ of the DM; candidates are typically *cold*, although *warm* DM is also allowed. The formation of structure and the role of DM in it, will be discussed more detailed in chapter 4.
- *Collisionless*: As we have learned from the bullet cluster, the DM is also collisionless. This means it does not (or only very weakly) interact with baryonic matter; it also sets constraints on the magnitude of DM self-interactions, albeit not very strongly.

In order to explain the observations of DM one can adopt two scenarios: 1) the DM consists of an unknown particle that fulfills the properties mentioned above, or 2) gravity behaves differently on larger scales. The latter explanation was initially proposed to explain DM without the need of introducing a new particle. Although these Modified Newtonian Dynamics (MOND) theories [38] can explain individual observations in a satisfactory way, they are not able to describe the phenomena on all scales at the same time. Furthermore they can only describe the Bullet Cluster successfully by invoking the existence of a non-baryonic, invisible type of matter component

²Neutrinos do make up a small amount of the DM. Their abundance is estimated to be $0.0009 < \Omega_\nu < 0.048$ [37]

2 *Dark Matter*

that is at least as large as the baryonic component [39], thereby removing the original motivation for these kind of models.

Thus, it seems that a DM explanation in the form of some new particle is more likely. Since the Standard Model (SM) does not contain a satisfying DM candidate, the explanation for DM must be found in a theory that goes beyond. A good DM candidate does therefore not only have to fulfill the above properties, it also must be well-motivated from a particle physics point of view.

In the next chapter we will discuss the most popular class of DM candidates, the Weakly Interacting Massive Particle (WIMP), since the focus of this thesis is on this type of DM. For other DM candidates, such as gravitinos [40], axions [41], axinos [42], sterile neutrinos [43], superWIMPs [44], etc., we refer the reader to the relevant literature (see e.g. [16] for a discussion on non-WIMP candidates).

3 Weakly Interacting Massive Particles

The need for a theory beyond the Standard Model (SM) is not only motivated by the existence of DM; other observations – such as the hierarchy problem, the discrepancy of the muon anomalous magnetic moment, etc. – are all examples of phenomena that cannot be explained by the SM. One possible realization of a beyond the SM model (BSM) is in the form of Weakly Interacting Particles (WIMPs). In this chapter we will explain why WIMPs are such interesting DM candidates, how they are thermally produced in the early Universe, and how one might be able to detect them. In section 3.2 we furthermore briefly introduce the most popular WIMP model the Minimal Super Symmetric Model and its DM candidate the neutralino.

3.1 Motivation and Dark Matter candidates

Many extensions have been proposed as a solution to the shortcomings of the SM around the electroweak scale (~ 100 GeV). They usually involve new, weakly interacting particles that – if stable on longer timescales – can provide us with good DM candidates. Such WIMPs, denoted with χ , are assumed to have been thermally produced in the early Universe, and could therefore have a significant cosmological abundance today.

In the hot, early Universe ($T \gg m_\chi$), WIMPs are in local chemical equilibrium with the heat bath. Number changing interactions, like annihilation of DM particles into SM particles¹, occur equally frequently in both directions, i.e., detailed balance is maintained. During this time, thermal equilibrium is ensured by elastic scattering processes. However, as the Universe expands, the temperature decreases; around $T \sim m_\chi$ the energy of the SM particles is too low to produce the heavier WIMPs and detailed balance is destroyed. The interaction in the other direction, however, can still take place, such that the (co-moving) number density of the WIMPs starts to decrease. At some point, this Boltzmann suppression of the number density causes the WIMP annihilation rate $n_\chi \langle \sigma v_{\text{rel}} \rangle$ to drop below the expansion rate Γ . From this moment onwards, the annihilations can no longer take place and at $T = T_{\text{cd}}$ the WIMPs *chemically decouple* from the heat bath; typically for WIMPs this occurs at temperatures of $T_{\text{cd}} \sim m_\chi/25$ (see also Fig. 3.2). The number density is forced to deviate from its equilibrium value and starts to decrease less rapidly until eventually the WIMP number density stays fixed and *freezes out* to the relic DM abundance.

The chemical decoupling of WIMPs will be discussed in great detail in 3.3. Here, however, we present a simple estimate for the order of magnitude of the WIMP relic abundance. As explained, the relic abundance depends greatly on the annihilation rate at chemical decoupling,

¹Here, only 2-body processes are considered.

3 Weakly Interacting Massive Particles

and can roughly be estimated by [45]

$$\Omega_\chi h^2 \simeq \frac{3 \times 10^{-27} \text{cm}^3 \text{s}^{-1}}{\langle \sigma v_{\text{rel}} \rangle|_{T_{\text{cd}}}}, \quad (3.1)$$

where $\langle \sigma v_{\text{rel}} \rangle|_{T_{\text{cd}}}$ is the thermally averaged annihilation rate of χ into SM particles at chemical decoupling. If we insert the annihilation rate for a new particle at the electroweak scale, $\sigma \sim \alpha_{\text{ew}}^2 c/m_\chi^2 \sim 10^{-4} (10^8 \text{m s}^{-1}) / (100 \text{GeV})^2 \sim \mathcal{O}(10^{-25}) \text{cm}^3 \text{s}^{-1}$, we obtain a cosmological abundance $\Omega_\chi h^2 \sim \mathcal{O}(0.1)$. This is remarkably close to the measured DM abundance in Eq. (2.28), especially if one considers the fact that n_χ scales exponentially with temperature around T_{cd} . Therefore this is also referred to as the *WIMP miracle*.

Besides this promising feature, WIMPs are interesting because they are detectable by other means than their gravitational interaction. Since the WIMPs weakly couple to SM particles, it is possible to observe the DM through their interactions. For example there is the possibility to produce WIMPs at colliders, directly detect them by their elastic recoil off heavy nuclei, or observe their annihilation products in the (extra)galactic cosmic-ray spectrum. For more information about the various detection methods see section 3.5.

Now that we have seen the advantages of a WIMP as DM, we would like to know what kind of theories naturally predict these kind of particles. A good model does not only provide us with a DM candidate, but is also well motivated from particle physics. Thus it should at least solve some of the problems that the SM fails to explain.

One of them is the so-called *hierarchy problem*, which deals with the enormous difference between the electroweak and the Planck energy scale ($\approx 1.22 \times 10^{19}$ GeV). This has serious consequences for the mass of scalar particles (in particular the Higgs), which receive radiative corrections that scale quadratically with the cutoff energy, $\delta m_s^2 \propto \Lambda^2$ (this is in contrary to the mass corrections of fermionic particles that only increase logarithmically with Λ). The stability of the electroweak scale is correspondingly affected if Λ is close to the Planck scale.

Supersymmetry (SUSY) provides a very elegant solution to this problem, by introducing a symmetry between bosons and fermions. Imagine that each particle has a superpartner with a similar mass, but a spin different by $1/2$. The radiative corrections to the scalar mass are then doubled, but the corrections coming from the new particles have the opposite sign w.r.t. their partners. This means that they cancel each other out, and as a result the quadratical divergence disappears in all orders of perturbation theory, guaranteeing a stable scalar mass. Furthermore, SUSY predicts a unification of the gauge couplings at $M_U \sim 2 \times 10^{16}$ GeV, which is interpreted as a strong hint for Grand Unified Theories (GUT). There are various implementations of SUSY, but the most studied one is probably the Minimal Supersymmetric Standard Model (MSSM), which we will discuss briefly in section 3.2.

Another possible good WIMP DM candidate can be found in Universal Extra Dimension (UED) theories (for a review, see [46]). One extra spatial dimension could exist if it were to be compactified on a scale R that is too small for us to resolve. The result of a field moving along the compactified direction would be a tower of Kaluza-Klein (KK) states with masses $m_{(n)}^2 \equiv m^2 + n^2/R^2$. Imposing symmetry arguments on the compactification results in the conservation of KK-parity $(-1)^n$, such that the lightest KK-odd particle (or LKP) cannot decay and is a viable DM candidate. In the same way, T-parity gives rise to the lightest T-odd particle (LTP) in Little

3.2 Basics of the Minimal Super Symmetric Model

Superfield	Bosons		Fermions		$SU(3)$	$SU(2)$	$U_Y(1)$
Gauge							
\mathbf{G}^a	gluon	g^a	gluino	\tilde{g}^a	8	0	0
\mathbf{V}^k	Weak	$W^k (W^\pm, Z)$	wino, zino	$\tilde{w}^k (\tilde{w}^\pm, \tilde{z})$	1	3	0
\mathbf{V}'	Hypercharge	$B (\gamma)$	bino	$\tilde{b}(\tilde{\gamma})$	1	1	0
Matter							
\mathbf{L}_i	sleptons	$\left\{ \begin{array}{l} \tilde{L}_i = (\tilde{\nu}, \tilde{e})_L \\ \tilde{E}_i = \tilde{e}_R \end{array} \right.$	leptons	$\left\{ \begin{array}{l} L_i = (\nu, e)_L \\ E_i = e_R^c \end{array} \right.$	1	2	-1
\mathbf{E}_i					1	1	2
\mathbf{Q}_i	squarks	$\left\{ \begin{array}{l} \tilde{Q}_i = (\tilde{u}, \tilde{d})_L \\ \tilde{U}_i = \tilde{u}_R \\ \tilde{D}_i = \tilde{d}_R \end{array} \right.$	quarks	$\left\{ \begin{array}{l} Q_i = (u, d)_L \\ U_i = u_R^c \\ D_i = d_R^c \end{array} \right.$	3	2	1/3
\mathbf{U}_i					3*	1	-4/3
\mathbf{D}_i					3*	1	2/3
Higgs							
\mathbf{H}_1	Higgses	$\left\{ \begin{array}{l} H_1 \\ H_2 \end{array} \right.$	higgsinos	$\left\{ \begin{array}{l} \tilde{H}_1 \\ \tilde{H}_2 \end{array} \right.$	1	2	-1
\mathbf{H}_2					1	2	1

Figure 3.1: Field content of the MSSM: for each SM particle there is a superpartner, plus an additional Higgs doublet and its superpartner. Table taken from [5].

Higgs models [47], and, as we will see in the next section, the conservation of R-parity provides us with a stable DM particle in SUSY models.

In this thesis, we will focus on WIMP models with Sommerfeld enhancements (see chapter 5 for an explanation of this effect). This includes sneutrino DM, which we will discuss in see chapter 6, and models where \sim TeV DM particles couple exclusively to some ‘dark’ force (see, e.g.,[48, 49]). The latter kind of models will be discussed extensively here in chapters 5, 7, and 8. In the following, when talking about a DM particle, we therefore tacitly assume it to be a WIMP.

3.2 Basics of the Minimal Super Symmetric Model

As briefly explained in section 3.1, SUSY theories extend the SM by introducing a symmetry between bosons and fermions. In this way, each SM particle obtains a superpartner with a spin that differs by 1/2. In this section we will introduce the basics of the Minimal Super Symmetric Model (MSSM), which is the minimal SUSY extension of the SM and will be of use in chapter 6 where we discuss sneutrino DM. To write this short overview we used information given in [5]: a full review of SUSY and MSSM is unfortunately beyond the scope of this section (see e.g. [50, 5] for a clear review on these topics).

In Fig. 3.1 the particle content for the MSSM is summarized: for each gauge boson, there is an additional gaugino with spin 1/2, and in the same way, each fermion helicity state has a corresponding scalar sfermion superpartner. On top of that there are two Higgs doublets H_1, H_2 (often also denoted as H_d, H_u , respectively) instead of only one like in the SM, which is necessary to cancel gauge anomalies. From the 8 degrees of freedom that these Higgs doublets and their

3 Weakly Interacting Massive Particles

superpartners contribute, 3 are Goldstone modes that give the gauge bosons their masses (like in the SM), and 5 of them are physical states: the standard Higgs boson h , an extra heavy version of the Higgs H , a neutral CP odd Higgs A , and two charged fields H^\pm .

Since we have not observed any super-particles with the same masses as their SM partners, it is obvious that SUSY must be broken. In order to preserve the natural hierarchy between the electroweak and Planck scale, *soft* SUSY breaking (SSB) terms are added to the SUSY Lagrangian. These contain only mass terms or couplings with positive mass dimension as not to spoil the relationships between the dimensionless couplings that guarantee the cancellation of the quadratic divergences in the scalar masses. Since the soft breaking can be done in many different ways, the theory is defined by its SSB terms.

In principle one can write down also terms that violate baryon and lepton number, but unfortunately, this would lead to interactions that would cause the proton to decay very fast². In order to prevent that from happening, the conservation of R-parity is often postulated, $R \equiv (-1)^{3B+L+2s}$, which is positive for SM particles and negative for all SUSY particles. As a result, the lightest SUSY particle (LSP) cannot decay and provides a stable DM candidate.

The SSB terms that conserve R-parity add a large number of free parameters to the theory that spoil the predictability of the model. Therefore one often adopts the GUT condition

$$\frac{M_1}{g_1^2} = \frac{M_2}{g_2^2} = \frac{M_3}{g_3^2}, \quad (3.2)$$

where the subscripts denote the respective gauge groups $U(1)$, $SU(2)$ and $SU(3)$, such that all gauge couplings and gaugino masses are unified at the GUT scale. In the *constrained* MSSM one further assumes universality of the soft parameters at some high energy scale, such that all scalars with spin 0 have a mass m_0 and gauginos have a common mass $m_{1/2}$. The SSB terms are then given by

$$\begin{aligned} \mathcal{L}_{\text{soft}} = & -m_0^2 \sum_i \varphi_i \varphi_i^* - \frac{1}{2} m_{1/2} \sum_a \tilde{\lambda}_a \tilde{\lambda}_a + \varepsilon_{ij} B \mu H_d^i H_u^j \\ & - \varepsilon_{ij} A \left(y_{ab}^u \tilde{Q}_a^j \tilde{U}_b^c H_u^i + y_{ab}^d \tilde{Q}_a^j \tilde{D}_b^c H_d^i + y_{ab}^L \tilde{L}_a^j \tilde{E}_b^c H_d^i \right), \end{aligned} \quad (3.3)$$

where φ_i are all scalar fields, $\tilde{\lambda}_a$ the gaugino fields, $\tilde{Q}, \tilde{U}, \tilde{D}$ the squarks, and \tilde{L}, \tilde{E} the leptons. The indices $i, j = 1, 2$ correspond to the $SU(2)$, $a, b = 1, 2, 3$ describe the generations, and the color indices are not shown. The first term describes the slepton and squark masses, the second the gaugino masses, and the third describes a Higgs mass term that is absent in the SM. The remaining terms are the trilinear terms, which couple a right- and a left-handed sfermion to the Higgs field with the trilinear coupling A and Yukawa couplings y_{ab} .

These SSB terms define the Higgs potential, from which the vacuum expectation values for the Higgs fields can be derived: $\langle H_1 \rangle \equiv v_1$, $\langle H_2 \rangle \equiv v_2$, where $\tan \beta \equiv v_2/v_1$. The Higgs mass

²This is in contradiction with the lower limit on the mean proton lifetime that was measured to be $\tau_p > 2.1 \times 10^{29}$ years [37].

3.2 Basics of the Minimal Super Symmetric Model

eigenstates are defined by this angle β and the mixing angle α :

$$\tan 2\alpha \equiv \tan 2\beta \left(\frac{m_A^2 + m_Z^2}{m_A^2 - m_Z^2} \right), \quad (3.4)$$

where m_A is the mass of the neutral CP odd Higgs, and m_Z the mass of the Z-boson. The constrained MSSM thus only contains 5 free parameters: $\mu, m_0, m_{1/2}, A, B$, where the latter parameter can also be exchanged for $\tan \beta$.

As mentioned, the LSP in the MSSM naturally provides us with an interesting DM candidate. The mass matrix for the gauginos and Higgsinos is non-diagonal, leading to a mixing between the states. The following mass terms are of particular interest to us:

$$\mathcal{L}_{\chi, \psi} = -\frac{1}{2} \tilde{\chi} M^{(0)} \chi - \left(\tilde{\psi} M^{(c)} \psi + \text{h.c.} \right), \quad (3.5)$$

where

$$\chi = \begin{pmatrix} \tilde{B}^0 \\ \tilde{W}^3 \\ \tilde{H}_1^0 \\ \tilde{H}_2^0 \end{pmatrix}, \quad \psi = (\tilde{W}^+ \tilde{H}^+), \quad (3.6)$$

are the Majorana neutralino and Dirac chargino fields, respectively. The neutralino mass matrix is given by

$$M^{(0)} = \begin{pmatrix} M_1 & 0 & -m_Z c_\beta s_W & m_Z c_\beta s_W \\ 0 & M_2 & m_Z c_\beta s_W & -m_Z c_\beta s_W \\ -m_Z c_\beta s_W & m_Z c_\beta s_W & 0 & -\mu \\ m_Z c_\beta s_W & -m_Z c_\beta s_W & -\mu & 0 \end{pmatrix}, \quad (3.7)$$

where $c_\beta = \cos \beta$ and $s_W = \sin \theta_W$ with θ_W the weak mixing angle. The mass matrix of the chargino is correspondingly given by

$$M^{(c)} = \begin{pmatrix} M_2 & \sqrt{2} m_W \sin \beta \\ \sqrt{2} m_W \cos \beta & \mu \end{pmatrix}. \quad (3.8)$$

The mass eigenstates of the neutralinos $\tilde{\chi}^0$ and charginos $\tilde{\chi}^\pm$ are obtained by a diagonalization of these matrices. The lightest neutralino $\tilde{\chi}_1^0$ is an excellent DM candidate for reasons explained in the previous section, and is usually written as

$$\tilde{\chi}_1^0 = N_{11} \tilde{B} + N_{21} \tilde{W}^3 + N_{31} \tilde{H}_1^0 + N_{41} \tilde{H}_2^0, \quad (3.9)$$

where $\sum_{j=1}^4 |N_{1j}|^2 = 1$. If the gaugino fraction $f_g = |N_{11}|^2 + |N_{21}|^2 > 0.5$, it is said that the lightest neutralino is gaugino-like, whereas if $f_g < 0.5$, it is more related to the Higgsino. We will not consider neutralino DM in this thesis specifically; for an extensive review see e.g. [45]. Another viable SUSY DM candidate is the right-handed sneutrino, which will be discussed in chapter 6.

3.3 Chemical decoupling

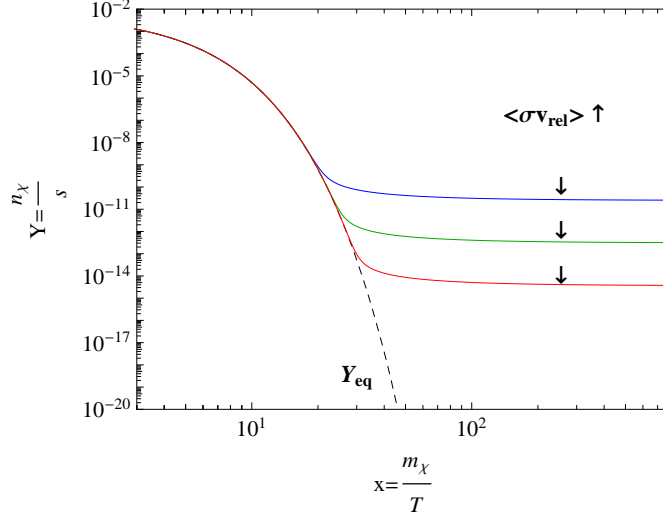


Figure 3.2: The DM number density closely follows the equilibrium distribution until the annihilation rate can no longer compete with the expansion of the Universe. The value of $\langle \sigma v_{\text{rel}} \rangle$ around chemical decoupling determines the final relic abundance.

In this section we will discuss in detail the process of chemical decoupling of WIMP DM, which is described by the Boltzmann equation (see, e.g., [51, 52])

$$E (\partial_t - H \mathbf{p} \cdot \nabla_{\mathbf{p}}) f = C[f], \quad (3.10)$$

where $f(\mathbf{p})$ is the WIMP phase-space density, $p^\mu = (E, \mathbf{p})$ are the co-moving WIMP momenta, $H = \dot{a}/a$ is the Hubble parameter, and we assumed a Friedmann-Robertson-Walker metric. The expression for the collision term on the right-hand side, which includes all number changing interactions, is rather lengthy:

$$\begin{aligned} C_{\text{ann}} &= \frac{1}{2g_\chi} \sum_X \int \frac{d^3k}{(2\pi)^3 2\omega} \int \frac{d^3\tilde{k}}{(2\pi)^3 2\tilde{\omega}} \int \frac{d^3\tilde{p}}{(2\pi)^3 2\tilde{E}} \times (2\pi)^4 \mathcal{D}^{(4)}(\tilde{p} + p - \tilde{k} - k) \\ &\quad \times \left[|\mathcal{M}|_{\tilde{\chi}\chi \rightarrow \tilde{X}X}^2 g(\omega) g(\tilde{\omega}) - |\mathcal{M}|_{\tilde{\chi}\chi \rightarrow \tilde{X}X}^2 f(E) f(\tilde{E}) \right] \\ &= g_\chi E \sum_X \int \frac{d^3\tilde{p}}{(2\pi)^3} v_{\text{rel}} \sigma_{\tilde{\chi}\chi \rightarrow \tilde{X}X} \times [f_{\text{eq}}(E) f_{\text{eq}}(\tilde{E}) - f(E) f(\tilde{E})]. \end{aligned} \quad (3.11)$$

Here, $k^\mu = (\omega, \mathbf{k})$ and $\tilde{k}^\mu = (\tilde{\omega}, \tilde{\mathbf{k}})$ denote the 4-momenta of the SM particles X , and $g = g_{\text{eq}} = (e^{\omega/T} \pm 1)^{-1}$ their distribution functions with a minus(plus)-sign for bosons (fermions)³.

³Pauli blocking or Bose enhancement factors are negligible here since for non-relativistic DM $E \approx m_\chi + p^2/(2m_\chi) > T$ and thus $f \ll 1$. On the other hand, energy-momentum conservation implies $\omega, \tilde{\omega} > m_\chi$ such that $g \ll 1$.

3.3 Chemical decoupling

In Eq. (3.11) the matrix elements squared $|\mathcal{M}|^2$ are summed over both SM and DM internal (spin) degrees of freedom $g_{X,\chi}$. To arrive at the final expression in Eq. (3.11) we have used that $|\mathcal{M}|_{\bar{\chi}\chi\rightarrow\bar{X}X}^2 = |\mathcal{M}|_{\bar{\chi}\chi\leftarrow\bar{X}X}^2$ because of CP invariance, and furthermore we have replaced $g(\omega)g(\tilde{\omega})$ with $f_{\text{eq}}(E)f_{\text{eq}}(\tilde{E})$. This last step is allowed because of thermal equilibrium, which causes annihilation and creation processes to happen with the same frequency. The relative velocity v_{rel} here is the Møller velocity: $v_{\text{rel}} = v_{\text{Møll}} \equiv (E\tilde{E})^{-1} \sqrt{(p \cdot \tilde{p})^2 - m_\chi^4}$.

The first moment of the Boltzmann equation is obtained by integrating Eq. (3.10) over $\int d^3p g_\chi / [(2\pi)^3 E]$, which results in the more familiar expression⁴

$$\frac{dn_\chi}{dt} + 3Hn_\chi = -\langle\sigma v_{\text{rel}}\rangle [(n_\chi)^2 - (n_\chi^{\text{eq}})^2]. \quad (3.12)$$

where n_χ is defined as

$$n_\chi \equiv g_\chi \int \frac{d^3p}{(2\pi)^3} f(\mathbf{p}), \quad (3.13)$$

and n_χ^{eq} is the number density in equilibrium, which in the non-relativistic regime is given by

$$n_\chi^{\text{eq}} = \frac{m_\chi^3 g_\chi T K_2(m_\chi/T)}{2\pi^2 m_\chi}, \quad (3.14)$$

where K_2 is the second order modified Bessel function. The thermally averaged equilibrium annihilation rate is defined as

$$\langle\sigma v_{\text{rel}}\rangle_{\text{eq}} \equiv \frac{g_\chi^2}{(n_\chi^{\text{eq}})^2} \int \frac{d^3p}{(2\pi)^3} \int \frac{d^3\tilde{p}}{(2\pi)^3} v_{\text{rel}} \sigma_{\bar{\chi}\chi\rightarrow\bar{X}X} f_{\text{eq}}(E) f_{\text{eq}}(\tilde{E}), \quad (3.15)$$

which is well approximated by [1].

$$\langle\sigma v_{\text{rel}}\rangle_{\text{eq}} \simeq \frac{4}{\sqrt{\pi}} \left(\frac{m_\chi}{T}\right)^{3/2} \int_0^1 dv (\sigma v_{\text{rel}}) v^2 e^{-v^2 m_\chi/T}, \quad (3.16)$$

for $T \lesssim m_\chi/10$.

We can transform the Boltzmann equation from Eq. (3.12) into a more convenient form, by introducing the dimensionless variables

$$x \equiv \frac{m_\chi}{T}, \quad (3.17)$$

$$Y \equiv \frac{n_\chi}{s}, \quad (3.18)$$

where T is the temperature of the heat bath, and the entropy density during radiation domination was given in Eq. (2.15). Using the fact that entropy is conserved in a co-moving volume, we

⁴Some (SUSY) theories include other, heavier new particles that eventually decay to the DM particle. The correct relic density is then obtained by including these *coannihilations* into the Boltzmann equation [53].

3 Weakly Interacting Massive Particles

arrive at

$$\frac{Y'}{Y} = - \left(1 - \frac{x}{3} \frac{g'_{*S}}{g_{*S}} \right) \frac{n_\chi \langle \sigma v_{\text{rel}} \rangle_{\text{eq}}}{Hx} \left(1 - \frac{Y_{\text{eq}}^2}{Y^2} \right), \quad (3.19)$$

where the derivatives are with respect to the new variable x : $' \equiv d/dx$. Note that this equation is only valid if the WIMPs have a thermal-like distribution, i.e. $f(E) \propto f_{\text{eq}}(E)$.

Eq. (3.19) can be solved numerically to obtain the evolution of the number density as a function of temperature. Integrating Eq. (3.19) up to $x_0 = m_\chi/T_0$, where $T_0 = 2.348 \times 10^{-4}$ eV is the photon temperature today, we obtain the final relic DM abundance

$$\Omega_\chi = m_\chi s_0 Y_0 / \rho_c = 2.742 \times 10^{11} h^{-2} \left(\frac{m_\chi}{\text{TeV}} \right) Y_0, \quad (3.20)$$

where s_0 is the entropy density today, and ρ_c is the critical density [37]. For a viable DM model this should be comparable to the measured value quoted in Eq. (2.28). Note that in models where the DM is not its own antiparticle, i.e. $\chi \neq \bar{\chi}$, Eq. (3.20) should be compared to $\Omega_{\text{DM}}/2$.

3.4 Kinetic decoupling

After the WIMPs have chemically decoupled from the heat bath, they are still kept in local thermal equilibrium by elastic scatterings off SM particles. This is possible simply because the SM particles are much more abundant in the early Universe than WIMPs, i.e. $n_X \gg n_\chi$. Of course, long after T_{cd} also these scattering processes cannot compete with the Hubble rate anymore, and the WIMPs *kinetically decouple* from the heat bath.

To describe this process we again need to consider the Boltzmann equation from Eq. (3.10), but now the collision term only includes processes that conserve the number of particles:

$$C_{\text{el}} = \frac{1}{2g_\chi} \sum_X \int \frac{d^3k}{(2\pi)^3 2\omega} \int \frac{d^3\tilde{k}}{(2\pi)^3 2\tilde{\omega}} \int \frac{d^3\tilde{p}}{(2\pi)^3 2\tilde{E}} (2\pi)^4 \delta^{(4)}(\tilde{p} + \tilde{k} - p - k) \\ \times |\mathcal{M}|_{\chi X \leftrightarrow \chi X}^2 \left[(1 \mp g^\pm(\omega)) g^\pm(\tilde{\omega}) f(\tilde{\mathbf{p}}) - (1 \mp g^\pm(\tilde{\omega})) g^\pm(\omega) f(\mathbf{p}) \right], \quad (3.21)$$

where ingoing 4-momenta have a tilde, and the matrix element squared is summed over all spin states like before.

This time, we are not interested in the first moment of the Boltzmann equation like in the case of chemical decoupling, but rather in its second moment [54, 55]. For this reason, it is very useful to define the WIMP temperature as

$$T_\chi \equiv \frac{g_\chi}{3m_\chi n_\chi} \int \frac{d^3p}{(2\pi)^3} \mathbf{p}^2 f(\mathbf{p}), \quad (3.22)$$

such that $T_\chi = T$ as long as the WIMPs have not thermally decoupled from the heat bath. Note that no assumptions on the form of $f(\mathbf{p})$ are required; the difference between T_χ and T simply indicates the deviation from thermal equilibrium.

In order to obtain an expression analogous to Eq. (3.19), we introduce here the dimensionless

variable

$$y \equiv \frac{m_\chi T_\chi}{s^{2/3}}. \quad (3.23)$$

After integrating Eq. (3.10) with the collision term of Eq. (3.21) over $\int d^3 p g_\chi \mathbf{p}^2 / [(2\pi)^3 E]$ and keeping only the leading order terms in \mathbf{p}^2/m_χ , we arrive at [1]

$$\frac{y'}{y} = -\frac{Y'}{Y} \left(1 - \frac{\langle \sigma v_{\text{rel}} \rangle_2}{\langle \sigma v_{\text{rel}} \rangle} \right) - \left(1 - \frac{x g'_{*S}}{3 g_{*S}} \right) \frac{2m_\chi c(T)}{Hx} \left(1 - \frac{y_{\text{eq}}}{y} \right), \quad (3.24)$$

with

$$\langle \sigma v_{\text{rel}} \rangle_2 \equiv \frac{g_\chi^2 x}{3m_\chi^2 n_\chi^2} \int \frac{d^3 p}{(2\pi)^3} \int \frac{d^3 \tilde{p}}{(2\pi)^3} p^2 (v_{\text{rel}} \sigma_{\tilde{\chi}\chi \rightarrow \tilde{X}X}) f(E) f(\tilde{E}) \quad (3.25)$$

$$\simeq \frac{2x^{3/2}}{\sqrt{\pi}} \int_0^1 dv (\sigma v_{\text{rel}}) v^2 \left(1 + \frac{2}{3} xv^2 \right) e^{-v^2 x}, \quad (3.26)$$

and [55]

$$c(T) = \frac{x}{12(2\pi)^3 m_\chi^5} \sum_X \int dk k^5 \omega^{-1} g^\pm (1 \mp g^\pm) \left| \mathcal{M} \right|_{t=0}^2 \Big|_{s=m_\chi^2+2m_\chi\omega+m_\chi^2}. \quad (3.27)$$

In deriving Eq. (3.24) it was assumed that $Y_{\text{eq}} \ll Y$, and Eq. (3.26) is only valid for $f(E) \propto e^{-E/T}$. The second term on the right-hand side in Eq. (3.24) describes the effect of scattering processes on y and looks very similar to the term in Eq. (3.19). The first term in Eq. (3.24) describes changes to the WIMP temperature caused by a change in the relic density.

To calculate the evolution of the WIMP temperature one usually sets $Y' = 0$ in Eq. (3.24), since it is assumed that the relic density does not change anymore after chemical decoupling. In this case the qualitative behavior of y can easily be understood: as long as there are enough scattering processes, i.e., $c(T)$ is large compared to H , T_χ closely follows the heat bath temperature T . At very late times, however, $c(T)$ becomes vanishingly small and y stays constant, i.e., the WIMP momenta are redshifted due to the expansion of the Universe, $T_\chi \propto s^{2/3} \propto a^{-2}$. This process is nicely visualized for a typical DM particle in Fig. 3.3.

Since kinetic decoupling happens on a rather short timescale [54, 55], the kinetic decoupling temperature can be defined by equating the two different regimes (see also Fig. 3.3)

$$x_{\text{kd}} = \frac{m_\chi}{T_{\text{kd}}} \equiv y \Big|_{x \rightarrow \infty}^{Y'=0} \times \frac{s^{2/3}}{T^2} \Big|_{T=T_{\text{kd}}}. \quad (3.28)$$

It has been shown that, as expected, kinetic decoupling happens much later than chemical decoupling. For example, in the case of neutralino DM, $x_{\text{kd}}/x_{\text{cd}} \sim 10 - 4000$ (or $T_{\text{kd}} \sim 5 \text{ MeV} - 5 \text{ GeV}$) [55].

An important part of this thesis is actually devoted to showing that there are cases in which Y' cannot be neglected after chemical decoupling. Here, the validity of Eq. (3.28) is not affected, since T_{kd} still marks the point at which scattering processes with the heat bath cease to be effective. Therefore one should always make sure to set $Y' = 0$ by hand in Eq. (3.28), before using

3 Weakly Interacting Massive Particles

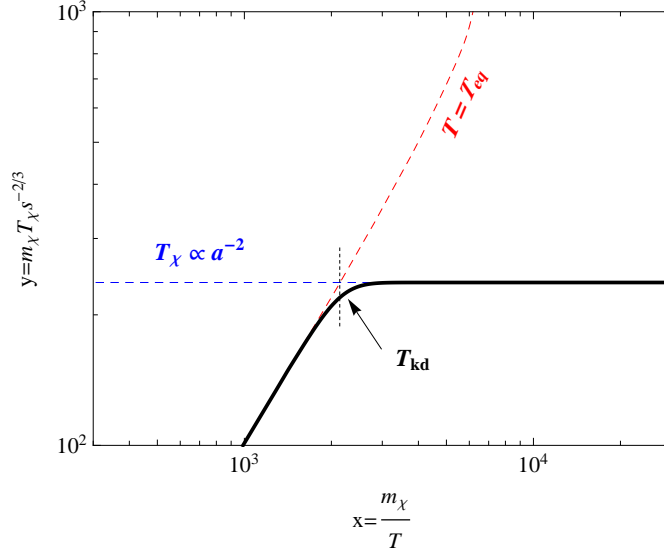


Figure 3.3: The standard evolution of T_χ as a function of x is shown for a typical DM particle with $m_\chi = 1$ TeV. The WIMP temperature closely follows the heat bath temperature until kinetic decoupling, which happens long after chemical decoupling ($x_{\text{kd}} \gg 25$) and on a rather short timescale. Afterwards, the WIMP temperature expands with the Universe, i.e., $T_\chi \propto a^{-2}$.

it.

In the special case that the scattering partners are relativistic ($m_\ell \rightarrow 0$) and the amplitude squared scales like a power of their energy ω , the integral in Eq. (3.27) can actually be solved analytically [54]. The kinetic decoupling temperature is then given by

$$\frac{T_{\text{kd}}}{m_\chi} = \left(\left(\frac{a}{n+2} \right)^{1/(n+2)} \Gamma \left[\frac{n+1}{n+2} \right] \right)^{-1}, \quad (3.29)$$

where Γ is the Euler gamma function, and

$$a \equiv \sum_X \left(\frac{10}{(2\pi)^9 g_{\text{eff}}} \right)^{1/2} g_X c_n N_{n+3}^\pm \frac{m_{\text{Pl}}}{m_\chi}. \quad (3.30)$$

Here, the sum runs over all relativistic scattering partners with internal d.o.f. g_X . The effective d.o.f. g_{eff} are evaluated at T_{kd} , c_n denotes the amplitude squared at small momentum transfer, $|\mathcal{M}|_{t=0}^2 \equiv c_n (\omega/m_\chi)^n + \mathcal{O}((\omega/m_\chi)^{n+1})$, and

$$N_j^+ \equiv (1 - 2^{-j})(j+1)\zeta(j+1), \quad \text{for bosonic } X, \quad (3.31)$$

$$N_j^- \equiv (j+1)\zeta(j+1), \quad \text{for fermionic } X, \quad (3.32)$$

where ζ is the Riemann zeta function. For more details, see [54].

Interestingly there is an observable connected to kinetic decoupling of WIMPs. In the same way that chemical decoupling sets the relic density, free streaming of the WIMPs after decou-

pling from the heat bath sets a scale M_{cut} for the smallest gravitationally bound objects (see 4.1). The reason for this is, as we will see in chapter 4, that DM is the dominant factor in the structure formation of the Universe.

3.5 Detectional prospects

A great virtue of WIMPs is that they are detectable by other means than their gravitational interaction. Through a detection one hopes to learn more about the true nature of DM, such as their mass and coupling strengths. Up till now there has not been a positive discovery yet, although some claims of a detection have been made in the last few years. Only with continued efforts to improve the experiments and gather more data we will know if these claims will hold. In the rest of this section we will briefly discuss the three different kinds of WIMP detection, which are nicely summarized in Fig. 3.4. For a good review on DM detection see e.g. [17, 56].

In experiments such as ATLAS [57] and CMS[58], particles are being collided with center-of-mass energies as high as 8 TeV⁵. These energies are high enough to produce DM particles in the collisions, which then would be invisible to the detector. One could recognize the WIMP by the missing energy in the collision products; the difficulty, however, is to prove that it is stable with a lifetime that is longer than the age of the Universe and that it gives the correct relic density. Measurements of other particle species that are produced at colliders provide constraints on the DM as well, albeit more indirectly. The long timescale of collider searches and the possibility that DM production and detection will be extremely difficult, motivate other, complementary DM searches.

For instance in direct detection experiments, one makes use of the fact that DM particles are expected to travel through our solar system with a galactic velocity $\sim 200 \text{ km s}^{-1}$ ($v/c \sim 10^{-3}$), which amounts to a flux of DM particles at earth that is roughly estimated to be $10^9 \text{ m}^{-2} \text{ s}^{-1}$ for a WIMP with a 100 GeV mass[17]. The idea behind direct detection is to measure the recoil energy of a nucleus after it has collided with a WIMP, which is quite a challenging task in several ways, despite the seemingly large flux. The most important process for direct detection is elastic DM scattering off nuclei, which unfortunately has an extremely small cross section. One distinguishes between the spin-dependent, where the neutralino couples to the spin of the nucleons, and spin-independent cross section. The latter usually gives the most important contribution because the cross section for the total nucleus is coherently enhanced with respect to the contributions of the single nucleons. The collision rate can be improved by increasing the amount of target nuclei, but the recoil energy from the target is rather small ($\mathcal{O}(100) \text{ keV}$), such that one has to make considerable efforts to suppress and understand the background signal. At the moment, direct detection experiments are able to measure recoil energies as low as 1-10 keV.

Some claims of a direct detection have been made in the past. For example DAMA/LIBRA [59] has measured a signal with an annual modulation. A DM explanation has been brought forward, in which the motion of the earth around the sun is responsible for the oscillating signal [60]. However, since results from other experiments are in tension with DAMA (see e.g. [61] and references therein), it remains uncertain if this is actually a positive DM detection. Other

⁵This is the status at the beginning of 2012; in the coming years it will increase to the 14 TeV the Large Hadron Collider was designed to handle.

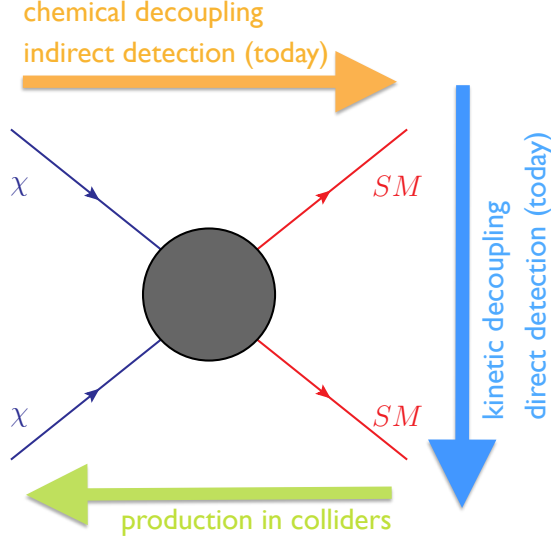


Figure 3.4: Schematic overview of the mechanism behind three different kinds of WIMP detection. Indirect detection (orange) depends on the DM annihilation cross section, which also governs the chemical decoupling. The reverse process of WIMP production is considered in collider searches (green). WIMP scattering (blue) is the interaction that is responsible for kinetic decoupling and provides the basis for direct detection experiments.

experiments, like CoGeNT [62] and CRESST [63], also claim to have observed DM. Unfortunately, the detections are also in tension with many other experiments such as CDMS [64] and XENON100 [65], which currently gives the most stringent bounds on the DM cross section. Although several theoretical efforts have been made to reconcile the various observation with each other, the direct detection results still remain an issue of debate.

In this thesis we are, however, mainly interested in the possibility to detect DM indirectly by observing its annihilation products in the sky, which can consist of γ -rays, neutrinos, anti-protons and positrons. Indirect DM searches with γ -rays have many advantages. For example, since photons are hardly deflected during their propagation, they point back to their source. This makes it possible to learn something about the DM distribution in our galaxy. Furthermore, the expected signal is quite strong due to large annihilation rates, and spectral signatures make it possible to distinguish a DM signal more easily from the background.

The flux of γ -rays,

$$\Phi(\psi, E_\gamma) = \frac{\langle \sigma v_{\text{rel}} \rangle}{8\pi m_\chi^2} \frac{dN_\gamma}{dE} \int_{\text{l.o.s.}} ds \rho_\chi^2(r(s, \psi)), \quad (3.33)$$

is obtained by integrating over the line of sight at a direction making an angle ψ with the Galactic Center (GC). Here, the factor in front of the integral depends on the particle physics (note that when the WIMP is not its own antiparticle, an additional factor of 1/2 should be included here), whereas the astrophysics is included in the integral.

The energy dependence of the flux is solely determined by the annihilation rate. Various spectral signatures are possible, depending on the photon production mechanism in the annihilation. Secondary photons from fragmentation or decay all have very similar spectra that are featureless

and have a power law behavior. Internal bremsstrahlung, either in the form of final state radiation (model-independent) or virtual internal bremsstrahlung (highly model-dependent), involves more pronounced features [66]. The latter has a very significant signature that is similar to a line.

A monochromatic γ -ray line is due to a loop-induced annihilation into two photons and can easily be distinguished from the background if the resolution is high enough. The fact that astrophysics cannot account for such a feature makes it a ‘smoking gun’ signal for DM. On the other hand the annihilation cross-section is loop-suppressed by $\mathcal{O}(\alpha_{\text{em}}^2)$, making it harder to detect such a line. A recent discovery of a line-signal in the public γ -ray data from Fermi-LAT has attracted a lot of interest [67, 68]; more data and statistics is needed to clarify if this is positive evidence for DM or a just a statistical fluctuation. For a recent, clear review on the status and prospects of gamma-ray signals from DM, see [69].

Obviously, to obtain an optimal signal one should look at regions where the DM annihilation rate is the largest; since $\Gamma_a \propto \rho_\chi^2$ this corresponds to regions where the DM density is the highest. In general, the DM distribution in our Milky Way is largely known from N-body simulations (see also section 4.2), but large uncertainties on $\rho_\chi(r)$ at smaller scales affect the precision of the calculated γ -ray flux. Probably the brightest γ -ray source is the dense GC; the large astrophysical background and many unknown or badly understood processes, however, make it a rather complicated region for detection. Another effect that should be taken into account is the enhancement of the flux by a so-called ‘boost’-factor due to the presence of substructure in the smooth DM halo [70–72].

Complementary to γ -ray searches for DM are the multi-wavelength searches (see [73] for a detailed review). In addition to SM particles, highly energetic electrons and positrons are also produced in DM annihilations, which correspondingly produce secondary radiation. The produced spectrum, affected by synchrotron radiation, bremsstrahlung, and inverse Compton emission, extends all the way from radio to X-ray wavelengths. The advantage is that this approach makes use of extra information and can therefore give more robust results.

Indirect detection through neutrinos from the galactic center is very similar to γ -ray searches, although the resulting limits are typically worse by a factor of $10^2 - 10^3$ since neutrinos are the least detectable of all SM particles. Detecting DM by looking for neutrinos from the earth or sun, where WIMPs are expected to accumulate in their center, is more promising. If a WIMP moves close to a celestial body it is attracted by its gravitational potential and moves towards it. However, if the velocity of the WIMP is smaller than the escape velocity, which is quite probable for the non-relativistic WIMPs, it cannot escape from its center anymore. This results in a DM density that is locally much higher, yielding an increased annihilation rate from the center of this object [74, 75]. Of all the annihilation products, especially neutrinos are interesting since they can escape from the inside and be detected on earth. High-energy neutrino telescopes like IceCube [76, 77], AMANDA [78], and ANTARES [79], measuring the Cherenkov light that is emitted by secondary muons in water or ice, are able to set constraints on the DM annihilation cross section into neutrinos.

Another interesting option is to look for anti-matter from DM annihilations in the flux of charged cosmic rays. Due to CP invariance, equal amounts of matter and anti-matter are to be expected from annihilations, whereas astrophysics only produces a small amount of anti-matter. This makes spectra of cosmic-ray antimatter a good place to look for signatures of DM.

3 *Weakly Interacting Massive Particles*

Numerical codes that simulate the propagation of cosmic rays and calculate the secondaries (that are produced when primaries scatter off the interstellar medium (ISM)) are essential to model the expected flux.

For anti-protons, which are purely secondary, the background is rather well understood, although a lack of knowledge on the thickness of the diffusion halo can introduce large uncertainties in the flux[80]. Up to now, data from experiments such as BESS [81], PAMELA [82] and AMS [83], has not shown any evidence for primary anti-protons from DM annihilation.

More interesting results have been found for positrons, for which the main background consists of primaries from SN remnants and secondaries from cosmic rays colliding with the ISM. The propagation of positrons is dominated by energy losses, which means that the origin of the positrons must be local. A lot of excitement was caused by the observation of an anomalous positron excess between 10 and 100 GeV measured by PAMELA [84]. Other experiments such as ATIC [85], Fermi-LAT [86] and H.E.S.S [87] observed a total electron and positron flux between 100 and 1000 GeV that was also higher than expected from astrophysics.

Although a DM explanation seemed possible, the signal corresponds to an annihilation cross section that is several orders of magnitude larger than what is necessary to produce the observed relic density. For this reason, people introduced Sommerfeld enhanced DM models (see, e.g., [48, 88, 89, 49, 90]), which have a velocity-dependent annihilation cross section that is larger today than it was at chemical decoupling. Later, however, it was found that an astrophysical origin of the excess, such as nearby pulsars [91, 92], is more likely [93]. Nevertheless, the positron excess has increased interest in Sommerfeld enhanced DM models. Since these models are the main topic of this work, the positron excess as an original motivation for Sommerfeld DM models will be discussed in more detail in section 5.1.

4 Structure formation in the Universe

In this chapter we will discuss the evolution of structure in the Universe. First, we will start with an introduction to the theory that describes the evolution of small density fluctuations. Here, we will focus on damping effects that suppress small scale perturbations in the power spectrum and the size of the first gravitationally bound objects. Since the analytical calculations are not sufficient to give a realistic picture of the observed structure, we discuss numerical simulations of Λ CDM cosmology in section 4.2. Although very successful on large scales, the results of these simulations are in tension with observations on smaller scales. In section 4.3 we will discuss the three most important small scale problems of Λ CDM and the proposed solutions. The discussion in this chapter is by no means exhaustive; we refer the reader to the supplied references for more details. Books in which more detailed information about structure formation can be found are, e.g., [94, 95, 14].

4.1 Theory of structure formation

Although the Universe is isotropic and homogeneous on larger scales, this is obviously not the case on smaller scales, where the presence of galaxies, clusters of galaxies, etc., is evident. The origin of this structure lies in tiny primordial density fluctuations of $\mathcal{O}(10^{-5})$ that were generated during inflation, which subsequently evolved under the influence of gravity and the expansion of the Universe. Understanding this evolution will tell us more about the initial conditions in the early Universe and the physical processes that were responsible for creating structure on various scales.

In order to say anything about the evolution of structure, we define the density contrast

$$\delta(\mathbf{x}) \equiv \frac{\rho(\mathbf{x}) - \bar{\rho}}{\bar{\rho}} \ll 1, \quad (4.1)$$

as a deviation from the homogeneous background density $\bar{\rho}(t)$. In order to tell different scales apart, it is convenient to consider also its Fourier transform

$$\delta_k = \int d^3x \delta(\mathbf{x}) e^{i\mathbf{k}\cdot\mathbf{x}}. \quad (4.2)$$

Furthermore we will use co-moving coordinates that stay constant with the expansion of the Universe, such that $\mathbf{x}_{\text{phys}} = a(t)\mathbf{x}$ and $k_{\text{phys}} = k/a(t)$. The wavelength of a perturbation associated with wavenumber k is given by $\lambda \equiv 2\pi/k$.

In fact there are two types of perturbations: adiabatic and isocurvature. The former affect the energy densities of the radiation and matter components by the same factor, and since they evolve in different ways, they are related by $\rho_r = 4\rho_m/3$ [95]. For isocurvature perturbations the entropy

4 Structure formation in the Universe

density of the various components changes, but the total energy density stays homogeneous, $\rho_r \delta_r = -\rho_m \delta_m$.

Inflationary models predict that the initial density perturbations are the result of quantum fluctuations. Because of the quantum commutation relation, modes with different scales k are uncorrelated: the density perturbations follow this behavior and are therefore well described by Gaussian statistics. Furthermore, since most models include one scalar field (the inflaton) that is responsible for the inflation, it can only create the simple adiabatic fluctuations. Isocurvature perturbations could only be produced by adding additional inflation fields to the theory [95]. We therefore only consider adiabatic perturbations in the following.

A very important quantity in the theory of structure formation is the *power spectrum* $\mathcal{P}_\delta(k)$ that is defined by the two-point correlation function

$$\langle \delta_{\mathbf{k}} \delta_{\mathbf{k}'}^* \rangle \equiv \frac{2\pi^2}{k^3} \mathcal{P}_\delta(k) \delta(\mathbf{k} - \mathbf{k}'). \quad (4.3)$$

Since the primordial density fluctuations follow a Gaussian distribution, different modes are thus uncorrelated. The behavior of the power spectrum can be described by a simple power-law

$$\mathcal{P}_\delta(k) \propto k^{3+n}, \quad (4.4)$$

where n is the spectral index. For $n = 1$ we obtain a scale-invariant spectrum, also known as Harrison-Zel'dovich spectrum. The only length scale that exists in the inflationary model at a given time is the horizon size H^{-1} (see 2.1), therefore fluctuations with this scale are bound to exist at all times. This means that the Universe will look the same for every mode on the scale of the horizon, $k = H$.

Since the perturbations are Gaussian, the probability that a spherical fluctuation with radius R lies between δ and $\delta + d\delta$ is

$$dp_R(\delta) = \frac{1}{(2\pi\sigma^2(R))^{1/2}} e^{-\delta^2/(2\sigma^2(R))} d\delta, \quad (4.5)$$

where $\sigma^2 = \langle \delta^2(R) \rangle$ is the variance of the density perturbation. It is convenient to smooth out density perturbations in the power spectrum below some smoothing length L , which is done by convolving the power spectrum with a window function $W_L(\mathbf{x})$, which is usually taken to be a top-hat function,

$$W_{TH}(R) = \begin{cases} (\frac{4}{3}\pi L^3)^{-1} & R < L \\ 0 & R \geq L. \end{cases} \quad (4.6)$$

The variance is then given by

$$\sigma^2(R) = \int_0^\infty \frac{dk'}{k'} W_{TH}^2(k'R) \mathcal{P}_\delta(k'), \quad (4.7)$$

where $W_{TH}^2(x) = 3x^{-3}(\sin x - x \cos x)$ is the Fourier transform of the top-hat window function.

The normalization of the power spectrum has to be derived from measurements, since it cannot be calculated theoretically. It is parameterized by σ_8 , the root-mean-square of a density perturba-

tion that is filtered by a top-hat function (Eq. (4.6)) with smoothing length $L = 11.4h^{-1} \text{ Mpc}^{-1}$. The value of L is chosen in such a way that $\sigma_8 \simeq 1$ (current observations give $\sigma_8 = 0.816 \pm 0.024$ [19]).

The primordial density fluctuations are modified by complicated effects that involve gravitation, pressure, dissipation, etc. These highly non-linear processes which are responsible for the formation of structure can only be solved numerically in N-body simulations (see section 4.2). The overall effect of this is contained in the transfer function [95],

$$T(k) = \frac{\delta_k(z=0)}{\delta_k(z)D(z)} \quad (4.8)$$

which relates the initial density fluctuations at some redshift z to the final perturbations today, as a function of the scale k . Here, z can be any redshift before scales that are important have entered the horizon. The growth factor is given by

$$D(z) = \frac{\delta_{k=0}(z=0)}{\delta_{k=0}(z)} \quad (4.9)$$

such that by definition $T(0) = 1$. It gives the increase in the amplitude of a density perturbation with mode $k = 0$ (i.e., in the limit of large scales) between redshifts 0 and z . The evolution of large scales can be described by linear perturbation theory (which will be discussed below) and thus can be calculated relatively easily. If linear perturbations would be valid until today, we could obtain the current matter power spectrum by simply multiplying the primordial power spectrum from inflation by the transfer function squared (Eq. (4.8)).

To get a feeling for the evolution of density perturbations, we consider a Newtonian analysis here that is valid for sub-horizon perturbations in a non-relativistic fluid (for more information, see e.g. [95, 52]). In the linear regime, $\delta_k < 1$, perturbations grow like $\lambda_{\text{phys}} = a(t)\lambda$. The fundamental hydrodynamic equations are as follows:

$$\begin{aligned} \text{Euler:} \quad & \dot{\mathbf{v}} + (\mathbf{v} \cdot \nabla)\mathbf{v} = -\frac{\nabla p}{\rho} - \nabla\Phi, \\ \text{continuity:} \quad & \dot{\rho} + \nabla(\rho\mathbf{v}) = 0, \\ \text{Poisson:} \quad & \nabla^2\Phi = 4\pi G_N\rho, \end{aligned} \quad (4.10)$$

where Φ is the Newtonian gravitational potential, the dot denotes a derivative w. r. t. time, and the spatial derivatives are $\nabla_{\mathbf{x}_{\text{phys}}} = a^{-1}\nabla_{\mathbf{x}}$. The velocity of the cosmic fluid can be written as $\mathbf{v} = \dot{\mathbf{x}}_{\text{phys}} = \dot{a}(t)\mathbf{x} + a(t)\mathbf{u}$, where \mathbf{u} is the co-moving peculiar velocity.

The next step is to substitute $\rho = \bar{\rho}(1 + \delta)$ (Eq. (4.1)) in Eq. (4.10) and expand around the background density. Keeping only terms that are linear in δ , we arrive at

$$\ddot{\delta}_k + 2H\dot{\delta}_k + \left(\frac{c_s^2 k^2}{a^2} - 4\pi G_N \bar{\rho} \right), \quad (4.11)$$

where $c_s^2 \equiv \partial p / \partial \rho$ is the sound speed. The critical length scale which follows from this equation

4 Structure formation in the Universe

is the *Jeans length*

$$\lambda_J = c_s \sqrt{\frac{\pi}{G_N \bar{\rho}}}, \quad (4.12)$$

for which a sound wave takes the same amount of time to cross an object as for the gravitational free fall collapse. Perturbations with a shorter wavelength than the Jeans length, $\lambda_{\text{phys}} \lesssim \lambda_J$, show acoustic oscillations with a slowly decaying amplitude. For wavelengths that are larger, $\lambda_{\text{phys}} \gtrsim \lambda_J$, Eq. (4.11) has both a growing (+) and decaying (−) solution:

$$\delta_k^+ \propto t^{2/3}, \quad \delta_k^- \propto t^{-1}, \quad (4.13)$$

where we assumed the Universe to be spatially flat ($k = 0$) and matter dominated, i.e., $4\pi G_N \bar{\rho} = \frac{3}{2}H^2$ (see also Eq. (2.11)) with $H = \frac{2}{3}t^{-1}$.

The above simplified description is of course not the whole story; the full relativistic analysis involves the evolution of metric perturbations on the FRW background metric, $g_{\mu\nu} = \bar{g}_{\mu\nu} + h_{\mu\nu}$, in the Einstein equation Eq. (2.10). A problem that arises here is the freedom to choose a set of coordinates that is related by the old coordinates by a gauge transformation, $x^\mu \rightarrow x'^\mu = x^\mu + \varepsilon^\mu(x)$. This does not only introduce a change in the metric perturbation, but also in the definition of the density contrast, meaning that the latter is actually not a physical variable. It is therefore very important to note which gauge is being used in an analysis; popular gauge choices include the Newtonian gauge (for which sub-horizon perturbations follow the Newtonian approximation sketched above), synchronous gauge, and co-moving gauge. Since the full treatment is beyond the scope of this introduction we refer to the literature (e.g., [14]) for the details, and concentrate on the most important results from the relativistic analysis in the rest of this section.

The size of the horizon w. r. t. the wavelength of the fluctuation is important for the evolution of the density perturbations. Super-horizon modes for all components grow like

$$\delta_k \propto \frac{t^2}{a^2(t)} \propto \begin{cases} t & \text{RD} \\ t^{2/3} & \text{MD}, \end{cases} \quad (4.14)$$

when co-moving gauge is assumed. Once a mode enters the horizon, the evolution evolves differently for each component, depending on the era at that time.

During the epoch of radiation domination the density fluctuations in photons and baryons do not grow once they enter the horizon. Instead, they oscillate

$$\delta_\gamma \simeq \delta_b \propto \cos kr_s, \quad (4.15)$$

with a frequency that depends on the co-moving size of the sound horizon, $r_s \equiv \int_0^t dt' c_s/a(t')$, where the sound speed is $c_s \approx 1/\sqrt{3}$ during the radiation era. The density fluctuations in the CDM fluid, however, grow logarithmically with time

$$\delta_\chi \propto \log t. \quad (4.16)$$

Once we enter the regime of matter-domination, the DM fluctuations start to grow with an increased rate, $\delta_\chi \propto t^{2/3}$, as was already foreseen in Eq. (4.13). Until recombination, the baryon fluid stays tightly coupled to the radiation, i.e., $\delta_\gamma \simeq \delta_b$, but their amplitude starts to grow slightly

under the influence of the gravitational potential wells that are induced by the DM. At recombination, the baryons fall into the DM potential wells and δ_b increases sharply for a short amount of time. Afterwards, the baryons now closely follow the density fluctuations of the DM

$$\delta_b \simeq \delta_\chi \propto a(t) \propto t^{2/3}. \quad (4.17)$$

The baryon perturbations thus grow faster than they would have without the presence of DM. In fact, without DM they would not have had enough time to collapse to form the structure we see today, making a large CDM component in cosmological models crucial. Finally, all fluctuations essentially stop to grow during the vacuum dominated era, i.e., $\delta_b \simeq \delta_\chi$ stay constant.

Up until now we have only discussed a growth of perturbations in the cosmic fluid, but there are also some damping effects that need to be taken into account. Density perturbations in the photon-baryon plasma are diminished on small scales by Silk (or collisional) damping around the time of recombination [96]. As photons start to decouple from the plasma, they erase perturbations that are below the diffusion scale. At recombination, this effect is captured in the CMB and shows up as a damping of the peaks in the CMB spectrum for modes beyond $l \sim 10^3$.

In addition, the Universe contains also collisionless species (e.g., neutrinos, DM, axions) that do not suffer from Silk damping. As the fluid decouples from the heat bath, it can move freely from overdense regions into underdense regions, washing out perturbations in the process. The effect of this *free streaming* causes damping of small scale density perturbations (also known as collisionless damping). No clustering occurs for scales $\lambda_{\text{phys}} < \lambda_{\text{fs}}$, where the physical free streaming scale is given by [14]

$$\lambda_{\text{fs}}(t) = a(t) \int_0^t dt' \frac{v(t')}{a(t')}, \quad (4.18)$$

and v is the velocity of the collisionless species. Since perturbations can only start to grow significantly during the matter dominated epoch, the free streaming scale can be approximated by $\lambda_{\text{fs}} \sim v(t_{\text{eq}})/H(t_{\text{eq}})$. The free streaming scale thus depends highly on the velocity of the species under consideration.

Usually the DM particles have a very large mass (order GeV to TeV) and are assumed to be non-relativistic around decoupling. As a result, they have almost negligible thermal velocities at present, and are therefore denoted as cold dark matter (CDM). The free streaming of the collisionless DM then only erases perturbations on the smallest scales. Structure formation takes place in a hierarchical way: the smallest scales collapse and enter the non-linear regime first, to merge only later and form larger structures.

Instead, hot or warm dark matter (HDM, WDM) is relativistic at kinetic decoupling, and thus induces a larger amount of free streaming than CDM. It therefore erases much more small-scale structure and correspondingly more modes are suppressed in the power spectrum. Whether we are dealing with HDM or WDM depends on the thermal decoupling of the particle species. Since decoupling happens when the DM is still relativistic, the final abundance is given by the equilibrium distribution around freeze-out, which in turn depends inversely on the entropy degrees of freedom g_{*S} . The earlier a species decouples, the larger g_{*S} is, the smaller the final relic density. Assuming the species to be (almost) massless, their temperature is given by

4 Structure formation in the Universe

$$T_{\text{rel,DM}} \simeq (4/g_{*S}(t_{\text{kd}}))^{1/3} T \text{ [52].}$$

The standard HDM candidate is a neutrino with a mass of order eV, which still has large velocities at late times and a temperature that is comparable to the photon temperature ($g_{*S}(t_{\text{kd}}) \simeq 11$). In this case, the free streaming length is large and structures such as galaxies are not able to form, which rules out HDM as the main DM component. Usually a sterile neutrino with a mass of the order of $\mathcal{O}(10)$ keV is taken as a WDM candidate, which decouples much earlier than ordinary neutrinos. At decoupling it is still relativistic but since $g_{*S} \gg 1$, its temperature is much smaller than the photons or neutrinos today. The free streaming wipes out density perturbations, but not as much as in the case of HDM, such that it is not in contradiction with the present observed structure. For more details on CDM and HDM see e.g. [52, 14].

We will see in the next subsection that free streaming of DM, among other effects, leaves a characteristic imprint in the power spectrum, and is important for the discussion of the first gravitationally bound objects in the Universe.

4.1.1 A cutoff in the power spectrum

As already mentioned, the DM fluid is tightly coupled to the radiation fluid (i.e., the heat bath) before kinetic decoupling, and, since the DM is in local thermal equilibrium, it can be described by a perfect fluid until T_{kd} . Correspondingly, perturbations in the DM density behave as sound waves that are damped by dissipative effects [97]. These include bulk viscosity, which transfers dissipation energy from the DM fluid to the radiation, and shear viscosity caused by the resistance to fluid flow. In contrast, heat conduction is negligible due to the fact that the DM particles are extremely slow. The viscosity coefficients, which have to be calculated from kinetic theory, enter in the decay rate for the oscillating fluctuations. The result is an exponential cutoff k_d in the power spectrum.

After kinetic decoupling, the CDM is no longer in local thermal equilibrium, but scatterings with the radiation fluid can still occur. These only cease after the time of last scattering, $T_{\text{ls}} < T_{\text{kd}}$, when collisions no longer take place. It is only for $T < T_{\text{ls}}$ that the DM obtains a fully non-relativistic equation of state ($p \approx 0$), and enters the free streaming regime: the viscosity coefficients vanish and the particles become collisionless. Therefore they can move freely from overdense to underdense regions, and wash out any density fluctuations that are present on small scales. The co-moving damping scale is well approximated by [98–100]

$$k_{\text{fs}} \approx \left(\frac{m_\chi}{T_{\text{kd}}} \right)^{1/2} \frac{a_{\text{eq}}/a_{\text{kd}}}{\ln(4a_{\text{eq}}/a_{\text{kd}})} \frac{a_{\text{eq}}}{a_0} H_{\text{eq}}, \quad (4.19)$$

such that only modes with $k \lesssim k_{\text{fs}}$ escape being wiped out and can start to grow. The time of equality is important, since DM fluctuations can start to grow significantly in the matter dominated era. As can be seen, the free streaming scale depends on size of the horizon at kinetic decoupling, since only sub-horizon scales can be washed out.

Another effect, which is physically independent from free streaming, is damping due to acoustic oscillations in the tightly coupled matter-radiation fluid. Usually density perturbations get a growth spurt when their mode enters the horizon and grow logarithmically afterwards. If a mode enters the horizon before the DM has decoupled from the heat bath, it oscillates together with

the plasma instead. Due to the fact that kinetic decoupling does not happen instantaneous, there is a period in which the scattering rate becomes comparable to the oscillation frequency of the acoustic waves. In this way, the decreasing scattering rate forces the amplitude of the density perturbations to zero. After kinetic decoupling the density perturbations start growing logarithmically, albeit with a fairly reduced amplitude in comparison to modes that became sub-horizon after decoupling. Like free streaming, it creates an exponential cutoff in the power spectrum, suppressing all perturbations with a mode $k \gtrsim k_{\text{ao}}$. The characteristic damping scale that is related to this effect depends on the co-moving size of the horizon at kinetic decoupling [101, 102]

$$k_{\text{ao}} \approx \frac{\pi a(t_{\text{kd}})}{d_H(t_{\text{kd}})} = \pi a(t_{\text{kd}}) \left(\int_0^{t_{\text{kd}}} \frac{dt'}{a(t')} \right)^{-1}. \quad (4.20)$$

It turns out that $k_{fs} \ll k_d$ for WIMPs, such that effectively the free-streaming determines the damping scale and the collisional damping can be neglected. Since the free-streaming and acoustic oscillation damping effects are of comparable size, yet independent, their cumulative effect is given by multiplying the two exponential damping scales. Therefore it is the smallest of Eq. (4.19) and Eq. (4.20) that ultimately determines the cutoff. Thus for CDM, the time of kinetic decoupling sets the scale for the cutoff in the matter power spectrum, making the small scale structure very sensitive to the details of the WIMP model.

Information about the matter power spectrum can be extracted from the (closely related) CMB power spectrum, and can be further probed by galaxy redshift surveys and measurements of the Lyman- α forest. Clouds of neutral hydrogen between the earth and very luminous, energetic sources such as quasars absorb emitted ultraviolet light with a wavelength of 1216 Å. Since these clouds appear at different redshifts, the observed spectrum shows a collection of absorption lines at smaller wavelengths. Therefore Lyman- α measurements can trace the distribution of galaxies even on the smallest scales, where the influence of the above described damping effects could become visible. By combining the CMB, galaxy redshift and Lyman- α data, it is possible to obtain limits on the cutoff scale.

Usually, numerical simulations are performed in order to replicate the structure formed by a certain type of DM candidate. These N-body simulations (which we will come to in section 4.2), often work with WDM candidates to generate a cutoff in the simulated power spectrum. The resulting cutoff or free-streaming scale is conventionally expressed in the mass of the WDM candidate [103]:

$$k_{\text{fs,WDM}} = 4.6 \left(\frac{\Omega_M h^2}{0.13} \right)^{-1/3} \left(\frac{m_{\text{WDM}}}{\text{keV}} \right)^{4/3} \text{Mpc}^{-1}, \quad (4.21)$$

where m_{WDM} denotes the mass of the WDM particle. The combination of observational data and N-body simulations allows us to constrain DM models based on their structure formation and damping properties. We will further explore this in chapter 8.

4.1.2 The first protohalos

Since the power spectrum contains all information about the density perturbations, it forms the initial conditions for the structure evolution that follows. In hierarchical structure formation small scales collapse first, which are actually the ones that appear close to the cutoff we spoke

4 Structure formation in the Universe

about in the previous section. Therefore the cutoff is directly related to the mass of the smallest gravitational bound objects in the Universe.

For this reason it is useful to consider the DM mass that is contained in a sphere with radius (π/k_{cut}) [54, 55]

$$M_{\text{cut}} = \frac{3}{4}\pi \left(\frac{\pi}{k_{\text{cut}}} \right)^3 \rho_{\chi}, \quad (4.22)$$

where k_{cut} is either k_{fs} or k_{ao} , and ρ_{χ} is the DM density today. The definition of the radius follows the convention for the Jeans mass, which is the mass within a radius $\lambda_J/2$ (see Eq. (4.12)). Since kinetic decoupling happens well before matter-radiation equality, we can assume the Universe to be radiation dominated, $H_{\text{r}}^2 = \frac{4\pi^3}{45m_{\text{pl}}^2} g_{\text{eff}} T^4$, where $g_{\text{eff}}(T)$ denotes the effective degrees of freedom of the radiative component.

The free streaming mass can be well approximated by

$$M_{\text{fs}} \approx 2.9 \times 10^{-6} \left(\frac{1 + \ln \left(g_{\text{eff}}^{1/4} T_{\text{kd}} / 50 \text{ MeV} \right) / 19.1}{\left(\frac{m_{\chi}}{100 \text{ GeV}} \right)^{1/2} g_{\text{eff}}^{1/4} \left(\frac{T_{\text{kd}}}{50 \text{ MeV}} \right)^{1/2}} \right)^3 M_{\odot}, \quad (4.23)$$

where $M_{\odot} = 1.9885(2) \times 10^{30}$ kg is the mass of our sun [37], and $g_{\text{eff}} = g_{\text{eff}}(T_{\text{kd}})$ is evaluated at decoupling. It can be seen from Eq. (4.23) that besides T_{kd} , the free streaming mass also depends on the mass of the WIMP.

The characteristic cutoff mass determined by acoustic oscillations is correspondingly given by

$$M_{\text{ao}} \approx 3.4 \times 10^{-6} \left(\frac{T_{\text{kd}} g_{\text{eff}}^{1/4}}{50 \text{ MeV}} \right)^{-3} M_{\odot}, \quad (4.24)$$

which basically only depends on T_{kd} .

The mass of the first protohalos is then given by the largest of Eq. (4.23) and Eq. (4.24) [54, 55]

$$M_{\text{cut}} = \text{Max} [M_{\text{fs}}, M_{\text{ao}}]. \quad (4.25)$$

Objects with a mass corresponding to the smallest of the two cutoff scales will not be able to form, because the damping effect that wipes out the largest scale dominates. The final cutoff mass has been shown to be very model dependent since it highly depends on the kinetic decoupling temperature. For example in the case of neutralino DM, the cutoff mass spans a range from 10^{-11} to $10^{-3} M_{\odot}$ [55].

Depending on the WIMP candidate and the primordial power spectrum, the first gravitationally bound objects start to form between redshift 40 and 80 [99]. Whether these first and smallest halos survive until today is not clear. They can be destroyed in the process of merging or disrupted by star formation. Assuming that the first density fluctuations to enter the non-linear regime are rather rare, their density contrast can be larger by an order of magnitude compared to the others, which increases their survival probability. Numerical simulations [104, 105] show that while the first halos lose mass during structure formation, they survive until today with their inner density still intact.

Through the detection of these smallest subhalos, we could learn a lot about the nature of the

DM particle. Unfortunately, this is a rather challenging task. As a dense DM object, subhalos would appear as a point-like γ -ray source through an increased annihilation rate in the center. It turns out, however, that the expected fluxes are too small to be resolved [106]. Anisotropy studies of the diffuse γ -ray background could prove to be more fruitful; the substructure in the galactic halo could be inferred from the probability density function [107], or the angular power spectrum could include a resolvable DM signal for $M_{\text{cut}} \gg M_{\odot}$ [108–110].

Another possibility to detect protohalos with a mass larger than a few solar masses, is through microlensing; the position of background stars seem to change as a compact halo moves through the sky [111]. Even a strong gravitational lensing effect could be observed for sub-solar halos, when one combines multiple measurements of the gravitational potential perturbations. Especially time-varying images are less affected by systematic uncertainties and degeneracies [112, 113]. See also [114] for a review on detectional prospects of DM halos with sub-solar masses.

Besides these direct detection methods, one can also probe the protohalos indirectly by substructure enhancement of a DM annihilation signal [115, 116]. Results from numerical simulations of structure formation have to be extrapolated to the DM cutoff masses, since they do not reach an adequate resolution. Assuming that this gives a reliable prediction for the substructure, one can calculate the expected γ -ray flux from annihilations, which is boosted w. r. t. the expected flux from a smooth halo. This can then be compared to γ -ray observations of galaxy clusters to infer constraints on M_{cut} . For DM models where the annihilation cross section is enhanced by the Sommerfeld effect (see chapter 5), the expected flux is even larger since the subhalos are kinematically cold [117–119]: an additional boost is obtained when it is assumed that the subhalos also contain substructure [120].

Recently, it was realized that M_{cut} strongly correlates with the spin-dependent scattering rate for neutralino and Kaluza-Klein DM [121]. These rates are important for direct detection experiments and indirect DM searches looking for neutrinos from the sun. If a signal would be observed in these experiments, it would allow us to place limits on the cutoff mass. Even though this is a very promising prospect, probing the mass of the smallest subhalos remains very challenging at present. To obtain more insight on the formation of structure on all scales, numerical simulations are therefore of great importance.

4.2 Numerical simulations of Λ CDM

The theory of structure formation that we discussed in section 4.1 was only to linear order in perturbation theory. In this regime, density perturbations may grow but their shape remains the same, and since the perturbations are Gaussian, the shape of underdensities are indistinguishable from overdensities. Once we enter the non-linear regime, however, this is no longer true, and the evolution of the density fluctuations can no longer be calculated analytically. Clusters, galaxies and stars are all the result of highly non-linear processes; it is therefore necessary to perform numerical simulations of structure formation in order to learn more about cosmology. Comparing the results from simulations to the observations will give us insight on the validity of the Λ CDM cosmology. More information about non-linear structure formation can be found in e.g. Chapter 9.2 of [94]; here we summarize the main points of the discussion there. A clear,

recent review on numerical simulations can also be found in [122].

An initial spherical underdense region will grow and become less dense as the Universe expands, since the gravitational pull is too small to slow the receding movements. It will form a so-called *void*, which is separated from other voids by a higher density surface. After some time the voids become so large that they collide: the matter that envelopes them is pressed into *filaments* with a high density that attract even more matter from nearby. The gravitational attraction causes the overdense regions to shrink in volume, in contrary to the voids. The structure in the Universe begins to look like a *cosmic web*, as can be seen in Fig. 4.1.

At the intersection of filaments *nodes* will form, which are the origin of the first and oldest objects such as clusters of galaxies. The subsequently cooling and condensation of gas is responsible for the formation of galaxies. DM halos of many different sizes are constantly being evolved by collision and merger processes: a *primary halo*, characterized by the presence of infalling matter around it, can host several, less massive *subhalos*. The formation of the cosmic structure thus takes place in a *hierarchical* or *bottom-up* way, meaning that the smallest structures form first and merge only later into larger structures.

To get a feeling for non-linear structure evolution, let us consider the idealized spherical collapse of a positive density perturbation. A few characteristic stages can be recognized in its evolution: at *turnaround*, the gravitational force balances against the expansion; the radius reaches its maximum value r_{max} and the collapse of the spherical overdensity starts. In an oversimplified model, the density perturbation would collapse to a singularity. In practice, dissipative effects will cause the DM to eventually settle into an equilibrium state. This process of relaxation and phase mixing is called *virialization*, since at the end the halo should obey the virial equation (see also section 2.2).

From the virial theorem, one can derive that the half-mass radius, i.e., the radius of a sphere that contains half of the total halo mass, is $r_h \simeq 0.375r_{\text{max}}$. Assuming that the time it takes for the system to virialize is twice the time until turnaround, i.e., $t = 2t_{\text{max}}$, the mean density inside a sphere with radius r_h is about ~ 200 times the background density. For this reason people often define the *virial radius* r_{200} at which the density is a factor 200 larger than the critical density. The mass contained in a sphere with r_{200} is then taken to be the total halo mass [94].

The evolution of the primordial density fluctuations is usually carried out by N-body simulations. Here, the fluctuations are represented by discrete particles, each of which moves under the influence of gravitational attraction of other nearby objects and expansion of the Universe. In each step, the equations of motions have to be solved, yielding the change in position and velocity for each particle, which correspondingly generates a whole new gravitational potential that has to be taken into account in the next step. This process is then iterated until numerical convergence is achieved.

The reliability of an N-body simulation depends on various aspects. First of all, one needs to choose a finite box size that is large enough to represent a significant amount of the Universe; a length of $\gtrsim 50$ Mpc should suffice [95] (in comparison, the size of the visible Universe is $H_0^{-1} = 4.3h^{-1}$ Gpc). No structures are supposed to form at $\gtrsim 100$ Mpc, since the Universe is homogeneous and isotropic on large scales. Furthermore, one needs to specify a grid onto which the density field is averaged. Needless to say that a finer grid produces better results but takes more computing time.

In addition, one needs to specify the number of particles that are being used and the particle

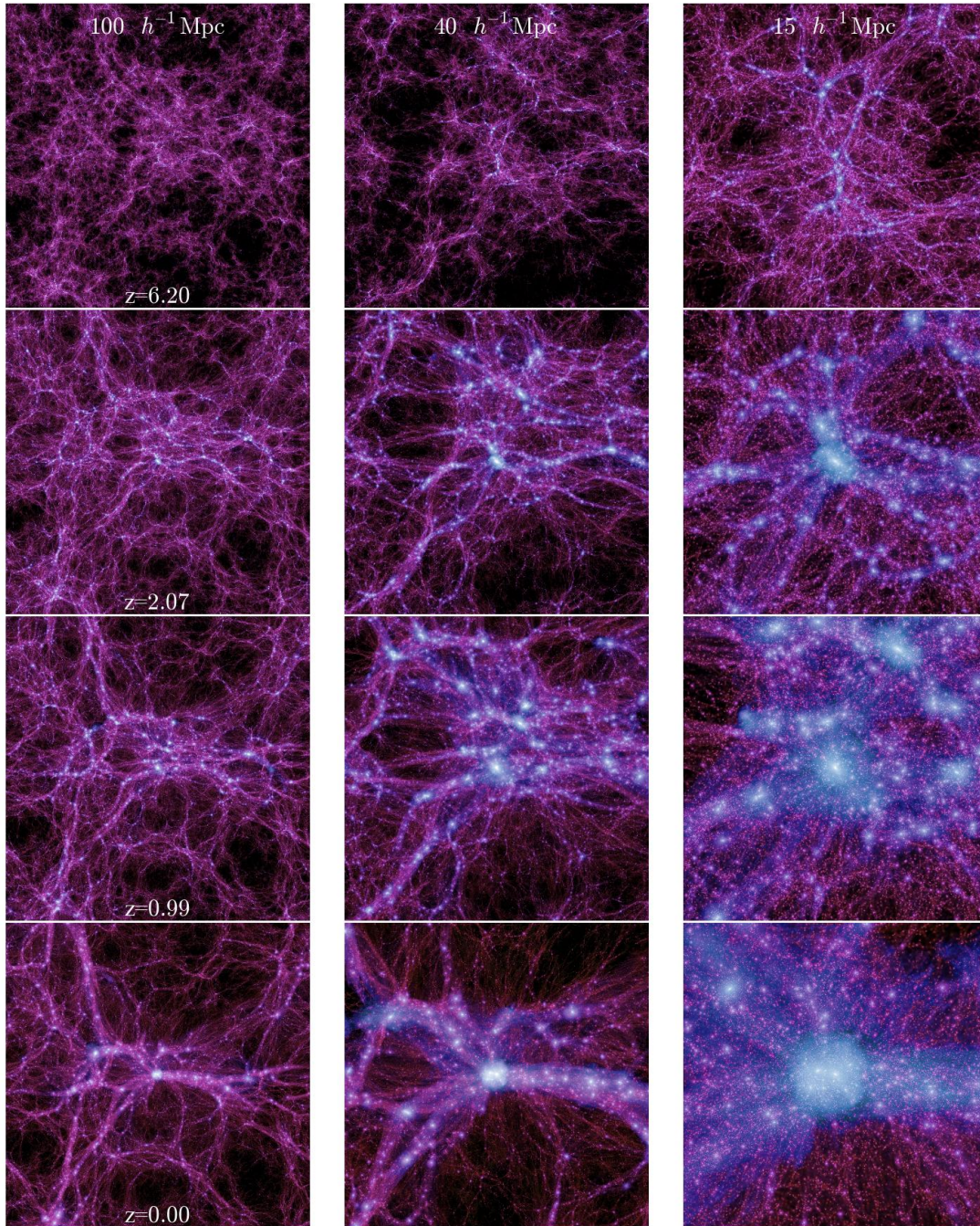


Figure 4.1: The evolution of a large halo in the Millennium-II simulation is shown at three different length scales (indicated in top panels) at four different redshifts (indicated in first column) [6]. The cosmic structure on larger scales looks like a web, consisting of voids, filaments, and nodes. The hierarchical formation of structure is obvious; smaller structures form first and later collapse and merge into a larger halo.

4 Structure formation in the Universe

mass: each particle in the simulation actually represents a collection of objects in reality. Numerical artifacts may arise when two or more of these massive particles encounter each other in the simulation. The gravitational force between them ($\propto r^{-2}$) creates a singularity as the relative distance between the objects approaches zero, and as a result, the velocities of the bodies could become arbitrarily high. Usually this effect is suppressed by defining a certain *softening* length, below which the gravitational force is set to a constant to avoid collisions. This is equivalent to replacing the bodies, which are described by delta-functions, by extended mass distributions [123].

To give an idea of the dimensions of such a simulation: the largest N-body simulation that has been performed up until now is the Millennium-XXL, which includes 303 billion particles, a box length of 4.1 Gpc, and a softening length of 13.7 kpc [124]. Although this is an immense project with very reliable results, the finite resolution of such simulations will always introduce limitations, which are especially present on small scales.

The information that one can derive from these simulations is condensed in several functions. The most important ones for our purpose will be discussed here. The mass function, which gives the number density of halos as a function of their mass, can be calculated from Press-Schechter theory [125]. Their idea is based on the fact that the density fluctuations are Gaussian and can be described in a spherical collapse model. Smoothing the density fluctuations with a top hat function as described in section 4.1, one can already identify protohalos before they collapse as a region where the average density is larger than some critical density, which Press and Schechter defined to be $\delta_c = 1.686$. Instead of the mass, it is easier to work with the mass variance $\sigma^2(M, z)$ extrapolated to the redshift z at which the halos are identified, which is obtained by multiplying the usual variance (see Eq. (4.7)) by the growth factor squared $D^2(z)$ (see Eq. (4.9)). The mass function is then defined as [126]

$$f(\sigma, z) = \frac{M}{\bar{\rho}} \frac{dn(M, z)}{d \ln \sigma^{-1}(M, z)}, \quad (4.26)$$

where $n(M, z)$ is the number density of halos at z that have a mass below M , and $\bar{\rho}$ is the mean density at that time. In Press-Schechter theory the mass function is given by the simple expression [125, 94, 126]

$$f(\sigma) = \sqrt{\frac{2}{\pi}} \frac{\delta_c}{\sigma(M, z)} \exp \left[-\frac{\delta_c^2}{2\sigma^2(M, z)} \right]. \quad (4.27)$$

Mass functions calculated from Press-Schechter theory are in reasonable agreement with those derived from numerical simulations. For an overview about the halo mass function and other analytical approximations see [126].

Simulations show that primary halos are accompanied by a large population of subhalos for which one can derive an approximate expression for the subhalo mass function. It is easiest to assume that the distribution of normalized subhalo masses, i.e., m/M , where m is the mass of a subhalo and M that of the host halo, is the same for all primary halos. This distribution function should drop quickly as $m/M \rightarrow 1$, and we can assume it to follow a power law for $m/M \ll 1$.

The subhalo mass function should then obey [94]

$$dn = c \left(\frac{m}{M} \right)^a e^{-km/M} \frac{dm}{M}, \quad (4.28)$$

where a, c, k are constants whose value can be derived from N-body simulations. This means that the subhalo distribution for primary halos of different mass are approximate self-similar. However, the satellite populations of galaxies with different luminosities do not appear to follow this behavior (see subsection 4.3.1 for further details).

Finally, we discuss the radial density profile of DM halos in numerical simulations. For a primary halo, the density scales like $\rho \propto r^{-3}$ for very large radii. Interestingly, numerical simulations show that halos can be fitted by a universal density profile

$$\rho(r) = \frac{\tilde{\rho}_0}{\left(\frac{r}{r_s}\right)^\alpha \left(1 + \frac{r}{r_s}\right)^{\beta-\alpha}} \quad (4.29)$$

where the central density $\tilde{\rho}_0$ and the scale radius r_s are free parameters and vary for each halo. A good fit to numerical simulations is obtained for the constants $\alpha = 1, \beta = 3$, which is also known as the Navarro-Frenk-White (NFW) profile [127]. The halo concentration $c \equiv r_{200}/r_s$, was shown to decrease monotonically with increasing halo mass [128], meaning that smaller objects are more concentrated. The innermost part of a (main) halo seems to follow a power law, $\rho \propto r^{-\alpha}$, with $\alpha \approx 1$.

More recently it was observed that the Einasto profile [129]

$$\rho_{\text{Ein}}(r) = \rho_{-2} \exp \left[-2n \left[\left(\frac{r}{r_{-2}} \right)^{1/n} - 1 \right] \right], \quad (4.30)$$

provides even a better fit to the Λ CDM halos from simulations [130]. Here, the subscript -2 denotes the value of the parameter at the point where the local slope is -2 and the Einasto index n describes the shape of the density profile. Analysis of halos in the Aquarius simulation show that the inner density profiles do not converge to a fixed asymptotic slope as in the NFW case but are better fitted by the gently curving Einasto profile [131].

Although these profiles can fit the numerical simulations quite accurately, they are less successful when applied to observations of dwarf galaxies and other DM dominated objects. An often used model for this purpose is the isothermal profile [132], which has a finite central density. Observations thus seem to prefer a more core like inner structure, which is in tension with the cuspy subhalo profiles obtained from N-body simulations. We will come back to this issue in subsection 4.3.2.

Comparison of results from N-body simulations to observations show that the Λ CDM model is very successful in explaining the large scale structure of the Universe. However, there is still many to be done to improve the model, especially on small scales. In the next section, we will therefore focus on the most important discrepancies between numerical simulations of Λ CDM and observations.

4.3 Small-scale problems

Although the Λ CDM paradigm has been proven to be very successful on larger scales, there remain a number of puzzles on scales from a few kpc to tens of pc. Various observations of the abundances and internal density profiles of (dwarf) galaxies and galactic satellites are in tension with results from N-body simulations. In this section we will discuss the various small-scale problems in detail, including the solutions that were proposed in terms of astrophysics and modifications to the CDM paradigm.

4.3.1 Missing satellites problem

Observations show that the number of satellites around a galaxy system highly depends on the luminosity or mass of the system. For instance thousands of satellites are observed around the dominant galaxy in the brightest galaxy clusters, whereas the Milky Way (MW) or Andromeda have only a dozen, and faint dwarf galaxies hardly have any luminous satellites at all. This is in sharp contrast with the results from N-body simulations, where the subhalo distribution function is more or less the same for the mass normalized to the host halo mass (see Eq. (4.28)). This is more generally known as the substructure problem (for a good review, see [7]). Concerning the luminous satellites of our MW and Andromeda as a function of the circular velocity (see below), the discrepancy with the predicted number of small subhalos is referred to as the “missing satellites” problem¹ [133].

In order to connect the results from numerical calculations to the observations in a suitable way, one needs to quantify the subhalo and satellite populations. For subhalos, this is done by measuring the maximum circular velocity

$$V_{\max} = \text{Max} \left[\left(\frac{G_N m(< r)}{r} \right)^{1/2} \right], \quad (4.31)$$

which either refers to the velocity of stars around the center of the subhalo, or the subhalo velocity around the center of the host halo. Here, $m(< r) = 4\pi \int_0^r dr' r'^2 \rho(r')$ is mass within a sphere of radius r . Since the potential energy of a self-gravitating system is proportional to $V \propto V_{\max}^2$, Eq. (4.31) gives us information about the depth of the potential. The advantage of this definition is that it is fairly easy to calculate, and it does not depend on the size or boundary of the subhalo. The latter is actually difficult to determine, especially in the inner regions of the host system where densities are higher and subhalos can hardly be distinguished from each other, or from the host halo.

The few dozen satellite galaxies around the MW and Andromeda that we know of span a wide range of luminosities. The brightest ones, like the Large and Small Magellanic Clouds (LMC and SMC), have been known for many centuries, whereas the faintest only have been discovered recently by the Sloan Digital Sky Survey (SDSS) [134]. The galaxies can therefore be divided into ‘classical’ dwarfs, which have luminosities larger than $\sim 10^5 L_{\odot}$, and ‘ultra-faint’ dwarfs, which can have luminosities as low as $\sim 10^3 L_{\odot}$.

¹This is a rather confusing name for the problem: the satellites are too abundant in the simulations rather than missing in the observations.

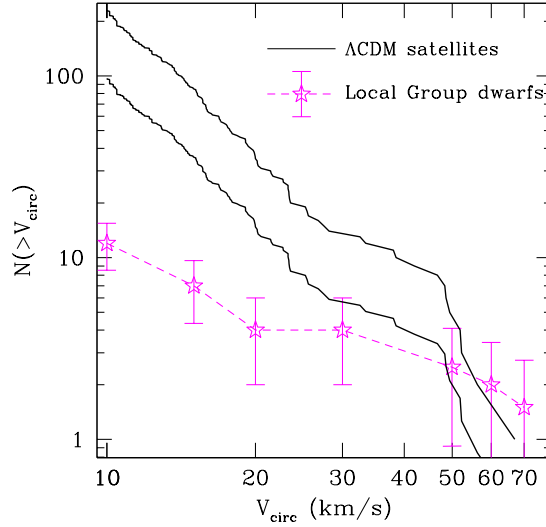


Figure 4.2: Cumulative circular velocity function $N(>V_{\text{max}})$ of subhalos for a host halo with $V_{\text{max}} = 160$, and 208 km s^{-1} (solid, black). Circular velocities of MW satellites (pink stars) have been estimated from line-of-sight velocity dispersions (see text). Predicted subhalos at small V_{circ} are much more abundant than the observed MW dwarfs. Taken from [7]

The former group of dwarf galaxies have been shown to exist within 300 kpc from the MW center, and can be divided into several categories [135]. There are the dwarf irregular galaxies (dIrrs), like the LMC and SMC, which have a low surface brightness, an irregular shape, and continue to form stars. The dwarf spheroidal galaxies (dSphs), e.g., Draco and Fornax, also have a low surface brightness but hardly form stars anymore. Finally, the dwarf elliptical galaxies (dEs), such as M32, have a high surface brightness but a low luminosity, and no star formation at present.

The ultra-faint dwarfs, like Segue 1, only host a very small population of stars. Since these are highly DM dominated objects, their mass profiles cannot be determined by gas rotation curves; instead, their total mass is derived by using kinematics of the stars. Because they are so faint, we have only managed to get a good picture of them within $\sim 30 - 50$ kpc from the galactic center [136]. Extrapolating our knowledge of radial distribution of dwarfs, we expect to find at least a hundred faint ones within 400 kpc with future experiments [137].

This last fact has been interpreted as a possible explanation for the missing satellite problem, however, this is not the case. Even though still many satellites are undiscovered, it by no means could account for the predicted number, which is $\sim 10^5$ for subhalo masses above $10^5 M_{\odot}$. It is therefore much clearer to state the problem not in terms of number of satellites, but in the slope of the cumulative circular velocity function.

This is what can be seen in Fig. 4.2, where the solid lines are the predicted velocity functions from N-body simulations for host halos with $V_{\text{max}} = 160$, and 208 km s^{-1} . The maximum circular velocity of our MW is assumed to lie somewhere in between these numbers, and usually a total virial mass of $M_{\text{vir}} \approx 10^{12} M_{\odot}$ is assumed. The velocity function of the observed satellites was derived from the line-of-sight velocity dispersions σ_r , using $V_{\text{max}} = \sqrt{3}\sigma_r$. Although this

conversion is too simplistic and probably not very accurate, it is sufficient to point out the main problem, namely that there is a great disagreement between the slopes of the predicted and measured velocity functions. A more accurate conversion factor would not help to overcome this discrepancy, unless it strongly depends on V_{\max} , for which there is no observational evidence.

Of course many possible solutions to the substructure problem have been proposed. Astrophysical solutions all boil down to suppressing galaxy and/or star formation in the simulations by physical processes that have not been taken into account in the standard Λ CDM simulations.

For instance, the suppression of galaxy formation can be obtained by increasing the entropy of the gas before it collapses onto the DM halo to such a degree that it will not be able to follow the DM. Photoionization [138, 139] or an induced shock by the accretion of gas [140, 141] can cause heating, which correspondingly suppresses the formation of dwarf galaxies. However, results of numerical simulations that take these processes into account show that the amount of subhalos is still larger than what is implied by observations [142]. Another way to increase the entropy is to include heating by blazars, which are active galactic nuclei that expel highly energetic material in relativistic jets [143].

Furthermore, since stars form by the radiative cooling of the ISM, one can suppress star formation by decreasing the cooling efficiency of the collapsing baryons. This depends greatly on the chemical composition of the gas: metals, by which elements heavier than hydrogen and helium are denoted, are very efficient in cooling by line emission due to recombination of the ionized atoms. An intrinsic low metallicity of the gas will therefore suppress the cooling efficiency [144]. Cooling in gas with a low metallicity is mostly due to neutral hydrogen (HI). This can quickly be dissociated by photoionization, which correspondingly also suppresses the formation of stars [145].

Besides increasing the gas entropy or suppressing the cooling efficiency, the removal of gas will also result in a suppressed star formation rate. Once dwarf galaxies have formed, their gas can be removed by photo-evaporation [146, 147], or by feedback from supernovae, the most violent explosions in the Universe [148–150]. Unfortunately, the stellar content and HI mass distributions in simulations with this kind of feedback are in conflict with the most recent observations [151].

Finally it is possible to adjust the DM model in the numerical simulations, assuming it is not correct on smaller scales. One can either change the seed perturbation spectrum of the Λ CDM itself, or consider modifications of the CDM paradigm, such as strongly self-interacting DM (SIDM). In these kind of models the DM has a large, constant self-scattering cross-section, which can result in a suppressed amplitude of density fluctuations at small scales [152]. However, it was later shown to be in conflict with various observations (see also the next subsection 4.3.2)

The abundances of subhalos do in fact depend on the amplitude of the power spectrum on scales that correspond to the mass of the primary halo. If one can suppress the amplitude of the density fluctuations on these scales, the population of subhalos will become smaller. Most successful are WDM models that, as we have seen in subsection 4.1.1, suppress small scale density fluctuations by free streaming effects [153–156]. Moreover, the WDM particles have tiny primordial thermal velocities that cause the inner density of the halos to become less dense (see e.g. [153]). They are therefore more easily disrupted by tidal forces as they fall into the host halo.

Although WDM models can suppress the subhalo population to the required amount, these models are strongly constrained by Lyman- α bounds. Combining this data with CMB and observations of galaxy clusters, a lower limit of $m_{\text{WDM}} > 2$ keV was inferred [157, 158]. However, when less reliable data due to systematic errors is not taken into account, this bound weakens to $m_{\text{WDM}} > 0.9$ keV [159]. More details on the allowed parameter range will be discussed in chapter 8. Here, we will also show that the formation of subhalos can be successfully suppressed for DM models with velocity dependent self-interactions (vdSIDM). This is a model that will come up in the discussion of the next two small scale problems, but has not been considered in connection to the missing satellite problem before.

4.3.2 Cusps vs. Cores

Low mass galaxies are interesting subjects for testing the predictions of Λ CDM, since they have a large DM component and effects induced by the baryonic component are less pronounced. As we saw in section 4.2, numerical simulations predict a universal matter density profile for subhalos with a sharp NFW cusp in the center (Eq. (4.29) with $\alpha = 1, \beta = 3$). It was found in observations of low mass spiral galaxies, however, that they have a flat, constant inner density core, which is well fitted by a Burkert profile [160]

$$\rho(r) = \frac{\tilde{\rho}_0}{\left(1 + \frac{r}{r_s}\right) \left(1 + \frac{r^2}{r_s^2}\right)}, \quad (4.32)$$

which for $r \ll r_s$ is similar to an isothermal profile, i.e., $\rho \propto r^{-\alpha}$ with $\alpha = 0$. Later, other studies obtained similar results for spiral galaxies [161, 8, 162, 163]. For example, Fig. 4.3 shows that the data from various studies of low surface brightness galaxies prefer a constant density core with $\alpha = 0$ at small radii. For a review on attempts to determine the inner density of dwarf galaxies, see [164].

Other studies have instead focused on dSphs, for which the density profile was constrained by using Jeans modeling [165]. Although these galaxies all seem to prefer a cored inner density profile, another study showed that the inner density profiles of four dwarf satellites could be described by a moderate cusp [166]. It must be noted that this method requires certain assumptions about the system, which is usually taken to be spherical symmetric and isotropic. It was noted by [167], however, that the preference for a cored or cuspy inner density profile is highly dependent on the assumptions made about the anisotropy. This was later confirmed by [168], which showed that a cored isotropic velocity distribution is degenerate with a cuspy anisotropic one in combination with a large inclination of the galactic disk (see also [169]). Therefore assuming a large anisotropy could alleviate the tension between observations and simulations.

Other studies have used methods that are supposedly less affected by the anisotropy. Some dSphs contain populations of tracer stars, which can be used to model the underlying DM profile more accurately. For each population, which is subject to the same gravitational potential, one can measure stellar velocities, positions and spectral indices. These can be used to infer the mass enclosed within the half-light radius for each stellar subcomponent. The result is a measurement of dynamical mass with a small uncertainty at least two locations in the galaxy. Combining these, one can infer the slope in the DM profile of the dSph. The results of these methods applied to

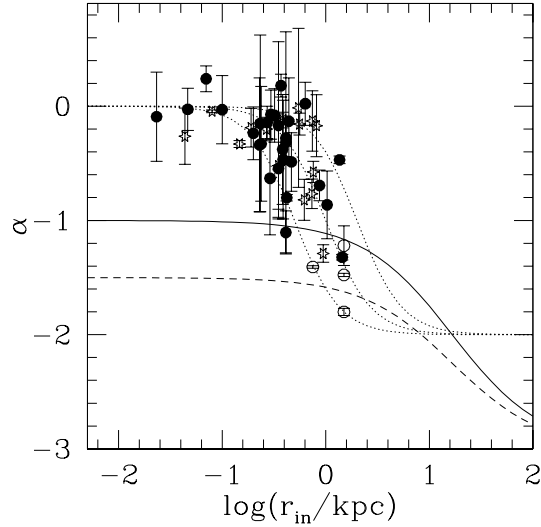


Figure 4.3: Low surface brightness galaxies seem to agree better with pseudo-isothermal profiles (dotted lines) than with a NFW profile (solid line) or with an even cuspier profile $\rho^{-1.5}$ (dashed). The data-points are taken from various studies. For more details, see [8], where this figure originates from.

Sculptor [170] and both Fornax and Sculptor [171], show that a cored profile is preferred over a NFW cusp.

A completely different method is Schwarzschild modeling, which allows one to measure the enclosed mass and anisotropy of a galaxy by using the line-of-sight velocity distributions. Applied to Fornax, the measurements again show that a steep slope with $\alpha = 1$ is rejected with high confidence, and a cored slope with $\alpha = 0$ is preferred. More recent studies for the Sculptor dSph galaxy have shown, however, that although steep cusps with $\alpha > 1.5$ are ruled out, the line-of-sight data is still too sparse to make a distinction between a flat core and a shallower cusp with $\alpha \leq 1$ [172].

Alternatively, one could alleviate the tension by adding a mechanism that alters the inner density structure of the halo in the simulations. It has been shown that baryonic feedback processes, like a supernova explosion, could reduce the central DM cusp [173]. The rapid oscillating gravitational potential allows baryons to transfer energy to the DM, such that their velocity dispersion increases. However, these kind of feedback processes result in a stellar content that was shown to be in tension with observational constraints on Low Surface Brightness galaxies [174]. Moreover, earlier simulations that included baryonic feedback did not result in more core-like inner structures for subhalos [175]. Another possibility would be to assume that the baryonic mass in the form of stars and gas, which dominates over the DM mass in the center of a galaxy, is distributed like a core.

Solutions in the form of alterations to the Λ CDM model are few. Although the WDM seems to be very good in suppressing the formation of small subhalos as discussed in the last subsection, it unfortunately is less successful in forming large cores. In order to form a core of ~ 1 kpc, a WDM candidate with such a small mass is needed that dwarf galaxies would not be able to form in the first place; this is also known as the ‘catch 22’ problem [176].

It has also been proposed that strongly self-interacting DM (SIDM) with a constant scattering cross section would produce cored dwarf galaxies [152]. In SIDM the DM has a mean free path between ~ 1 kpc and ~ 1 Mpc, that would affect the halo properties at the scale of dwarf galaxies. The increased entropy of the SIDM in the center of a subhalo would cause infalling matter to scatter more frequently and result in a more flattened distribution. Unfortunately, it was shown that the SIDM is ruled out by various astrophysical constraints. The shallow and spherical cores of SIDM are in contradiction with the dense and ellipsoidal cores of galaxy clusters [177, 178]. In contrary to CDM subhalos, which after virialization essentially stay the same, SIDM halos would undergo a process of thermal relaxation. In this process, mass and energy is transferred from the core to the extended halo, which causes the core to shrink in size and mass while the density and temperature increase. Eventually, the core would collapse to a singular state, a so-called gravothermal catastrophe. Since this state is not observed, it places limits on the relaxation time and thus on the self-scattering interactions [179]. Subhalos would additionally be expected to be destroyed by collisions with high-velocity particles from their host halo [180]. Finally, the implied self-interacting cross-section is difficult to reconcile with popular WIMP models.

However, self-interacting DM with a velocity dependent cross section (vdSIDM) is much more promising. These are theories in which the DM interacts only through a ‘dark force’ that can greatly enhance the self-interaction cross-section, i.e., the Sommerfeld enhanced models that are the subject of this work. Not only does vdSIDM evade all astrophysical bounds that were mentioned above [181], it also has been shown to form cored density profiles on dwarf galaxy scales [13]. As we will see in the next subsection, this model can also alleviate another small-scale problem.

4.3.3 ‘Too big to fail’-problem

In 4.3.1 we saw that there is a discrepancy between the number of simulated subhalos and the observed satellites of the MW. Since each subhalo is potentially capable of forming a galaxy, it is therefore usually assumed that the brightest satellites correspond to the most massive subhalos in simulations. However, the mass of a subhalo is subject to changes due to e.g. tidal stripping, such that it is not entirely clear how to define the most massive subhalos. We can distinguish between two broad classes of models: ones where the luminosity of the satellite is related to the present halo mass, and ones where it is related to the mass of the halo before tidal stripping. For both cases it has recently been shown that the most massive subhalos in Λ CDM simulations are too dense to host any of the brightest observed dwarf galaxies of the MW [182, 9]. Since these most massive subhalos are *too big to fail* in forming stars, we should have been able to observe them. The fact that we do not, indicates that there is something seriously wrong with the dynamics of the simulated subhalos, hence explaining the name of this problem.

The Λ CDM predictions were inferred from six DM halos taken from the Aquarius simulation², which are comparable in size to the MW ($0.95 - 2.19 \times 10^{12} M_{\odot}$). In each halo, subhalos were identified and characterized according to their maximum circular velocity V_{\max} (see Eq. (4.31)), and r_{\max} , the radius at which they obtained V_{\max} . Furthermore, the properties of

²In the earlier work [182] also one MW sized halo from Via Lactea-II was included. The conclusions reached for this halo are the same as for the Aquarius halos.

4 Structure formation in the Universe

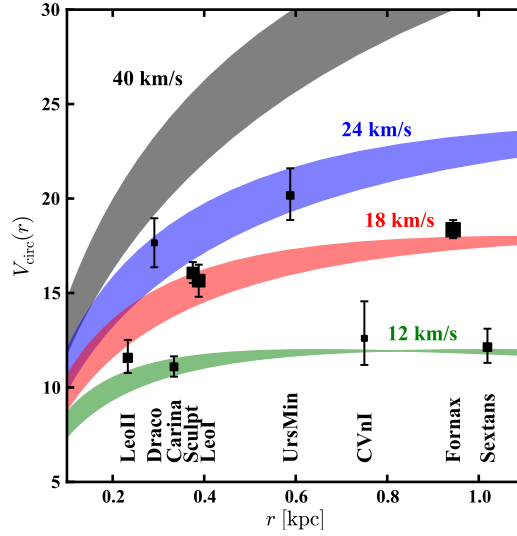


Figure 4.4: The brightest dSphs in the MW (squares) all have a maximal circular velocity that is less than 24 km s^{-1} . The shaded bands indicate the rotation curves for the subhalos (assuming a NFW profile) with a 1σ deviation. Each of the simulated halos in the Aquarius simulation contains at least 10 subhalos that are much denser than the MW satellites, i.e., $V_{\text{max}} > 24 \text{ km s}^{-1}$ [9].

the subhalo, such as the maximum circular velocity $V_{\text{infall}} = V_{\text{max}}(z_{\text{infall}})$ and the virialized mass $M_{\text{infall}} = M_{\text{vir}}(z_{\text{infall}})$, were computed at the time its mass was maximal, i.e., prior to infall on the host halo.

To compare this with observations, one must look at kinematics of satellites in the MW. Often used are the deprojected half-light radius $r_{1/2}$, the radius of a sphere that contains half of the luminosity of the total system, and the mass enclosed within this sphere, $M_{1/2}$. The dynamical masses of dSphs have shown to be well constrained by line-of-sight velocity measurements, e.g., the circular velocity at half-light radius is well approximated by $V_{\text{circ}}(r_{1/2}) = \sqrt{3}\sigma_r$. From the dSphs, only the brightest were chosen with $L_V > 10^5 L_{\odot}$, because they have the most reliable kinematic data and were most suitable for the analysis. After removal of the Sagittarius dwarf, which is not a good candidate since it most likely not in equilibrium like the others, a set of nine dSphs remains which are all highly DM dominated at $r_{1/2}$. Both the Magellanic clouds were considered separately, since they are much brighter and more massive than the dSphs, and conservative limits indicate that $V_{\text{max}} > 40 \text{ km s}^{-1}$ and $V_{\text{infall}} > 60 \text{ km s}^{-1}$.

Subhalo masses are well described by a NFW profile, from which V_{max} as a function of r_{max} was inferred. These were then compared to the $V_{\text{circ}}(r_{1/2})$ of the nine brightest dwarfs, as can be seen in Fig. 4.4. It shows that the MW satellites are consistent with DM subhalos of $V_{\text{max}} = 12 - 24 \text{ km s}^{-1}$, and only Draco could be consistent with a larger V_{max} . However, in each simulated halo at least 10 to 24 subhalos with $V_{\text{max}} > 25 \text{ km s}^{-1}$ reside, which have no bright counterparts in the MW. These subhalos are not massive enough to host any of the Magellanic clouds either.

To exclude the case that the mass profiles of some subhalos are not well described by a NFW profile, another analysis was carried out using the raw particle data, thereby removing any uncertainties regarding the DM density profile. Additionally, it was considered that the galaxy

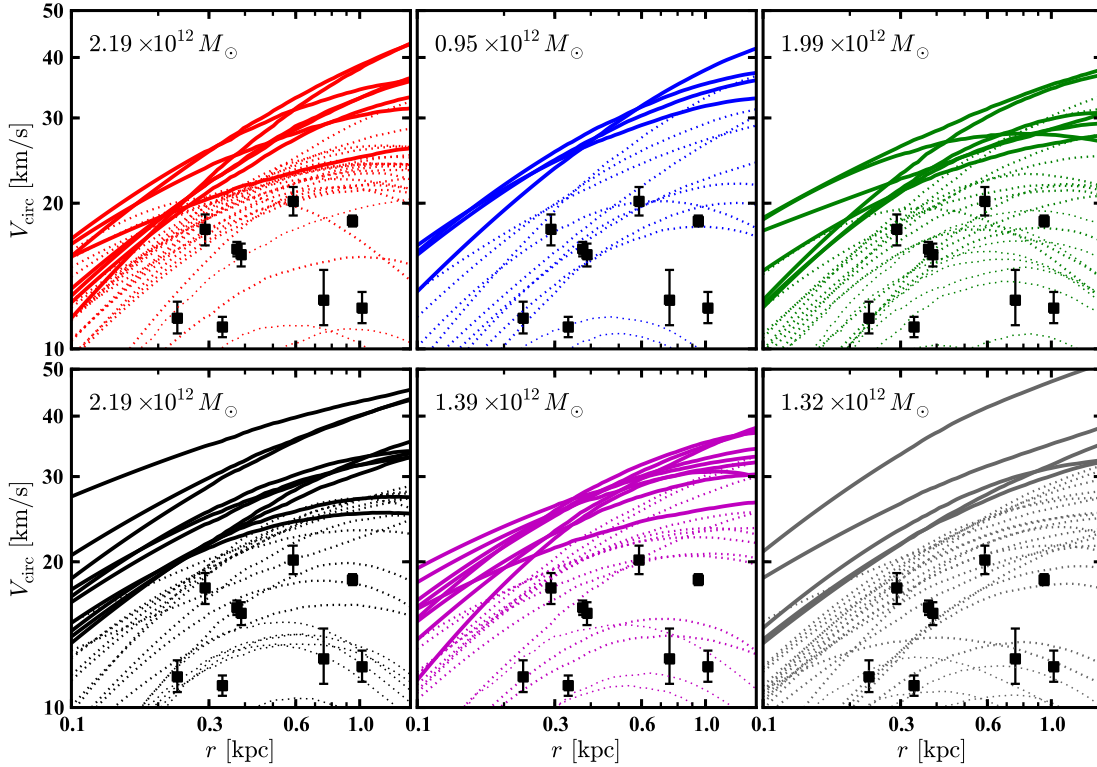


Figure 4.5: Each panel shows the subhalo rotation curves with $V_{\text{infall}} > 30 \text{ km s}^{-1}$ and $V_{\text{max}} > 10 \text{ km s}^{-1}$ for one simulated MW halo (mass indicated in upper left corner) in comparison with the observed dSphs (squares). No assumptions about the simulated DM density profiles were made, and subhalos comparable to the Magellanic clouds were excluded. Subhalos denser than the dwarfs by more than 2σ (solid lines) are much too dense to host any of the bright satellites. Among the remaining subhalos (dotted lines) there are also subhalos that do not correspond to any of the bright dwarfs. [9]

luminosity would correlate with V_{infall} rather than with $V_{\text{max}}(z=0)$. For this reason the circular velocities of the most massive subhalos with $V_{\text{infall}} > 30 \text{ km s}^{-1}$ and $V_{\text{max}}(z=0) > 10 \text{ km s}^{-1}$ were compared to $V_{\text{circ}}(r_{1/2})$ of the dwarfs. The results showed that in all cases there are always subhalos present that are more massive than the dSphs, i.e., their velocity curves are inconsistent with the dynamics of the most luminous MW satellites.

Shown in Fig. 4.5 are the rotation curves for all subhalos with $V_{\text{infall}} > 30 \text{ km s}^{-1}$ and $V_{\text{max}}(z=0) > 10 \text{ km s}^{-1}$ for each of the six simulated MWs. The subhalos which are more massive than every dwarfs by 2σ are plotted in solid lines, whereas the remaining subhalos are plotted in dotted lines. Squares with error bars correspond to $V_{\text{max}}(r_{1/2})$ of the brightest MW satellites. It shows clearly that the most massive subhalos are far too dense to host any of the observed brightest dwarf galaxies, i.e., for a given radius r , their maximum circular velocity (which is related to the mass, see Eq. (4.31)) is too high to fit the data. Moreover there are also subhalos that do have a rotation curve that is comparable to that of the dSphs, but they are not accounted for in the observations. This indicates that the dynamics of the most massive subhalos do not resemble the population of dSphs at all.

4 Structure formation in the Universe

Using abundance matching one can assign a stellar mass M_* to a subhalo, which is done by relating galaxy abundances to subhalo populations, e.g., $n(> M_*) = n(> V_{\text{infall}})$. From this one can derive a luminosity function for the simulated subhalos by extrapolating for small halo masses; in the analysis discussed here it was used that $M_*/L_V = 2$. Comparisons to luminosity functions of the MW show that they are in good agreement both in amplitude and slope. However, it turns out that the subhalos that would host the bright dwarfs have a much larger V_{max} than the ones that are calculated for the dSphs. This means that although some subhalos seem dynamically consistent with the bright satellites, these are not the ones that are predicted to host these dwarfs.

A solution to this discrepancy could be found by assuming that the MW mass is smaller than what was assumed in these simulated halos, i.e., $\lesssim 8 \times 10^{11} M_\odot$ [183, 184]. The precise mass of the MW is still uncertain, however, the consensus is that the MW mass lies in the range $1 - 2 \times 10^{12} M_\odot$, which is in good agreement with the halo masses used in the simulations discussed here. Moreover, numerical simulations show that a halo of $10^{12} M_\odot$ has less than a 10 % chance to host two satellites that are as large as the Magellanic clouds [185, 186]. Observations carried out by SDSS of satellites hosted by systems that are similar to the MW indicate that this probability only decreases for lower galaxy masses [187–189]. A lower limit of $1.8 \times 10^{12} M_\odot$ on the mass of the Local Group, a system which is dominated by the MW and Andromeda, was inferred by studying orbiting times [190]. All the above arguments disfavor a small MW mass solution.

Another possibility is to include baryonic feedback that would cause large outflows of baryonic matter from the galaxies. This might affect the dynamics of the system enough to reduce the central DM densities. In [9] the effect of supernova explosions was taken into account to estimate the change in the subhalo rotation curves. It was shown that the circular velocities could indeed be reduced, but not enough to accommodate all bright satellites. In fact the resulting V_{circ} profile was only consistent with two of the least luminous dwarfs that were considered. To match their density would require the removal of at least two orders of magnitude more mass than what was considered.

A last astrophysical explanation to the problem could be that galaxy formation is highly stochastic for halos with $V_{\text{infall}} \lesssim 50 \text{ km s}^{-1}$. This would mean that the stellar mass or luminosity does not correlate with the DM halo mass at the scales of dwarfs. However, this would be in contradiction with results from abundance matching, which show that the stellar mass is an increasing function of the maximum mass that a halo ever obtained. This is confirmed by stacking analyses of gravitational lensing and studies of satellite dynamics of SDSS galaxies [191].

Finally a solution might exist in terms of a DM candidate. A good option would be WDM, which could reduce the amount of massive subhalos, and decrease the inner density of the subhalos that are formed [192]. In addition it was shown that the vdSIDM models, which were briefly mentioned at the end of the previous subsection, produce cored dwarf-like subhalos that in addition match the velocity profiles of the brightest MW satellites [13]. Encouraged by these results, we will therefore further investigate the substructure formation of this interesting model in chapter 8. First, it is necessary to give the reader a detailed introduction to the underlying theory of these kind of models, in which the repeated exchange of a force carrier results in a Sommerfeld enhanced cross section.

5 Sommerfeld Enhancement

5.1 Introduction

The topic of this chapter is the non-relativistic quantum effect named after its discoverer Arnold Sommerfeld, who first described it in 1931 when he calculated the scattering of a slowly moving electron-positron pair [193]. When their kinetic energy is low enough, the Coulomb force between the electron and positron becomes important and distorts the wave-functions of the incoming particles, such that they have a larger probability to undergo a short-range interaction. In this way, the Sommerfeld effect thus effectively enhances the $e^+e^- \rightarrow \gamma\gamma$ cross section.

In quantum field theory this process can be visualized by Feynman diagrams, which remind of ladders with the exchanged mediator particles (here photons) as rungs (see Fig. 5.1). Due to the fact that the electron and positron can interact through the photon, a threshold singularity is generated in their annihilation process. Usually, each exchanged photon contributes a factor α to the amplitude of the diagram, such that higher order diagrams are less important and perturbation theory can be used to calculate the interaction. However, when the relative velocity v of the e^+e^- pair is smaller than the photon coupling α , each exchanged photon contributes a factor α/v to the amplitude of the diagram. This means that higher order diagrams become more and more important as they exchange more photons, and a perturbative expansion in α fails. The Sommerfeld effect is thus a non-perturbative effect, and in order to correctly calculate the cross section, it is therefore necessary to perform a resummation over all diagrams as depicted in Fig. 5.1.

After Sommerfeld developed the mechanism to take this effect into account, it since has been applied to correctly predict the cross sections for many other non-relativistic particle systems. In cases where the force carrier has a mass, the repeated exchange of the mediator creates an attractive Yukawa potential instead. The Sommerfeld effect then arises when the mass of the annihilating particles is much larger than the mediator mass. The finite range of the potential can cause the particles to form a quasi bound state for which the annihilation cross section even becomes resonant.

Since most popular DM candidates are WIMPs, i.e., heavy, non-relativistic particles, the Som-

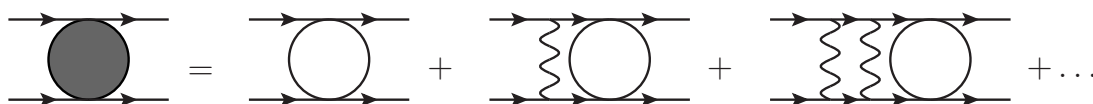


Figure 5.1: The white blob includes all short-range interactions, whereas the exchange of a mediator particle is a long-range effect. The grey blob includes all interactions with the Sommerfeld effect taken into account, which is obtained by performing a resummation over all possible ladder diagrams, where the mediator particles represent the rungs on the ladder.

merfeld effect is also relevant in DM annihilation processes. This was first realized in 2003, when the authors of [194] included the Sommerfeld effect in calculations of the annihilation cross section of (wino- or Higgsino-like) neutralino DM into two photons. The incoming neutralinos can form a two-body state that exchange Z and/or W bosons between them. Additionally, the neutralino pair can be converted into a chargino pair, which correspondingly can exchange virtual photons. The non-perturbative corrections to the neutralino annihilation cross section were calculated in non-relativistic field theory, and were found to be non-negligible. The same authors further worked out this theory in a collection of papers, discussing the relevance of Sommerfeld enhancements on the expected cosmic ray spectrum [195, 196] and thermal relic DM abundance [197]. Another group performed similar calculations for minimal DM, where the DM consist of one multiplet added to the SM, which has only gauge interactions and mass term that is invariant under $SU(2)_L$ [198].

It was not until an anomalous positron excess was measured by PAMELA in 2008 [84], that Sommerfeld enhanced DM models started to attract a lot of attention. The cosmic positron fraction $e^+/(e^+ + e^-)$ earlier measured by HEAT [199] showed a small rise in the spectrum between 10 and 50 GeV, but was still consistent with the background within the errors. Similar results were later obtained by AMS-01 [200]. PAMELA, however, was able to measure the positron flux with much better precision and up to energies of 100 GeV in 2008. The results showed a large excess between 10 and 100 GeV, which could not be explained by the secondary production of positrons through cosmic ray interactions with the interstellar medium. The excess therefore had to be of primary origin, either in the form of annihilating DM or some astrophysical source (see discussion below).

Other experiments, not able to distinguish between electrons and positrons, measured the combined e^-e^+ flux. ATIC first measured a peak in the spectrum between roughly 300 and 800 GeV [85]. Although their observations were consistent (within the statistical and systematic errors) with later data from H. E. S. S., the latter excluded a peak as large as measured by ATIC [201, 87]. The spectrum as measured by Fermi-LAT, also did not reveal such a large prominent feature, although its spectrum was much harder as expected from conventional diffusion models [86] (for an overview of different interpretations of the measured electron-positron spectrum, see [202]).

These measurements of an increased leptonic flux led people to believe that this might well be the first direct evidence of DM. However, a DM explanation for the PAMELA excess in terms of annihilating WIMPs was not so obvious at first sight. In fact, the DM has to fulfill three properties in order to do so: (1) In order to obtain a flux of electrons and positrons as large as observed, the DM annihilation cross section must be much larger than the one that is inferred from the thermal relic abundance (see Eq. (3.1)), (2) the DM should have a large annihilation cross section into leptons to fit the hard positron spectrum, (3) in order to be consistent with measurements of the antiproton flux by PAMELA, which did not show an excess [82], a suppressed annihilation into hadrons is required. These restrictions to the model make a thermal DM explanation for the lepton excess rather difficult, however, not impossible: its annihilation cross section needs to be boosted somehow and the DM has to be *leptophilic* [203–208, 89].

In order to overcome these issues, a DM model was proposed that interacts only through a dark force, i.e., a light boson which decays dominantly into leptons [48]. In these kind of models the annihilation cross section for slowly moving DM particles is naturally enhanced by

the Sommerfeld effect. In this way, the larger velocities around chemical decoupling ($v/c \sim 0.3$) would have resulted in an annihilation rate that gives the observed relic density, whereas much smaller WIMP velocities today ($v/c \sim 10^{-3}$) would give an enhanced annihilation rate into electrons and positrons. These kind of leptophilic models thus could rather easily accommodate the measured positron and antiproton fluxes and still be consistent with the relic abundance [209, 89], albeit that the motivation for such models remained rather weak. Various implementations of these kind of models in relation to the positron excess have since been investigated by many groups (e.g. [88, 49, 90]).

Alternatively, the positron excess could be explained in terms of astrophysical effects (for a review, see [93]). For example, the DM annihilation cross section can be boosted by the substructure that is present in our galaxy [205, 206] (see e.g. [117] for the effect of substructure in combination with a Sommerfeld enhanced DM model). It was also noted that astrophysical objects such as nearby pulsars, ejecting electron-positron pairs with high energies, could also account for the observed excess [91]. Using standard assumptions, the signal is unlikely to be explained by one pulsar alone, but two or more pulsars can easily produce a flux as observed [210]. Therefore, in view of the rather contrived leptophilic models, it is more likely that the source of the excess is of astrophysical origin. Moreover, the leptophilic models designed to explain the PAMELA positron excess are severely constrained by many other observations, including the anti-proton cosmic rays [211], gamma rays and radio observations from the Galactic center [212], gamma rays in the Galactic halo from inverse Compton scattering [213], gamma rays from galaxy clusters [115, 116], the CMB [214–217], and even by BBN [218] (see e.g. [119] for an overview of the constraints).

Nevertheless, the positron excess has rekindled interest in the Sommerfeld effect that by itself is an interesting phenomenon. For instance, a full analysis of the Sommerfeld effect in the MSSM has been worked out, and has shown to give some significant corrections for certain regions in parameter space [219–221]. The Sommerfeld effect is a general mechanism that, if present, cannot be neglected if one wants to obtain correct predictions for DM related observables. Therefore we will spend a chapter on explaining the theory behind the Sommerfeld enhancement, before discussing its effect and applications to various DM related topics in the rest of this thesis.

In the next section we will discuss the calculation of the Sommerfeld effect for the annihilation of a non-relativistic electron and positron, for which a resummation over all ladder diagrams is necessary. Fortunately, the different spatial ranges of the non-perturbative corrections and the annihilation make it possible to calculate the interaction in a much simpler and equivalent way in a non-relativistic field theoretical framework. The ladder diagrams, which represent the multiple exchange of the force carriers, create a Coulomb potential that can be taken into account by considering its effect on the wave-function of the metastable bound state of the electron-positron pair known as *positronium*. We will see that, in the end, finding the Sommerfeld enhancement factor boils down to solving the Schrödinger equation for the two-body wave-function of the annihilating particles. With the distorted wave-functions one then calculates the short-range interaction, i.e., the annihilation or scattering, in non-relativistic scattering theory which we will discuss in section 5.3 and 5.4, respectively.

5.2 Resummation of ladder diagrams

As explained in the previous section, the Sommerfeld effect is a long-range effect caused by the exchange of virtual photons between the annihilating particles, whereas the annihilation itself is a highly relativistic process that occurs on a short range. The different scales of these interactions make it possible to factorize the non-perturbative corrections from the annihilation in a non-relativistic effective field theory (see e.g. [222, 194, 196]). The relativistic scales are then integrated out, and in order to compensate for their removal, correction terms have to be added to the theory. The long-range interaction is therefore replaced by a local one, such that the non-perturbative effect can be taken into account by a renormalization of the coupling constants. We can then use ordinary perturbation theory to expand in the new, renormalized coupling and calculate the desired interactions. From this non-relativistic action a two-body effective action is derived that now includes the Sommerfeld effect as a long range potential that affects the wave function of the two-body system. Finally, the equations of motions for the two-body system are derived, which take the form of the well-known Schrödinger equation.

The framework that we use here is the same as in [194, 196], and is very clearly worked out and explained in [223]. To illustrate the technique, we will perform the calculation in non-relativistic quantum electro dynamics (NRQED) to calculate the Sommerfeld enhancement for an electron-positron pair annihilating into two photons. Based on [224], this derivation serves as a simple example of the treatment, which can be applied and generalized to other theories in a straightforward way. In this section, we will give a sketch of the complete calculation along with the most important results; the details of the calculation can be found in Appendix section A.1.

A different, but completely equivalent approach to derive the Sommerfeld effect is worked out in [225, 226]. Here, the focus is on the relation between the bare amplitude of the diagram, i.e., without long-range effect, and the complete amplitude including the Sommerfeld effect. The resummation of the ladder diagrams can be taken into account by writing the full annihilation amplitude in a recursive form. The advantage of this method is that the bare amplitude can be totally generic, and does not have to be an S-wave annihilation process. This treatment will not be discussed here and we point the reader to the references for more details.

5.2.1 Preliminaries

The optical theorem

Since we will make good use of it in the treatment given below, we will here briefly explain the optical theorem. Basically, it is a method to relate the imaginary part of a forward scattering amplitude to the sum of all possible intermediate states. For more details e.g. see [227].

The S-matrix, the quantity that relates initial to final states, can be written as

$$S = 1 + iT, \tag{5.1}$$

where the T -matrix contains all information regarding interactions. The optical theorem is simply a consequence of the unitarity of the S-matrix, i.e., $S^\dagger S = 1$, such that one can derive that

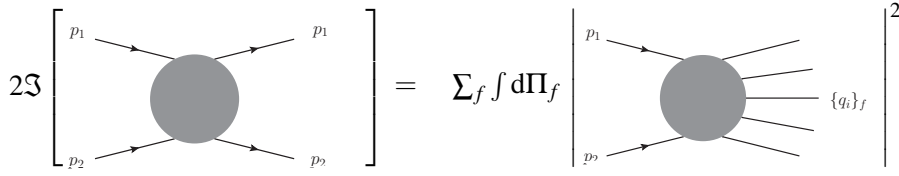


Figure 5.2: The optical theorem relates the imaginary part of the forward scattering matrix element to the squared modulus of the matrix element that describes annihilation into all possible final states.

$$T^\dagger T = i(T^\dagger - T). \quad (5.2)$$

When we evaluate this expression between some particle states a and b , we get the following expression:

$$i(\langle b|T^\dagger|a\rangle - \langle b|T|a\rangle) = \sum_f \langle b|T^\dagger|f\rangle \langle f|T|a\rangle, \quad (5.3)$$

where we have inserted a complete set of intermediate (multi-particle) states f on the right hand side. We can express Eq. (5.3) in terms of the invariant matrix element \mathcal{M} as

$$i(\mathcal{M}^*(k_1 k_2 \rightarrow p_1 p_2) - \mathcal{M}(p_1 p_2 \rightarrow k_1 k_2)) = \sum_f \int d\Pi_f \mathcal{M}^*(k_1 k_2 \rightarrow \{q_i\}_f) \mathcal{M}(p_1 p_2 \rightarrow \{q_i\}_f). \quad (5.4)$$

where we have introduced a shorthand notation for

$$\int d\Pi_f = \left(\prod_{i=1}^f \int \frac{d^3 q_i}{(2\pi)^3} \frac{1}{2E_i} \right) (2\pi)^4 \delta^{(4)}(P - \sum q_i), \quad (5.5)$$

and P denotes the total incoming momentum. Obviously, since $z - z^* = 2i\Im[z]$, the left hand side of Eq. (5.4) is equal to $2\Im[\mathcal{M}(p_1 p_2 \rightarrow k_1 k_2)]$, provided that $\mathcal{M}(k_1 k_2 \rightarrow p_1 p_2) = \mathcal{M}(p_1 p_2 \rightarrow k_1 k_2)$.

We are interested in the special case that the incoming states are the same as the outgoing, i.e., $p_1 = k_1, p_2 = k_2$, for which Eq. (5.4) takes the simple form;

$$2\Im[\mathcal{M}(p_1 p_2 \rightarrow p_1 p_2)] = \sum_f \int d\Pi_f |\mathcal{M}(p_1 p_2 \rightarrow \{q_i\}_f)|^2. \quad (5.6)$$

As one can see in Fig. 5.2, this means that the imaginary part of a forward scattering amplitude is equal to the squared modulus of the annihilation amplitude, summed over all possible final states. It is then straightforward to derive the relation between the imaginary part of the scattering amplitude and the annihilation cross section into f final states, which is given by

$$\sigma_f = \frac{1}{4E_1 E_2 v_{\text{rel}}} \int d\Pi_f |\mathcal{M}(p_1, p_2 \rightarrow \{q_i\}_f)|^2. \quad (5.7)$$

Defining the total annihilation cross section in all possible final states as $\sigma_{\text{tot}} = \sum_f \sigma_f$, we arrive

5 Sommerfeld Enhancement

at

$$\sigma_{\text{tot}V_{\text{rel}}} = \frac{1}{2m^2} \mathfrak{S}[\mathcal{M}(p_1 p_2 \rightarrow p_1 p_2)], \quad (5.8)$$

where we have used that $E_1 = E_2$ in the center of mass frame, and the energy of the incoming particle is approximately equal to the rest mass, $E_1 \simeq m$, in the non-relativistic regime we are interested in.

Non-relativistic expansion of Dirac spinors

Here we briefly review how one obtains two-component spinors from four-component spinors in the non-relativistic limit. We start with the Dirac equation

$$(i\cancel{\partial} - m)\chi = 0, \quad (5.9)$$

where $\cancel{\partial} = \gamma_\nu \partial^\nu$ and χ is a fermionic particle with spin $\frac{1}{2}$. The gamma matrices γ^ν are in the Dirac representation given by

$$\gamma^0 = \begin{pmatrix} 1 & 0 \\ 0 & -1 \end{pmatrix}, \quad \gamma^i = \begin{pmatrix} 0 & \sigma^i \\ -\sigma^i & 0 \end{pmatrix} \quad (5.10)$$

where σ^i are the Pauli sigma matrices. We can express the field χ as a superposition of the positive and negative energy solutions in the following way

$$\chi = u(p)e^{-ip \cdot x} + v(p)e^{ip \cdot x}, \quad (5.11)$$

where the four-component vectors $u(p)$ and $v(p)$ must obey

$$(\cancel{p} - m)u(p) = 0 \quad (5.12)$$

$$(\cancel{p} + m)v(p) = 0 \quad (5.13)$$

which follows from the Dirac equation.

Expressing $u(p)$ and $v(p)$ in two-component spinors,

$$u(p) = \begin{pmatrix} \eta_1 \\ \eta_2 \end{pmatrix}, \quad v(p) = \begin{pmatrix} \xi_1 \\ \xi_2 \end{pmatrix} \quad (5.14)$$

we find that they are related to each other, by inserting Eq. (5.14) into Eq. (5.12) and Eq. (5.13). After diagonalizing the resulting matrix, the solutions are

$$u(p) = \begin{pmatrix} \eta \\ \frac{\mathbf{p} \cdot \boldsymbol{\sigma}}{p_0 + m} \eta \end{pmatrix}, \quad v(p) = \begin{pmatrix} \frac{\mathbf{p} \cdot \boldsymbol{\sigma}}{p_0 + m} \xi \\ \xi \end{pmatrix}. \quad (5.15)$$

With this information we can construct a general form of χ that is expressed in two-component spinors

$$\chi = \begin{pmatrix} \eta e^{-ip \cdot x} + \frac{\mathbf{p} \cdot \boldsymbol{\sigma}}{p_0 + m} \xi e^{ip \cdot x} \\ \frac{\mathbf{p} \cdot \boldsymbol{\sigma}}{p_0 + m} \eta e^{-ip \cdot x} + \xi e^{ip \cdot x} \end{pmatrix}. \quad (5.16)$$

Now we are ready to perform the non-relativistic expansion of this spinor. We first begin by noting that $\mathbf{p} \cdot \boldsymbol{\sigma} e^{\pm i\mathbf{p}\cdot\mathbf{x}}$ can be replaced by $\mp i\nabla \cdot \boldsymbol{\sigma} e^{\pm i\mathbf{p}\cdot\mathbf{x}}$, since the derivative works on the x in the exponential. The final step is to use that $p_0 = m \gg \mathbf{p}$ in the non-relativistic limit, such that we can approximate $e^{\pm i\mathbf{p}\cdot\mathbf{x}}$ by $e^{\pm imt}$. We thus obtain the following result for the non-relativistic expansion of the spinor χ :

$$\chi = \begin{pmatrix} \eta e^{-imt} + i\frac{\nabla\cdot\boldsymbol{\sigma}}{2m}\xi e^{imt} \\ -i\frac{\nabla\cdot\boldsymbol{\sigma}}{2m}\eta e^{-imt} + \xi e^{imt} \end{pmatrix}. \quad (5.17)$$

We note that, if χ is its own anti-particle, i.e., a Majorana fermion, the derivation above changes slightly. In this case, $u(p)$ and $v(p)$ are related to each other by the charge conjugation matrix $C = i\gamma^2\gamma^0$, such that the spinor components are related through $\zeta^c = -i\sigma^2\zeta^*$. The Majorana equivalent to Eq. (5.17) then becomes (see e.g. [223] for a derivation):

$$\chi = \begin{pmatrix} \zeta e^{-imt} + i\frac{\nabla\cdot\boldsymbol{\sigma}}{2m}\zeta^c e^{imt} \\ -i\frac{\nabla\cdot\boldsymbol{\sigma}}{2m}\zeta e^{-imt} + \zeta^c e^{imt} \end{pmatrix}. \quad (5.18)$$

Majorana fermions, however, will not be considered in this work.

5.2.2 Deriving the non-relativistic effective action

In this section we will discuss how one obtains a non-relativistic action from the action that describes the full theory. In particular we consider quantum electrodynamics (QED), since we want to evaluate the annihilation of an electron-positron pair into photons. The general QED action is given by

$$S_{\text{QED}}[\psi, \bar{\psi}, A_\mu] = \int d^4x \left[\bar{\psi}(iD_\mu - m)\psi - \frac{1}{4}F^2 - \frac{1}{2\xi_g}(\partial_\mu A^\mu)^2 \right], \quad (5.19)$$

where m is the mass of the electron (positron), $F_{\mu\nu} = \partial_\mu A_\nu - \partial_\nu A_\mu$ is the electromagnetic field tensor, and $D_\mu = \partial_\mu - ieA_\mu$ is the covariant derivative. The gauge parameter ξ_g is equal to 1 in Feynman gauge, and 0 in Landau gauge. Explicitly working out all terms in Eq. (5.19) we obtain

$$\mathcal{L}_{\text{QED}} = \bar{\psi}(i\partial - m)\psi - e\bar{\psi}\boldsymbol{\gamma}^\mu\psi A_\mu - \frac{1}{2}A_\mu \left[\left(1 - \frac{1}{\xi}\right)\partial^2 g^{\mu\nu} - \partial^\mu\partial^\nu \right] A_\nu, \quad (5.20)$$

where the first term is the kinetic term of the fermions, the second the interaction term, and the last is the kinetic term of the photon.

In the following we will make use of the generating functional

$$Z[\psi, \bar{\psi}, A_\mu] = \int \mathcal{D}\psi \mathcal{D}\bar{\psi} \mathcal{D}A e^{iS_{\text{QED}}}, \quad (5.21)$$

which is similar to the partition function known from statistical mechanics, and will be very helpful in calculating the desired quantities (see e.g. [227] for more information on functional integration).

In the following we will derive an effective non-relativistic field theory, which is defined

5 Sommerfeld Enhancement

by the energy scale of the annihilating particles, i.e., the electron (positron) mass m . We thus exclude all particles from the theory that have a larger energy scale by integrating them out. Discarding these states of course will affect the low-energy theory, but we take that into account by adding correction terms to the effective Lagrangian. The long-range effect is replaced by a local interaction that is identical in form, such that the net effect is a renormalization of the coupling constants. In this way we are able to take into account the non-perturbative effect without having to perform the resummation over all diagrams. For the details of the calculation see Appendix subsection A.1.1.

Integrate out light fields

We start by integrating out the light fields, in this case the photon A_μ , in Eq. (5.21). For this purpose we consider separately

$$Z[A_\mu] = \int \mathcal{D}A \exp \left\{ i \int d^4x \left(-e \bar{\psi} \gamma^\mu \psi A_\mu - \frac{1}{2} A_\mu \left[\left(1 - \frac{1}{\xi_g}\right) \partial^2 g^{\mu\nu} - \partial^\mu \partial^\nu \right] A_\nu \right) \right\}, \quad (5.22)$$

where we now only have included terms from the Lagrangian that include the photon field. In order to solve this functional integral, we will need to complete the square in A_μ , which can be done by shifting the A -field

$$A'_\mu(x) = A_\mu(x) - \int d^4y G_{\mu\nu}(x-y) J^\nu(y) \quad (5.23)$$

where $G_{\mu\nu}(x-y)$ is a Green's function that represents the photon propagator between points x and y and $J^\nu(y) = -e \bar{\psi}(y) \gamma^\nu \psi(y)$ is the Dirac current. The functional derivative in Eq. (5.22) then simply transforms to $\mathcal{D}A \rightarrow \mathcal{D}A'$.

Substituting these definitions into the Lagrangian from Eq. (5.22), we get after a little algebra:

$$S[A'] = \int d^4x \left[\frac{1}{2} A'_\mu(x) M^{\mu\nu}(x) A'_\nu(x) + i \frac{1}{2} \int d^4y J^\mu(x) G_{\mu\nu}(x-y) J^\nu(y) \right], \quad (5.24)$$

where we introduced $M^{\mu\nu} = - \left[\left(1 - \frac{1}{\xi_g}\right) \partial^2 g^{\mu\nu} - \partial^\mu \partial^\nu \right]$. We can now simply perform the integration over the first term, which is the kinetic term for the gauge field A'_μ . We can focus our attention now on the second term, which now only depends on J^μ (and therefore only on ψ and $\bar{\psi}$).

Integrate out relativistic parts of fields

The next step is to integrate out the relativistic parts of the fermionic fields. We do this by splitting the fields in a relativistic and non-relativistic part by going to Fourier space

$$\begin{aligned} \psi(x) &= \int_{\text{NR}} \frac{d^4p}{(2\pi)^4} \tilde{\psi}(p) e^{-ipx} + \int_{\text{R}} \frac{d^4p}{(2\pi)^4} \tilde{\psi}(p) e^{-ipx} = \psi_{\text{NR}}(x) + \psi_{\text{R}}(x), \\ \bar{\psi}(x) &= \int_{\text{NR}} \frac{d^4p}{(2\pi)^4} \bar{\tilde{\psi}}(p) e^{ipx} + \int_{\text{R}} \frac{d^4p}{(2\pi)^4} \bar{\tilde{\psi}}(p) e^{ipx} = \bar{\psi}_{\text{NR}}(x) + \bar{\psi}_{\text{R}}(x), \end{aligned} \quad (5.25)$$

where the non-relativistic momentum space is defined as

$$NR = \left((p_0, \vec{p}) \mid p_0 = \pm m + \delta p^0, \quad \mathcal{O}(\delta p^0) \sim \mathcal{O}\left(\frac{\vec{p}^2}{2m}\right) \ll m \right), \quad (5.26)$$

and relativistic momentum space is basically defined as everything that does not satisfy the above.

We substitute Eq. (5.25) into the terms in the action that contain fermions fields, i.e., the kinetic term and the source term derived in the previous subsection. We end up with many terms, but fortunately we do not have to consider all of them. For example, we can neglect any terms containing an odd number of ψ_{NR} (implying an odd number of $\bar{\psi}_{NR}$), since they are simply kinematically impossible due to momentum conservation. The action containing all relevant non-relativistic interactions is then given by

$$\begin{aligned} S[\psi_{NR}, \bar{\psi}_{NR}] &= S_{0,NR} + S_R[\psi_{NR}, \bar{\psi}_{NR}], \\ &= \int d^4x [\bar{\psi}_{NR}(i\gamma - m)\psi_{NR}] \\ &\quad + \frac{ie^2}{2} \int d^4x d^4y [\bar{\psi}_{NR}(x)\gamma^\alpha \psi_{NR}(x) G_{\alpha\beta}(x-y) \bar{\psi}_{NR}(y)\gamma^\beta \psi_{NR}(y)] \\ &\quad - i \log \left(\int \mathcal{D}\psi_R \mathcal{D}\bar{\psi}_R e^{iS_{0,R} + iS_{\text{int}}[\bar{\psi}_{NR}, \bar{\psi}_R, \psi_{NR}, \psi_R]} \right), \end{aligned} \quad (5.27)$$

where $S_{0,NR}$ is defined by the first two terms in Eq. (5.27); the second term containing four non-relativistic fields represents the *potential term*, which describes the Sommerfeld effect. The last term in Eq. (5.27) contains both relativistic and non-relativistic fields: $S_{0,R}$ takes the same form as $S_{0,NR}$ except with all non-relativistic fields replaced by relativistic ones, and S_{int} is essentially defined by everything that was not included in the previous terms. We will focus on integrating out the relativistic fields in S_{int} to calculate the *annihilation term*.

The tree level $e^+e^- \rightarrow \gamma\gamma$ annihilation diagram in which we are interested in, can in fact not properly be described by our non-relativistic theory, since the resulting photon states are relativistic. This is actually true for all interactions in S_{int} that have relativistic initial or final states. We can, however, combine the tree level diagrams in such a way that a higher order diagram is obtained in which the relativistic states are virtual and can be integrated out without any problem. The kinematically allowed tree level diagrams are summarized in Fig. 5.3 on the left, which we can combine to the higher order diagrams shown on the right. We, however, will only consider the box diagram as depicted in the top right, since with the use of the optical theorem we can relate the imaginary part of the box amplitude to the annihilation diagram by putting the intermediate photon states on-shell. In this way we are able to correctly include the annihilation into our non-relativistic description, even though relativistic end states are involved. The other higher order diagrams shown in Fig. 5.3 on the right do not relate to interactions we are interested in, and we will therefore not consider them any further.

There are in fact four terms in S_{int} that correspond to the diagram shown in the top left of Fig. 5.3, each with a factor $ie^2/2$. In order to obtain the interaction terms corresponding to the box diagram (proportional to e^4), we use perturbation theory to expand S_R to second order

5 Sommerfeld Enhancement

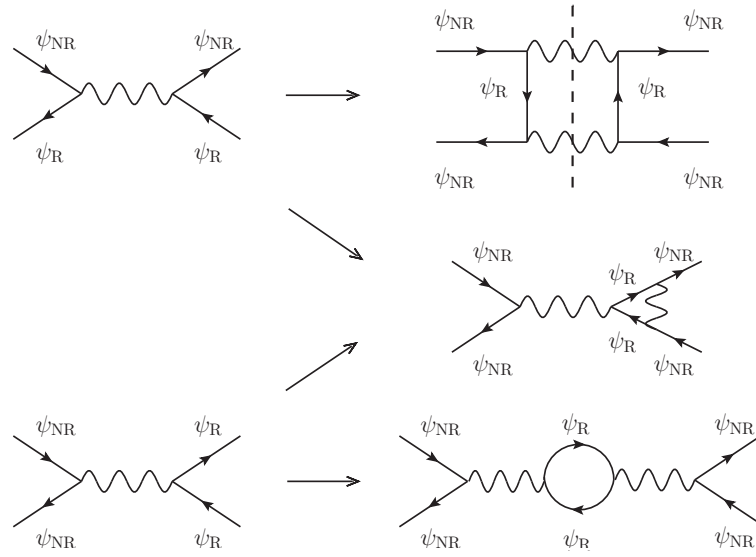


Figure 5.3: Tree level diagrams on the left correspond to kinematically allowed terms in S_{int} in Eq. (5.27) and cannot correctly be described by our non-relativistic theory due to their relativistic initial or final states. Combining them as indicated, we obtain a higher order diagram (right) with only non-relativistic initial and final states and relativistic virtual states that can be integrated out. The box diagram (top right) can be related to the annihilation diagram into two photons by cutting the diagram in half over the dashed line by using the optical theorem. The other two diagrams on the right correspond to interactions we are not interested in, and will therefore not be considered in our further discussion.

in $ie^2/2$. After the integration over the relativistic fields (see Appendix subsection A.1.1), the renormalized four-point correlation function that describes the box diagram has the form

$$\int d^4x d^4y d^4z d^4w i\beta_4(x, y, z, w) \bar{\psi}_{\text{NR}}(x) \psi_{\text{NR}}(y) \bar{\psi}_{\text{NR}}(z) \psi_{\text{NR}}(w), \quad (5.28)$$

where β_4 is given by

$$\begin{aligned} i\beta_4(x, y, z, w) \bar{\psi}(x) \psi(y) \bar{\psi}(z) \psi(w) = \\ \frac{e^4}{2} \bar{\psi}(x) \gamma^\beta S(x-y) \psi(y) \gamma^\mu G_{\mu\nu}(y-z) \bar{\psi}(z) \gamma^\nu S(z-w) \gamma^\alpha \psi(w) G_{\alpha\beta}(w-x) \\ + \frac{e^4}{2} \bar{\psi}(x) \gamma^\beta S(x-y) \psi(y) \gamma^\mu G_{\mu\nu}(y-w) \bar{\psi}(z) \gamma^\nu S(z-w) \gamma^\alpha \psi(w) G_{\alpha\beta}(z-x), \end{aligned} \quad (5.29)$$

where $S(x-y)$ is the propagator of a relativistic field between x and y (see Eq. (A.15)), and we have omitted the subscripts NR from the non-relativistic fields for simplicity. The first term corresponds to the t-channel diagrams (Fig. 5.4, left), and the second term to the u-channel diagrams (Fig. 5.4, right). In the following we will no longer explicitly denote that the fields are non-relativistic, since there is no danger of confusion.

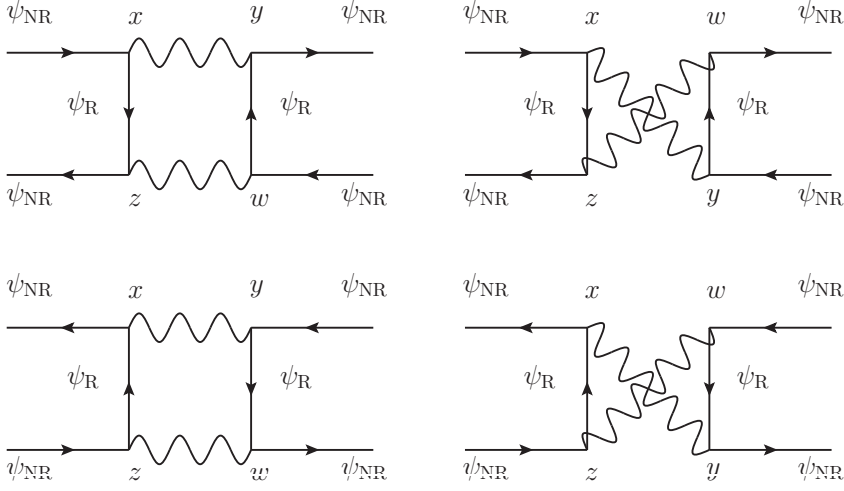


Figure 5.4: The different box diagrams that are described by the four-point correlation function: the t-channel diagrams (left) actually contribute the same amount to the four-point correlation function Eq. (5.29). The same is true for the u-channel diagrams on the right. For more information, see Appendix section A.1.

Non-relativistic expansion of the action

Next, we will perform a non-relativistic expansion of the fields in the action that we just derived. We start with the kinetic term to obtain the correct normalization of the fields. The non-relativistic expression for ψ was already shown in Eq. (5.17), such that we can simply substitute it in the kinetic term and write everything in two-component form. This results in quite a number of terms, most of which can be discarded due to the reasons we will discuss below.

First, we should understand the physical interpretation of the two-component spinors: η and η^\dagger correspond to positive energy solutions, i.e., fermions, whereas anti-fermions are described by ξ and ξ^\dagger . The spinor $\eta(x)$ ($\eta^\dagger(x)$) describes an incoming (outgoing) electron that is annihilated (created) at x , whereas $\xi(x)$ ($\xi^\dagger(x)$) creates (annihilates) an outgoing (incoming) positron at x . Therefore, in the context of a kinetic term, the only sensible combinations of the two-component spinors are $\eta^\dagger \eta$ and $\xi^\dagger \xi$, and all terms with other spinor combinations disappear.

Furthermore, we are in the non-relativistic regime where $\mathbf{p} \ll m$, such that we can neglect terms that are of order $\mathcal{O}(\frac{\mathbf{p}^2}{m^2})$ or higher. It is important to work out all time derivatives working on the terms with $e^{\pm imt}$ that arise from the non-relativistic expansion of the spinor fields (see Eq. (5.17)), since a few terms will cancel in this way. After some algebra we arrive at the following simple expression for the non-relativistic kinetic term

$$S_k[\eta^\dagger, \eta, \xi^\dagger, \xi] = \int d^4x \eta^\dagger(x) \left(i\partial_t + \frac{\nabla^2}{2m} \right) \eta(x) + \xi^\dagger(x) \left(i\partial_t - \frac{\nabla^2}{2m} \right) \xi(x), \quad (5.30)$$

where we used that $(\vec{\nabla} \cdot \vec{\sigma})^2 = \nabla^2$.

5 Sommerfeld Enhancement

Next, we want to do the same for the potential term

$$S_p = \frac{ie^2}{2} \int d^4x d^4y \left[\bar{\psi}(x) \gamma^\alpha \psi(x) G_{\alpha\beta}(x-y) \bar{\psi}(y) \gamma^\beta \psi(y) \right], \quad (5.31)$$

which was introduced in Eq. (5.27). The potential term corresponds to a t-channel diagram with the exchange of a photon. For this reason, we only consider the same combinations $\eta^\dagger \eta$ and $\xi^\dagger \xi$ as explained above. In the non-relativistic expansion up to leading order in (\mathbf{p}/m) , only the temporal part (i.e., $\alpha = \beta = 0$) of the potential term gives a significant contribution (see Appendix subsection A.1.1). Finally we end up with

$$-\frac{1}{2} \int d^4x d^4y \frac{\alpha \delta(x^0 - y^0)}{|\mathbf{x} - \mathbf{y}|} \left[\eta^\dagger(x) \eta(x) + \xi^\dagger(x) \xi(x) \right] \left[\eta^\dagger(y) \eta(y) + \xi^\dagger(y) \xi(y) \right], \quad (5.32)$$

where α is the usual fine-structure constant.

Terms containing only η and only ξ represent $e^- e^-$ and $e^+ e^+$ scattering respectively, which will give a repulsive contribution. We are only interested in the attractive configuration of $e^- e^+$ scattering, which is given by the two terms: $\eta^\dagger(x) \eta(x) \xi^\dagger(y) \xi(y)$ and $\xi^\dagger(x) \xi(x) \eta^\dagger(y) \eta(y)$. However, in order for them to describe a 2-particle state we need to rearrange the spinors.

In fact there are two possible configurations, depending on the spins of each particle: a singlet state 1S_0 with antiparallel spins (para-positronium) and a triplet state 3S_1 with parallel spins (ortho-positronium). Since the interaction should be invariant under the interchange of particle and antiparticle states, charge conjugation parity, given here by $(-1)^S$, is conserved. For one photon, the charge conjugation parity is given by (-1) , since it reverses the polarization of the electric field. Therefore, the singlet state with $S = 0$ can only decay in an even number of photons, whereas the triplet state can decay in an odd number of photons (except into one photon, which is forbidden by momentum conservation). Since we are interested in the decay in two photons, we therefore only consider the singlet state. The expression for the potential term then becomes

$$S_p = \frac{1}{2} \int d^4x d^4y \eta^\dagger(x) \xi(y) \frac{\alpha \delta(x^0 - y^0)}{|\mathbf{x} - \mathbf{y}|} \xi^\dagger(y) \eta(x), \quad (5.33)$$

where the change in sign is due to the Fierz reshuffling of the spinors (see e.g. [227]). We clearly recognize the attractive Coulomb potential in this expression, which arises from the multiple photon exchange between the electron and positron.

Finally, we want to derive an expression for the annihilation term in terms of the two-component spinors. For this, we use the optical theorem to obtain the annihilation of the electron-positron pair into two photons, from the two box diagrams that we derived before. In the next chapter we will consider a special case of sneutrino DM, where a full calculation of the box diagram will be given. Here, however, we prefer a more simple approach by considering quarkonium, a bound state of a quark and anti-quark, i.e., the equivalent of positronium in QCD. Calculations were performed by using non-relativistic QCD [222], where the effect of annihilation was included by introducing effective 4-fermion operators. Although the results apply to the QCD case, they are easily adapted for our QED case at hands.

In analogy to our case, we consider here the two box diagrams that describe quarkonium scattering with intermediate photon states (t- and u-channel). As before, we are only concerned

with spin singlet states, for which the corresponding term in the Lagrangian is

$$\delta\mathcal{L}_{\gamma\gamma}(^1S_0) = \frac{f_{\gamma\gamma}(^1S_0)}{m^2} O(^1S_0), \quad (5.34)$$

where the 4-fermion operator is given by $O(^1S_0) = \psi_1^\dagger \psi_2 \psi_2^\dagger \psi_1$. Only the imaginary part of the coefficient $f_1(^1S_0)$ is interesting to us, since this is the part that is related to the annihilation rate by the optical theorem. This was in fact calculated in [222] by substituting two-component spinors for the Dirac fields, similarly like we did in for the potential term, and comparing the resulting expression to Eq. (5.34). Up to leading order in the quark velocity $v \ll 1$, the result is

$$\Im[f_{\gamma\gamma}(^1S_0)] = \pi Q^4 \alpha, \quad (5.35)$$

where Q is the electric charge of the quark. To adapt this result to the case of positronium, we adjust the value of Q for electrons (positrons) accordingly, such that we obtain

$$S_a = \int d^4x \left[(\text{real part}) + \eta^\dagger(x) \xi(x) \left(i \frac{\pi \alpha^2}{m^2} \right) \xi^\dagger(x) \eta(x) \right], \quad (5.36)$$

for the annihilation term.

In summary, we have now derived the following non-relativistic action

$$\begin{aligned} S_{\text{NR}} &\simeq S_k + S_a + S_p, \\ &= \int d^4x \left[\eta^\dagger(x) \left(i\partial_t + \frac{\nabla^2}{2m} \right) \eta(x) + \xi^\dagger(x) \left(i\partial_t - \frac{\nabla^2}{2m} \right) \xi(x) \right] \\ &\quad + \frac{1}{2} \int d(xy) \eta^\dagger(t, \mathbf{x}) \xi(t, \mathbf{y}) \left[\frac{\alpha}{|\mathbf{x} - \mathbf{y}|} + i \frac{2\pi\alpha^2}{m^2} \delta^{(3)}(\mathbf{x} - \mathbf{y}) \right] \xi^\dagger(t, \mathbf{y}) \eta(t, \mathbf{x}), \end{aligned} \quad (5.37)$$

where $\int d(xy) \equiv \int dt d^3x d^3y$, and we have evaluated the delta-function in the potential term. We also introduced a 3-dimensional delta-function in the annihilation term, which reflects the fact that this interaction takes places locally.

5.2.3 Two-body effective action

In order to calculate the effect of the Coulomb potential on the electron-positron pair, we want to derive a two-body effective action and solve for the equations of motion. We start by describing the fields in the non-relativistic action as a two-body wave-function that defines the positronium state. For this purpose, we define the two-body action as follows

$$S^{\text{II}} \equiv -i \log \left[\int \mathcal{D}\eta \mathcal{D}\eta^\dagger \mathcal{D}\xi \mathcal{D}\xi^\dagger e^{iS_{\text{NR}}} \right], \quad (5.38)$$

where S_{NR} is given by Eq. (5.37). In order to perform this functional integration over the one-particle fields, we introduce auxiliary fields $\sigma(t, \mathbf{x}, \mathbf{y})$ and $s(t, \mathbf{y}, \mathbf{x})$ which allows us to replace $\eta^\dagger \xi$ with the two-body function s^\dagger , and $\xi^\dagger \eta$ with s . In the end we arrive at an expression for $S^{\text{II}}[\sigma, \sigma^\dagger]$ in terms of the two-body wave-function σ and its Hermitian conjugate. For the details

5 Sommerfeld Enhancement

of this calculation we refer the reader to Appendix subsection A.1.2.

Then we introduce new coordinates that separate the motions of the center of mass from the relative motions. We perform the following change of variables

$$R = \begin{pmatrix} t \\ \frac{\mathbf{x}+\mathbf{y}}{2} \end{pmatrix}, \quad \mathbf{r} = \mathbf{x} - \mathbf{y} \quad (5.39)$$

such that

$$\sigma(\mathbf{r}, P) = \int d^4R \sigma(t, \mathbf{x}, \mathbf{y}) e^{iPR}, \quad (5.40)$$

where P is the momentum of the center of mass and furthermore we have $\int d(xy) = d^4R d^3r$. The final result for the two-body action in the new coordinates (see Appendix subsection A.1.2) is given by

$$\begin{aligned} S^{II}[\sigma, \sigma^\dagger] &= \frac{1}{2} \int \frac{d^4P}{(2\pi)^4} d^3r \left(-\sigma^\dagger(\mathbf{r}, P) \frac{r}{\alpha} \left[1 + i \frac{2\pi r \alpha}{m^2} \delta^{(3)}(\mathbf{r}) \right]^{-1} \sigma(\mathbf{r}, P) \right. \\ &\quad \left. + \int d^3r' \sigma^\dagger(\mathbf{r}', P) \zeta(\mathbf{r}' - \mathbf{r}, E) \sigma(\mathbf{r}, P) \right), \end{aligned} \quad (5.41)$$

where $E = P^0 - |\mathbf{P}|^2/4m$ is the internal energy of the two-body state and ζ is the function

$$\zeta(\mathbf{r}, E) = \int \frac{d^3k}{(2\pi)^3} \frac{m e^{-i\mathbf{k}\cdot\mathbf{x}}}{|\mathbf{k}|^2 - mE - i\epsilon}, \quad (5.42)$$

which satisfies

$$\left(-\frac{\nabla^2}{m} - E \right) \zeta(\mathbf{r}, E) = \delta^{(3)}(\mathbf{r}). \quad (5.43)$$

Finally we want to obtain the Euler-Lagrange equations of motion for the auxiliary fields σ, σ^\dagger . For this, we demand that the variation of the two-body action w. r. t the field is zero

$$\frac{\delta S^{II}}{\delta \sigma^\dagger} = -\frac{r}{\alpha} \left[1 + i \frac{2\pi r \alpha}{m^2} \delta^{(3)}(\mathbf{r}) \right]^{-1} \sigma(\mathbf{r}, P) + \int d^3r' \zeta(\mathbf{r}' - \mathbf{r}, E) \sigma(\mathbf{r}, P) \equiv 0. \quad (5.44)$$

This expression can greatly be simplified by introducing the wave-function

$$\varphi_P(\mathbf{r}) \equiv \frac{mr}{\alpha} \left(1 + i \frac{2\pi r \alpha}{m^2} \delta^{(3)}(\mathbf{r}) \right)^{-1} \sigma(\mathbf{r}, P), \quad (5.45)$$

and the potential

$$V(\mathbf{r}) = -\frac{\alpha}{r} - i \frac{2\pi \alpha^2}{m^2} \delta^{(3)}(\mathbf{r}). \quad (5.46)$$

The variation of the action then yields the following expression

$$\boxed{\left(-\frac{\nabla^2}{m} + V(\mathbf{r}) \right) \varphi_P(\mathbf{r}) = E \varphi_P(\mathbf{r})}, \quad (5.47)$$

which we recognize as the Schrödinger equation. As anticipated, the Sommerfeld effect is incorporated into the potential of the Schrödinger equation and we can calculate its effect on the wave function of the positronium state by solving for ϕ_P . In the next section we will show how to obtain the enhancement factor for the bare cross section from this expression and discuss its general properties.

For completeness we note that the two-body effective action can then also be written as

$$S^H = \int d^4x d^3r \phi^\dagger(x, \mathbf{r}) \left(i\partial_{x^0} + \frac{\nabla_x^2}{4m} + \frac{\nabla_r^2}{m} - V(\mathbf{r}) \right) \phi(x, \mathbf{r}), \quad (5.48)$$

where

$$\phi(x, \mathbf{r}) \equiv \int \frac{d^4P}{(2\pi)^4} \phi_P(\mathbf{r}) e^{-iPx}, \quad (5.49)$$

since the variation of this action will yield the same equations of motion.

5.3 Annihilation and the enhancement factor

The possibility to exchange a light force carrier between annihilating particles results in a non-perturbative correction to the annihilation diagram in the non-relativistic regime. As we saw in the introduction, a resummation over the ladder diagrams is therefore necessary to take the Sommerfeld effect into account. In the last section we have shown how to perform the resummation of ladder diagrams in the framework of a non-relativistic field theory. We have factorized the long-range Sommerfeld effect from the short-range annihilation process, which allowed us to take it into account by a renormalization of the theory. The non-relativistic action was then derived by a perturbative expansion in the new couplings. In the end we arrived at the Schrödinger equation for the two-body system, where the potential $V(r)$ actually consists of a potential and an annihilation part (see Eq. (5.46)).

The former is generated by the multiple exchange of force carriers, and the latter is responsible for the finite lifetime of the bound state due to the decay of the two-body system. The annihilation part will only be important in the special case that such a quasi bound state is formed, and will therefore not be included for the moment being. Instead we focus only on the potential part, which can significantly alter the wave-function of the incoming particles. We thus want to solve the Schrödinger equation and calculate how the Sommerfeld effect affects the annihilation cross section. As already discussed briefly in the introduction of this chapter, modifications to the DM annihilation cross section can have significant consequences for indirect detection of DM, but are also important for the calculation of the relic density (see also chapter 7).

Since the annihilating particles have to be on-shell, the internal energy is given by the kinetic energy of the two particles in the center-of-mass frame $E = mv^2$. The Schrödinger equation from Eq. (5.47) then reads

$$-\frac{1}{2\mu} \nabla^2 \psi_k = \left(\frac{k^2}{2\mu} - V(r) \right) \psi_k, \quad (5.50)$$

where $k = mv$ is the momentum of each particle, $\mu = m/2$ is the reduced mass of the system, and the potential $V(r)$ depends on the relative distance between the two particles r .

5 Sommerfeld Enhancement

Since the annihilation takes place locally at $r = 0$, we can include the Sommerfeld effect by looking at how the wave-function has been changed at that position, and define

$$S(v) = |\psi_k(0)|^2, \quad (5.51)$$

where ψ_k is the solution to Eq. (5.50) and is normalized as

$$\psi \rightarrow \exp^{ikz} + f(\theta) \frac{\exp^{ikr}}{r} \quad \text{for } r \rightarrow \infty. \quad (5.52)$$

where $f(\theta)$ is the scattering amplitude. This normalization makes sure that we can simply multiply the bare cross section with the Sommerfeld factor from Eq. (5.51), i.e., $\sigma = S(v)\sigma_0$, in order to obtain the full annihilation cross section including the enhancement. The fact that the annihilation occurs on a short distance and the Sommerfeld effect works on much larger scales ensures the validity of the factorization as presented here.

For the positronium state considered in section 5.2, the potential $V(r) = -\alpha/r$ is just the Coulomb potential, and it is possible to solve for ψ_k analytically. Since $V(r)$ is rotationally symmetric, we can expand $\psi_k(r, \theta)$ into products of Legendre polynomials and radial functions R_{kl}

$$\psi_k(r, \theta) = \sum_l A_l P_l(\cos \theta) R_{kl}(r), \quad (5.53)$$

where the coefficients A_l

$$A_l = \frac{1}{k} i^l (2l+1) e^{i\delta_l}, \quad (5.54)$$

are chosen such that ψ_k obeys the boundary conditions in Eq. (5.52). The radial functions are associated with angular momentum l , and can be written as

$$R_{kl}(r) = \frac{u_l(r)}{r}, \quad (5.55)$$

where the function $u_l(r)$ is a solution to the radial Schrödinger equation

$$\frac{1}{m} \frac{d^2 u_l}{dr^2} = \left(V(r) + \frac{l(l+1)}{mr^2} - mv^2 \right) u_l. \quad (5.56)$$

and is normalized as

$$u_l(r) \rightarrow \sin \left(kr - \frac{l\pi}{2} + \delta_l(r) \right), \quad \text{for } r \rightarrow \infty, \quad (5.57)$$

where the phaseshift $\delta_l(r) \ll kr$ for $r \rightarrow \infty$. Since the Coulomb potential does not diverge faster than $1/r$ for $r \rightarrow 0$, we can ignore it with respect to the kinetic term such that the solution for $u_l(r)$ is proportional to r^{l+1} around the origin. The only non-zero contribution from $u_l(r \rightarrow 0)$

thus comes from $l = 0$, and the Sommerfeld factor can then be written as

$$S(\nu) = |\Psi_{k0}(0)|^2 = \left| \frac{R_{k0}(0)}{k} \right|^2 = \left| \frac{du_0}{dr}(0) \right|^2, \quad (5.58)$$

where in the last step we have used that $u_0(r) \rightarrow 0$ for $r \rightarrow 0$ implies that $u_0(r) \rightarrow r \frac{du_0}{dr}(0)$.

The analytical solution to Eq. (5.56) is given in terms of Bessel functions. We will not perform the full calculation of $S(\nu)$ here, which e.g. can be found in [215], but simply quote the final result

$$S(\nu) = \frac{\pi/\varepsilon_\nu}{1 - e^{-\pi/\varepsilon_\nu}}, \quad (5.59)$$

where we have introduced $\varepsilon_\nu \equiv v/\alpha$. The characteristic behavior of the enhancement factor can be understood as follows: for large velocities, $\varepsilon_\nu \gg 1$, there will be no enhancement, i.e., $S \approx 1$, whereas for small velocities, $\varepsilon_\nu \ll 1$, the Sommerfeld enhancement is given by $S \simeq \pi/\varepsilon_\nu$. In the most common case for s-wave annihilation this will result in an annihilation rate of $\sigma_{\text{ann}} v \propto 1/v$, which can be understood by looking at a classical analogy. The cross section for a point particle colliding with a star of radius R is given by $\sigma = \pi R^2$. However, when the gravitational pull of the star is taken into account, the cross section is enhanced by a factor $(1 + v_{\text{esc}}^2/v^2)$, where v_{esc} is the escape velocity from the surface of the star (see e.g. [48] for a clear explanation). If the velocity of the particle is smaller than the escape velocity, the annihilation rate will thus have the same $\sigma v \propto 1/v$ scaling as for the Sommerfeld effect.

In most cases however, the exchanged particle is not massless as in the Coulomb case, and the potential is a Yukawa one: $V(r) = -(\alpha/r)e^{-m_\phi r}$, with $m_\phi \ll m$ the mass of the force carrier. Unfortunately, for a Yukawa potential it is no longer possible to find an analytical solution to Eq. (5.51). We do, however, find that in a certain regime, the Sommerfeld factor is given by the Coulomb one from Eq. (5.59). To see this, we expand the Yukawa potential around $m_\phi r$, which gives us $V \sim -\alpha/r + \alpha m_\phi + \mathcal{O}(r^2)$, and substitute this in Eq. (5.50). When $\alpha m_\phi \ll m_\chi v^2$ is satisfied, we recover the Coulomb potential in the Schrödinger equation. We can therefore safely use Eq. (5.59) even for a massive mediator, as long as $\varepsilon_\nu^2 \gg \varepsilon_\phi \equiv m_\phi/(\alpha m_\chi)$ is satisfied.

In order to find the solution for $S(\nu)$ outside this range, we need to solve the Schrödinger equation numerically. We can rewrite Eq. (5.56) for $l = 0$ as

$$\frac{d^2 u_0}{dx^2} = \left(-\frac{e^{-x}}{\varepsilon_\phi x} + \left(\frac{\varepsilon_\nu}{\varepsilon_\phi} \right)^2 \right) u_0, \quad (5.60)$$

with the following boundary conditions:

$$u_0(0) = 0, \quad (5.61)$$

$$u_0(r) = \sin \left(\frac{\varepsilon_\nu}{\varepsilon_\phi} x + \delta \right) \quad \text{for } r \rightarrow \infty, \quad (5.62)$$

where we have introduced the dimensionless quantity $x \equiv m_\phi r$. However, to numerically solve Eq. (5.60) it is not convenient to have a boundary condition at infinity. Instead, we can solve for a function \tilde{u} , and setting $d\tilde{u}/dx = 1$ at $x = 0$ as a boundary condition instead of Eq. (5.62) (see

5 Sommerfeld Enhancement

[215] for a clear treatment). The asymptotic waveform then has the form $\tilde{u} \rightarrow A \sin\left(\frac{\varepsilon_v}{\varepsilon_\phi} x + \delta\right)$ with an amplitude A that is given by

$$A = \sqrt{\tilde{u}^2 + \left(\frac{\varepsilon_\phi}{\varepsilon_v} \frac{d\tilde{u}}{dx}\right)^2}. \quad (5.63)$$

The solution we are looking for is then just $u_0 = \tilde{u}/A$, such that the Sommerfeld enhancement is given by

$$S(v) = \left| \frac{\varepsilon_\phi}{A\varepsilon_v} \right|^2. \quad (5.64)$$

In order to get a correct value of S , it is important to evaluate the wave-function \tilde{u} far enough from the origin such that A has converged.

The result of the numerical calculation of S as a function of ε_ϕ (left) and ε_v (right) is shown in Fig. 5.5. Clearly, the enhancement factor grows with decreasing ε_ϕ and ε_v , but what is more striking are the resonances visible in the lefthand panel. These are induced by the finite range of the Yukawa potential for $\varepsilon_v^2 \lesssim \varepsilon_\phi$, and correspond to quasi bound states of the incoming pair of annihilating particles. We can get some more insight in the behavior of these resonances by considering the Hulthén potential

$$V_H(r) = \frac{\alpha \tilde{m} e^{-\tilde{m}r}}{1 - e^{-\tilde{m}r}}, \quad (5.65)$$

which for $\tilde{m} = \pi^2 m_\phi / 6$ resembles the Yukawa potential the most, and has the advantage to be analytically solvable [228, 229]. In contrary to the Yukawa case, it is possible to exactly predict where the resonances appear, i.e., at values of $\tilde{m} = \alpha m / n^2$, where n is a positive integer. The Sommerfeld factor for the Hulthén potential at a resonance is given by $S \simeq \varepsilon_\phi / \varepsilon_v^2$, which corresponds nicely to the $1/v^2$ behavior that is observed for Yukawa resonances [229, 230]. This scaling is also visible for the solutions that are nearly on resonance (magenta and green lines) in the right plot in Fig. 5.5: for larger values of ε_ϕ the enhancement follows the $1/v$ behavior and is well described by the Coulomb solution (black, dashed line), but for $\varepsilon_v \lesssim \sqrt{\varepsilon_\phi}$ this approximation is no longer valid and the enhancement grows as $1/v^2$.

The $1/v^2$ scaling would suggest, however, that the annihilation cross section could become infinite when precisely on resonance, which is unphysical and violates the unitarity bound

$$\sigma_{\text{ann}} v < \frac{4\pi}{m^2 v}, \quad (5.66)$$

which arises from the partial wave solutions to the Schrödinger equation. The total scattering cross section is given by $\sigma_{\text{tot}} = \sum_{l=0}^{\infty} \sigma_l$, with the partial cross section given by

$$\sigma_l = \frac{4\pi}{m^2 v^2} (2l+1) \sin^2 \delta_l \quad (5.67)$$

where δ_l is the phaseshift corresponding to angular momentum l . The partial cross section for $l = 0$ thus results in the bound above.

5.3 Annihilation and the enhancement factor

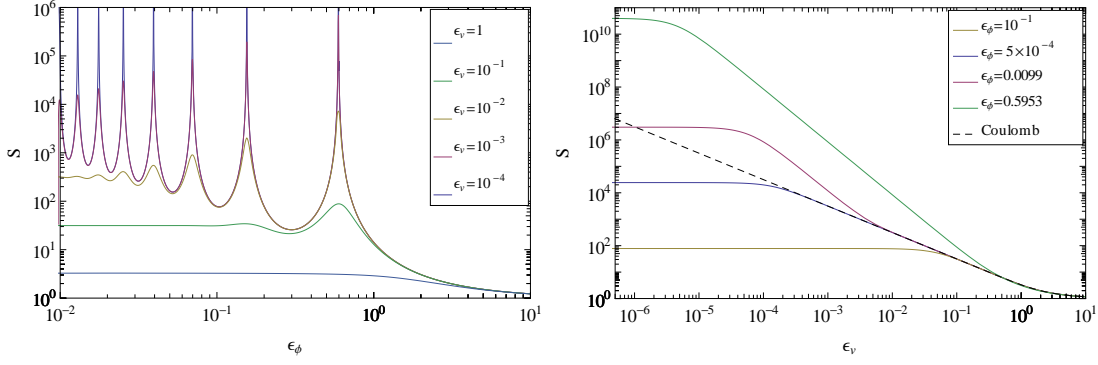


Figure 5.5: Left: Full numerical Sommerfeld factor as a function of ε_ϕ for different values ε_ν . It can be seen that the enhancement factor increases for smaller values of ε_ν and ε_ϕ . Resonances appear for specific values of ε_ϕ and sufficiently small values of ε_ν . Right: Plotting the Sommerfeld factor as a function of ε_ν one can clearly see the saturation of the factor for small enough values of ε_ν , in contrast to the analytical solution for the Coulomb potential (black, dashed). For large enough values of ε_ν the numerical solution is well approximated by the Coulomb enhancement. Off resonance (blue, yellow) the enhancement factor grows like $1/\nu$ for $\nu \rightarrow 0$, whereas on a resonance (green) it follows a $1/\nu^2$ behavior. When the configuration is near, but not precisely on resonance, there is a transition from $1/\nu$ to $1/\nu^2$ behavior when ε_ν decreases (red).

In reality, the finite lifetime of the bound state, i.e., the annihilation part of the potential Eq. (5.46) that we did not consider in our discussion above, places a limit on the magnitude of the Sommerfeld factor such that it does not diverge as $\nu \rightarrow 0$. Considering a potential well with a depth equal to the range of the Yukawa potential, $V' \propto \alpha m_\phi$, the annihilation rate is saturated for [196]

$$v \lesssim mV'\Gamma \sim \alpha m_\phi m\Gamma, \quad (5.68)$$

For annihilation into photons, the absorptive part is given by $\Gamma = \pi\alpha^2/m^2$, such that a saturation occurs for [230]

$$v \lesssim \alpha^3 \frac{m_\phi}{m} \implies \varepsilon_\nu \lesssim \varepsilon_\nu^{\text{cut,on}} \equiv \alpha^3 \varepsilon_\phi. \quad (5.69)$$

To take this saturation into account, it is therefore advisable to use $S(\varepsilon_\nu < \varepsilon_\nu^{\text{cut,on}}) = S(\varepsilon_\nu^{\text{cut,on}})$.

If we are not near or exactly on a resonance, it is clear that the full numerical solution to S does not obtain such high values for $\nu \rightarrow 0$ as in the case of a resonance. The solution therefore saturates already for much larger velocities, as can nicely be seen in the right hand plot in Fig. 5.5, and stays constant for [117]

$$\varepsilon_\nu \lesssim \varepsilon_\nu^{\text{cut,off}} \equiv 0.5 \varepsilon_\phi, \quad (5.70)$$

where the numerical factor 0.5 was obtained empirically. The reason for this can be understood if we look again at the Taylor expansion of the Yukawa potential; the total effective energy as seen by a Coulomb-like potential, $E_{\text{eff}} \sim \alpha m_\phi + mv^2$, essentially no longer depends on the velocity in this regime.

Finally, we consider for completeness the more general case, where the annihilating particles can exchange more than one type of force carrier in the ladder. Each will result in its own characteristic potential that has taken into account by summing over the various contributions

5 Sommerfeld Enhancement

in the potential part V . Furthermore, in some models (e.g., MSSM, sneutrino DM) the DM particle is actually composed of the lightest mass state, which is given by a specific mixing of interaction states. In this case, it is possible for the DM to interact with the heavier mass states, which complicates the ladder diagrams describing the Sommerfeld effect. In order to describe these additional mixings, it is necessary to adopt a matrix version of the Schrödinger equation as derived in 5.2.3.

Imagine a pair of annihilating DM particles described by the mass state i that transforms into a pair of states j after exchanging a mediator particle in the t -channel, we can denote the two-body state with the wave-function Ψ_{ij} . Furthermore, we arrange the potentials in a matrix \mathbf{V} , where \mathbf{V}_{ij} denotes the potential that is composed of all contributions of mediators that can change the two-body state associated with i into a state j . The Schrödinger equation now becomes a matrix equation [198]

$$\left\{ \left(\frac{1}{m_i} \frac{d^2}{dr^2} + K \right) \mathbf{1} - \mathbf{V}(r) \right\} \Psi(r) = 0, \quad (5.71)$$

where $K = m_i v^2$ is the kinetic energy of the system with v the velocity of each particle in the center of mass system. Here we have assumed that the mass splitting $\delta m = m_j - m_i > K$ between the two mass states is larger than the kinetic energy, such that in practice the only available on-shell states are the lightest mass states, i.e., the DM particles; the heavier mass states will then only be produced virtually. Note that although $\Psi(r)$ is presented in matrix form, it still describes a quantum-mechanical wave-function.

The Schrödinger matrix equation will form a system of coupled Schrödinger equations, which can be numerically solved for the wave-functions in a similar way as described above, by adopting the following boundary conditions:

$$\frac{d\Psi_{ij}(r)}{dr} = im_i v \Psi_{ij}(r), \quad \text{for } r \rightarrow \infty \quad (5.72)$$

$$\Psi_{ij}(0) = \delta_{ij}. \quad (5.73)$$

The total s -wave cross section including Sommerfeld effect is then defined as [196, 198]

$$\sigma_i v_{\text{rel}} = c_i \left(\Psi \Big|_{r \rightarrow \infty} \cdot \Gamma \cdot \Psi^\dagger \Big|_{r \rightarrow \infty} \right)_{ii}, \quad (5.74)$$

which in component form is written as

$$\sigma_i v_{\text{rel}} = c_i \sum_{a,b} (\Psi_{ia} \Gamma_{ab} \Psi_{ib}^*) \Big|_{r \rightarrow \infty}. \quad (5.75)$$

Here, $\Psi(r \rightarrow \infty)$ is the wave-function solution to the coupled Schrödinger equations in Eq. (5.71) at infinity. The coefficient c_i is for normalization purposes: $c_i = 2$ if the initial states indistinguishable, $c_i = 1$ if they are distinguishable. The matrix Γ is what encodes the annihilation terms for the different incoming and outgoing states of the box diagrams. It is related to the imaginary part, i.e., annihilation part, of the potential (see e.g. Eq. (5.46)) by

$$\Im [\mathcal{V}_{ij}(r)] \equiv -2\Gamma_{ij} \delta^{(3)}(r), \quad (5.76)$$

for $i, j = 1, 2$ the different two-body states. We will make use of this more general treatment in the next chapter, where we discuss the Sommerfeld effect for sneutrino DM.

5.4 Self-Scattering

Now that we considered annihilation, we continue with the case of self-scattering, which is explicitly allowed in particle models that include a Sommerfeld enhancement. Self-scattering in DM models is interesting for a number of reasons; mainly it has some important consequences for structure formation. As discussed in 4.3, numerical simulations with self-scattering DM can produce subhalos with an inner density core and velocity profiles that are in agreement with observations. Furthermore, the momentum transfer between the DM particles can cause the velocity distribution to keep a Maxwellian form, even after kinetic decoupling, such that we can easily calculate the thermal averages in the Boltzmann equations that describe the evolution of the relic density and the WIMP temperature. Unless otherwise specified, the information in this section was taken from [231].

The two cases of annihilation and self-scattering are very similar to one another, except that in the latter we do not include the annihilation part but only consider the potential part, such that our problem is again described by Eq. (5.56) and Eq. (5.57). The repeated exchange of the force carrier now not only affects the incoming, but also the final state wave-function, such that in principle we need to take into account all angular momentum contributions l to the total cross section (see Eq. (5.67)).

We are, however, interested in the rate at which energy is transferred between the particles while they scatter. This information is contained in a quantity called the *transfer cross section*

$$\sigma_T \equiv \int d\Omega (1 - \cos \theta) \frac{d\sigma_{tot}}{d\Omega} \quad (5.77)$$

$$= \frac{4\pi}{m^2 v^2} \sum_{l=0}^{\infty} [(2l+1) \sin^2 \delta_l - 2(l+1) \sin \delta_l \sin \delta_{l+1} \cos(\delta_{l+1} - \delta_l)], \quad (5.78)$$

which is a weighted average over the differential scattering cross section.

The phaseshift δ_l can be determined from the proper normalized wave-function (Eq. (5.57)) that is a solution to Eq. (5.56). In most cases a numerical treatment is necessary, since the force carrier is massive and we are dealing with a Yukawa potential. In principle one would have to solve an infinite amount of Schrödinger equations, each one with a different value of l , which is practically impossible. Moreover, the time that it takes to numerically solve the Schrödinger equation increases with l , such that it is useful to define a maximum number L up to which the contributions in the sum are relevant. All contributions $l > L$ are then neglected in the sum.

To estimate the maximum relevant angular momentum, we follow [10], and consider the momentum k of the system and the maximal impact range of the particle b_{\max} . The latter is the range at which the Yukawa potential is equal to the kinetic energy of the system. We expect that for $r \gg b_{\max}$ there is hardly any scattering and therefore the contributions $l > L \equiv kb_{\max}$ should be negligible. For example, one can approximate Eq. (5.78) by assuming the phase-shift to be

5 Sommerfeld Enhancement

maximal for $l \leq L$, and minimal for $l > L$, i.e. $\sin^2 \delta_l = 1$ and 0 respectively. With this simplification, the total cross section becomes $\sigma_{\max} = 4\pi/(m^2 v^2)(1+L)^2$, whereas the expression for σ_T becomes

$$\sigma_{\min} = \frac{4\pi}{m^2 v^2}(1+L). \quad (5.79)$$

Numerical calculations show that the full solution lies somewhere between σ_{\min} and σ_{\max} [10]. However, this approximation is not valid in the Born regime, where either the potential is negligible ($\epsilon_\phi \gg 1/2$) or the velocities are sufficiently large ($\epsilon_v \gg 1$), since in this case $L = 0$ and $\delta_0 \propto \alpha m k / m_\phi^2$. We can therefore only safely use Eq. (5.79) in the regime where $\epsilon_\phi \lesssim \epsilon_v \ll 1$.

For the models we will consider in chapter 7, we are particularly interested in very small velocities ($\epsilon_v \ll \epsilon_\phi$) that correspond to times long after chemical decoupling. In this case the above approximation fails (unless we are near a resonance, which we will discuss below) and the cross section actually becomes velocity independent. When $kR \ll 1$ is satisfied, where $R = m_\phi^{-1}$ is the effective range of the Yukawa potential, the phase-shift is given by

$$\delta_l \propto k^{2l+1}, \quad (5.80)$$

such that all phaseshifts with $l \neq 0$ are negligible compared to δ_0 . We can therefore approximate the transfer cross section as $\sigma_T \simeq \sigma_{l=0}$. The velocity independent *effective potential cross section* is given by [231]

$$\sigma^{\text{pot}} \equiv \sigma_{l=0}(kR \ll 1) = 4\pi a^2, \quad (5.81)$$

where we used that $\sin^2 \delta_l \simeq \delta_l^2 \equiv a^2 k^2$, and the scattering length $a \propto \alpha m / m_\phi^2$ is independent of velocity.

Since the case of self-scattering is very similar to that of annihilation, resonances will appear at the same values of ϵ_ϕ for low-velocity scattering. Whenever the system is close enough to a resonance, the phase-shift $\delta_0 \simeq ak$ as given by Eq. (5.80) will receive a considerable contribution from it:

$$\delta_0^{\text{res}} = \delta_0 + \arctan\left(\frac{\Gamma}{E_0 - E}\right), \quad (5.82)$$

where E_0 is the energy at which the resonance, a quasi-bound state with a width Γ , appears, and $E = mv^2$ is the kinetic energy of the system. When the system is close enough to the resonance, i.e., $|E - E_0| \ll \Gamma$, the second term on the right hand side of Eq. (5.82) can no longer be neglected as in the off-resonance case, and gives rise to an extra term in the transfer cross section

$$\sigma_T \simeq \sigma = \sigma^{\text{pot}} + \sigma^{\text{res}}, \quad (5.83)$$

where

$$\sigma^{\text{res}} = \frac{4\pi \Gamma^2 - 2ak\Gamma(E - E_0)}{k^2 (E - E_0)^2 + \Gamma^2}, \quad (5.84)$$

is the *resonance scattering cross section* [231]. In fact, Eq. (5.84) scales like $1/k^2$ and it is safe to neglect σ^{pot} near a resonance. Exactly on a resonance, we have

$$\sigma_T \simeq \sigma^{\text{res}}(E = E_0) = \frac{4\pi}{m_\chi^2 v^2}, \quad (5.85)$$

which is the same as Eq. (5.79) with $L = 0$.

If one takes a closer look at Eq. (5.84), one sees that the resonance contribution is actually negative for $\Gamma/(E - E_0) < 2ak$. The cross section even disappears when the full phase-shift in Eq. (5.82) becomes zero for $\Gamma/(E - E_0) = \tan(ak)$. These so-called ‘anti-resonances’ due to the *Ramsauer-Townsend effect* [232] are the result of destructive interference between the potential and resonance scattering amplitude, cf. Eq. (5.83). Like the resonances, they only appear for special combinations of parameters, such that in order for this case to be applicable, a certain amount of fine-tuning of the model will be necessary. Since we are only interested in an enhancement of the transfer cross section and certainly not a reduction, we do not take into account the Ramsauer-Townsend effect in this work, but only note its existence.

Now that we have discussed in detail the resonance case, we need to take a critical look at the situation when we are off-resonance. As we have seen, σ^{pot} becomes velocity independent as $v \rightarrow 0$, such that we cannot use Eq. (5.79) for σ_T in the full velocity regime: using Eq. (5.79) for small velocities would result in an overestimation of σ_T . We would like to have a conservative estimation of σ_T , which will be helpful in chapter 7, where we want to compare the scattering rate with the Hubble rate to obtain a reliable prediction of the time until when we can assume that the velocity distribution of the WIMPs is still Maxwellian. It is therefore advisable to only use Eq. (5.79) down to the velocity at which σ_T reaches the value of the asymptotic numerical solution for $\sigma_{l=0}(v \rightarrow 0)$, and keep σ_T constant as in Eq. (5.81) for smaller velocities. In reality, the full numerical solution for σ_T is larger than $\sigma_{l=0}(v \rightarrow 0)$ around the transition point, because of the behavior of $\sigma_{l=0}$ and higher angular momentum contributions that have been neglected here, such that this approach is rather conservative and represents a lower limit on σ_T .

Finally, we discuss a completely different estimation of the transfer cross section in the off-resonance case, which has been used e.g. in numerical simulations of structure formation with self-scattering DM [13]. Interestingly, the origin of this approximation can be traced back to the analysis of slowly moving, highly charged particles in a plasma [11, 12]. The interaction between these particles is described by a screened Coulomb potential, which the authors of [11, 12] approximated with a Yukawa potential. Their studies are therefore directly applicable to our case here, in which they found that their numerical results are well approximated by the following self-interaction transfer cross-section:

$$\sigma_{\text{tr}} \approx \begin{cases} \frac{4\pi}{m_\phi^2} \beta^2 \ln(1 + \beta^{-1}), & \beta \lesssim 0.1 \\ \frac{8\pi}{m_\phi^2} \beta^2 / (1 + 1.5\beta^{1.65}), & 0.1 \lesssim \beta \lesssim 1000 \\ \frac{\pi}{m_\phi^2} (\ln \beta + 1 - \frac{1}{2} \ln^{-1} \beta)^2, & \beta \gtrsim 1000 \end{cases} \quad (5.86)$$

where $\beta = \pi\alpha m_\phi/(mv^2)$ and v is the relative velocity between the DM particles. In the context of structure formation, the velocity v_{max} at which $\sigma_{\text{tr}v_{\text{rel}}}$ is maximal, and the size of the transfer-cross-section at v_{max} : $\sigma_{\text{tr}}^{\text{max}} = 22.7/m_\phi^2$, are most important. We note that all different approximations to the transfer cross section that have been discussed here agree with each other in the intermediate velocity regime, as can be seen from Fig. 5.6 for a specific example of a DM model; note, however, that this does not apply to the case of resonances.

5 Sommerfeld Enhancement

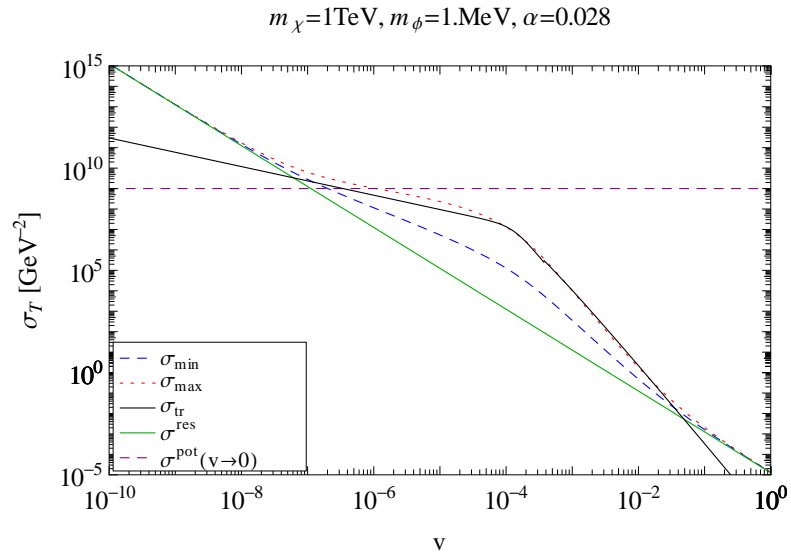


Figure 5.6: An overview of different approximations to the transfer cross section as a function of v for a model with DM mass $m_\chi = 1 \text{ TeV}$, mediator mass $m_\phi = 1 \text{ MeV}$, and coupling $\alpha = 0.028$. The min (blue, dashed) and max (red, dotted) approximations from [10] are in good agreement with the approximation σ_{tr} (black) from [11, 12] in the intermediate regime $10^{-7} \lesssim v \lesssim 10^{-1}$. The full cross section becomes independent of v for values $v \lesssim 10^{-6}$ and approaches the asymptotic value of σ^{pot} (purple, dashed), such that the other approximations become invalid in this region. The conservative approach described in the text corresponds to taking $\sigma^{\text{pot}}(v \rightarrow 0)$ in the low velocity regime, and σ_{\min} for higher velocities, where the transition is defined by the intersection point between these two curves. For completeness the transfer cross section for a resonance is shown in green.

6 Right-handed sneutrino Dark Matter

In this chapter we will consider a model where the DM is made up by sneutrinos, the superpartners of ordinary neutrinos. In particular we are interested in this model because there is the possibility of a Sommerfeld enhancement in the sneutrino annihilation cross section. After first giving a brief introduction to the model, we will calculate the Schrödinger equation from the full action for a simple toy model. Afterwards we will consider the more complicated calculation for the sneutrino model, that involves two sneutrino mass states and the Higgs and Z -boson as mediators. We will derive the analytical expressions for the potential and annihilation matrix, discuss the results, and give an outlook on how to solve the problem numerically.

6.1 Introduction

Considering the SUSY theories, it was soon realized that the scalar superpartner of the neutrino, i.e., the left-handed sneutrino, could be a potential DM candidate [233, 234]. Annihilation occurs mainly through Z -boson exchange in the s -channel, and the correct relic density is obtained for $600 \text{ GeV} \lesssim m_{\tilde{\nu}} \lesssim 700 \text{ GeV}$ [235]. However, the relatively large coupling of the sneutrino with the Z boson results in large interaction rates with nuclei that can be constrained by Direct Detection (DD) experiments [236]. The spin-independent scattering cross section per nuclei exceeds current DD limits by more than four orders of magnitude, which rule out the left-handed sneutrino as the (dominant contribution to the) observed DM.

In order to explain neutrino oscillations and obtain a non-zero neutrino mass [237, 238], however, the SM needs to be extended (see e.g. [239] for an overview of models with a neutrino mass). The simplest way is to add righthanded neutrinos to the theory and a Dirac mass term. It has not been established yet whether the neutrino is a Majorana or a Dirac particle, such that in principle both options are still open. The most often used scenario is to assume the neutrinos are Majorana particles and the see-saw mechanism naturally explains the smallness of the neutrino masses [240]. This mechanism relies on the fact that right-handed neutrinos are not charged under any SM gauge symmetries, such that their mass term can be of arbitrary value. Choosing their mass comparable to the GUT scale, and the Dirac mass – generated by a Yukawa interaction with the Higgs field – comparable to the weak scale, the resulting neutrino mass eigenstates will have a small mass of the order of eV.

The SUSY extension of this model naturally includes a right-handed sneutrino, which could serve as a possible DM candidate. The authors of [241] showed that it is possible to generate small Dirac neutrino masses by supersymmetry breaking in the hidden sector. Unlike the MSSM, in these models it is possible to generate a trilinear term with coupling $A_{\tilde{\nu}}$ that is not proportional to the tiny Yukawa couplings. This induces a large mixing between the right-handed and left-handed sneutrinos, which causes the right-handed sneutrino to be able to interact with SM gauge

6 Right-handed sneutrino Dark Matter

and Higgs bosons. Imposing R-parity makes sure the lightest supersymmetric particle (assuming the slepton masses are much heavier than the Dirac sneutrino masses, $m_{\tilde{L}} \gg m_{\tilde{N}}$) is a sneutrino. For other type of models that include a right-handed sneutrino that mixes with the left-handed sneutrino, see e.g., [242, 243].

The coupling with the Z is in this case suppressed by a factor of $\sin^2 \theta_{\tilde{\nu}}$, where $\theta_{\tilde{\nu}}$ is the mixing angle between the right- and left-handed sneutrino fields and can be chosen freely. It is therefore possible to evade the stringent bounds from DD and the invisible width of the Z , which is given by [244]

$$\Delta\Gamma_Z = \sum_{i=1}^{N_f} \Gamma_{\nu} \frac{\sin^2 \theta_{\tilde{\nu}_i}}{2} \left(1 - \left(\frac{2m_{\tilde{\nu}_i}}{m_Z} \right)^2 \right)^{3/2} < 2 \text{ MeV}, \quad (6.1)$$

where $\Gamma_{\nu} = 166 \text{ MeV}$ is the partial width into one neutrino flavor, and $m_{\tilde{\nu}}$ is the sneutrino mass. In fact, for $m_{\tilde{\nu}} \gtrsim 10 \text{ GeV}$ and (usually) $\sin \theta_{\tilde{\nu}} \sim 0.01$, the sneutrino could be a viable DM candidate.

In [244], this model was analyzed for light DM with a mass below $m_{\tilde{\nu}} < 10 \text{ GeV}$, motivated by the hints for a light DM particle from DD experiments such as DAMA [59], CoGeNT [62] and CDMS [245]. In these models the mixing angle should be large enough in order to yield the correct relic density, but not too large in order to evade bounds from the Z invisible decay width. A scan over the sneutrino and gaugino parameters showed that viable models are obtained in the range $m_{\tilde{\nu}} = 1 - 8 \text{ GeV}$.

Here, however, we want to focus on an entirely different part of parameter space, considering very heavy sneutrino DM, i.e., $m_{\tilde{\nu}} \sim \mathcal{O}(\text{TeV}) \gg m_Z, m_h$. We expect that the sneutrino annihilation cross section will be enhanced by the Sommerfeld effect in this mass range, since the exchanged bosons are massive but much lighter than the sneutrinos. To be precise, the model we consider is the one in [241, 244], i.e., the MSSM with the usual soft breaking terms as in Eq. (3.3), extended with

$$\Delta\mathcal{L}_{\text{soft}} = m_{\tilde{N}_i}^2 |\tilde{N}_i|^2 + A_{\tilde{\nu}_i} \tilde{L}_i \tilde{N}_i H_u + \text{h.c.} \quad (6.2)$$

where the sneutrino mass term $m_{\tilde{N}_i}^2$ and the trilinear coupling $A_{\tilde{\nu}_i}$ are of the weak scale and assumed to be flavor diagonal. The sneutrino mass matrix for one generation is given by

$$m_{\tilde{\nu}}^2 = \begin{pmatrix} m_L^2 + \frac{1}{2} m_Z^2 \cos 2\beta & \frac{1}{\sqrt{2}} A_{\tilde{\nu}} v \sin \beta \\ \frac{1}{\sqrt{2}} A_{\tilde{\nu}} v \sin \beta & m_N^2 \end{pmatrix}, \quad (6.3)$$

in the $(\tilde{\nu}_L, \tilde{\nu}_R)$ basis, where the tiny Dirac masses have been neglected. Here, $v = \sqrt{v_1^2 + v_2^2} = 246 \text{ GeV}$, where $v_{1,2}$ are the Higgs vacuum expectation values, and $\tan \beta = v_2/v_1$ as usual (see 3.2). Whenever $A_{\tilde{\nu}}$ is large, a large mixing between the interaction states is induced, and the mass eigenstates are given by

$$\tilde{\nu}_1 = -\tilde{\nu}_L \sin \theta_{\tilde{\nu}} + \tilde{\nu}_R \cos \theta_{\tilde{\nu}} \quad (\text{light}), \quad (6.4)$$

$$\tilde{\nu}_2 = \tilde{\nu}_L \sin \theta_{\tilde{\nu}} + \tilde{\nu}_R \cos \theta_{\tilde{\nu}} \quad (\text{heavy}), \quad (6.5)$$

where

$$\theta_{\tilde{\nu}} = \frac{1}{2} \tan^{-1} \left[\frac{\sqrt{2} A_{\tilde{\nu}} v \sin \beta}{m_{\tilde{L}}^2 + \frac{1}{2} m_Z^2 \cos 2\beta - m_{\tilde{N}}^2} \right]. \quad (6.6)$$

$$\sim \frac{A_{\tilde{\nu}} v \sin \beta / \sqrt{2}}{m_{\tilde{L}}^2}, \quad (6.7)$$

and in the last step we have assumed that $m_{\tilde{L}} \gg m_{\tilde{N}}, A_{\tilde{\nu}}, m_Z$. It follows that we have 3 new free parameters in addition to the ones from the MSSM: $A_{\tilde{\nu}}, \theta_{\tilde{\nu}}, m_{\tilde{\nu}_1}$, which can be chosen in such a way that the $\tilde{\nu}_1$ is the LSP with its mass much smaller than all other masses involved.

We have not one, but four different mediators that interact with the sneutrinos: the Z-boson (Z), and three Higgs bosons; the SM Higgs (h), the heavier Higgs (H), and the CP odd neutral Higgs (A). Since the annihilation cross section is important to obtain the correct relic DM abundance, we are interested in temperatures around chemical decoupling. These are low with respect to the masses of both A and H ($\mathcal{O}(TeV)$ or higher) such that their contributions will only be significant in relativistic interactions, and we can neglect them here.

The lightest sneutrino, $\tilde{\nu}_1$, therefore has interactions with itself, $\tilde{\nu}_2$, Z and the SM Higgs h . The Feynman rules for the sneutrino processes include:

$$Z^\mu \tilde{\nu}_1^*(p') \tilde{\nu}_1(p) : \quad -i \frac{e}{\sin 2\theta_W} (p+p')^\mu \sin^2 \theta_{\tilde{\nu}}, \quad (6.8)$$

$$Z^\mu \tilde{\nu}_2^*(p') \tilde{\nu}_1(p) : \quad -i \frac{e}{\sin 2\theta_W} (p+p')^\mu \sin \theta_{\tilde{\nu}} \cos \theta_{\tilde{\nu}}, \quad (6.9)$$

$$Z^\mu \tilde{\nu}_2^*(p') \tilde{\nu}_2(p) : \quad -i \frac{e}{\sin 2\theta_W} (p+p')^\mu \cos^2 \theta_{\tilde{\nu}}, \quad (6.10)$$

$$h \tilde{\nu}_1^*(p') \tilde{\nu}_1(p) : \quad -i \frac{em_Z \sin(\alpha + \beta)}{\sin 2\theta_W} \sin^2 \theta_{\tilde{\nu}} + i\sqrt{2} A_{\tilde{\nu}} \cos \alpha \cos \theta_{\tilde{\nu}} \sin \theta_{\tilde{\nu}}, \quad (6.11)$$

$$h \tilde{\nu}_2^*(p') \tilde{\nu}_1(p) : \quad -i \frac{em_Z \sin(\alpha + \beta)}{\sin 2\theta_W} \sin \theta_{\tilde{\nu}} \cos \theta_{\tilde{\nu}} - i \frac{1}{\sqrt{2}} A_{\tilde{\nu}} \cos \alpha (\cos^2 \theta_{\tilde{\nu}} - \sin^2 \theta_{\tilde{\nu}}), \quad (6.12)$$

where the mixing angle α was defined in Eq. (3.4). In the following we will set $m_A = 1$ TeV and $\tan \beta = 10$, from which it follows that $\cos \alpha \sim \sin(\alpha + \beta) \sim 1$. The interactions between the sneutrinos and bosons are given in Fig. 6.1, where we have introduced a practical shorthand notation, where A_{ij} (B_{ij}) couples a h (Z) to an i - and j -sneutrino. Since $\theta_{\tilde{\nu}} \ll 1$, and $A_{\tilde{\nu}}$ and m_Z are of the same order of magnitude, we can approximate Eq. (6.11) with $\sim i\sqrt{2} A_{\tilde{\nu}} \sin \theta_{\tilde{\nu}}$, and Eq. (6.12) with $\sim -i A_{\tilde{\nu}} / \sqrt{2}$, such that the shorthand couplings corresponding to Fig. 6.1 are

6 Right-handed sneutrino Dark Matter

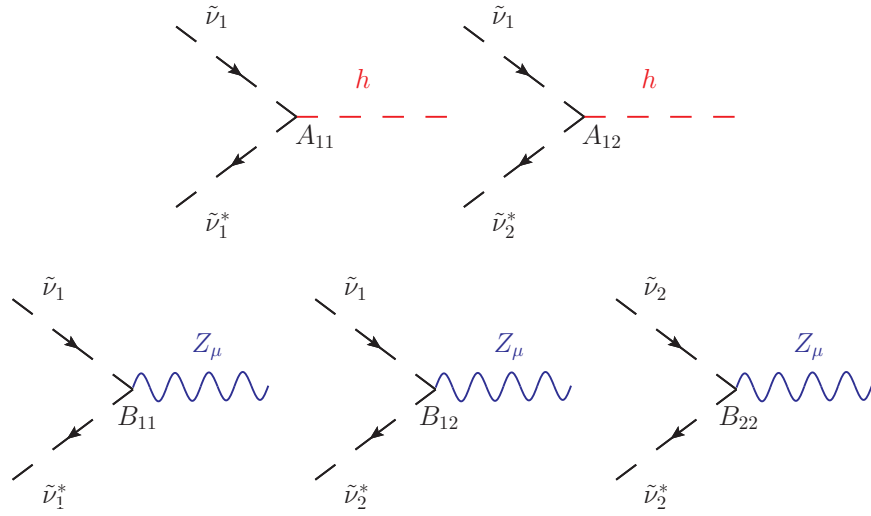


Figure 6.1: All possible couplings between the two sneutrino species and the h and Z boson. For clarity shorthand notations for the couplings c.f. Eq. (6.13) - (6.17) are included.

then given by

$$A_{11} = \sqrt{2}A_{\tilde{\nu}} \sin \theta_{\tilde{\nu}}, \quad (6.13)$$

$$A_{12} = -\frac{A_{\tilde{\nu}}}{\sqrt{2}}, \quad (6.14)$$

$$B_{11} = \frac{e}{\sin 2\theta_W} \sin \theta_{\tilde{\nu}}^2, \quad (6.15)$$

$$B_{12} = \frac{e}{\sin 2\theta_W} \sin \theta_{\tilde{\nu}} \cos \theta_{\tilde{\nu}}, \quad (6.16)$$

$$B_{22} = \frac{e}{\sin 2\theta_W} \cos \theta_{\tilde{\nu}}^2. \quad (6.17)$$

In the next section we will consider a simple toy model to get a feeling for the calculation of all interaction diagrams, before continuing on to the Sommerfeld enhancement in the more involved sneutrino model.

6.2 A scalar toy model

We consider here a toy model with heavy H and light l scalar fields, which will play the role of the sneutrino DM particle and the Higgs boson, respectively. The Lagrangian is given by

$$\mathcal{L} = \frac{1}{2} \partial^\mu l \partial_\mu l - \frac{m_l}{2} l^2 + \frac{1}{2} \partial^\mu H \partial_\mu H - \frac{m_H}{2} H^2 - \frac{A}{2} l H^2, \quad (6.18)$$

where A is the coupling constant between the two H and l . In this section we will derive the Schrödinger equation that describes the non-relativistic two-body state of the HH pair to get a

general idea of the problem for the sneutrino model. The derivation is similar to the one shown for the positronium in chapter 5.2. The main difference with QED is that in the toy model the fields are scalar, such that we do not have to worry about spin statistics. Here we only show central results; the details of the calculation can be found in Appendix section A.2, both of which are based on [246].

As usual, the starting point is the Lagrangian from Eq. (6.18), and the first step is to integrate out the light fields l . We do this by shifting the light field

$$l'(x) = l(x) - i \int d^4y D_l(x-y) j(y), \quad (6.19)$$

where $D_l(x-y)$ is the propagator of the light field and current is here defined as $j(x) \equiv \frac{A}{2} H^2(x)$. Following the steps as in 5.2.2 is straightforward, and we find that the effective Lagrangian is given by

$$S_{\text{eff}}[H] = \int d^4x \left[\frac{1}{2} \partial^\mu H \partial_\mu H + \frac{m_H^2}{2} H^2 \right] + \frac{i}{2} \int d^4x d^4y j(x) D_l(x-y) j(y). \quad (6.20)$$

Integrating out the relativistic parts of the heavy fields is very similar to what we have done in 5.2.2. The non-relativistic regime is defined as in Eq. (5.26), and the fields are split up in a non-relativistic and relativistic part in momentum space in the same fashion. Expanding all terms in the effective action, we find that the interaction term with only non-relativistic fields gives the potential term equivalent to Eq. (5.31):

$$S_{\text{pot}}[H_{\text{NR}}] = i \frac{A^2}{8} \int d^4x d^4y H_{\text{NR}}^2(x) D_l(x-y) H_{\text{NR}}^2(y), \quad (6.21)$$

which corresponds to the diagram on the left in Fig. 6.2.

Concentrating on the box diagram from which we will derive the heavy scalar annihilation into light fields, we obtain the annihilation action

$$\begin{aligned} S_{\text{ann}}[H_{\text{NR}}] = & -i \frac{A^4}{8} \int d^4x d^4y d^4z d^4w \\ & [H_{\text{NR}}(x) D_l(x-y) H_{\text{NR}}(y) D_H^{\text{R}}(y-z) H_{\text{NR}}(z) D_l(z-w) H_{\text{NR}}(w) D_H^{\text{R}}(w-x) \\ & + H_{\text{NR}}(x) D_l(x-y) H_{\text{NR}}(y) D_H^{\text{R}}(y-w) H_{\text{NR}}(w) D_l(w-z) H_{\text{NR}}(z) D_H^{\text{R}}(z-x)], \end{aligned} \quad (6.22)$$

where the two different terms again correspond to t-channel (shown in Fig. 6.2 on the right) and u-channel box diagrams as for the positronium case (see Eq. (5.29)). The details of the derivation are summarized in Appendix section A.2.

In order to perform the non-relativistic expansion of the action, we need to derive the correct normalization of the heavy field, which is done by looking at the kinetic terms. We find that the non-relativistic H -field should have the form

$$H_{\text{NR}}(x) = \frac{1}{\sqrt{2m_H}} [\phi(x) e^{-im_H t} + \phi^\dagger(x) e^{im_H t}], \quad (6.23)$$

6 Right-handed sneutrino Dark Matter

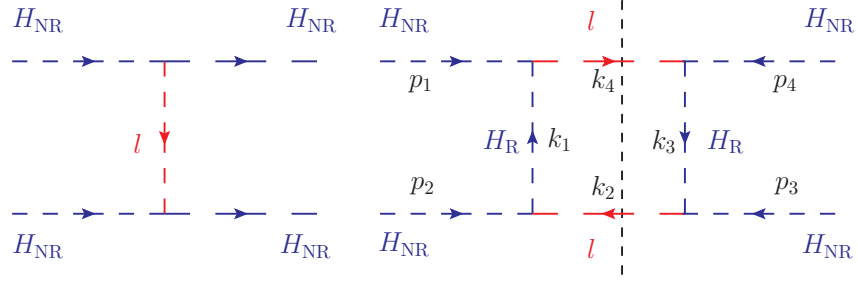


Figure 6.2: On the left, the potential diagram with light scalar (red) exchange between the heavy scalars (blue) in the t-channel. On the right, the box diagram is shown that relates to the annihilation of two h into two l by cutting the diagram along the black dashed line. The arrows denote the direction of momentum.

where the phases are just a convention and not physical. It must be understood that $\phi^\dagger(x)$ creates a heavy field and $\phi(x)$ annihilates one at x .

For the potential term we need to consider the non-relativistic expansion of the product $H_{\text{NR}}^2(x)$. Since we are interested in the t-channel diagram, we can ignore the terms proportional to $\phi_x^\dagger \phi_x^\dagger$ (two outgoing heavy fields created at x) and $\phi_x \phi_x$ (two incoming heavy fields annihilated at x). The contributions $\phi_x \phi_x^\dagger$ and $\phi_x^\dagger \phi_x$ are actually the same, since the fields are scalar and the ordering is irrelevant. After some algebra we obtain

$$S_{\text{pot}} = \frac{A^2}{8m_H^2} \int d^4x d^4y \frac{\delta(x^0 - y^0) e^{-m_l(x-y)}}{4\pi|\mathbf{x} - \mathbf{y}|} (\phi^\dagger \phi)_x (\phi^\dagger \phi)_y. \quad (6.24)$$

As expected, the action now includes a Yukawa potential since the force carrier l is massive. Furthermore we can see that the sign in front of the potential is positive and therefore attracting, i.e., this will give an enhancement of the annihilation cross section. The fields should be reshuffled as to correspond to a scalaronium state, $(\phi_x^\dagger \phi_y^\dagger)(\phi_x \phi_y)$, where the right hand annihilates a spin-0 scalaronium state and the left hand creates one.

Finally, we have to do the same for the annihilation term given in Eq. (6.22), which requires a bit more work. In order to derive the annihilation term, we calculate the box diagram and apply the optical theorem. Here, we quote the final result:

$$S_{\text{ann}} = i \frac{3A^4}{1024\pi m_H^6} \int d^4x (\phi(x) \phi^\dagger(x))^2 \frac{\sqrt{1 - \frac{m_l^2}{m_H^2}}}{1 - \frac{m_l^4}{4m_H^4}}, \quad (6.25)$$

and point the reader to Appendix section A.2 for the full calculation.

The two-body action is obtained in the same way as for the positronium state by introducing auxiliary fields and we can therefore closely follow the derivation as discussed in 5.2.3. After carefully noting the subtleties, we end up with exactly the same expression as in Eq. (5.41), but with a slightly different form of \mathcal{V} . The equations of motion result in a Schrödinger equation

6.3 Sommerfeld effect for right-handed sneutrino Dark Matter

exactly as in Eq. (5.47), but now with the potential given by

$$V(r) = -\frac{A^2}{16\pi m_H^2} \frac{e^{-m_l r}}{r} - i \frac{3}{512\pi} \frac{A^4}{m_H^6} \frac{\sqrt{1 - \frac{m_l^2}{m_H^2}}}{1 - \frac{m_l^4}{4m_H^4}} \delta^{(3)}(r), \quad (6.26)$$

where in the first term we recognize the Yukawa potential as a function of the light mass m_l , and the second term represents the annihilation.

6.3 Sommerfeld effect for right-handed sneutrino Dark Matter

Now that we have warmed up with the simple example of the toy model, it is time to consider the more involved sneutrino model. Here, it is necessary to adopt the matrix approach as introduced in section 5.3, since there is a mixing present between the two sneutrino mass states. Although the DM is composed of the lightest sneutrino, $\tilde{\nu}_1$, there is also the slightly heavier sneutrino $\tilde{\nu}_2$ that plays a role in the ladders. For example, an incoming pair of light sneutrinos could change into a pair of heavy sneutrinos after exchanging a Z or h , or vice versa. Denoting the pair of $\tilde{\nu}_1 \tilde{\nu}_1^*$ with the index 1, and a pair of $\tilde{\nu}_2 \tilde{\nu}_2^*$ with 2, we can denote the two-body state with an incoming pair i and outgoing (i.e. before annihilating) pair j with the matrix element Ψ_{ij} . The wavefunction for the sneutrino annihilation is then described by a system of coupled Schrödinger equations as introduced in Eq. (5.71), where the potential \mathbf{V}_{ij} includes both the contributions of h and Z exchange between states i and j . The annihilation matrix Γ_{ij} is related to the imaginary part of the box diagrams with initial state i and final state j cf. Eq. (5.76), from which one can calculate the annihilation cross section using Eq. (5.75). This section is therefore divided into two parts: first we concentrate on the ladder diagrams that give the actual enhancement, second we have a look at the annihilation of the sneutrinos.

6.3.1 Potential term

Here we calculate the potential term for the sneutrino model in a general way, which means that we do not explicitly define the sneutrinos by its index 1 or 2. In this way, we can use the results for all four possible interactions between the different two body states. In order to keep the notation simple and clear, we also define new couplings A and B , which later can be exchanged by the real couplings from the Lagrangian introduced in 6.1. Our Lagrangian then takes the form:

$$\begin{aligned} \mathcal{L}_{\text{eff}} = & (\partial^\mu \tilde{\nu}) (\partial_\mu \tilde{\nu}^*) - m_{\tilde{\nu}}^2 \tilde{\nu} \tilde{\nu}^* + \frac{1}{2} (\partial^\mu h) (\partial_\mu h) - \frac{1}{2} m_h^2 h^2 \\ & - \frac{1}{2} Z_\mu (\partial^2 g^{\mu\nu} - \partial^\mu \partial^\nu) Z_\nu - \frac{1}{2} m_Z^2 Z_\mu Z^\mu - Ah \tilde{\nu} \tilde{\nu}^* - BZ_\mu \tilde{\nu}^* \overleftrightarrow{\partial}^\mu \tilde{\nu}, \end{aligned} \quad (6.27)$$

where the last two terms describe the interactions between the sneutrino and the h and Z , respectively, and $\tilde{\nu}^* \overleftrightarrow{\partial}^\mu \tilde{\nu} \equiv \tilde{\nu}^* (\partial^\mu \tilde{\nu}) - (\partial^\mu \tilde{\nu}^*) \tilde{\nu}$. Note that the coupling A has mass dimension 1, and B is dimensionless, which corresponds to the couplings as defined in Eqs. (6.13) – (6.17). We

6 Right-handed sneutrino Dark Matter

adopt here the unitarity gauge ($\xi \rightarrow \infty$) for simplicity, such that ghost particles disappear.

We proceed according to the method described in subsection 5.2.2 to obtain the non-relativistic action. After integrating out the Higgs and Z -boson field, we are left with

$$\begin{aligned} S_{\text{eff}} = & \int d^4x i\tilde{\nu}_x^* D_{\tilde{\nu}}^{-1}(x) \tilde{\nu}_x \\ & + i\frac{A^2}{2} \int d^4x d^4y (\tilde{\nu}_x^* \tilde{\nu}_x) D_h(x-y) (\tilde{\nu}_y^* \tilde{\nu}_y) \\ & - i\frac{B^2}{2} \int d^4x d^4y (\tilde{\nu}_x^* \overleftrightarrow{\partial}^\mu \tilde{\nu}_x) D_{Z,\mu\nu}(x-y) (\tilde{\nu}_y^* \overleftrightarrow{\partial}^\nu \tilde{\nu}_y), \end{aligned} \quad (6.28)$$

where we have defined the propagators and their inverse as

$$D_i(x) = \int \frac{d^4p}{(2\pi)^4} \frac{ie^{-ipx}}{p^2 - m_i^2 + i\epsilon}, \quad \text{with } i = \tilde{\nu}, h, \quad (6.29)$$

$$D_i^{-1}(x) = i(\partial_x^2 + m_i^2), \quad (6.30)$$

$$D_{Z,\mu\nu}(x) = \int \frac{d^4p}{(2\pi)^4} \frac{-ie^{-ipx}}{p^2 - m_Z^2 + i\epsilon} \left(g_{\mu\nu} - \frac{p_\mu p_\nu}{m_Z^2} \right), \quad (6.31)$$

$$D_{Z,\mu\nu}^{-1}(x) = -i(\partial_x^2 g^{\mu\nu} - \partial_x^\mu \partial_x^\nu + m_Z^2 g^{\mu\nu}). \quad (6.32)$$

This means that the propagators obey $D_i^{-1}(x)D_i(x-y) = \delta^{(4)}(x-y)$, and in the same way $D_{Z,\mu\nu}^{-1}(x)D_Z^{\alpha\beta}(x-y) = \delta_\mu^\alpha \delta_\nu^\beta \delta^{(4)}(x-y)$.

After integrating out the relativistic fields, the potential term takes a similar form as in (A.2), except that now we have one term for each mediator:

$$iS_{h,\text{pot}} = -\frac{A^2}{2} \int d^4x d^4y (\tilde{\nu}_x^* \tilde{\nu}_x) D_h(x-y) (\tilde{\nu}_y^* \tilde{\nu}_y), \quad (6.33)$$

$$iS_{Z,\text{pot}} = \frac{B^2}{2} \int d^4x d^4y (\tilde{\nu}_x^* \overleftrightarrow{\partial}^\mu \tilde{\nu}_x) D_{Z,\mu\nu}(x-y) (\tilde{\nu}_y^* \overleftrightarrow{\partial}^\nu \tilde{\nu}_y), \quad (6.34)$$

where the NR -subscripts have been omitted for clarity, but it is understood that all fields are non-relativistic (as defined in Eq. (5.26)). Their non-relativistic expansion results in

$$\tilde{\nu}_{\text{NR}}(x) = \frac{1}{\sqrt{2m_{\tilde{\nu}}}} \left[a_x e^{-imx^0} + b_x^* e^{imx^0} \right], \quad (6.35)$$

where now a_x annihilates a sneutrino and b_x^* creates an anti-sneutrino at x . After the non-relativistic expansion of Eq. (6.33) and Eq. (6.34), we are only interested in terms that describe t -channel $\tilde{\nu}\tilde{\nu}^*$ scattering, i.e., combinations $a_{x1}a_{x1}^*b_{x2}^*b_{x2}$. We find that for the Higgs potential, $\tilde{\nu}_x^*\tilde{\nu}_x\tilde{\nu}_y^*\tilde{\nu}_y$ gives two of such terms, which makes the total factor in front $1/(2m_{\tilde{\nu}}^2)$. For the Z it is slightly more complicated, since we are dealing with a derivative that works in two directions. One can show that $\tilde{\nu}^*\overleftrightarrow{\partial}^\mu\tilde{\nu} = i(bb^* - aa^*)$, such that in the end, we have two aa^*bb^* terms in the potential term.

6.3 Sommerfeld effect for right-handed sneutrino Dark Matter

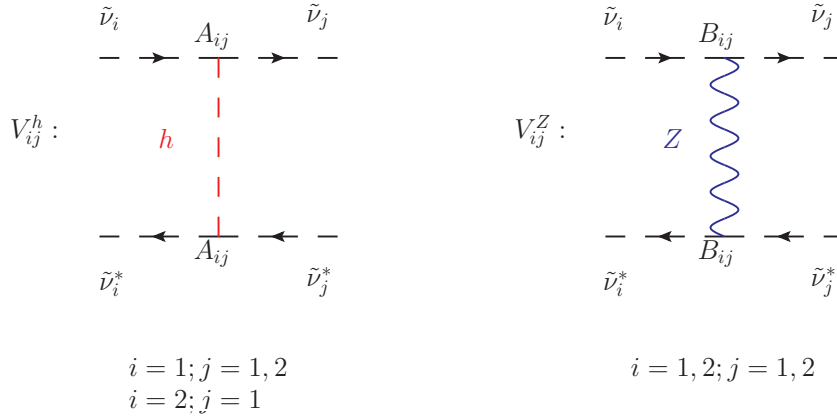


Figure 6.3: Diagrams that contribute to the potential matrix for h (left) and Z (right). Note that the Higgs boson does not mediate $\tilde{\nu}_2 \tilde{\nu}_2^* \rightarrow \tilde{\nu}_2 \tilde{\nu}_2^*$ scattering (see Eqs. (6.13) – (6.17)), such that the diagram corresponding to V_{22}^h does not exist.

Following the same steps as described for the positronium, we finally arrive at

$$S_{\text{pot}} = \frac{1}{2} \int d(xy) (a_x b_x^*) \left[\frac{A^2}{8\pi m_{\tilde{\nu}}^2} \frac{e^{-m_h |\mathbf{x}-\mathbf{y}|}}{|\mathbf{x}-\mathbf{y}|} + \frac{B^2}{2\pi} \frac{e^{-m_Z |\mathbf{x}-\mathbf{y}|}}{|\mathbf{x}-\mathbf{y}|} \right] (a_y^* b_y). \quad (6.36)$$

Since we know that the term inside the square brackets is exactly the potential $V(r)$ with $r = |\mathbf{x} - \mathbf{y}|$ for the scattering of $\tilde{\nu}^* \tilde{\nu}$, it is now straightforward to derive all matrix elements in $\mathbf{V}(r)$ for the various two-body states of the sneutrino model, by substituting A and B according to the couplings as defined in Eqs. (6.13) – (6.17). Here we must be careful to include combinatorial factors that arise from the two-body states. For each initial or final two-body state, a factor of $\frac{1}{\sqrt{2}}$ should be included in the final potential when the two particles are indistinguishable. Since the two-body states here consist of a sneutrino and anti-sneutrino that are Majorana particles, the total factor for each t-channel diagram is $\frac{1}{2}$.

The possible diagrams for sneutrino scattering in the t-channel are depicted in Fig. 6.3, where interactions with the Higgs and Z -boson are shown on the left and right, respectively. Note that the Higgs does not mediate scattering between $\tilde{\nu}_2^* \tilde{\nu}_2 \rightarrow \tilde{\nu}_2^* \tilde{\nu}_2$ because the coupling A_{22} describing this process is zero (see also Eqs. (6.13) – (6.17)). Splitting up the contributions from h and Z , the potential due to the former is given by

$$\mathbf{V}^h(r) \simeq -\frac{\alpha_{\tilde{\nu}} e^{-m_h r}}{2r} \begin{pmatrix} \sin^2 \theta_{\tilde{\nu}} & \frac{1}{4} \\ \frac{1}{4} & 0 \end{pmatrix}, \quad (6.37)$$

where we have introduced the shorthand notation $\alpha_{\tilde{\nu}} \equiv A_{\tilde{\nu}}^2 / (4\pi m_{\tilde{\nu}}^2)$. As expected, $V_{22}^h = 0$ and the other diagonal term, corresponding to scattering of $\tilde{\nu}_1^* \tilde{\nu}_1 \rightarrow \tilde{\nu}_1^* \tilde{\nu}_1$ through a Higgs, can only occur when electroweak symmetry is broken, i.e. $v \neq 0$ or in other words $\theta_{\tilde{\nu}} \neq 0$. Even then, this process is suppressed by $\sin^2 \theta_{\tilde{\nu}}$ with respect to the sneutrino changing scatterings, meaning that only the mixed terms give a significant contribution.

6 Right-handed sneutrino Dark Matter

For the Z-boson potential we derive

$$\mathbf{V}^Z(r) = -\frac{\alpha e^{-m_Z r}}{\sin^2 2\theta_W r} \begin{pmatrix} \sin^4 \theta_{\tilde{\nu}} & \cos^2 \theta_{\tilde{\nu}} \sin^2 \theta_{\tilde{\nu}} \\ \cos^2 \theta_{\tilde{\nu}} \sin^2 \theta_{\tilde{\nu}} & \cos^4 \theta_{\tilde{\nu}} \end{pmatrix}. \quad (6.38)$$

Here, the dominant contribution comes from \mathbf{V}_{22}^Z . For all other processes to occur, again electroweak symmetry breaking effects are necessary.

6.3.2 Annihilation term

In order to determine the annihilation matrix for the sneutrino DM, we have to calculate the box diagrams for all possible incoming and outgoing two-body states. The diagonal elements are given by the box diagrams which have the same incoming as outgoing two-body state; i.e., they correspond to the annihilation diagram of the incoming particles to the intermediate states under consideration. However, there exist also box diagrams that have the desired intermediate states, but a different incoming as outgoing state, which we also have to take into account.

As for the potential matrix, we use the effective Lagrangian given in Eq. (6.27). First we consider the box diagram with the intermediate states being two Higgs bosons. Since they are scalar particles, like the light particles l considered in the toy model calculation of the box diagram in Appendix section A.2, we can (almost) directly adopt the result for the toy model annihilation action quoted in Eq. (A.82). We redefine the heavy and light masses to $m_h \rightarrow m_{\tilde{\nu}}$ and $m_l \rightarrow m_h$, respectively, and we have to substitute the coupling $A \rightarrow 2A$ because of the different normalization factor in the Lagrangian. The product of $(\tilde{\nu}^* \tilde{\nu})^2$ is calculated according to Eq. (6.3.1), and as mentioned before, this gives $aa^*b^*b/(2m_{\tilde{\nu}}^2)$.

Since in this model we are dealing with two different sneutrinos that have a slightly different mass, it is convenient to keep track of all sneutrinos during the calculation of the box diagram. We therefore denote the masses of the initial sneutrinos with subscript i and final state with f , since we know that for the off-diagonal elements we have to include diagrams where these are not the same states. The same holds for the virtual, relativistic sneutrinos, which we keep track of with the indices R, i for the initial and R, f for the final one. This will be important for diagrams where the initial two-body state interacts with a different sneutrino in the t-channel

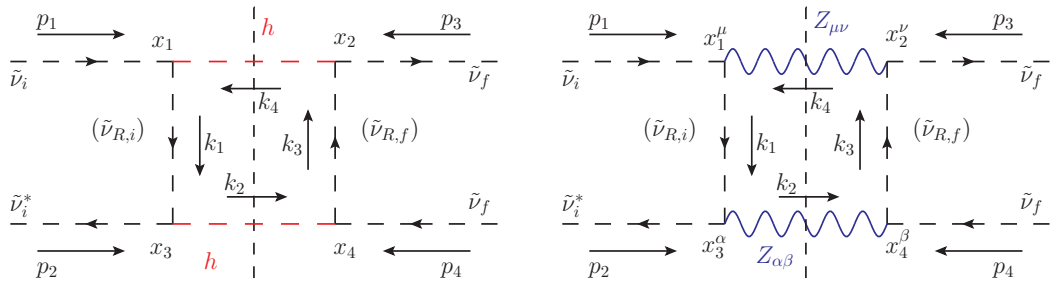


Figure 6.4: Box diagram for Higgs (left) and Z-boson (right) intermediate states. All initial, final and relativistic states are indicated with corresponding subscripts, and the direction of the momenta are indicated with arrows. The box diagrams are cut along the dashed line.

(see also Fig. 6.4).

After carefully denoting the different states and implementing the substitutions for the sneutrino model we arrive at

$$S_{\text{ann}}^h = i \frac{(A/m_{\tilde{\nu},i})^4}{2048\pi m_{\tilde{\nu},i} m_{\tilde{\nu},f}} \int d^4x [a_i(x)a_i^*(x)b_f^*(x)b_f(x) + a_f(x)a_f^*(x)b_i^*(x)b_i(x)] \times \sqrt{1 - \frac{m_h^2}{m_{\tilde{\nu},i}^2} \left(1 - \frac{m_h^2}{2m_{\tilde{\nu},i}^2} - \frac{\Delta_i}{2m_{\tilde{\nu},i}^2}\right)^{-1} \left(1 + \frac{m_h^2}{2m_{\tilde{\nu},i}^2} + \frac{\Delta_f}{2m_{\tilde{\nu},i}^2}\right)^{-1}}, \quad (6.39)$$

where we have introduced $\Delta_n = (m_{\tilde{\nu},n}^2 - m_{\tilde{\nu},R,n}^2)$. It can be seen that this rather complicated result simplifies to the toy model result – apart from the necessary substitutions for the involved sneutrino and Z fields, masses and couplings – when one assumes that the initial and final states are the same, and if the relativistic states are the same as the in- or outgoing ones, i.e. $\Delta_i = \Delta_f = 0$. The imaginary part of the potential is correspondingly given by

$$\Im [V^h(r)] = -\frac{c_{if}(A/m_{\tilde{\nu},i})^4 \delta^{(3)}(r)}{1024\pi m_{\tilde{\nu},i} m_{\tilde{\nu},f}} \sqrt{1 - \frac{m_h^2}{m_{\tilde{\nu},i}^2}} \times \left(1 - \frac{m_h^2}{2m_{\tilde{\nu},i}^2} - \frac{\Delta_i}{2m_{\tilde{\nu},i}^2}\right)^{-1} \left(1 + \frac{m_h^2}{2m_{\tilde{\nu},i}^2} + \frac{\Delta_f}{2m_{\tilde{\nu},i}^2}\right)^{-1}, \quad (6.40)$$

where the coefficient $c_{if} = 2$ for equal initial and final states, and $c_{if} = 1$ for $i \neq f$.

The calculation of the box diagram of the Z -boson requires a little bit more work, and can be found in Appendix subsection A.3.1. As can be seen from Eq. (A.99), the result resembles the one obtained for the Higgs, except for an additional factor. The resulting imaginary part of the potential due to annihilation into two Z -bosons is

$$\Im [V^Z(r)] = -\frac{c_{if}B^4 \delta^{(3)}(r)}{64\pi m_{\tilde{\nu},i} m_{\tilde{\nu},f}} \left(\frac{m_{\tilde{\nu},i}}{m_Z}\right)^4 \times \left(1 - \frac{m_Z^2}{m_{\tilde{\nu},i}^2}\right)^{5/2} \left(1 - \frac{m_Z^2}{2m_{\tilde{\nu},i}^2} - \frac{\Delta_i}{2m_{\tilde{\nu},i}^2}\right)^{-1} \left(1 + \frac{m_Z^2}{2m_{\tilde{\nu},i}^2} + \frac{\Delta_f}{2m_{\tilde{\nu},i}^2}\right)^{-1}. \quad (6.41)$$

Finally, we could also have a box diagram with one Higgs and one Z -boson. Here one should be careful to consider the u - and t -channel box diagram separately, since it follows that they differ by a factor -1 in the leading order approximation such that they cancel each other out. In the t -channel diagram the Z couples to two (anti-)sneutrinos, but in the u -channel it couples to one anti- and one sneutrino. Setting the momenta just as indicated in the right diagram in Fig. 6.4, one finds that the derivative that comes from the Z -boson coupling, $\tilde{\nu}^* \overleftrightarrow{\partial}_\mu \tilde{\nu}$, will give an extra minus sign in the u -channel case. One should keep in mind, though, that annihilation into one h and one Z is merely suppressed; higher order terms will not exactly cancel each other out. Here, however, the tree level approximation is sufficient and we can safely neglect the annihilation into mixed states.

By using Eq. (5.76) we can now derive the annihilation matrix from the (imaginary) potentials

6 Right-handed sneutrino Dark Matter

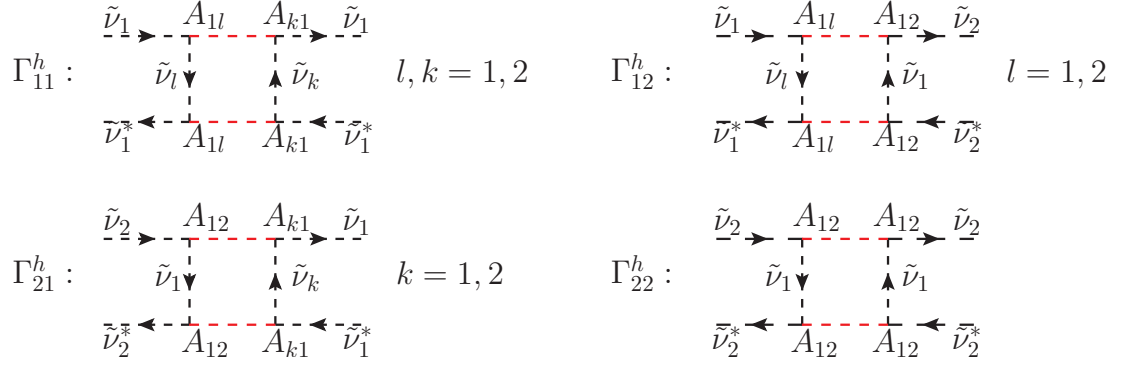


Figure 6.5: All box diagrams that correspond to annihilation to hh , ordered according to the matrix element to which they belong. The fact that $A_{22} = 0$ restricts the total number of box diagrams to nine.

that are shown above. As mentioned before, the diagonal elements of the annihilation matrix Γ_{ii} are given by box diagrams with the same incoming as outgoing states, that are simply related to the annihilation of the particular sneutrino pair $\tilde{\nu}_i\tilde{\nu}_i^*$ into hh or ZZ . The off-diagonal terms Γ_{ij} , however, correspond to box diagrams that have different in- and outgoing states $\tilde{\nu}_i\tilde{\nu}_i^* \rightarrow \tilde{\nu}_j\tilde{\nu}_j^*$.

For each matrix element (either diagonal or off-diagonal) Γ_{ij} , we must take into account all possible diagrams that have the corresponding initial $\tilde{\nu}_i\tilde{\nu}_i^*$ and final $\tilde{\nu}_j\tilde{\nu}_j^*$ states. Since the two different sneutrino states can couple to each other, in some cases this gives rise to a number of diagrams that only differ by the relativistic virtual sneutrino that is mediated by the in- and outgoing sneutrinos. All possibilities should be taken into account by summing the different diagrams for each matrix element.

We will clarify this procedure with an example. In the matrix for annihilation into two Higgs bosons, the diagonal term Γ_{11}^h contains all possible box diagrams with in- and outgoing $\tilde{\nu}_1\tilde{\nu}_1^*$ states and intermediate hh . As we can see from Fig. 6.5, there are four possible diagrams that need to be taken into account, since the initial and final sneutrino-pair can mediate either a $\tilde{\nu}_1$ or $\tilde{\nu}_2$. If we consider Γ_{22}^h , which corresponds to $\tilde{\nu}_2\tilde{\nu}_2^* \rightarrow \tilde{\nu}_2\tilde{\nu}_2^*$, we see from Fig. 6.5 that only one diagram exists. The reason for this is that there is no $h\tilde{\nu}_2^*\tilde{\nu}_2$ coupling, and therefore the $\tilde{\nu}_2\tilde{\nu}_2^*$ pair can only interact via $\tilde{\nu}_1$ exchange. All possible diagrams for sneutrino annihilation into hh are given in Fig. 6.5, which amounts to a total of nine diagrams. For annihilation into Z -bosons the allowed diagrams are much simpler determined because the Z mediates interactions between all possible sneutrino states, as shown in Fig. 6.6.

The expression for one diagram is obtained by combining Eq. (5.76) with either Eq. (6.40) in case of annihilation into two Higgs bosons, or Eq. (6.41) for annihilation into two Z -bosons. In these equations we need to replace the couplings, which can be read off from the diagrams in Fig. 6.5 and Fig. 6.6, with the correct ones given by Eqs. (6.13) – (6.17). Furthermore, we need to make sure that we substitute the correct fields and masses for the different sneutrino states, i.e. reinstate the subscripts 1 and 2. Finally, we should take into account the same combinatorial factors arising from the initial and final two-body states as discussed for the potential matrix elements, which amount to $(1/\sqrt{2})^2 = 1/2$ for each box diagram.

After having done this tedious task, we arrive at the full expressions for the annihilation matrices. Since they are rather lengthy, they are summarized in Appendix subsection A.3.2.

6.3 Sommerfeld effect for right-handed sneutrino Dark Matter

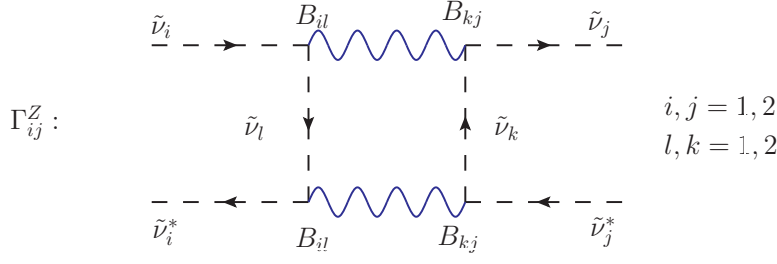


Figure 6.6: All sixteen box diagrams that correspond to annihilation to ZZ . Each matrix element Γ_{ij}^Z contains the sum of four possible diagrams which differ by the virtual sneutrino states l, k exchanged in the t-channel.

Here, to get a feeling for the full solutions, we consider the results in the case of electroweak symmetry, i.e. $\theta_{\tilde{\nu}} \rightarrow 0$, for which the expressions become considerably shorter. For annihilation into hh , we obtain the following matrix elements:

$$\Gamma_{11}^h|_{\theta_{\tilde{\nu}} \rightarrow 0} = \frac{A_{\tilde{\nu}}^4}{2048\pi m_{\tilde{\nu},1}^2} \sqrt{1 - \frac{m_h^2}{m_{\tilde{\nu},1}^2}} \times (-\delta m^4 - 4m_{\tilde{\nu},1}(\delta m^3 + \delta m^2 m_{\tilde{\nu},1} - m_{\tilde{\nu},1}^3) + 2\delta m(\delta m + 2m_{\tilde{\nu},1})m_h^2 - m_h^4)^{-1}, \quad (6.42)$$

$$\Gamma_{12}^h|_{\theta_{\tilde{\nu}} \rightarrow 0} = \frac{A_{\tilde{\nu}}^4}{4096\pi m_{\tilde{\nu},1}(\delta m + m_{\tilde{\nu},1})} \sqrt{1 - \frac{m_h^2}{m_{\tilde{\nu},1}^2}} \times ((\delta m^2 + 2m_{\tilde{\nu},1}(\delta m + m_{\tilde{\nu},1}))^2 - m_h^4)^{-1}, \quad (6.43)$$

$$\Gamma_{21}^h|_{\theta_{\tilde{\nu}} \rightarrow 0} = \frac{A_{\tilde{\nu}}^4}{4096\pi m_{\tilde{\nu},1}(\delta m + m_{\tilde{\nu},1})} \sqrt{1 - \frac{m_h^2}{(\delta m + m_{\tilde{\nu},1})^2}} \times ((\delta m^2 + 2m_{\tilde{\nu},1}(\delta m + m_{\tilde{\nu},1}))^2 - m_h^4)^{-1}, \quad (6.44)$$

$$\Gamma_{22}^h|_{\theta_{\tilde{\nu}} \rightarrow 0} = \frac{A_{\tilde{\nu}}^4}{2048\pi(\delta m + m_{\tilde{\nu},1})^2} \sqrt{1 - \frac{m_h^2}{(\delta m + m_{\tilde{\nu},1})^2}} \times (\delta m^2 + 2m_{\tilde{\nu},1}(\delta m + m_{\tilde{\nu},1}) - m_h^2)^{-1} (3\delta m^2 + 2m_{\tilde{\nu},1}(3\delta m + m_{\tilde{\nu},1}) + m_h^2)^{-1}. \quad (6.45)$$

Here, we have replaced the mass of the heavier sneutrino by $m_{\tilde{\nu},1} + \delta m$, where δm is the mass difference between the two sneutrinos. In the special case that the two sneutrinos are degenerate in mass, i.e. $\delta m = 0$, all Higgs matrix elements reduce to

$$\Gamma_{ij}^h|_{\theta_{\tilde{\nu}} \rightarrow 0, \delta m = 0} = \frac{A_{\tilde{\nu}}^4}{2048\pi m_{\tilde{\nu},1}^2} \sqrt{1 - \frac{m_h^2}{m_{\tilde{\nu},1}^2}} (4m_{\tilde{\nu},1}^4 - m_h^4)^{-1}, \quad (6.46)$$

except for an additional factor $\frac{1}{2}$ for the off-diagonal elements. We would therefore expect that for small δm , the full results for different Γ_{ij}^h are very similar to each other.

6 Right-handed sneutrino Dark Matter

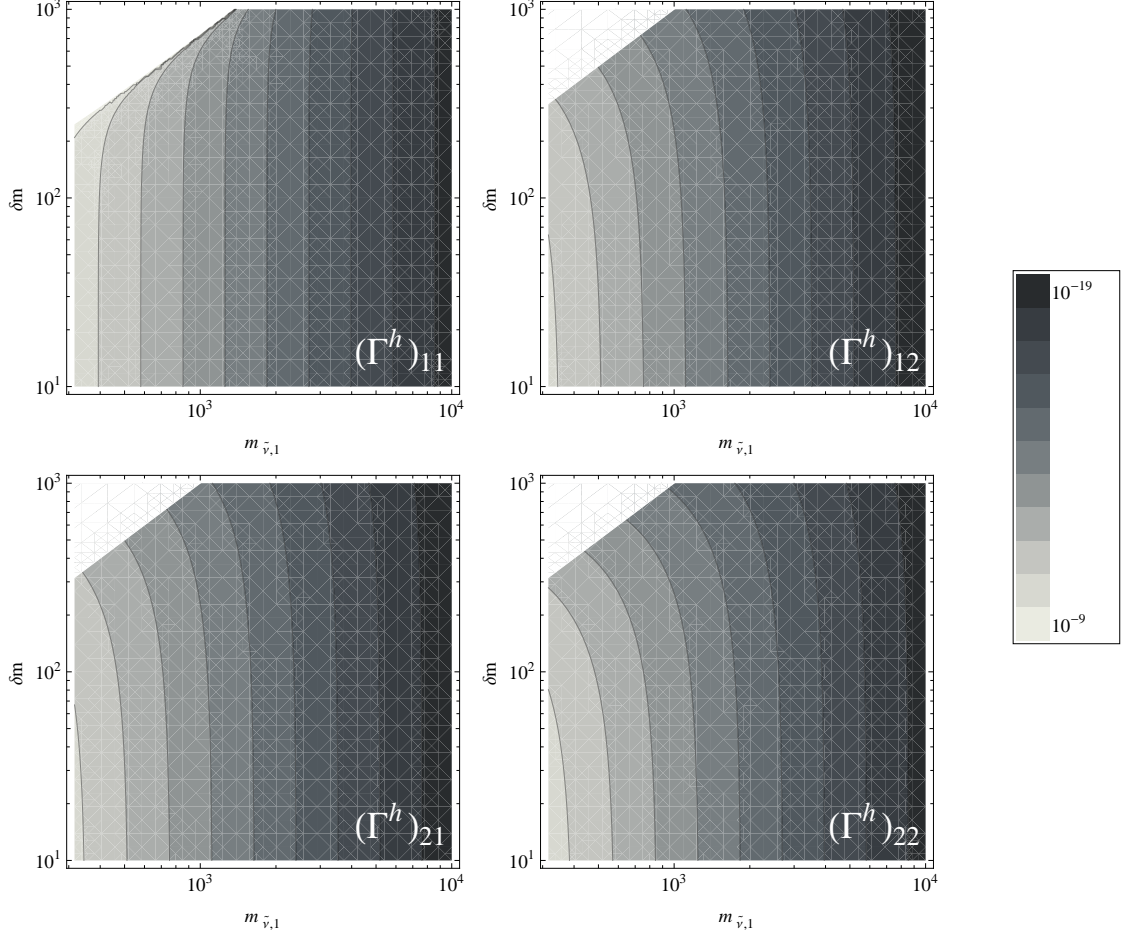


Figure 6.7: Full solutions for the hh annihilation matrix elements as a function of the lightest sneutrino mass $\tilde{\nu}_1$ and the mass difference between the two sneutrino generations δm . Values of $A_{\tilde{\nu}} = 100$ and $m_{\tilde{L}} = 1$ TeV were used throughout the calculation. It can be seen that all box diagrams give rather similar contributions for small mass differences.

Considering the results for ZZ in the same approximation, annihilation into two Z -bosons can only occur through a $\tilde{\nu}_2\tilde{\nu}_2^*$ interaction:

$$\Gamma_{22}^Z|_{\theta_{\tilde{\nu}} \rightarrow 0} = \frac{\pi\alpha^2(\delta m + m_{\tilde{\nu},1})^2}{2\sin^4 2\theta_W m_Z^4} \sqrt{1 - \frac{m_Z^2}{(\delta m + m_{\tilde{\nu},1})^2} \frac{((\delta m + m_{\tilde{\nu},1})^2 - m_Z^2)^2}{(4(\delta m + m_{\tilde{\nu},1})^4 - m_Z^4)}}, \quad (6.47)$$

all other matrix elements, $\Gamma_{11}^Z = \Gamma_{12}^Z = \Gamma_{21}^Z = 0$, disappear. This would suggest that a $\tilde{\nu}_2\tilde{\nu}_2^*$ final state in the ladder is most probable before annihilation into two Z -bosons.

In Fig. 6.7 and Fig. 6.8 we have plotted the full results for the annihilation matrices in a contour plot as a function of the lightest sneutrino mass and the mass difference. For the sneutrino mixing angle we used Eq. (6.7), where we set $m_{\tilde{L}} = 1$ TeV and $A_{\tilde{\nu}} = 100$ GeV. In these graphs we have excluded the region where $\delta m > m_{\tilde{\nu},1}$, because in general we assume that the mass

6.3 Sommerfeld effect for right-handed sneutrino Dark Matter

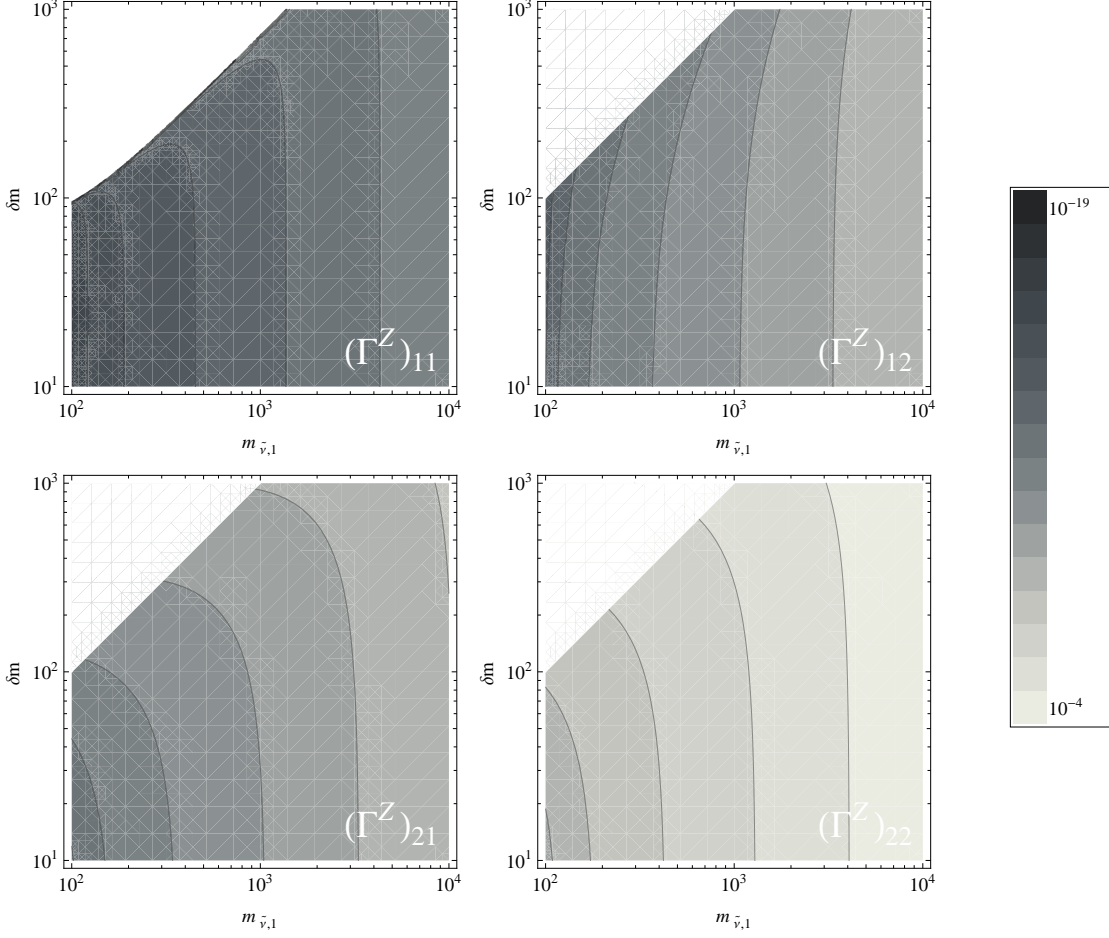


Figure 6.8: Contour plots showing full solutions for the ZZ annihilation matrix elements as a function of the lightest sneutrino mass $\tilde{\nu}_1$ and the mass difference between the two sneutrino generations δm . A mixing angle $\theta_{\tilde{\nu}}$ was used with $m_L = 1$ TeV and $A_{\tilde{\nu}} = 100$. Γ_{22}^Z is dominant since no electroweak symmetry breaking effects are necessary for this process to occur.

difference is smaller than the lightest sneutrino mass.

For annihilation into hh , the results are almost identical to the ones for $\theta_{\tilde{\nu}} = 0$ (graphs not included), which tells us that this approximation is quite reliable. It can be seen from Fig. 6.7 that for small δm all matrix elements are very similar, which we would have expected from the electroweak symmetry approximation. The various matrix elements only start to differ from each other for large δm . Furthermore we see that the closer the lightest sneutrino and the h are in mass, the larger the probability for annihilation into Higgs bosons becomes.

For annihilation into two Z -bosons there is more difference between the various matrix elements. It can clearly be seen that the 22 element gives the largest contribution and the other three elements are suppressed, as expected from the $\theta_{\tilde{\nu}} = 0$ approximation. All matrix elements grow with increasing $m_{\tilde{\nu},1}$, in contrary to the Higgs results. As expected, the element 11 is the most suppressed, and the two mixed elements are of the same order of magnitude.

6.4 Conclusions and discussion

In this chapter we have considered sneutrino DM in the (multi-)TeV range, where the annihilation cross section receives an enhancement due to the Sommerfeld effect. Dealing with scalar DM particles simplified our calculation in the sense that we did not have to deal with spin statistics. As a warming up exercise we showed how to derive the Schrödinger equation from a simple toy model Lagrangian. The results proved useful in the derivation of the annihilation cross section of sneutrinos.

Since there are two sneutrinos mass states which can interact with themselves and each other, it is necessary to solve a matrix Schrödinger equation for the wave-function that includes all possible in- and outgoing states. Similarly, the potential matrix encodes the possible t-channel interactions between the various states. Here we took care to include all possible mediators, which in this case consist of the SM Higgs and a Z-boson, by adding their contributions in the potential matrix. In the ladder diagrams, we found that the most important contributions come from sneutrino changing interactions mediated by a Higgs, and heavy sneutrino scattering mediated by the Z. Since the mass of $\tilde{\nu}_2$ is larger than the kinetic energy of the bound state, the latter interactions only take place with virtual heavy sneutrino states.

To obtain the annihilation cross section, we used the optical theorem to calculate the box diagram contributions. Here we adopted an effective Lagrangian with a general sneutrino field, coupling and mass to simplify the calculation, such that we could obtain the desired results by substituting the relevant sneutrino mass states in the final step. We then calculated the annihilation matrix by adding all possible diagrams with same initial and final states for each matrix element. Annihilation matrix elements that need electroweak symmetry breaking effects showed a suppression with respect to the other elements. In the symmetric approximation, the results for the annihilation into hh showed good agreement with the full solutions. For annihilation into ZZ , the matrix element corresponding to $\tilde{\nu}_2\tilde{\nu}_2^* \rightarrow \tilde{\nu}_2\tilde{\nu}_2^*$ gives the most important contribution.

We have shown here the full analytical treatment; the obvious continuation of this work is to implement the expressions of this chapter into a program and solve them numerically. First, one would need to find a solution for the wave-function elements by solving the system of coupled Schrödinger equations with the given boundary conditions. For instance, it is possible to find public algorithms to tackle these kind of differential equations in Fortran. Once the solutions for the wave-functions have been obtained, they can be combined with the annihilation matrices as described earlier in this chapter, to obtain the Sommerfeld enhanced annihilation cross section for sneutrino DM. If there are resonances in the cross section due to the Sommerfeld effect, including the annihilation part will cause these resonances to have a finite value.

Then, one can use the obtained annihilation cross sections in the Boltzmann equations to calculate the relic abundance of DM. Since this has to agree with the value that is measured today, we can eliminate one free parameter of the sneutrino model in this way. As we will learn in the next chapter, standard calculations of the relic density can give very wrong results when dealing with Sommerfeld enhanced DM. Therefore we advocate to only use the approach as explained in detail in chapter 7 for sneutrino DM. Finally, one could use the enhanced cross sections to obtain the expected flux of SM particles today from DM annihilations. Comparing this to current observational limits, one could place constraints on the remaining free parameters of the sneutrino model.

6.4 *Conclusions and discussion*

In conclusion, heavy TeV right-handed sneutrinos are interesting DM candidates that annihilate through a Sommerfeld enhanced cross section. It would be interesting to see how large the enhancement factor actually is, and to find out whether these heavy sneutrinos are viable DM candidates. For this, however, additional numerical analyses are necessary.

7 Thermal decoupling of Sommerfeld enhanced Dark Matter

In this chapter we will revisit the thermal evolution of WIMPs in the early universe, in particular for models with a velocity dependent enhancement of the annihilation cross section, e.g., the Sommerfeld effect. In these cases, chemical and kinetic decoupling are not separate processes but can have a large influence on each other. We introduce a simple leptophilic model for illustration purposes, and discuss in detail the differences between our approach and the standard thermal decoupling scenario. We perform a full analysis over the parameter space of our model, where we distinguish between the Sommerfeld enhancement being not near a resonance (off resonance), and being exactly on a resonance. For more details see [1], in which the results discussed in this chapter were published.

7.1 Interplay between chemical and kinetic decoupling

The standard calculation of thermal evolution of DM assumes chemical and kinetic decoupling are two processes that can be viewed separately from each other. The reason for this is that they happen on completely different timescales; $T_{cd} \sim m_\chi/25 \ll T_{kd}$. However, in the case that the DM model allows the annihilation cross section to be enlarged by the Sommerfeld enhancement this is no longer true.

As we have seen in Chapter 5, the Sommerfeld enhancement factor depends on the inverse of the DM velocity (or squared inverse for resonances). At the time of chemical decoupling the temperature of the WIMPs is still too high for this enhancement effect to make a difference. However, as the Universe expands, the WIMPs cool down until at some point the enhancement factor becomes non-negligible. This means it would be possible even *after* chemical decoupling for the annihilation cross section to become large enough to restart the depletion of the DM abundance.

Not only could this have a large impact on the final relic density (depending on how large the enhancement factor can become), it can also affect the thermal distribution of the WIMPs after kinetic decoupling. When annihilations take place because of the Sommerfeld effect, the DM particles with the lowest velocity are likely to disappear first, which would cause an increase of the average WIMP temperature. As a result, the velocity dispersion could be quite different for Sommerfeld enhanced models than in the standard scenario, where the asymptotic WIMP temperature is set by kinetic decoupling. As explained in subsection 4.1.2, this temperature can be related to a cutoff in the power spectrum, such that we need to take this affect into account when calculating the size of the first protohalos.

We can make this claim more qualitative by looking at the Boltzmann equation for the relic density as derived in Eq. (3.19). In the standard case where $x_{kd} \gg x_{cd}$, the equilibrium solution

7 Thermal decoupling of Sommerfeld enhanced Dark Matter

for the relic density Y_{eq} is negligible with respect to the relic density around kinetic decoupling, such that righthand factor in Eq. (3.19) can be neglected. By multiplying both sides with $-Y^{-1}$, the solution can be written as

$$Y(x)^{-1} = Y(x_i)^{-1} + \int_{x_i}^x \left(1 - \frac{x g'_{*S}}{3 g_{*S}}\right) \frac{s \langle \sigma v_{\text{rel}} \rangle}{Hx} dx. \quad (7.1)$$

During radiation domination we can replace the Hubble parameter with

$$H_r = \frac{2\pi^{2/3}}{m_{\text{Pl}}} \sqrt{\frac{g_{\text{eff}}}{45}} T^2, \quad (7.2)$$

and furthermore we use Eq. (2.15) for the entropy density. For the annihilation rate we assume a simple power law $\sigma v_{\text{rel}} = \sigma_0 v^{2n}$, such that when using Eq. (3.16) to calculate the thermal average, we arrive at $\langle \sigma v_{\text{rel}} \rangle \simeq \tilde{\sigma}_0 x^{-n}$, where $\tilde{\sigma}_0 \equiv \frac{2\sigma_0}{\sqrt{\pi}} \Gamma(n + \frac{3}{2})$. This allows us to write Eq. (7.1) as

$$Y(x)^{-1} - Y(x_i)^{-1} = \lambda \int_{x_i}^x dx x^{-(n+2)}, \quad (7.3)$$

which can of course easily be solved. Here we introduced

$$\lambda \equiv \frac{g_{*S}}{\sqrt{g_{\text{eff}}}} \left(1 - \frac{x g'_{*S}}{3 g_{*S}}\right) \sqrt{\frac{\pi}{45}} m_{\text{Pl}} m_\chi \tilde{\sigma}_0, \quad (7.4)$$

which is assumed to be a constant¹.

To be precise, we have to include the effect of kinetic decoupling on the velocity of the WIMPs. As discussed in section 3.4, the WIMP temperature before and after kinetic decoupling can roughly be approximated by

$$T_\chi = \begin{cases} T, & \text{for } T > T_{\text{kd}} \\ T^2/T_{\text{kd}}, & \text{for } T \leq T_{\text{kd}} \end{cases}, \quad (7.5)$$

where T is the temperature of the heat bath. The velocity and temperature of the WIMPs are related by $v \simeq p/m_\chi \propto \sqrt{T_\chi/m_\chi}$, such that we can estimate the velocity before and after kinetic decoupling as $v \propto x^{-1/2}$ and $v \propto x^{-1}$, respectively. In this way we can express the effect of kinetic decoupling on the annihilation rate as $\langle \sigma v_{\text{rel}} \rangle \propto x^{-\tilde{n}}$, where

$$\tilde{n} = \begin{cases} n & \text{for } x \lesssim x_{\text{kd}} \\ 2n & \text{for } x \gtrsim x_{\text{kd}} \end{cases}. \quad (7.6)$$

¹The effective degrees of freedom g_{eff} and entropy degrees of freedom g_{*S} depend on the number of relativistic particle species in the Universe, which means that in principle they are functions of the temperature. It is safe here, however, to assume they are constant, since chemical decoupling happens long before the QCD phase transition at ~ 170 MeV [247]

7.1 Interplay between chemical and kinetic decoupling

We thus replace $n \rightarrow \tilde{n}$ in Eq. (7.3) such that we get

$$Y(x)^{-1} - Y(x_i)^{-1} \simeq \lambda \begin{cases} \frac{1}{1+\tilde{n}} \left(\frac{1}{x_i^{1+\tilde{n}}} - \frac{1}{x^{1+\tilde{n}}} \right) & \text{for } \tilde{n} \neq -1 \\ \ln(x/x_i) & \text{for } \tilde{n} = -1 \end{cases}. \quad (7.7)$$

This approximation tells us that for $x > x_i$, the relic density can only change by a large amount in the case that $\tilde{n} \leq -1$. In the standard WIMP scenario with s-wave annihilation one has $n = \tilde{n} = 0$, such that there is no possibility for the relic abundance to change significantly after freeze out. Annihilation with higher partial waves, like p -waves with $n = 1$, are even more suppressed. This is in agreement with the standard calculation of the relic density where one assumes $Y' = 0$ after chemical decoupling (see section 3.4 for more details).

However, in the case that we are dealing with Sommerfeld enhanced DM, the situation is entirely different. Assuming s-wave annihilation with an enhancement factor $S \propto v^{-1}$, the annihilation rate scales with $n = -1/2$, which implies $\tilde{n} = -1$ after kinetic decoupling. From this it follows that there may exist a new era of annihilations that decreases the relic density after the usual freeze-out [248]. In the case that the Sommerfeld enhancement is resonant, we would even have $\langle \sigma v_{\text{rel}} \rangle \propto v^{-2}$, such that the decrease in Y after kinetic decoupling would even be larger with $\tilde{n} = -2$. This would also imply that the annihilation rate is important already before kinetic decoupling when $\tilde{n} = -1$.

Now that we have sketched the intertwined nature of chemical and kinetic decoupling for Sommerfeld enhanced DM models, the question is how to correctly take it into account when calculating the thermal evolution. It was realized that the Boltzmann equations (3.19) and (3.24) that we derived earlier are actually coupled as follows [1]

$$\frac{Y'}{Y} = -\frac{1 - \frac{x}{3} \frac{g'_* S}{g_* S}}{Hx} sY \langle \sigma v_{\text{rel}} \rangle \Big|_{x=m_\chi^2/(s^{2/3}y)} \left(1 - \frac{Y_{\text{eq}}^2}{Y^2} \right) \quad (7.8)$$

$$\frac{y'}{y} = -\frac{1 - \frac{x}{3} \frac{g'_* S}{g_* S}}{Hx} \left[2m_\chi c(T) \left(1 - \frac{y_{\text{eq}}}{y} \right) - sY \left(\langle \sigma v_{\text{rel}} \rangle - \langle \sigma v_{\text{rel}} \rangle_2 \right) \Big|_{x=m_\chi^2/(s^{2/3}y)} \right]. \quad (7.9)$$

The WIMP temperature y is fed back into the equation for Y in the thermal averaged annihilation rate, whereas y now also depends on changes in Y that occur *after* kinetic decoupling. These expressions clearly show that the two equations *in general* cannot be considered separately.

In the limit that $x \gg x_{\text{kd}}$, the scattering term in Eq. (7.9) proportional to $c(T)$ can be neglected, which enables us to derive an simpler expression that gives us some insight about its asymptotic behavior. The second moment of the annihilation rate was defined in Eq. (3.26). Assuming again $\sigma v_{\text{rel}} \propto v^{2n}$, it simplifies to

$$\frac{\langle \sigma v_{\text{rel}} \rangle_2}{\langle \sigma v_{\text{rel}} \rangle} = 1 + \frac{n}{3}. \quad (7.10)$$

With these ingredients, we find that

$$\frac{y'}{y} \simeq \frac{n Y'}{3 Y} = \frac{\tilde{n} Y'}{6 Y}. \quad (7.11)$$

From this we see that a change in relic density clearly causes a change in WIMP temperature. For $n < 0$, a decrease in Y will thus result in an increase in y after kinetic decoupling. This is exactly what we expected; when the DM phase-space density is depleted of low velocity particles, the average velocity of the WIMPs increases.

We note that for the thermal averages that appear in Eqs. (7.8) – (7.9), we derived simple approximations as given in Eq. (3.16) and Eq. (3.26). Here, however, it was assumed that the velocity distribution of the WIMPs is proportional to a Maxwellian velocity distribution, i.e.,

$$f(v) \propto f_{\text{Max}}(v) = \sqrt{\frac{2}{\pi}} \left(\frac{m_\chi}{T_\chi} \right)^{3/2} v^2 e^{-\frac{1}{2} m_\chi v^2 / T_\chi}. \quad (7.12)$$

If this would not be the case, Eqs. (3.16) and (3.26) would have to be adjusted accordingly and would become considerably more difficult to solve; for arbitrary $f(v)$, assumptions would have to be made about the velocity distribution in order to solve the integrals. As long as the WIMPs are still coupled to the heat bath one can assume that $f(E) \propto f_{\text{eq}}(E) = e^{-E/T}$, ensuring a correct usage of Eq. (7.8) and Eq. (7.9) at least until T_{kd} . Since the interesting effects of the coupled equations are expected to happen after kinetic decoupling, one needs to make sure that the velocity distribution is Maxwellian even in this range. It is therefore very important to check for each model separately if this condition is satisfied when using Eqs. (7.8) – (7.9) in combination with Eqs. (3.16) and (3.26).

The presence of a new era of annihilations can greatly affect the relic density, and therefore we are interested in the mechanisms that cause the DM annihilations to finally come to an end. The temperature at which this happens will determine the final relic density. The first and most important effect is that the Sommerfeld enhancement does not continue to grow as $v \rightarrow 0$, but saturates below some cutoff velocity (see section 5.3). From that moment on, DM annihilations will no longer be able to keep up with the expansion of the universe.

Another relevant effect is the onset of matter domination, which we can see directly by using

$$H^2(T) = \frac{4\pi^3}{45m_{\text{Pl}}^2} g_{\text{eff}} T^4 + \frac{8\pi}{3m_{\text{Pl}}^2} \rho_{\text{m},0} a^{-3}(T) \quad (7.13)$$

$$\equiv H_{\text{r}}^2(x) + H_{\text{m}}^2(x) \quad (7.14)$$

in combination with Eq. (7.1). Here, $\rho_{\text{m},0} = \Omega_{\text{m}} \rho_{\text{c}} \approx 1.10 \times 10^{-47} \text{GeV}^4$ is the matter density today [37]. Since $H_{\text{r}}(x) \propto x^{-2} g_{\text{eff}}^{1/2}$ and $H_{\text{m}}(x) \propto x^{-3/2} g_{\text{S}}^{1/2}$, the difference between the two epochs is given by a factor $x^{1/2}$ (ignoring the dependence of the d. o. f.). This can be taken into account into the evolution of the DM density by replacing \tilde{n} in $\langle \sigma v_{\text{rel}} \rangle \propto x^{-\tilde{n}}$ by $n' = \tilde{n} + 1/2$. Now an appreciable change in Y is only possible for $n' \leq -1$, which can no longer be achieved with a $1/v$ enhancement after kinetic decoupling ($n' = -1/2$). Only in the special case that we are on a resonance, we would have $n' = -3/2$ after kinetic decoupling has taken place, and annihilations could continue even beyond matter-radiation equality.

Finally, the onset of structure formation around $z_{\text{struc}} \sim \mathcal{O}(100)$ will cause all DM annihilations to come to an end. As significant gravitational potentials are formed, the DM will move towards the potential wells and fall into them. During this process, their velocities increase such that any Sommerfeld enhancement will be diminished, even on a resonance.

Not only the relic density can be significantly altered by the effect of kinetic decoupling; the new era of annihilations, in turn, will increase the WIMP temperature. This correspondingly affects the DM velocity distribution at the onset of structure formation, which is translated to a small-scale cutoff M_{cut} in the power spectrum of matter density fluctuations. As we saw in section 4.1, this corresponds to the mass of the smallest gravitationally bound objects [100].

Since y can now still increase after kinetic decoupling, it is no longer correct to use this quantity to calculate the cutoff mass. Instead, we define the *asymptotic* decoupling temperature

$$x_{\text{dec}}^{\infty} = \frac{m_{\chi}}{T_{\text{dec}}^{\infty}} \equiv y|_{x \rightarrow \infty} \times \frac{s^{2/3}}{T^2} \Bigg|_{T=T_{\text{dec}}^{\infty}}, \quad (7.15)$$

as the intersection of $y(T_{\chi} = T)$ (i.e. the heat bath temperature) with the asymptotic value of y when de DM annihilations and scatterings finally have ceased. In this way, we can simply express the asymptotic DM temperature or velocity dispersion as $T_{\chi} = T^2/T_{\text{dec}}^{\infty}$, which allows us to replace $T_{\text{kd}} \rightarrow T_{\text{dec}}^{\infty}$ in any expression that relates the kinetic decoupling temperature to the cutoff in the power spectrum of matter density fluctuations (see subsection 4.1.2). This holds in particular for the expressions of the free streaming mass Eq. (4.23) and the acoustic oscillation mass Eq. (4.24), of which the largest of both determines the final cutoff mass M_{cut} . The temperature as defined in Eq. (7.15) does not have any intuitive interpretation, and can actually be quite larger than the temperature at which the annihilations stop. An upper bound on the asymptotic decoupling temperature is simply given by $T_{\text{dec}}^{\infty} = T_{\text{kd}}$, which is the result when there is no second era of annihilation.

7.2 Leptophilic Dark Matter

To demonstrate the treatment that was introduced in the previous section, we will look at a simple class of leptophilic dark matter models like described in Chapter 5. Although these models have been originally motivated by the observed positron excess as explained in section 5.1, here we use them mostly for the purpose of illustration.

The toy model that we consider consists of a fermionic DM particle χ that only interacts with a light scalar ϕ_s and a pseudo-scalar ϕ_p via

$$\mathcal{L} \supset g_{\chi}^s \phi_s \bar{\chi} \chi + g_{\chi}^p \phi_p \bar{\chi} \gamma^5 \chi, \quad (7.16)$$

The (pseudo-)scalar particles in turn couple to standard model leptons, through

$$\mathcal{L} \supset g_{\ell}^s \phi_s \bar{\ell} \ell + g_{\ell}^p \phi_p \bar{\ell} \gamma^5 \ell, \quad (7.17)$$

where the coupling strengths g_{ℓ}^s and g_{ℓ}^p can be thought of as effective couplings arising, e.g., from higher-dimension operators. An example of this kind of model can be found in [49], where the new postulated particles (χ, ϕ_s, ϕ_p) are embedded in a full supersymmetric scenario. Here we will assume for simplicity that the couplings to all lepton generations are equal, i.e., $g_e^{s,p} = g_{\mu}^{s,p} = g_{\tau}^{s,p}$. Couplings to quarks are not taken into account here, since typically they do not change the phenomenology of our model for the mass ranges considered here. Below we

will discuss a few important aspects of the leptophilic model.

7.2.1 Annihilation and the Sommerfeld enhancement

We assume the DM mass lies in the 100 GeV to 5 TeV range, such that annihilation cross section is enhanced by the Sommerfeld effect mediated by the scalar particle. We include a pseudo-scalar particle nevertheless, since parity conservation causes the annihilation $\chi\chi \rightarrow \phi_s\phi_s(\phi_p\phi_p)$ to be a p -wave process which vanishes in the non-relativistic $v \rightarrow 0$ limit. Even with the Sommerfeld factor included, the annihilation rate for this process would disappear in the low velocity limit², and it would not be possible to study the expected effect as explained in 7.1. This problem is solved by including pseudo-scalar particles, since the process $\chi\chi \rightarrow \phi_s\phi_p$ does have an s -wave contribution. This also makes sure that the cosmic ray lepton flux today is sizable and observable by current (or future) indirect detection experiments.

The relic density therefore is to a large extent determined through this channel and thus mainly depends on the parameter

$$\alpha \equiv \frac{g_\chi^s g_\chi^p}{4\pi}. \quad (7.18)$$

To keep the discussion simple, we will assume $g_\chi^s = g_\chi^p$ in the following, noting that the relic density is essentially only set by *one* effective coupling constant anyway. Annihilation directly into SM particles through the s -channel could occur, but is strongly suppressed by the coupling $(g_\ell^{s,p})^2$ and therefore does not play a role.

The Sommerfeld enhancement is easily calculated for this type of models, and corresponds exactly to the case discussed in Section 5.3. The Schrödinger equation contains a Yukawa potential that depends on the mass of the scalar mediator m_s . This is solved numerically to obtain the Sommerfeld factor in terms of the velocity of the WIMPs v , the coupling α and the masses of both χ and ϕ_s .

7.2.2 Dark Matter scattering off heat bath particles

The DM scattering at low-momentum transfer, i.e., $t \rightarrow 0$, is important for the kinetic decoupling process. For scattering off leptons, only the scalar particle mediates DM scattering at $t = 0$, with the matrix element squared given by

$$|\mathcal{M}^s|_{t \rightarrow 0}^2 = \frac{16g_\ell^{s2} g_\chi^{s2} m_\chi^2 m_\ell^2}{m_s^4}. \quad (7.19)$$

Including nonzero neutrino couplings in our model would thus not have a large impact on the results, since the DM scattering cross section would be negligible due to the scaling with the neutrino mass. The matrix element for scattering off leptons mediated by a pseudo-scalar is proportional to t and thus disappears in the low-momentum transfer limit.

²In the special case of a resonant Sommerfeld effect ($S \propto v^{-2}$) the p -wave annihilation rate would actually become constant for $v \rightarrow 0$. However, this would still not allow us to study the thermal evolution of DM with enhanced annihilation rates for small velocities.

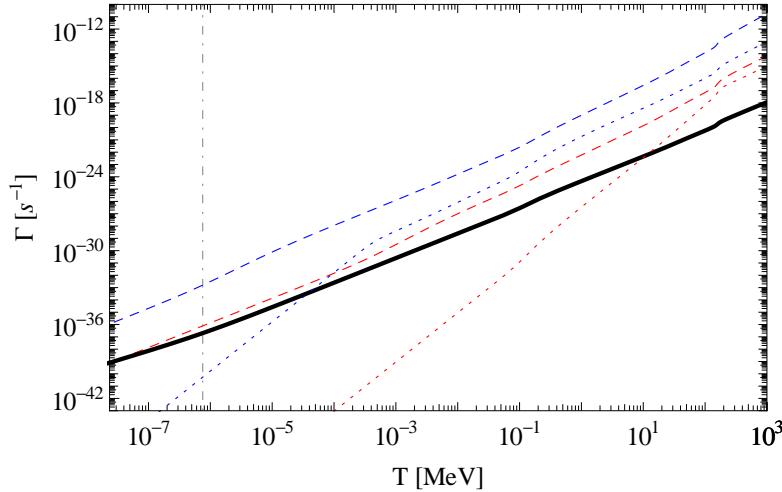


Figure 7.1: The Hubble rate (black) is shown in comparison to the effective DM self-scattering rate from Eq. (7.20) as a function of temperature. The minimal (red) and maximal (blue) possible self-scattering rates for the leptophilic model are plotted for the on- and off-resonant case as dashed and dotted lines, respectively. Once the self-scattering rate becomes comparable to the Hubble rate, i.e. $\Gamma_s(T_{\text{nt}}) \sim H(T_{\text{nt}})$ the DM velocity distribution starts to deviate from a Maxwellian form. For resonant Sommerfeld enhancements this occurs even after matter-radiation domination, which is indicated by a dash-dotted line [1].

Actually, we will see that scattering off the light (pseudo-)scalar mediators can be much more effective in the range where n_ϕ is not yet Boltzmann suppressed. The scattering cross section for $\chi\phi_s \rightarrow \chi\phi_p$ is present, but in general suppressed with respect to the contributions from pure (pseudo-)scalar scattering. In the work here we only have included scattering of scalar mediators for simplicity; we will come back to this point later in the discussion. The relevant matrix elements for all processes can be found in Appendix C of [1].

A requirement for these scatterings off light bosons to keep the DM in kinetic equilibrium is that they are in thermal equilibrium with the heat bath. It turns out that annihilation rates for the mediators are not sufficient enough to ensure a thermal equilibrium state. In fact, taking only $2 \leftrightarrow 2$ processes into account, the mediators would never have been in thermal equilibrium. Fortunately, the mediators are quite unstable – unlike the DM – such that the decay process $\phi \leftrightarrow \bar{l}l$ occurs frequently enough in both directions to keep them thermal (for more details, see also Appendix C of [1]).

7.2.3 Dark Matter self-scattering

An important requirement for our treatment described in section 7.1 is a Maxwellian shaped velocity distribution of the DM until long after kinetic decoupling. Since our model features the Sommerfeld effect, we expect the self-scattering cross section to be enhanced in a similar fashion as the annihilation cross section (see also section 5.4). These self-scatterings can happen so frequently that they are able to keep the WIMP velocity distribution Maxwellian even after they have kinetically decoupled from the heat bath [249, 10, 230].

7 Thermal decoupling of Sommerfeld enhanced Dark Matter

In order to check this statement, we have calculated the self-scattering rate by which the velocities change by $\mathcal{O}(1)$ [230, 249]

$$\begin{aligned}\Gamma_s &= n_\chi \langle \sigma_T v_{\text{rel}} \frac{v_{\text{rel}}^2}{v_0^2} \rangle, \\ &= \frac{g_\chi^2}{n_\chi} \int \frac{d^3 p}{2\pi^3} \frac{d^3 \tilde{p}}{2\pi^3} \sigma_T v_{\text{rel}} \frac{v_{\text{rel}}^2}{v_0^2} f(E) f(\tilde{E}), \\ &\simeq \frac{16n_\chi}{\sqrt{\pi}} \left(\frac{m_\chi}{T_\chi} \right)^{5/2} \int_0^1 \sigma_T \frac{v^5}{(1+v^2)^3} e^{-v^2 \frac{m_\chi}{T_\chi}} dv,\end{aligned}\tag{7.20}$$

where in the last step $f \propto e^{-E/T_\chi}$ was used, and the most probable velocity is given by $v_0 = \sqrt{2T_\chi/m_\chi}$. We follow here a conservative approach for the numerical calculation of the transfer cross section σ_T (described in more detail in 5.4), as to not overestimate the scattering rate. To derive the temperature T_{nt} at which the DM velocity distribution becomes non-thermal, we compare the scattering rate Γ_s to the Hubble expansion rate

$$\Gamma_s(T_{\text{nt}}) \equiv H(T_{\text{nt}}).\tag{7.21}$$

In Fig. 7.1 the evolution of $\Gamma_s(T)$ and $H(T)$ for two sets of parameters of the leptophilic model that represent the most extreme cases is shown, in the case of a resonant and non-resonant Sommerfeld enhancement. On resonance, the self-scattering rate is always able to keep the DM velocity distribution thermal beyond matter-radiation equality at $T_{\text{eq}} \approx 0.75 \text{ eV}$ [19]. If the Sommerfeld effect is not resonant, Γ_s will drop below H for much larger temperatures, i.e., $\mathcal{O}(10) \text{ MeV} \lesssim T_{\text{nt}} \lesssim \mathcal{O}(100) \text{ eV}$. We find that $T_{\text{nt}} < T_{\text{kd}}$ is satisfied in all cases relevant to our discussion of the leptophilic toy model such that we can safely assume a Maxwellian WIMP velocity distribution.

7.2.4 Model constraints

The most obvious constraint comes from the observed DM relic density (see Eq. (2.28)), which we can use to constrain one free model parameter. The relic density is obtained from the value of Y today (see Eq. (3.20)), and we demand that the leptophilic model reproduces the observed value within 3σ . In the case discussed here, we assume the DM is not its own antiparticle, such that we have $\Omega_\chi = \Omega_{\text{DM}}/2$. In the numerical calculations, the coupling α that sets the annihilation rate from Eq. (7.18) is adjusted accordingly to yield a relic density that is acceptable according to our definition.

Apart from this constraint, there are various indirect and direct experimental limits on new light bosons that couple to leptons. The strongest indirect constraint comes from measurements of the anomalous magnetic moment of the muon, $a_\mu \equiv (g_\mu - 2)/2$, which would receive extra loop-contributions due to new particles coupling to muons. The currently experimentally measured value of a_μ deviates 3.6 times the estimated 1σ error from the theoretically expected value [37]. If we demand that the existence of these new (pseudo-)scalars do not worsen this discrepancy beyond the 5σ level, we obtain a limit on the coupling to muons of roughly $g_\ell^{s,p} \lesssim 10^{-3}$,

which weakens if we consider degenerate (pseudo)scalar masses and couplings.

Direct constraints are derived from e.g. beam dump experiments, where one looks for new light bosons in the decay products behind the stopped electron beam. Unfortunately there are not many beam dump experiments that probe scalar particles in the mass range we are interested in ($m_\phi = 100 \text{ MeV} - 5 \text{ GeV}$). The only constraint comes from E137 at Fermilab, which excludes couplings to electrons in the small range $g_\ell^\phi \sim 10^{-7} - 10^{-6}$ for $100 \text{ MeV} \lesssim m_\phi \lesssim 400 \text{ MeV}$ [250]. Another constraint for $m_\phi > 2m_\mu \approx 210 \text{ MeV}$ arises from the BaBar search for Υ decays into light (pseudo)scalar particles, which roughly constrains the coupling to be $g_\ell^\phi \lesssim 10^{-3}$.

Here, our toy model is mostly motivated by pedagogical reasons and less by the cosmic ray excess. However, if one were to take this connection serious, additional strong constraints would arise due to the requirement to fit the cosmic ray lepton data. The large annihilation rates that would be needed are potentially in conflict with various astrophysical observations. For more details see Appendix B in [1] and references therein.

7.2.5 Thermal evolution on and off resonance

In order to show the difference of the thermal evolution of this leptophilic model with respect to the standard scenario, we show here two special cases that are of particular interest. We have chosen two parameter sets; one for which we have a more general enhancement, i.e., not near a resonance (also denoted as *off* resonance), and one on resonance. It will be useful here (and in the following subsections) to explain what we exactly mean by that. As mentioned in 5.3, the Sommerfeld enhancement effectively only depends on two parameters such that the resonances occur at fixed values of $\varepsilon_\phi = m_\phi / (\alpha m_\chi)$. To be *exactly* on a resonance, however, requires a great deal of fine-tuning: in practice, we only sampled the first 5 resonances, because higher resonances are more and more densely distributed. In order to include them consistently, we only considered values of ε_ϕ very close to these resonances for which we obtained a maximal enhancement factor $S_{\text{max}} = 10^{11}, 10^{12}, 10^{13}, 10^{14}$ in the limit that $\varepsilon_\nu \rightarrow 0$. The bulk of Sommerfeld factors in the $(\varepsilon_\phi, \varepsilon_\nu)$ parameter space qualify as off resonance: by randomly sampling the ε_ϕ range, chances are extremely low to hit a resonance exactly. Ideally, in the low velocity regime these would all follow a $S \propto v^{-n}$ behavior with $n = 1$, however, we see that in many cases $n > 1$ in regions where the Coulomb approximation is no longer valid (see for example the small ‘bump’ in the full solution for $v \lesssim 2 \times 10^{-3}$ in Fig. 7.2).

In this section, we additionally consider two different approximations to the full numerical solution for the Sommerfeld factor, as illustrated in Fig. 7.2. Approximation 1 (shown as a dotted line) assumes $S = 1$, i.e., no enhancement, for $v > \pi\alpha$. For the intermediate regime we adopt a simple v^{-1} behavior given by $S = \pi\alpha/v$, and finally we let the enhancement saturate at the same magnitude as the full solution, $S(v \leq v_{\text{max}}) \equiv S_{\text{max}}$. Approximation 2 (shown as a dashed line) is slightly better, especially at larger velocities, where the analytical expression for a Coulomb enhancement (Eq. (5.59)) is used down to v_{max} , and $S = S_{\text{max}}$ for smaller velocities. For the case of resonances, we adjusted these approximations correspondingly: in approximation 1 we used $S \propto v^{-2}$ instead of $S \propto v^{-1}$, and in approximation 2 we used the Coulomb expression down to velocities where the enhancement follows the v^{-2} behavior.

We will refer to the *full* solution obtained by solving the coupled set of Eqs. (7.8, 7.9). Furthermore we will consider an approximation to the full solution that is denoted with *sudden*

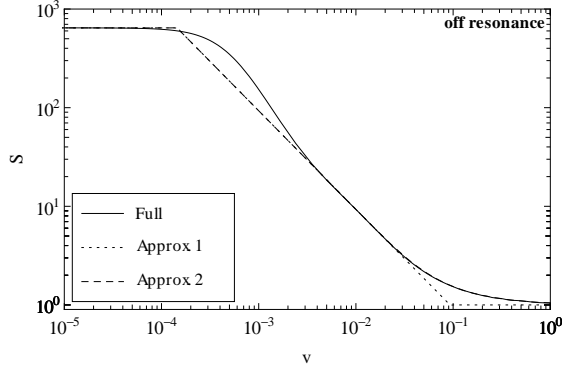


Figure 7.2: The full numerical solution for the Sommerfeld factor (solid) and two analytic approximations (dotted, dashed) are shown for $m_\chi = 1$ TeV, $m_\phi = 5$ GeV and $\alpha = 0.03$ [1].

decoupling, where we assume that the WIMP temperature is given by Eq. (7.5), and substitute it into the thermally averaged annihilation rate in the standard Boltzmann equation (Eq. (3.19)). For kinetic decoupling we consider Eq. (3.24) and neglect the term proportional to Y' in as is usually done. By the *uncoupled* solution we refer to the case where kinetic decoupling is assumed to have no influence on the evolution of the WIMP number density and vice versa, i.e., the standard calculation.

In Fig. 7.3, the solutions for y and Y are shown for one particular parameter set for which the Sommerfeld enhancement is not in the neighborhood of a resonance. The different approximations start to differ from one another after kinetic decoupling, which for this set of parameters happens at $x_{\text{kd}} \sim 2.92 \times 10^3$. The relic density for the coupled solution is, as expected, lower than the uncoupled solution: the difference amounts to $\sim 10\%$. For comparison we also show the uncoupled solution without Sommerfeld enhancement, which is much larger than all other solutions (at most a factor ~ 1.8 than the coupled solution). Sudden decoupling works very well as an approximation to Y ; the lines are completely obscured by the full solution in the left-hand plot in Fig. 7.3. Also visible is that approximation 2 reproduces the full numerical result much better than approximation 1, for which the relic density is overestimated. The annihilations cease around $x \sim 3 \times 10^5$ because of the saturation of the Sommerfeld factor, and both y and Y stay constant afterwards. We find that sudden decoupling, shown in red in the right-hand plot of Fig. 7.3, is a reasonable approximation to the full evolution of y^3 .

The results for a resonant Sommerfeld enhancement, shown in Fig. 7.4 for a particular set of parameters where $S = 10^{14}$, are even more interesting. It is clearly visible that there is a striking difference with respect to the uncoupled Boltzmann equations for $x \gtrsim 10^7$. From that moment on, a new era of annihilations begins that decreases the relic density by a factor of ~ 400 . Interestingly, the annihilations continue even after matter-radiation equality $T \approx 0.75$ eV (indicated by the dash-dotted vertical line) and finally cease around $x \simeq 2 \times 10^{13}$, when the Sommerfeld en-

³We have found a more delayed decoupling process than for standard WIMPs in cases where the lepton couplings are very small and ϕ -scattering is negligible. To keep the DM in thermal equilibrium thus many scattering events are necessary, and as a result the decoupling occurs more gradually. The validity of the sudden decoupling approximation in this case will be worse than the example shown in Fig. 7.3.

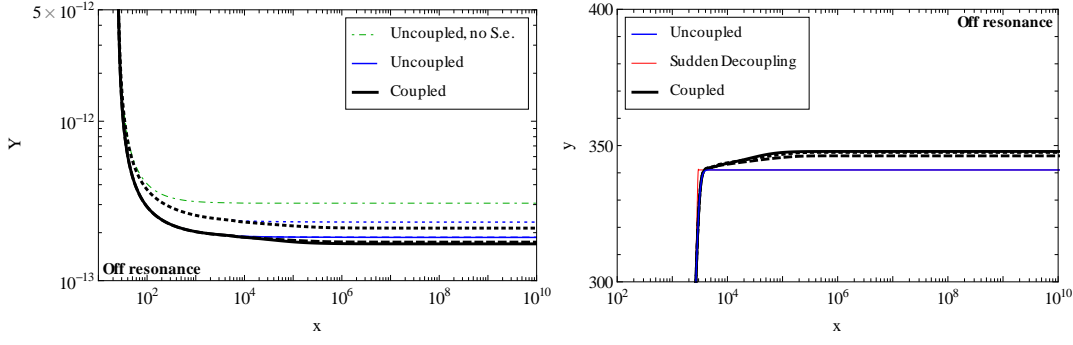


Figure 7.3: For a parameter set where the Sommerfeld enhancement is not near a resonance ($m_\chi = 1$ TeV, $m_\phi = 5$ GeV, $\alpha = 0.03$, and $g_\ell = 10^{-7}$), we show the evolution of the relic density Y (as defined in Eq. (3.17)), and the WIMP temperature y (as defined in Eq. (3.23)). The solution to the full set of coupled Boltzmann equations (black) is shown in comparison to the solution to the standard, uncoupled equations (blue). As a further approximation we show results for assuming sudden kinetic decoupling (red; not visible in left-hand plot). Different approximations to the Sommerfeld enhancement are shown according to Fig. 7.2 by dotted, dashed, or solid lines. Additionally, the solution without Sommerfeld enhancement is shown in the left-hand panel (green, dash-dotted) [1].

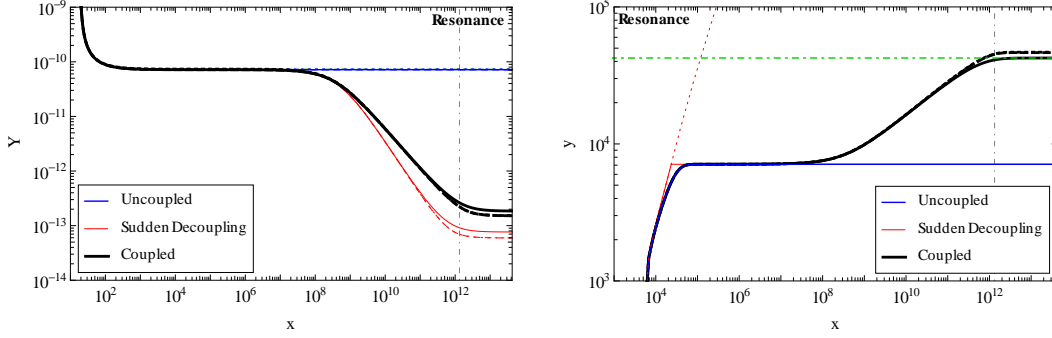


Figure 7.4: We show the same results as in Fig. 7.3, but now for a parameter set where the Sommerfeld enhancement is resonant ($m_\chi = 1$ TeV, $m_\phi = 1$ GeV, $\alpha = 0.00168$ and $g_\ell = 4.6 \times 10^{-5}$). The full solutions show a significant difference with the standard calculation for $x \geq 10^7$; after kinetic decoupling a new era of annihilations takes place and simultaneously the WIMP temperature increases again. Annihilations even continue until after matter-radiation equality (denoted as a gray, dash-dotted line). In the right-hand panel, the intersection of the asymptotic WIMP temperature (green, dash-dotted) with the temperature of the heat bath (red, dotted) denotes T_{dec}^∞ as defined in Eq. (7.15) [1].

hancement saturates. As discussed in the beginning of this chapter, we would also have expected a more efficient decrease in the relic density before and directly after kinetic decoupling (which for this choice of parameters happens at $x_{\text{kd}} \simeq 2.35 \times 10^4$). This is not observed, however, because at early times the velocities of the WIMPs are still large enough to be in the Coulomb regime and, even though we are on a resonance, the Sommerfeld enhancement follows a $S \propto 1/v$ rather than $S \propto 1/v^2$ behavior (see also 5.3).

On the right-hand side of Fig. 7.4, it is visible that sudden decoupling is a very bad approximation to y , at least for $x \gtrsim 10^7$. From this time on, y increases with respect to the sudden decoupling solution (obscured by uncoupled solution in this range), because the restarted anni-

hilitations deplete the WIMP distribution from particles with the lowest velocity. Surprisingly, sudden decoupling does catch the overall behavior of a large decrease in Y rather well, although it underestimates the final relic density by at least a factor of 2. However, the different approximations to the Sommerfeld enhancement give comparable results both for y and Y .

In the right-hand plot of Fig. 7.4 we show also an extrapolation of the asymptotic value of y to smaller values of x as a green, dash-dotted line. Its intersection point with the heat bath temperature – shown as a red, dotted line – gives the asymptotic decoupling temperature T_{dec}^{∞} as defined in Eq. (7.15). One should use this temperature instead of the kinetic decoupling temperature T_{kd} as an input to calculate the minimal mass of the first subhalos, since the WIMP velocity distribution only reaches its asymptotic value at $x_{\text{dec}}^{\infty} \gtrsim x_{\text{kd}}$.

7.2.6 Off resonance analysis

Here we discuss a more general analysis for the full possible range of our off resonance model parameters. This is interesting for two reasons: it more or less represents the generic behavior of the model and the parameter dependence is quite straightforward to discuss. We specified a grid in parameter space and solved the coupled equations with Mathematica for each point in the grid. We considered four values for the masses each: $m_{\chi} = 0.1, 0.5, 1, 5$ TeV, and $m_{\phi} = 0.1, 0.5, 1, 5$ GeV, whereas for the lepton coupling we scanned the range $10^{-7} \leq g_{\ell} \leq 10^{-1}$. From all solutions we rejected the ones which did not give a final relic density within our specified boundaries, i.e., $0.184 \leq \Omega_{\text{DM}} \leq 0.274$. This resulted in a coupling range $0.00335 \leq \alpha \leq 0.0985$ for which correct relic densities were obtained.

Looking at the kinetic decoupling temperature in Fig. 7.5, we see that T_{kd} decreases for larger g_{ℓ} , which is due to the fact that a strong lepton coupling will keep the WIMPs longer in local thermal equilibrium. If the decoupling happens rather late, $T_{\text{kd}} \lesssim 7$ MeV, only DM scattering with electrons is effective just before the DM particles completely leave thermal equilibrium. At higher temperatures also muons start to contribute very efficiently to the scattering process, resulting in a flattening of $T_{\text{kd}}(g_{\ell})$ for smaller values of g_{ℓ} . Since the scattering rate in Eq. (7.19) depends on m_{ℓ}^2 , even highly non-relativistic muons give a contribution because of their relatively large mass. At even higher decoupling temperatures scattering with mediator particles is dominant. It ensures that the kinetic decoupling temperature does not increase arbitrarily high even for negligible lepton couplings, which explains the plateau that appears at roughly $g_{\ell} \lesssim 10^{-5}$.

We have seen in Eq. (7.19) that the lepton scattering cross section decreases strongly with increasing m_{ϕ} , which is nicely reflected in Fig. 7.5 by the increasing decoupling temperature for higher mediator masses. In the range where mediator scattering is dominant, the same dependence on mediator mass is visible, which is explained by the Boltzmann suppression of the mediator number density, $n_{\phi}/s \sim (m_{\phi}/T)^{3/2} \exp(-m_{\phi}/T)$. The dependence of the decoupling temperature on the DM mass m_{χ} , on the other hand, is very weak. Also the spread in T_{kd} (for given values of m_{ϕ}, m_{χ} , and g_{ℓ}) due to the different values of the relic density that were obtained by changing the coupling α accordingly, is essentially negligible.

From the discussion in section 7.2.5 we expect the coupled solution to result in a slightly smaller relic density than the full solution, but not more than $\sim 10\%$. The ratio of the uncoupled solution with respect to the coupled is plotted in Fig. 7.6 as a function of x_{kd} . We note that the observed decrease in relic density due to the coupled Boltzmann equations is smaller than

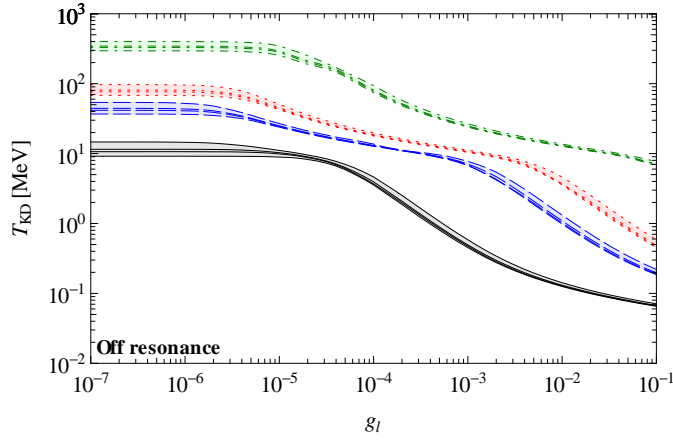


Figure 7.5: For models where the Sommerfeld enhancement is not on a resonance, the kinetic decoupling temperature is shown as a function of the mediator particle coupling to leptons, for $m_\phi = 100$ MeV (black, full), 500 MeV (blue, dashed), 1 GeV (red, dotted), and 5 GeV (green, dash-dotted). From bottom to top, the lines correspond in each case to a DM mass of $m_\chi = 100, 500, 1000, 5000$ GeV [1].

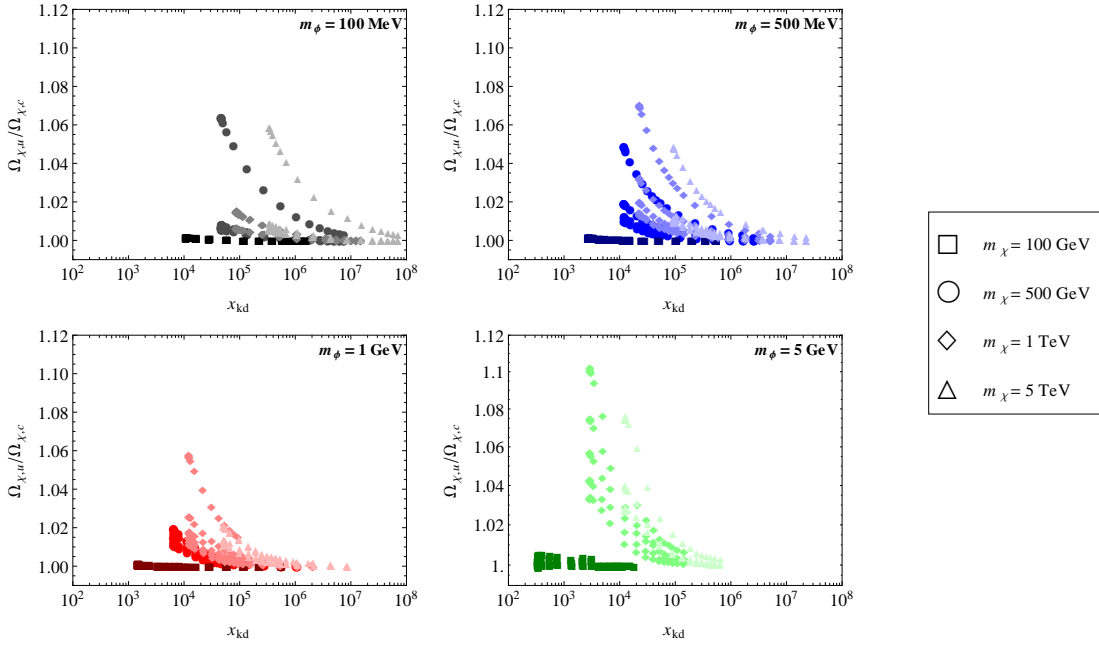


Figure 7.6: For off resonance models, the ratio of the uncoupled solution for the relic DM abundance is shown w. r. t. the coupled solution as a function of the kinetic decoupling temperature. Each panel shows the results for one particular mediator mass m_ϕ (indicated in panel, color coding matches that of Fig. 7.5). The ratio increases for earlier kinetic decoupling, since the restarted annihilations can then continue for a longer time before the Sommerfeld enhancement saturates. The maximal (minimal) ratio is obtained for the highest (lowest) DM mass m_χ (see legend). The dependence of the ratio on x_{kd} , however, depends highly on the DM coupling and thus the magnitude of the Sommerfeld enhancement; for a fixed m_ϕ and m_χ , each ‘chain’ of markers is defined by a particular value of α . See text for more details.

7 Thermal decoupling of Sommerfeld enhanced Dark Matter

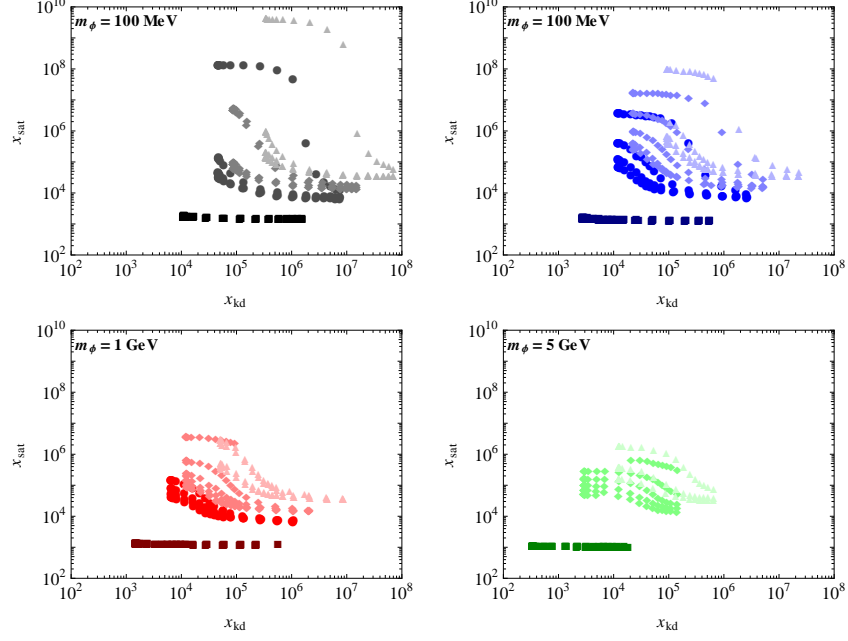


Figure 7.7: Same as Fig. 7.6, but here the saturation temperature as a function of kinetic decoupling is shown for the off resonance models. As expected, the saturation happens later for earlier decoupling, since the era of annihilations will be more pronounced. Since large Sommerfeld enhancements are obtained for small values of $m_\phi/(\alpha m_\chi)$, the saturation temperature increases for smaller mediator masses and large DM masses.

claimed in e.g., [248]. Although a new era of annihilations is barely visible for off resonance models (see Fig. 7.3), its effect is still recognizable in Fig. 7.6 by an increase of the relic density ratio for smaller x_{kd} . As the kinetic decoupling takes place earlier, the annihilations can decrease the DM relic density for a longer period of time, before the Sommerfeld enhancement saturates and the relic density finally stays constant. This becomes also apparent from the saturation temperature, which is plotted against the kinetic decoupling temperature in Fig. 7.7, where we defined T_{sat} by $Y(T_{\text{sat}})/Y_0 \equiv 0.99$. We observe that for many models with large lepton couplings we have $T_{\text{sat}} > T_{\text{kd}}$, indicating that the effect of reentering an era of annihilations is negligible, whereas for small g_ℓ we find that $T_{\text{kd}}/T_{\text{sat}}$ can reach values up to $\mathcal{O}(10^4)$. Annihilations off-resonance finally come to an end here for temperatures ranging from $T_{\text{sat}} \sim 100$ MeV to ~ 1 keV.

Besides T_{kd} , the magnitude of the Sommerfeld determines how significant the effect of the new era of annihilations is. The relic density is very roughly set by $\langle \sigma v_{\text{rel}} \rangle \propto \alpha^2/m_\chi^2$, such that for a higher DM mass a larger DM coupling is necessary to obtain the correct order of magnitude of the relic density. Since S grows with decreasing $\epsilon_\phi = m_\phi/(\alpha m_\chi)$ for off resonance models, larger enhancements are expected for higher WIMP masses. This can be seen in Fig. 7.6 by a general tendency for the ratio $\Omega_{\chi,u}/\Omega_{\chi,c}$ to increase with larger WIMP masses. However, in some cases the enhancement is unexpectedly larger because the value of ϵ_ϕ is close to a resonance but still qualifies as off resonance⁴. Since the resonances occur more frequently with decreasing ϵ_ϕ ,

⁴Results for $m_\phi = 5$ GeV and $m_\chi = 500$ GeV have been left out in Fig. 7.6 and Fig. 7.7 because their behavior

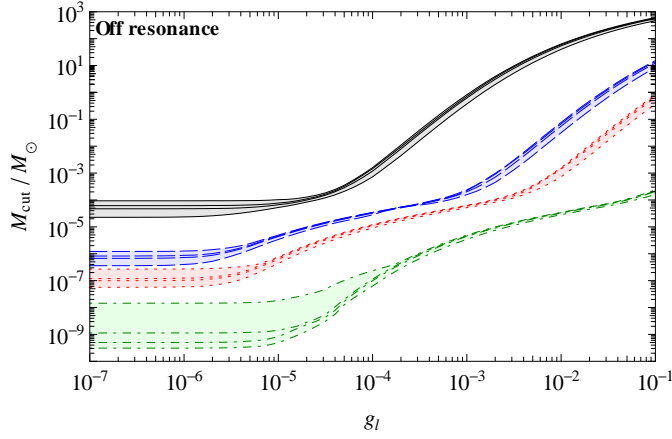


Figure 7.8: For models where the Sommerfeld enhancement is not on a resonance, the cutoff mass is shown as a function of the lepton coupling, for $m_\phi = 100$ MeV (black, full), 500 MeV (blue, dashed), 1 GeV (red, dotted), and 5 GeV (green, dash-dotted). From top to bottom, the lines correspond in each case to a DM mass of $m_\chi = 100, 500, 1000, 5000$ GeV [1].

the probability to have a large enhancement grows. This is also reflected in Fig. 7.7, where the minimal x_{sat} is more or less independent of m_ϕ , whereas the maximal x_{sat} is significantly larger for small mediator masses. In this way, a small change in the coupling can thus make a visible difference in the relic density and saturation temperature, which explains the presence of multiple ‘chains’ of the same markers in each panel, which share the same mediator and DM mass, but have slightly different α . Unlike T_{kd} , the saturation temperature and the difference in relic density thus depend a lot more on grid size of couplings in the scan and the definition that one uses for off resonance.

Due to the mild effect of the new era of annihilations, the asymptotic decoupling temperature T_{dec}^∞ only differs at most 3% from T_{kd} . The corresponding mass of the smallest gravitationally bound objects calculated from T_{dec}^∞ are shown in Fig. 7.8, where it can be seen that the possible cutoff mass spans a wide range of $M_{\text{cut}}/M_\odot \sim \mathcal{O}(10^{-10} - 10^3)$. Even when taking into account existing constraints on the lepton coupling (see section 7.2.4), much larger cutoff masses than in the standard WIMP case thus seem possible: imposing $g_\ell < 10^{-3}$, e.g. results in $M_{\text{cut}} \lesssim M_\odot$ (whereas $M_{\text{cut}} \lesssim 10^{-3}M_\odot$ for neutralino DM [55]). Compared to T_{kd} and T_{dec}^∞ , M_{cut} can have a stronger dependence on m_χ , visible by the spread of the bands for $g_\ell \lesssim 10^{-4}$. This is due to the fact that in this region of parameter space the free-streaming mass M_{fs} (that depends, among other things, on m_χ , see Eq. (4.23)), dominates over the acoustic oscillation cutoff mass M_{ao} . The impact of the different couplings and definition of what qualifies as off resonance on the resulting M_{cut} is negligible.

did not match with the rest of our off resonance models: unfortunately, the range of α for which the correct relic density is obtained is in the close vicinity of a resonance

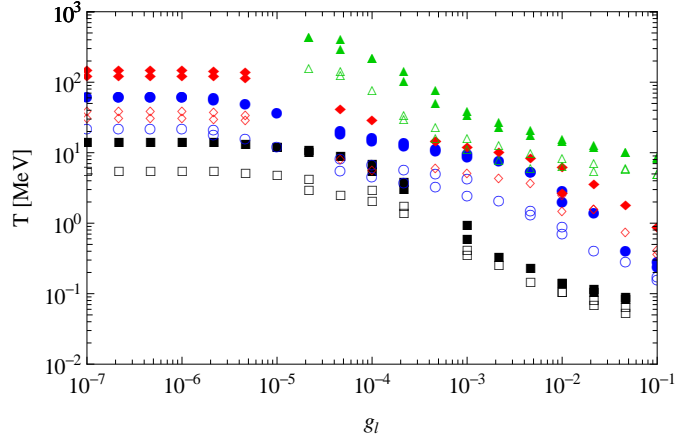


Figure 7.9: For models where the Sommerfeld enhancement is resonant, the kinetic decoupling temperature T_{kd} (filled) in comparison to the effective asymptotic decoupling temperature T_{dec}^{∞} (empty) is shown. Again $m_{\phi} = 100$ MeV (black, squares), 500 MeV (blue, circles), 1 GeV (red, diamonds), and 5 GeV (green, triangles). Comparing this figure to Fig. 7.5, we see that here T_{kd} is a little bit higher, however T_{dec}^{∞} , which determines the mass of the first protohalos, is in general lower. For more details, see text.

7.2.7 Resonance analysis

Here we discuss a similar analysis as presented in the previous section, except now we consider only models that are exactly on a resonance according to the definition in section 7.2.5. This is interesting because we expect much stronger effects as compared to the standard scenario. Numerically it is more challenging to perform this analysis than for the off resonance case, since the resonances only appear for specific values of ϵ_{ϕ} , and the coupling cannot be adjusted easily to obtain the correct relic density. As we have seen previously in the off resonance analysis, the impact of the new era of annihilation depends highly on the decoupling temperature. For a fixed m_{ϕ} , m_{χ} and α , we therefore scanned the whole range of lepton couplings, $g_{\ell} = 10^{-1} - 10^{-7}$, to see whether the correct relic density could be obtained for some value of g_{ℓ} ; the parameter sets that were not able to satisfy the relic density constraint were excluded from the analysis.

In Fig. 7.9 we show the results for both the kinetic decoupling temperature (solid markers) and the asymptotic decoupling temperature (empty markers). The overall behavior looks very similar to the off resonance case in Fig. 7.5: T_{kd} rises with increasing mediator masses and decreasing g_{ℓ} . The dependence on m_{χ} is not explicitly shown due to lack of solutions with the right relic density. This is also the reason for the gaps for particular g_{ℓ} and m_{ϕ} ; no correct relic density could be obtained for these combinations of parameters. This could, in principle, be improved by increasing the amount of sampled DM and mediator masses, although we must note that for some parameter sets it will be simply not possible to be on a resonance *and* obtain the correct relic density at the same time.

We see that T_{kd} is a little bit higher for resonances compared to the off resonance case (Fig. 7.5). This is due to the fact that the relic density constraint makes a smaller coupling α necessary to compensate for the large Sommerfeld effect, which in turn decreases the amount of DM scattering off ϕ_s , so that WIMPs decouple slightly earlier than in the off resonance case.

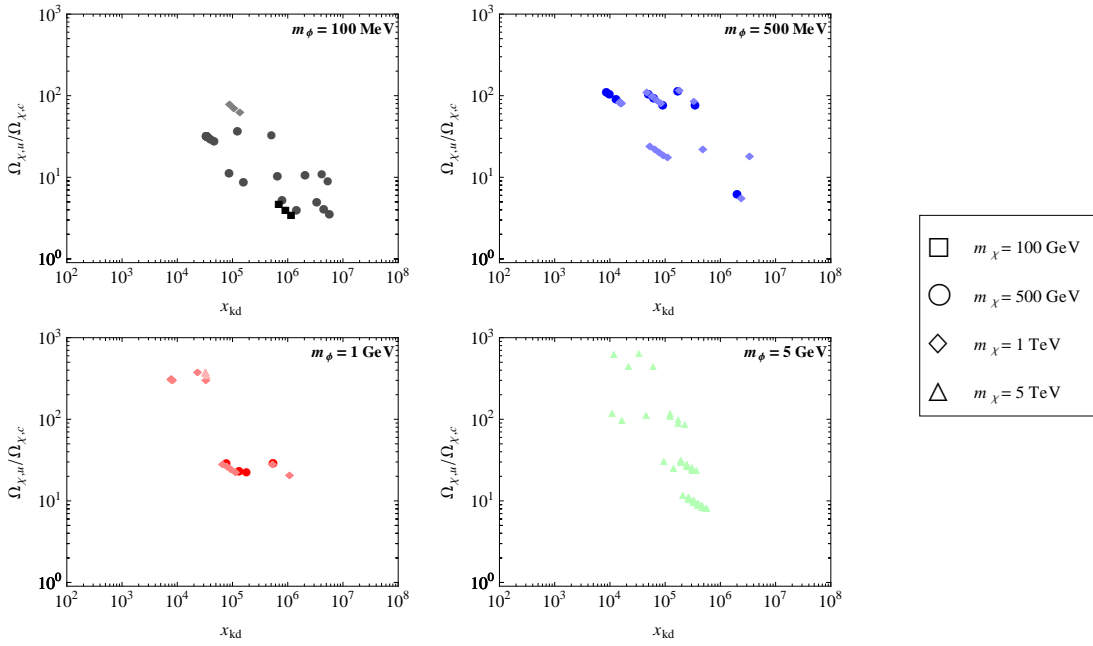


Figure 7.10: Same as Fig. 7.6, but now for models where the Sommerfeld enhancement is on a resonance and the correct relic density is obtained. As expected, there is a vast difference between the coupled and uncoupled solutions for the relic density, with ratios ranging from ~ 2 up to almost $\sim 10^3$. Again, smaller relic densities are obtained in models where kinetic decoupling happens earlier.

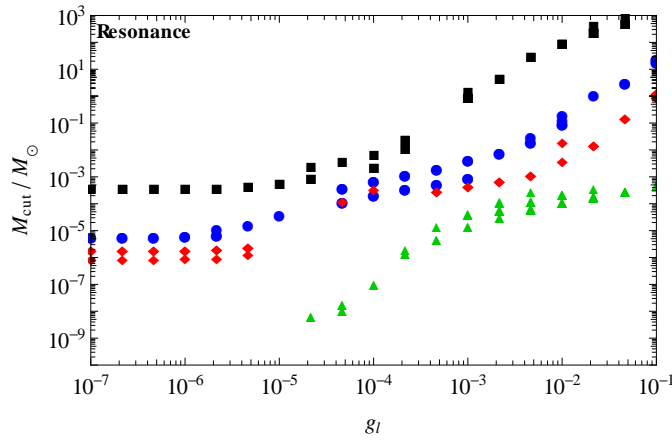


Figure 7.11: The cutoff mass M_{cut} as a function of the lepton coupling for models where the Sommerfeld enhancement is resonant, for $m_\phi = 100$ MeV (black, squares), 500 MeV (blue, circles), 1 GeV (red, diamonds), and 5 GeV (green, triangles). The values of M_{cut} are in general higher than in the off resonance case shown in Fig. 7.8 due to the lower values of asymptotic decoupling temperatures.

7 Thermal decoupling of Sommerfeld enhanced Dark Matter

	Off-resonance	On-resonance
x_{cd}	$\sim 24 - 27$	$\sim 20 - 25$
$T_{\text{kd}}[\text{MeV}]$	$\sim 0.07 - 400$	$\sim 0.09 - 450$
$T_{\text{dec}}^{\infty}[\text{MeV}]$	$\sim 0.07 - 400$	$\sim 0.06 - 170$
$T_{\text{sat}}[\text{keV}]$	$\sim 1 - 10^5$	$\sim 10^{-6} - 10^{-2}$
$\Omega_{\chi,u}/\Omega_{\chi,c}$	$\sim 1 - 1.1$	$\sim 3.5 - 670$
$M_{\text{cut}}[M_{\odot}]$	$\sim 3 \times 10^{-10} - 600$	$\sim 7 \times 10^{-9} - 1100$

Table 7.1: For the leptophilic model and parameter ranges considered here, we show an overview of the resulting ranges of the decoupling temperatures, change in relic density with respect to the standard calculation, and the smallest subhalo masses, where we considered non-resonant and resonant Sommerfeld enhancements separately [1].

The value of the kinetic temperature is not sensitive to the details of the new era of annihilations, and thus to the definition of the resonance. It could, however, have a modest effect on the asymptotic decoupling temperature T_{dec}^{∞} , which can be up to a factor of ~ 5 smaller than T_{kd} in our results. Furthermore, we find that T_{dec}^{∞} is always smaller than in the off-resonant case, the difference more pronounced for small values of g_{ℓ} .

As expected, the change in Y by considering the coupled Boltzmann equations rather than the uncoupled equation can be significant. As visible from Fig. 7.10 (which can be compared to Fig. 7.7 for the off resonance case), our approach yields a relic density that can be a factor $\sim 3.5 - 670$ smaller than the one obtained by the standard calculation. This is of course highly dependent on our definition of resonance and the sampling of m_{χ} and m_{ϕ} , however, it is very likely that the relic density could probably not continue to decrease a lot more. In most models, the annihilations even continue after matter-radiation-equality, and decrease the relic density up to a factor of 4 before reaching its final value: $\Omega_{\chi}(T_{\text{eq}}) \lesssim 4\Omega_{\chi}(T_0)$. However, the onset of matter domination and the increasing WIMP velocities due to the formation of gravitational potentials at the onset of structure formation will make sure that there is an upper limit on the decrease in relic density due to the new era of annihilations. We therefore expect that the largest difference we see here due to the new era of annihilations represents (almost) the maximum effect. In all cases we find that $\Omega_{\chi,u}/\Omega_{\chi,c}$ is larger than any value that was obtained for off the resonances (See also Table 7.1) and the relic density correspondingly saturates at very low temperatures, $\mathcal{O}(10) \text{ eV} \gtrsim T_{\text{sat}} \gtrsim \mathcal{O}(10^{-3}) \text{ eV}$.

Finally, we discuss briefly the resulting cutoff masses M_{cut} for resonances, which are shown in Fig. 7.11. As expected from Fig. 7.9, the smallest subhalo masses are larger than in the off resonance case. This effect is most pronounced for small values of g_{ℓ} , corresponding to large values of T_{dec}^{∞} and thus smallest values of M_{cut} . As a result, the lowest possible cutoff mass is a factor ~ 20 larger than for off-resonance, while the largest possible value increases by a factor ~ 2 (see also Table 7.1). The sampling of our model parameters and our definition of resonance probably have only a modest influence on these numbers. Naively using T_{kd} instead of T_{dec}^{∞} to calculate M_{cut} would result in values up to 2 orders of magnitude smaller in the resonance case. For convenience, we have summarized the main results of the off- and on resonance analysis that were discussed above in Table 7.1.

7.3 Conclusions and discussion

In this chapter we have reviewed the standard calculation for the thermal decoupling of WIMPs. We have shown that for a model where the annihilation cross section is enhanced at small velocities, e.g. by the Sommerfeld effect, the WIMP temperature and density can have a profound influence on each other. In this situation, the chemical and kinetic decoupling can no longer be treated separately, and a new era of annihilations could take place. The only way to take this effect correctly into account, is by solving the system of coupled Boltzmann equations that were given in Eq. (7.8) and Eq. (7.9). For illustration, we have applied our treatment to a particular leptophilic toy-model that was introduced in 7.2. We saw that the effect of the new era of annihilations can be significant, especially in the case of resonant models, where annihilations can continue even until after matter-radiation equality and decrease the relic density by more than two orders of magnitude. The induced effect on the WIMP temperature can cause the cutoff mass to be larger by almost two orders of magnitude than naively expected for these resonance models.

As shortly mentioned in 7.2.2, we have assumed the mediator particles to be in thermal equilibrium, which for $T \gtrsim T_{\text{kd}}$ is guaranteed because of the very efficient (inverse) decay processes $\phi \leftrightarrow \ell^+ \ell^-$. As we have seen, DM scattering off the mediators is most effective for small lepton couplings and high decoupling temperatures. If one were to neglect $\chi\phi \leftrightarrow \chi\phi$ scatterings, and only take into account DM scattering with standard model leptons, the kinetic decoupling temperature would rise indefinitely for smaller values of g_ℓ^ϕ and it would seem that one could even obtain $T_{\text{kd}} > T_{\text{cd}}$. However, this possibility is ruled out since the thermal production of χ requires a thermal population of ϕ around chemical decoupling, which places a lower bound on g_ℓ^ϕ in order to maintain the (inverse) decay processes.

Furthermore, we only took into account DM scattering with scalar particles and neglecting the pseudo-scalars. Including them would only affect the kinetic decoupling directly by shifting it to slightly lower values: T_{kd} decreases at most $\sim 20\%$ for values of $g_\ell \lesssim 10^{-4}$ (here $g_\ell^s = g_\ell^p$ and $m_s = m_p$). The other observables, such as the relic density, are affected only indirectly by the coupling between y and Y , and therefore change less than T_{kd} . For larger values of the lepton coupling, $g_\ell > 10^{-4}$, the addition of pseudo-scalar scattering hardly makes a difference because the lepton scattering determines the kinetic decoupling temperature. Assuming the mediators not to couple to quarks, was justified by the fact that kinetic decoupling almost always happens *after* the QCD phase transition at $T_{\text{QCD}} \sim 170 \text{ MeV}$ [251, 252], when there are no free quarks around anymore. A non-negligible coupling of the exchange particles to quarks, $g_q^s \neq 0$, would therefore not affect our determination of T_{kd} in a significant way.

Finally, we assumed that the DM particles couple with the same strength to both scalars and pseudo-scalars, i.e. $g_\chi^s = g_\chi^p$. In principle, however, the coupling strength α (Eq. (7.18)) that roughly sets the relic density is not the same as the coupling strength $\alpha^s \equiv g_\chi^{s,2}/4\pi$ that determines the Sommerfeld enhancement. We chose not to consider the case $g_\chi^s \neq g_\chi^p$ here, but the difference with the results presented here are not expected to be large (see [1] for a more detailed discussion).

Although we have chosen a simple, leptophilic toy-model here, it is important to stress that our formalism can be applied to any model. In fact, it is *necessary* for all DM models with an annihilation rate that is inversely proportional with the WIMP velocity, $\langle \sigma v_{\text{rel}} \rangle \propto v^{-n}$, where

$n > 1$, since the standard calculation could predict a relic abundance and smallest subhalo mass that differs a non-negligible amount from the correct result. Especially when the enhancement is large, i.e. $n \gtrsim 2$, the difference can be several orders of magnitude. Models to which our treatment would apply include more realistic models motivated by the cosmic ray anomalies (see e.g. [253, 119] for a recent discussion), the ‘standard’ heavy neutralino DM [197, 219, 220], or models with an enhanced annihilation rate either through the formation of bound states [254] or an s -channel resonance [255–258].

A condition for using the treatment as described here is the assumption that the WIMP velocity distribution has a Maxwellian shape until the both the relic abundance and the WIMP temperature finally reaches its asymptotic value. This has to be carefully checked for any model before applying the treatment described in this chapter. We showed that for the leptophilic model, self-scattering is sufficiently strong after kinetic decoupling to meet this condition. However, in some special regions of parameter space, where the annihilation cross section becomes negligible due to the Ramsauer-Townsend effect, our results should be interpreted with care.

The same holds for the calculation of M_{cut} in resonant cases where the asymptotic behavior of the WIMP temperature is reached only after matter-radiation equality. In the derivation of the expressions Eq. (4.23) and Eq. (4.24) it was assumed that the velocity distribution f reaches its asymptotic value in a highly radiation dominated Universe, and it is similar to one in the standard WIMP case at that time (see [98–102]). When these conditions are not satisfied, the results obtained for M_{cut} by the method described here can only give an indication of the real value. Since we find quite a number of resonant models in which the asymptotic behavior indeed only sets in around or after matter-radiation equality, it would be interesting to find an exact relation between decoupling temperature and cutoff mass during this period.

A detection of M_{cut} would provide us with a very interesting new way to probe the parameter space of the DM models (see the end of 4.1.2 for possible detection methods). Our results show that the cutoff mass for the leptophilic model can be between $\mathcal{O}(10^{-10}M_{\odot})$ and $\mathcal{O}(10M_{\odot})$ depending on the chosen parameters and experimental bounds. Since these values are much larger than for usual WIMPs such as neutralino or Kaluza-Klein DM (see [259, 55]), future probes of the cutoff mass could prove to be useful in distinguishing between these different classes of models. Observations of gamma-rays from galaxy clusters already place limits on small values of M_{cut} [116], which are obtained for early kinetic decoupling thus small lepton couplings. In this way, these measurements probe the parameter space from a different direction than anomalous magnetic moment measurements or beam dump experiments.

Note that higher cutoff masses could easily be obtained for leptophilic models by choosing $m_s \ll 100$ MeV (in this case the decay into the heavier leptons π and μ could then only occur through the pseudo-scalar ϕ_p , which is still heavy enough). The possibility of very large cutoff masses will also be explored in the next chapter, where we focus on the small scale structure problems of the Universe.

8 Sommerfeld enhanced Dark Matter and the small-scale problems of Λ CDM

In section 4.3 we saw that the Λ CDM model suffers from a range of problems on small scales. Proposed astrophysical and DM solutions have shortcomings, or can explain at most two of the three problems. In this chapter we will demonstrate that a particular class of Sommerfeld enhanced DM models can *simultaneously* account for all three problems. We will discuss how self-scattering can help to alleviate tension between observations and simulations regarding the inner density and velocity profiles of satellites. Furthermore, we show that kinetic decoupling in these models can happen sufficiently late to suppress the formation of small satellites. In section 8.3 we will address particle physics bounds and model building challenges for such models. Finally, we conclude with a discussion. The results presented in this chapter were published in [2].

8.1 Self-scattering Dark Matter with late kinetic decoupling

As discussed in section 4.3, simulations of Λ CDM seem to be in contradiction with observations on the scales of dwarf galaxies. Astrophysical and DM solutions for the three problems are abundant, and some suggestions even quite promising. Nevertheless, none of these solutions is able to address all problems at once.

One of the more successful attempts to solve the Λ CDM issues involves the assumption that DM has velocity dependent self-interactions (vdSIDM). These vdSIDM models are in fact exactly equivalent to the Sommerfeld enhanced models that were introduced in chapter 5. It was proposed in [181] that CDM interacting through a light mediator could explain the observed cores in dwarf galaxies without affecting the dynamics of much larger systems. In contrast to IDM models that were also proposed to solve the cusp/core problem, vdSIDM models are not ruled out by astrophysical constraints (see also 4.3.2): the transfer cross-section is velocity-dependent in such a way, that it affects the properties of dwarf galaxies, but is able to evade bounds on larger scales where WIMP velocities are much larger.

To test this idea, detailed numerical simulations of vdSIDM were carried out by the authors of [13]. For the DM self-scattering cross-section $\sigma_T(v)$, simple analytical approximations were used that were obtained in studies of screened Coulomb potentials in a plasma [11, 12, 249] (see Eq. (5.86)). Although these parametrizations are given in terms of particle physics parameters, it is the maximal transfer cross section $\sigma_T^{\max} \equiv \sigma_T(v_{\max})$ and the velocity v_{\max} that determine the astrophysics. The value of σ_T^{\max} is constrained by the previously mentioned astrophysical constraints, whereas v_{\max} should be in the same range as typical velocity dispersions encountered in dwarf galaxies $\sigma_v \sim \mathcal{O}(10)$ km/s, in order to address problems with structure formation on

these scales. Simulations were therefore carried out for two benchmark models in the allowed $(\sigma_T^{\text{max}}/m_\chi, v_{\text{max}})$ parameter range.

For these models it was shown that the main halo remains the same as in CDM simulations outside a radius of ~ 1 kpc, whereas inside a core develops. Furthermore, cored inner density profiles are obtained on subhalo scales, and as a result, the inner circular velocity profiles are altered in comparison with the CDM case. The inner density of the most massive subhalos changes significantly because of the formation of cores in the center, and are consistent with the observed brightest dSphs in the MW. No halos are present that are more dense than what is observed in the MW, and therefore these simulated vdSIDM models also propose a solution to the ‘too big to fail’-problem. However, the subhalo abundance and the radial number density functions are not affected w. r. t. CDM, which means the missing satellites problem still exists for vdSIDM.

We have seen in chapter 4 that a cutoff in the power spectrum on the scale of dwarf galaxies could solve this problem; cutoffs on this scale are however only obtained for WDM and in general not for CDM. As we saw earlier, the cutoff mass depends greatly on the time of kinetic decoupling: the size of the horizon at decoupling determines the scale at which density perturbations could have been wiped out, such that large M_{cut} is obtained for small values of T_{kd} (see also 4.1.1 and 4.1.2). Therefore, the DM scatterings with the heat bath would have to be very efficient and continue for as long as possible. Late kinetic decoupling ($T_{\text{kd}} \sim 0.1$ keV) was considered before as potential solution to the missing satellites problem [260]. Here, the size of the smallest primordial structures was translated into damping scales and correspondingly used to set limits on the cross-section of DM at decoupling. However, in this analysis the kinetic decoupling temperature of neutralino WIMPs was significantly underestimated [261].

The results from [1] that were discussed in chapter 7, however, showed that larger cutoff masses than in the standard case are expected for Sommerfeld enhanced models with light mediators. Based on these results, even larger cutoff masses could be obtained for mediator masses with a mass below $m_\phi \ll 100$ MeV¹. Decreasing the mass of the scalar mediator will, however, not result in an arbitrary late kinetic decoupling: the number density of the scattering partners becomes Boltzmann suppressed as temperature decreases, $n_\ell \propto \exp(-m_\ell/T)$. Therefore, in this case, kinetic decoupling cannot occur much later than $T_{\text{kd}} \sim 0.1$ MeV, the temperature at which there are hardly enough electrons around anymore for the DM to scatter with.

A solution to this problem is to consider neutrinos as scattering partners, which do not suffer from this problem. The scattering cross section, however, scales with the mass of the lepton squared, as is evident from the expression presented earlier in Eq. (7.19). Since neutrinos have a tiny mass of the order of eV, non-zero neutrino couplings will therefore not result in efficient DM-neutrino scatterings and their contribution will always be negligible. Scattering off photons would also be very efficient in keeping the DM thermal, and in fact, the DM-photon coupling is allowed via a lepton-loop. However, the scattering amplitude for this process becomes negligible in the limit of small momentum transfer ($t \rightarrow 0$).

Instead, if we look at a model where the mediator is a *vector* boson V with non-zero mass, we

¹In addition, the presence of a new era of annihilations could also increase the cutoff mass, although this would only have a significant effect if the enhancement is resonant; this situation is not assumed in the vdSIDM models, however, since the expression for the transfer cross-section that is used is only valid off resonance.

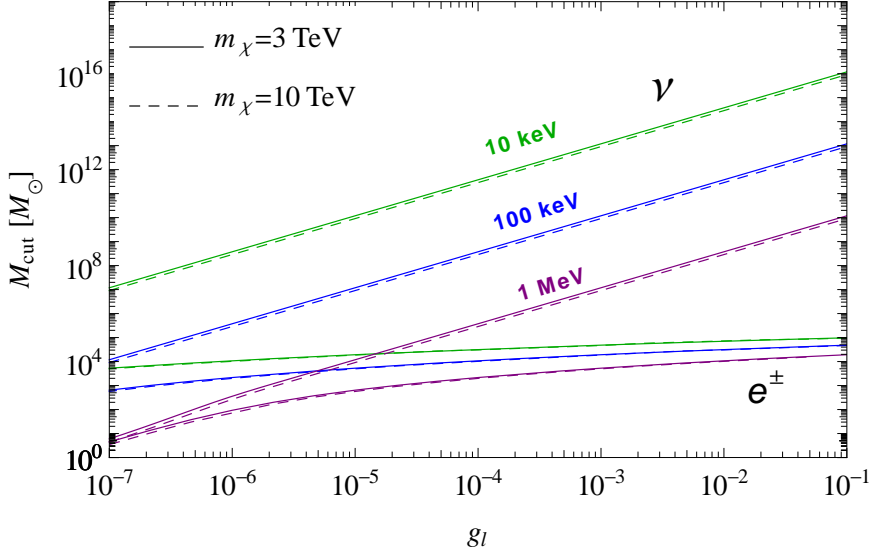


Figure 8.1: Cutoff mass M_{cut} as a function of the lepton coupling g_ℓ for Sommerfeld enhanced models where the mediator is a vector boson with a mass $m_V = 10$ keV (green), 100 keV (blue), or 1 MeV (purple). When the DM only couples to electrons, the cutoff mass reaches an asymptotic value of $\sim 10^5 M_\odot$ due to the Boltzmann suppression of the electron number density. However, when neutrino scatterings are taken into account, the cutoff scale grows steadily with larger values of g_ℓ and can reach values up to order $\sim 10^{16} M_\odot$. Different values of DM mass, $m_\chi = 3$ TeV (solid) and 10 TeV (dashed), hardly make any difference.

find that the scattering amplitude (at small momentum transfer) scales with the energy instead of the mass of the leptonic scattering partner:

$$\sum_{\text{all spins}} |\mathcal{M}|_{\chi v \leftrightarrow \chi v}^2 = 64 g_\chi^2 g_V^2 \frac{m_\chi^2 E_V^2}{m_V^4}. \quad (8.1)$$

If the vector boson couples to neutrinos, the scattering amplitude would now not be negligible since $E_V \gg m_V$, and thus possibly result in a very late kinetic decoupling and high cutoff masses.

The results for the cutoff mass obtained for a Sommerfeld enhanced model with a vector mediator are shown in Fig. 8.1. We see that if the mediator only couples to electrons, the cutoff mass cannot grow much larger than $\mathcal{O}(10^5 M_\odot)$ as expected from the Boltzmann suppression. However, if we allow non-zero couplings to neutrinos, we see that the cutoff mass can grow almost arbitrarily high with decreasing mediator mass and increasing lepton coupling. For mediator masses not larger than $\mathcal{O}(\text{MeV})$, the cutoff scale can reach values that are in the range of dwarf galaxies, and possibly make a connection to the missing satellites problem.

Encouraged by the successes of the vdSIDM simulations, in the next section we will investigate the particle physics model that would correspond to the astrophysical parameters that were used in the simulations. If vector mediator masses in the keV–MeV range are allowed, kinetic decoupling could happen sufficiently late to suppress the formation of structures on dwarf galaxy scales, and it might be possible to solve also the last problem of the missing satellites.

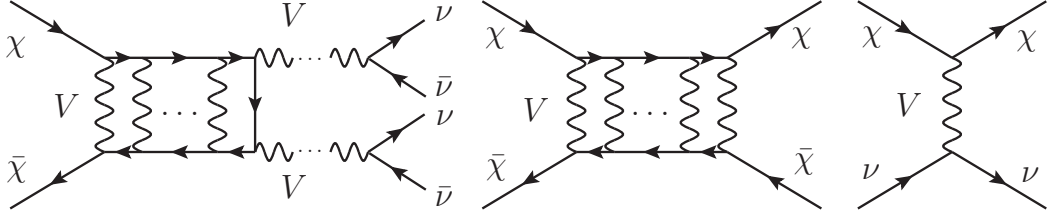


Figure 8.2: The relic density is set by the Sommerfeld enhanced annihilation of DM into vector bosons, which eventually decay into neutrinos (left). The properties of dwarf halos are affected by the induced DM self-scattering, which changes inner velocity and density profiles (middle), and DM scattering off neutrinos, which suppresses the formation of small subhalos (right). [2]

8.2 Model setup and results

We introduce a model here for phenomenological purposes only, where the DM is made up by heavy Dirac fermions χ that only couple to light vector bosons V . As explained in the previous section, we require the V to additionally couple to neutrinos in order to obtain late kinetic decoupling:

$$\mathcal{L}_{\text{int}} \supset -g_\chi \bar{\chi} \gamma^\mu \chi V_\mu - g_\nu \bar{\nu} \gamma^\mu \nu V_\mu. \quad (8.2)$$

Here, we only specify couplings that explicitly enter our analysis and impose no restrictions on the nature of the vector boson, e.g., V does not have to be a gauge boson, such that couplings to other SM particles remain unspecified. Therefore g_ν is essentially a free parameter in our approach while g_χ is fixed by the requirement to obtain the correct relic density.

As discussed, the light vector messenger induces a long-range attractive Yukawa potential between the DM particles. The DM is then thermally produced in the early universe via Sommerfeld enhanced $\bar{\chi}\chi \leftrightarrow VV$ processes as shown in Fig. 8.2 on the left, where the annihilation products VV will eventually decay into four neutrinos. The kinetic decoupling temperature, on the other hand, will be set by χ - ν scattering, and is shown in the righthand diagram in Fig. 8.2. The scattering amplitude obeys Eq. (8.1) with ℓ strictly replaced by neutrinos ν . Our model also induces self-scatterings due to the (multiple) exchange of a vector boson (Fig. 8.2, middle diagram), which changes the inner structure and velocity profiles of dwarf halos.

Assuming g_ν is small, but large enough to thermalize V at early times, the relic density is roughly given by

$$\Omega_\chi h^2 = \Omega_{\bar{\chi}} h^2 \simeq \frac{0.11}{2} \left(\frac{g_\chi}{0.683} \right)^{-4} \left(\frac{m_\chi}{\text{TeV}} \right)^2. \quad (8.3)$$

The parameter scaling of this expression can be understood by looking at e.g. Eq. (3.1), where we see that the relic density is inversely proportional to the annihilation cross section $\Omega_\chi h^2 \propto \langle \sigma_{\text{vrel}} \rangle^{-1} \propto \alpha^{-2} m_\chi^2 \propto g_\chi^{-4} m_\chi^2$. Eq. (8.3) additionally receives $\mathcal{O}(1)$ corrections due to the Sommerfeld effect, which in our analysis was fully taken into account. Furthermore, we took into account the intertwined nature of chemical and kinetic decoupling, which – as we have shown in the previous chapter – can be important in models with Sommerfeld enhanced annihilation rates. However, the kinetic decoupling happens so late in these models that the Sommerfeld enhancement factor, which is of modest size with $S \sim \mathcal{O}(100)$, is already saturated by that time. A new

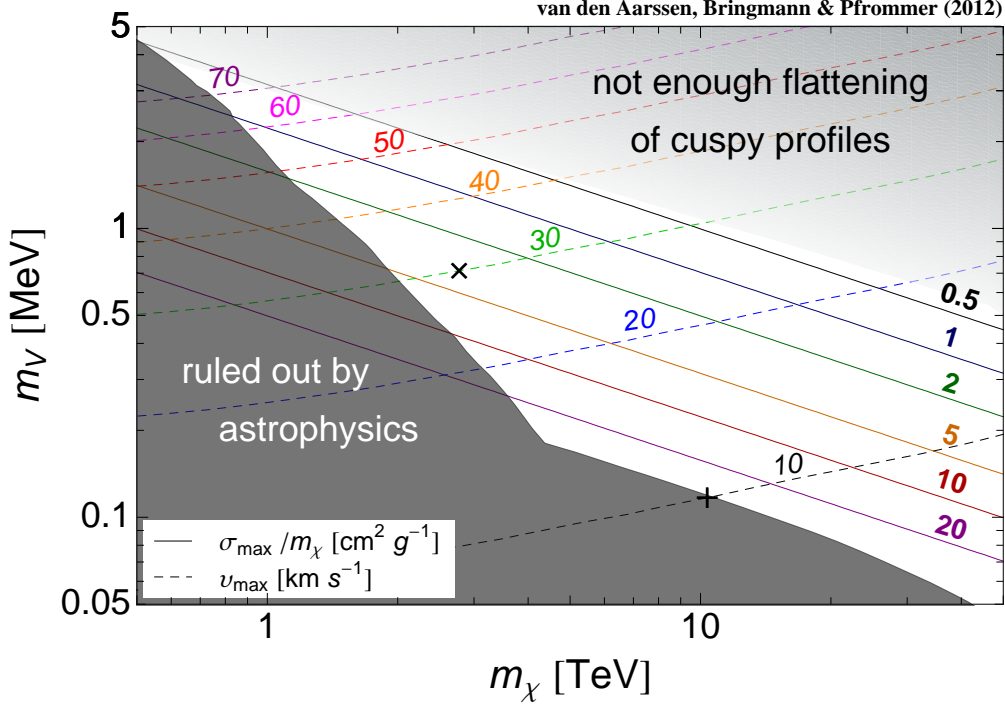


Figure 8.3: Models with DM and mediator masses that lie in the white area may be able to solve the ‘cusp vs. core’ problem without being ruled out by astrophysical bounds. The two crosses denote benchmark models from [13] for which detailed simulations have shown that they additionally solve the ‘too big to fail’ problem. Dashed and solid lines show contours of the astrophysical relevant quantities σ_{\max}^T and v_{\max} . Figure taken from [2].

era of annihilation does therefore not take place and we can safely use the standard, decoupled Boltzmann equations for our model.

If we fix g_χ by demanding the production of the observed relic density, there is a one-to-one correspondence between the particle physics input (m_χ, m_V) and the astrophysical relevant parameters $(v_{\max}, \sigma_T^{\max})$ given by Eq. (5.86). We show this in Fig. 8.3, where different values of v_{\max} and σ_T^{\max} are shown as dashed and solid contour lines, respectively. We also display the strongest astrophysical bounds on large DM self-interaction rates taken from [181] that we discussed previously at the end of subsection 4.3.2. For $m_\chi \lesssim 4 \text{ TeV}$, they are due to DM scattering with high-velocity particles from the host halo that would destroy the subhalos, while at larger m_χ the possibility of a gravothermal catastrophe constrains the relaxation time of the subhalo, and thus the self-interaction strength. Models with high DM and mediator masses would produce too cuspy subhalos that are not able to solve the cusp vs. core problem. We can see that a solution to the cusp/core and ‘too big to fail’ problem may then indeed be possible for DM masses of $m_\chi \gtrsim 600 \text{ GeV}$ and a mediator mass in the (sub-) MeV range. The two benchmark models from [13] for which we know the simulations give good results, are plotted as black crosses.

Fortunately, the models that are capable of solving the two problems have vector boson masses in the region where we expect large cutoff masses cf. Fig. 8.1. The kinetic decoupling temper-

ature in case of scattering with relativistic neutrinos, can actually be calculated analytically as has been done in Ref. [54] (see also section 3.4). Extending the treatment given there to allow for $T_V \neq T$, we find that the analytic expression for T_{kd} becomes:

$$\frac{T_{\text{kd}}}{m_\chi} = \left(\left(\frac{\tilde{a}}{n+2} \right)^{1/(n+2)} \Gamma \left[\frac{n+1}{n+2} \right] \right)^{-1} \frac{T_V}{T}, \quad (8.4)$$

which should be compared to Eq. (3.29). Here, we have rescaled the asymptotic behavior of T_χ in the high-temperature limit to correspond to T_V instead of T , and \tilde{a} is related to the old definition a from Eq. (3.30) by a similar temperature rescaling

$$\tilde{a} = a \left(\frac{T_V}{T} \right)^{n+4}. \quad (8.5)$$

Including the number of neutrino species N_V that couple to V , we then find that the kinetic decoupling temperature is given by

$$T_{\text{kd}} = \frac{0.062 \text{ keV}}{N_V^{1/4} (g_\chi g_V)^{1/2}} \left(\frac{T}{T_V} \right)_{\text{kd}}^{1/2} \left(\frac{m_\chi}{\text{TeV}} \right)^{1/4} \left(\frac{m_V}{\text{MeV}} \right). \quad (8.6)$$

If we combine this with Eq. (8.3) we expect that T_{kd} , and thus M_{cut} , are essentially independent of g_χ and m_χ , since the relic density constraint fixes the ratio of $m_\chi^{1/4} g_\chi^{-1/2}$.

For the small kinetic decoupling temperatures we are interested in here, acoustic oscillations are more efficient than free streaming effects to suppress the power spectrum [55, 262] (see also section 4.1.2). The resulting exponential cutoff can be translated into a smallest protohalo mass of

$$M_{\text{cut}} \approx \frac{4\pi}{3} \frac{\rho_\chi}{H^3} \Big|_{T=T_{\text{kd}}} = 1.7 \times 10^8 \left(\frac{T_{\text{kd}}}{\text{keV}} \right)^{-3} M_\odot, \quad (8.7)$$

where H is the Hubble rate and we assumed late kinetic decoupling such that the effective number of relativistic degrees of freedom are given by $g_{\text{eff}} = 3.37$.

We show in Fig. 8.4 contours of constant M_{cut} in the (g_V, m_V) plane for two different DM masses, where we have specified $N_V = 3$ and $T_V = (4/11)^{1/3} T_\gamma$. The result of the full numerical calculation is indeed extremely well described by Eqs. (8.7, 8.6) for $g_V \gtrsim 10^{-7}$, assuming $m_\chi \sim 1 \text{ TeV}$ and $m_V \sim 1 \text{ MeV}$. For larger DM masses m_χ and smaller vector masses m_V the agreement between the numerical calculation and the analytical approximation even holds for smaller values of g_V . For $g_V \lesssim 10^{-7}$ the deviation is due to DM scattering off non-relativistic mediator particles V that starts to dominate over scatterings with neutrinos, which is not taken into account in Eq. (8.6). Because of this, M_{cut} eventually becomes independent of g_V .

The question now is, which cutoff mass do we need in order to effectively suppress the formation of satellites on the right scale? The measured mass of a dwarf galaxy is based on its visible content, and usually defined as the mass within a certain radius smaller than the virial radius, for which reliable line-of-sight data is available. However, the (invisible) halo extends much further, such that the total mass of the halo will be larger. Moreover, the mass of a satellite that is bound

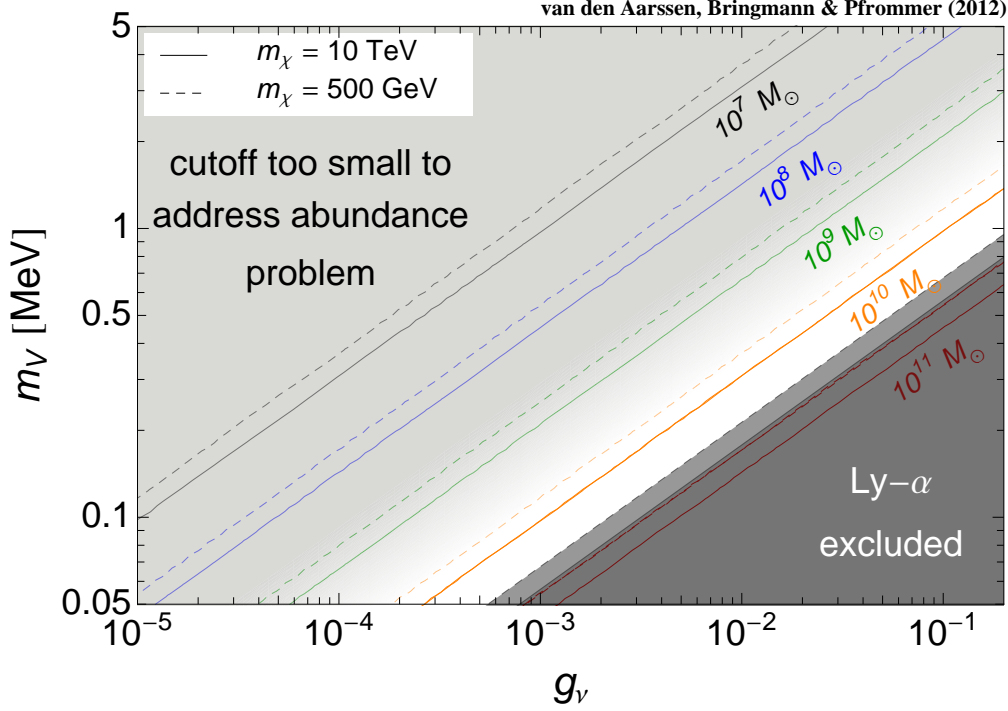


Figure 8.4: Contour lines of different values of M_{cut} are shown as a function of mediator mass m_V and coupling strength g_V . Large values of g_V and small values of m_V lead to late kinetic decoupling and thus a large mass M_{cut} of the smallest protohalos. Lyman- α data excludes $M_{\text{cut}} \gtrsim 5 \times 10^{10} M_{\odot}$, while $M_{\text{cut}} \gtrsim 10^9 M_{\odot}$ may solve the small-scale abundance problems of Λ CDM cosmology [2].

to a larger system is a decreasing function of time, since tidal stripping can remove some of the mass on the outer parts that is more loosely bound to the subhalo. The amount of mass that is removed in this way depends on the time that a satellite spends in the vicinity of a host and the pericenter of its orbit. A comparison between the cutoff mass and the observed mass of dwarf galaxies is therefore not so meaningful.

Instead, it is better to take a look at measurements of the Lyman- α forest, which are able to probe the matter power spectrum over a large range of redshifts down to the small scales we are interested in. As discussed earlier in section 4.1, WDM suppresses density perturbations on small scales due to free streaming effects. Although in our model the damping is set by acoustic oscillations, we can still compare it to the cutoff scale from WDM simulations, since both effects create an exponential cutoff in the power spectrum, which for WDM simulations is conventionally expressed in the mass m_{WDM} of a thermal WDM relic (see Eq. (4.21)). The cutoff scale as given by Eq. (4.21) was defined as the characteristic wavenumber for which the linear perturbation amplitude is suppressed by a factor of 2: $k_{\text{fs}} \equiv 0.46/R_{\text{fs}}$ [103]. Using this definition, we can write the characteristic filtering mass analogous to Eq. (4.22)

$$M_{\text{fs}} \equiv \frac{4\pi}{3} \bar{\rho}_m \left(\frac{\pi}{k_{\text{fs}}} \right)^3 = 5.1 \times 10^{10} \left(\frac{m_{\text{WDM}}}{\text{keV}} \right)^{-4} M_{\odot}. \quad (8.8)$$

Numerical simulations have shown that resulting halo statistics for cases where the initial density distribution has a sharp cutoff at $k_c = 2\pi/\lambda_{\text{fs}}$, are very similar to those obtained from an initial density field smoothed with a top-hat window function of radius $\lambda_{\text{fs}}/2$ [263]. Moreover, numerical simulations of WDM show a deviation of the mass function from CDM simulations on scales that correspond to Eq. (8.8) [264, 265]. These observations indicate that the choice of M_{fs} as defined above is justified.

The cutoff scale in the power spectrum can be constrained by combining data of the Lyman- α forest, the cosmic microwave background (CMB) and galaxy clustering. A 2σ -bound of $m_{\text{WDM}} > 2 \text{ keV}$ has been claimed [157, 158], however this bound weakens to $m_{\text{WDM}} > 0.9 \text{ keV}$ when one rejects data at $z > 3.2$ [157] that was affected by systematic errors and might be less reliable [159]. Another bound of $m_{\text{WDM}} > 1.7 \text{ keV}$ was obtained by revisiting Lyman- α data, which, however, is subject to systematic uncertainties at the $\sim 30\%$ level [266]. Moreover, in the derivation of this constraint, it was not taken into account that emission from blazars can heat the intergalactic medium, thereby affecting the Lyman- α forest [267].

We can conclude that Lyman- α data firmly excludes $m_{\text{WDM}} < 1 \text{ keV}$ or $M_{\text{fs}} > 5.1 \times 10^{10} M_{\odot}$. For $m_{\text{WDM}} \simeq 1 - 2 \text{ keV}$, WDM models are able to alleviate the ‘missing satellite problem’ [268], remove the excess of predicted faint galaxies to match the observed luminosity function [269], and match flattening of the HI velocity function in the low velocity regime measured in the ALFALFA survey [265]. For $m_{\text{WDM}} > 3 \text{ keV}$, the corresponding cutoff mass $M_{\text{fs}} < 6 \times 10^8 M_{\odot}$ is too small to have any impact on the faint-end of the galaxy luminosity function. We have included these bounds in Fig. 8.4 to demonstrate that the model proposed in this section can successfully address also the abundance problem of the smallest satellites in addition to the other two small scale problems that we have discussed.

8.3 Model building and particle physics bounds

In the previous section we introduced a simple model that is able to successfully address all three small-scale problems in Λ CDM structure formation. In the phenomenological approach we took here, it was sufficient to postulate the existence of a light vector messenger V that couples to both DM and neutrinos as defined in Eq. (8.2). If the vector boson does not couple to quarks or other leptons, the coupling g_V is essentially unconstrained. However, this setup is not well motivated from a particle physics point of view, and other, better motivated models would unavoidably introduce additional (loop-suppressed) couplings to other particles that might be very constrained. Regarding the very elegant way that such a model could solve the small-scale problems, it would certainly be worth to investigate concrete realizations of our model.

Probably the most straightforward way to embed a light vector boson in a theory is to assume it is a $U(1)$ gauge boson, also known as a *hidden photon* (see e.g. the leptophilic model proposed in [90]). In this case, a kinetic mixing is generated between the hidden and the visible photon through a lepton loop. These couplings are, however, severely constrained for sub-MeV vector masses by various astrophysical and particle physics bounds [270, 271]. Evading these bounds is probably the most difficult challenge in developing a realization of our model. Probably the most severe bounds on the loop-induced couplings come from the solar lifetime and horizontal branch stars. Kinetic mixing would cause photons in the star to change into $U(1)$ bosons that

can escape from the interior more easily, thereby inducing an energy loss that cannot exceed the luminosity of the star.

The couplings of the V to charged leptons are additionally constrained by e.g. measurements of the anomalous magnetic moment of the muon or electron, which receive extra contributions from the new allowed couplings [272]. Furthermore, results from fixed target experiments, where a beam of electrons is directed towards a dump and one looks for decay products behind the target, will apply (see [271] for an overview), as will measurements from low energy ν - e scattering [273]. However, these bounds are less stringent than the kinetic mixing bounds and might be evaded by generation specific couplings. A model independent analysis overview of the bounds that apply in the case that V couples to both neutrinos and electrons can be found in [274].

Furthermore, in order for the theory to be renormalizable we require anomaly cancellation for diagrams involving the hidden photon (see e.g. [227] for an explanation). The existence of this new particle will induce unwanted loop diagrams coupling three $U(1)$'s, which scale as $\propto g_\ell^3$, where g_ℓ is the coupling between the lepton and hidden photon. In order for these contributions to cancel each other out, one must, e.g. assume the hidden photon couples with opposite sign to only two lepton species.

Instead of the vector boson coupling to ‘ordinary’ neutrinos, a further option would be to consider it couples to *sterile* neutrinos ν_s . As long as the sterile neutrinos have a thermal velocity distribution in the early universe and are relativistic up to T_{kd} , the results derived in the previous chapter, in particular Eq. (8.6), would still hold. Interestingly, measurements of e.g. the CMB seem to indicate that besides the three known neutrinos one other relativistic species is preferred in our universe [275]. These kind of models with a new light force carrier coupling to sterile neutrinos can even provide an explanation for existing signals in direct DM detection experiments or probed in future experiments [276].

Finally, it is important to note that for typical galactic velocities $v \sim 10^{-3}$, the DM candidate we proposed in the previous section annihilates with a Sommerfeld-enhanced rate of $\langle\sigma v\rangle \sim 3 \times 10^{-24} (m_\chi/\text{TeV})^{-2} \text{cm}^3 \text{s}^{-1}$ into a VV pair, which then *exclusively* decays into neutrinos (for $m_V \leq 2m_e$). This signal could be detected by neutrino observatories; an annihilation rate of this magnitude will be in reach of future IceCube observations towards the Galactic Center [277]. Moreover, if the signal originates from a subhalo with substructure, this will produce a very large boost of the annihilation rate in combination with the Sommerfeld effect [120] (see also subsection 4.1.2). In this case, the signal may already be constrained by current observations that set a limit on the DM annihilation rate of $\langle\sigma v\rangle \sim 10^{-22} \text{cm}^3 \text{s}^{-1}$ [278].

8.4 Conclusions and discussion

In this chapter we have presented a DM model that is capable of addressing all three small scale problems discussed in section 4.3 simultaneously. The main ingredients for our model are: velocity dependent self-interactions mediated by a light vector boson, and thermal production with very late decoupling ($\mathcal{O}(\text{keV})$). The elastic scattering between the DM particles in the innermost parts of the smallest subhalos causes them to become less dense, such that both the velocity and density profiles are altered in such a way that they fit the observations. We have

shown that a (sub)MeV vector mediator particle is needed for the self-scatterings to have effect on the right scale, and that kinetic decoupling in these models can happen sufficiently late if the mediator couples to neutrinos. The resulting cutoff in the power spectrum will suppress the formation of small subhalos, thereby solving the missing satellite problem.

As shortly mentioned in subsection 4.3.2, one might expect there is a general problem with using a cutoff in the power spectrum and the formation of sufficiently large cores. This so-called ‘catch 22’ problem is observed for WDM, which removes density perturbations by free streaming and afterwards behaves as collisionless fluid [176]. In our case, however, the DM is not collisionless since it scatters with itself, and modifies only the densest parts of the halo, such that the core size is determined by the magnitude of the transfer cross section.

Obviously, additional work is needed in order to find out if the model proposed here is capable of adjusting the formation of small scale structure in the desired way. It is difficult to predict what the combined effect of adding velocity-dependent DM self-scattering to the simulations *and* a small scale cutoff in the power spectrum will be, since they could influence each other in some non-linear way. The only way to find out, is to actually perform numerical simulations including the indicated self-scattering and cutoff, and as a matter of fact, first groups are already running simulations to test our model. We thus expect to find out how our model affects the properties of the small subhalos in comparison to the usual Λ CDM simulations in the near future.

We not only expect that our model will be successful on small scales, there is also an indication that it can help to bring simulations in better agreement with observations on larger scales: the scattering cross section decreases for larger v such that for galaxy clusters only the very central density profile at $r \lesssim \mathcal{O}(1 - 10)$ kpc will be smoothed out. This would match observational evidence from improved lensing and stellar kinematic data [279] for a density cusp in Abell 383 that is slightly shallower than expected for standard CDM.

Here, we have used the approach as presented in [54, 55] to calculate the kinetic decoupling temperature, where only the leading order contribution of small momentum transfer is taken into account, i.e., $t = 0$. In the case of DM-photon scattering mediated by the vector boson this resulted in a negligible contribution since the scattering amplitude for this process is proportional to t . However, it might be interesting to take into account even higher orders in the approximation, like e.g. in [262]; even though these contributions are expected to be small, they could turn out to be non-negligible because photons are very effective in keeping the DM in local thermal equilibrium. If their contribution would turn out to be comparatively large, they could make the V coupling to neutrinos superfluous, which could also be interesting in view of the model building.

The model as presented in section 8.2 is only phenomenologically interesting and should be adapted to or embedded in an existing particle physics framework. The model would become more attractive if it additionally addresses some unexplained particle physics problems, for example in the neutrino sector. However, as discussed in the previous section, with the very constraining limits that apply to hidden massive photons and new particles coupling to leptons, this will not be an easy task. Nevertheless, since this is the first time that a single solution for all small scale problems was presented, it is certainly worth while to put effort into the model building. Moreover, the fact that a very specific neutrino signal is predicted that can be probed by IceCube, provides us with a very promising outlook to verify or invalidate the model in the near future.

9 Conclusions and outlook

Although the existence of DM on all possible scales in the Universe is now confirmed, its Nature still remains a mystery to us. As we have seen, the thermally produced WIMPs are very promising candidates, not in the least because their annihilation rate naturally predicts the observed DM density. In the standard scenario, the DM chemically decouples in the early Universe, after which the relic abundance remains constant. Afterwards, the DM still collides with much hotter particles such that local thermal equilibrium is maintained. Eventually, the DM will also kinetically decouple after the Universe has further expanded and cooled down, which sets the size of the first and smallest DM halos. Numerical simulations of Λ CDM that include the observed amount of DM are extremely successful in recreating the Universe on large scales. Unfortunately, however, the simulations seem to be in disagreement with observations of small scale structure, and a satisfying solution to these problems has not yet been found.

In this thesis we have focused on a particular class of WIMP models where the Sommerfeld effect needs to be taken into account. This non-relativistic quantum effect arises when two particles collide with each other and are able to interact through a force that is represented by a comparatively light mediator particle. The attractive Yukawa force that is generated by the mediator exchange can affect the wave function of the incoming particles when their kinetic energy is low enough. The result is an enhancement of the interaction cross section that is inversely proportional with the WIMP velocity. An especially large interaction rate is obtained when the two particles form a quasi bound state such that the enhancement factor is resonant.

The multiple exchange of the mediator particle between the colliding DM particles is a long range effect that can be expressed in a ladder diagram, which can be calculated from the full quantum theory. We have shown how this process works for the annihilation of right-handed sneutrino DM, where the two sneutrino states can interact with each other and exchange Higgs and Z-bosons. The result of this calculation can be expressed in a simple Schrödinger equation (which, in the case of the more complicated sneutrino model, is represented by a matrix equation) with a Yukawa potential that depends on the mass of the mediator. In order to find the enhancement factor, one needs solve for the distorted wave function of the interacting DM numerically.

With the analytical equations presented in chapter 6, it is possible to find out how large the Sommerfeld effect is for sneutrino annihilation. With this information, one could calculate the flux of annihilation products that is expected from DM dominated regions, such as low surface brightness galaxies or the center of our Galaxy. If this signal is in reach of current or future indirect DM detection experiments, this would allow us to place constraints on the sneutrino model or, in the most extreme case, rule it out or confirm it as the DM. In order to do this, however, one must first take into account the only constraint that is available to us at present, which is the DM abundance today.

However, in chapter 7 we have seen that for Sommerfeld enhanced models, the standard

9 Conclusions and outlook

calculation of the thermal evolution can lead to very wrong estimations. In fact, chemical and kinetic decoupling are not separate processes as is usually assumed, but can influence each other when we are dealing with velocity enhanced annihilation rates. We introduced a system of coupled Boltzmann equations that correctly takes this feedback into account, and as an example, used it on a Sommerfeld toy-model. After kinetic decoupling has taken place, the WIMPs cool down fast and their velocity decreases. The Sommerfeld effect causes the annihilation to restart, such that the relic density decreases even after regular freeze-out. This new era of annihilations can even continue until after matter-radiation for models where the Sommerfeld enhancement is resonant. The WIMPs with the lowest velocity annihilate first, such that the average WIMP temperature increases, which in turn affects the size of the smallest DM subhalos. It was shown that much larger cutoff masses are possible for Sommerfeld enhanced models than for standard neutralino DM.

Probing the scale of the smallest DM subhalos would be a new way to learn about the characteristics of the DM. Especially since it has been shown that the cutoff mass is very model dependent, it could help to distinguish between different DM candidates. There are quite a number of interesting DM models with velocity dependent annihilation rates for which the thermal evolution has not been determined properly. In the special case of a resonance, the resulting relic density could even be wrong by several orders of magnitude. It would therefore be interesting to see the effect of the intertwined nature of chemical and kinetic decoupling for well motivated model such as the Minimal Super Symmetric Model.

The large possible cutoff mass for Sommerfeld enhanced models in relation to the small scale problems of Λ CDM was also studied in this work. Numerical simulations of structure formation predict a much larger abundance of small subhalos than the observed satellites in our Milky Way. Furthermore, the inner density of these subhalos seem to disagree with the observed cores of dwarf galaxies. What is perhaps even worse, is that the simulated most massive subhalos are far too dense, such that the rotation velocities do not match up with the observed brightest dwarf galaxies.

It was already known from numerical simulations of structure formation that velocity dependent self-scattering DM could help to solve at least the latter two problems. The self-scattering causes the inner densities to become less dense, such that a core develops in the smallest subhalos and the velocity profiles agree nicely with the brightest satellites. We translated the astrophysical input of the simulations to particle physics parameters, and showed that it corresponds to Sommerfeld enhanced model with a WIMP interacting through a light vector boson mediator. We furthermore showed that very late kinetic decoupling is obtained for this model if the vector mediator is able to interact with neutrinos. In that case, the resulting cutoff mass is large enough to alleviate the subhalo abundance problem and at the same time evade bounds from Lyman- α data. With this model it would thus be possible – for the first time – to solve all small scale problems simultaneously.

Interestingly, the DM proposed here would annihilate into two vector bosons that exclusively decay into neutrinos. This signal could be picked up by future (and possibly present) neutrino detection experiments such as IceCube. Whether our proposed model is as successful in solving the small scale problems as we expect, can only be found out by performing detailed numerical simulations (which at the moment are already being prepared). Furthermore, the model as proposed here is useful for phenomenological purposes but not very appealing from a par-

ticle physics perspective. Additional model building, which will not be easy with the strong constraints that exist for new particles, is therefore a necessity, but with a possibly rewarding outcome.

In conclusion, we have shown that the Sommerfeld effect is an interesting phenomenon that can have important consequences for our understanding of and search for DM. Exciting times are ahead of us with the many different experiments that are looking for a possible hint of DM, and there are even more to come. We have now reached an era where our technology and knowledge has advanced so much, that we have great hopes for the near future to unveil at least some of the secrets that our fascinating cosmos holds in store for us.

A Calculation of Sommerfeld effect

A.1 Quantum electrodynamics

In this Appendix section we will present a more detailed calculation than given in section 5.2 for the Sommerfeld enhanced electron-positron annihilation into 2 photons. We consider the theory of Quantum electrodynamics, derive the non-relativistic action and subsequently calculate the two-body action.

A.1.1 Derivation of the non-relativistic effective action

Here we will provide the details of the calculation of the non-relativistic action from the full QED action (see Eq. (5.19)) that we have skipped in section 5.2.2.

Integrate out light fields

The first step is to integrate out the light fields, in this case A_μ from Eq. (5.22)

$$Z[A_\mu] = \int \mathcal{D}A \exp \left\{ i \int d^4x \left(-e \bar{\psi} \gamma^\mu \psi A_\mu - \frac{1}{2} A_\mu \left[\left(1 - \frac{1}{\xi_g}\right) \partial^2 g^{\mu\nu} - \partial^\mu \partial^\nu \right] A_\nu \right) \right\}, \quad (\text{A.1})$$

In order to do this, we shift the A -field

$$A'_\mu(x) = A_\mu(x) - \int d^4y G_{\mu\nu}(x-y) J^\nu(y), \quad (\text{A.2})$$

where $G_{\mu\nu}(x-y)$ is a Green's function such that

$$- \left[\left(1 - \frac{1}{\xi_g}\right) \partial^2 g^{\alpha\beta} - \partial^\alpha \partial^\beta \right] G_{\mu\nu}(x-y) = M^{\mu\nu}(x) G_{\mu\nu}(x-y) = i \delta_\nu^\beta \delta^{(4)}(x-y), \quad (\text{A.3})$$

and the current $J^\nu(y)$ is defined as

$$J^\nu(y) = -e \bar{\psi}(y) \gamma^\nu \psi(y). \quad (\text{A.4})$$

A solution to Eq. (A.3) is

$$G_{\mu\nu}(x-y) = -i \int \frac{d^4q}{(2\pi)^4} \frac{g_{\mu\nu} - (1 - \xi_g) \frac{q_\mu q_\nu}{q^2}}{q^2 + i\epsilon} e^{-iq \cdot (x-y)}, \quad (\text{A.5})$$

which represents the photon propagator between points x and y . The functional derivative in Eq. (5.22) simply transforms to $\mathcal{D}A \rightarrow \mathcal{D}A'$.

A Calculation of Sommerfeld effect

Substituting these definitions into the Lagrangian from Eq. (5.22), we get after a little algebra:

$$\begin{aligned}
S[A'] = \int d^4x \left[\frac{1}{2} A'_\mu(x) M^{\mu\nu}(x) A'_\nu(x) - \frac{1}{2} \int d^4y d^4z J^\alpha(y) G_{\mu\alpha}(x-y) M^{\mu\nu}(x) J^\beta(z) G_{\nu\beta}(z-x) \right. \\
+ i \frac{1}{2} \int d^4y J^\alpha(y) G_{\mu\alpha}(x-y) M^{\mu\nu}(x) A'_\nu(x) + i \frac{1}{2} \int d^4y A'_\mu(x) M^{\mu\nu}(x) J^\beta(y) G_{\nu\beta}(x-y) \\
\left. + J^\mu(x) A'_\mu(x) + i J^\mu(x) \int d^4y J^\nu(y) G_{\mu\nu}(x-y) \right], \quad (\text{A.6})
\end{aligned}$$

where we can use Eq. (A.3) to evaluate the integrals in the second, third and fourth term. The second term transforms to the last term, except for a factor $-\frac{1}{2}$. The third and fourth term end up giving the same contribution, i.e. $-\frac{1}{2} J^\mu(x) A'_\mu(x)$, that together cancel out the fifth term. Finally, we are left with the simple expression as given in Eq. (5.24):

$$S[A'] = \int d^4x \left[\frac{1}{2} A'_\mu(x) M^{\mu\nu}(x) A'_\nu(x) + i \frac{1}{2} \int d^4y J^\mu(x) G_{\mu\nu}(x-y) J^\nu(y) \right], \quad (\text{A.7})$$

Integrate out relativistic parts of fields

Integrating out the relativistic parts of the fermion fields is done by splitting the fields in a relativistic and non-relativistic part

$$\begin{aligned}
\psi(x) &= \int_{\text{NR}} \frac{d^4p}{(2\pi)^4} \tilde{\psi}(p) e^{-ipx} + \int_{\text{R}} \frac{d^4p}{(2\pi)^4} \tilde{\psi}(p) e^{-ipx} = \psi_{\text{NR}}(x) + \psi_{\text{R}}(x), \\
\bar{\psi}(x) &= \int_{\text{NR}} \frac{d^4p}{(2\pi)^4} \tilde{\bar{\psi}}(p) e^{ipx} + \int_{\text{R}} \frac{d^4p}{(2\pi)^4} \tilde{\bar{\psi}}(p) e^{ipx} = \bar{\psi}_{\text{NR}}(x) + \bar{\psi}_{\text{R}}(x),
\end{aligned} \quad (\text{A.8})$$

where the non-relativistic momentum space is defined as

$$\text{NR} = \left((p_0, \vec{p}) \mid p_0 = \pm m + \delta p^0, \quad \mathcal{O}(\delta p^0) \sim \mathcal{O}\left(\frac{\vec{p}^2}{2m}\right) \ll m \right), \quad (\text{A.9})$$

The relevant terms in the action that are obtained by this are given by

$$\begin{aligned}
S[\psi_{\text{NR}}, \bar{\psi}_{\text{NR}}] &= S_{0,\text{NR}} + S_{\text{R}}[\psi_{\text{NR}}, \bar{\psi}_{\text{NR}}], \\
&= \int d^4x [\bar{\psi}_{\text{NR}}(i\gamma - m)\psi_{\text{NR}}] \\
&\quad + \frac{ie^2}{2} \int d^4x d^4y [\bar{\psi}_{\text{NR}}(x) \gamma^\alpha \psi_{\text{NR}}(x) G_{\alpha\beta}(x-y) \bar{\psi}_{\text{NR}}(y) \gamma^\beta \psi_{\text{NR}}(y)] \\
&\quad - i \log \left(\int \mathcal{D}\psi_{\text{R}} \mathcal{D}\bar{\psi}_{\text{R}} e^{iS_{0,\text{R}} + iS_{\text{int}}[\bar{\psi}_{\text{NR}}, \bar{\psi}_{\text{R}}, \psi_{\text{NR}}, \psi_{\text{R}}]} \right), \quad (\text{A.10})
\end{aligned}$$

which is the expression from Eq. (5.27). Here we concentrate in particular on integrating out the relativistic fields from the term $S_{\text{int}}[\bar{\psi}_{\text{NR}}, \bar{\psi}_{\text{R}}, \psi_{\text{NR}}, \psi_{\text{R}}]$. For information about the other terms see subsection 5.2.2.

Since we are interested in a box diagram that is related to the annihilation of an electron-positron pair into photons, we will focus on terms that include two non-relativistic and two

relativistic fields. There are in fact six of such terms:

$$\begin{aligned}
S_{\text{int}}[\bar{\psi}_{\text{NR}}, \bar{\psi}_{\text{R}}, \psi_{\text{NR}}, \psi_{\text{R}}] = & \frac{ie^2}{2} \int d^4x d^4y \left[\bar{\psi}_{\text{NR}}(x) \gamma^\alpha \psi_{\text{R}}(x) G_{\alpha\beta}(x-y) \bar{\psi}_{\text{R}}(y) \gamma^\beta \psi_{\text{NR}}(y) \right] \\
& + \frac{ie^2}{2} \int d^4x d^4y \left[\bar{\psi}_{\text{R}}(x) \gamma^\alpha \psi_{\text{NR}}(x) G_{\alpha\beta}(x-y) \bar{\psi}_{\text{NR}}(y) \gamma^\beta \psi_{\text{R}}(y) \right] \\
& + \frac{ie^2}{2} \int d^4x d^4y \left[\bar{\psi}_{\text{NR}}(x) \gamma^\alpha \psi_{\text{R}}(x) G_{\alpha\beta}(x-y) \bar{\psi}_{\text{NR}}(y) \gamma^\beta \psi_{\text{R}}(y) \right] \\
& + \frac{ie^2}{2} \int d^4x d^4y \left[\bar{\psi}_{\text{R}}(x) \gamma^\alpha \psi_{\text{NR}}(x) G_{\alpha\beta}(x-y) \bar{\psi}_{\text{R}}(y) \gamma^\beta \psi_{\text{NR}}(y) \right] \\
& + \frac{ie^2}{2} \int d^4x d^4y \left[\bar{\psi}_{\text{R}}(x) \gamma^\alpha \psi_{\text{R}}(x) G_{\alpha\beta}(x-y) \bar{\psi}_{\text{NR}}(y) \gamma^\beta \psi_{\text{NR}}(y) \right] \\
& + \frac{ie^2}{2} \int d^4x d^4y \left[\bar{\psi}_{\text{NR}}(x) \gamma^\alpha \psi_{\text{NR}}(x) G_{\alpha\beta}(x-y) \bar{\psi}_{\text{R}}(y) \gamma^\beta \psi_{\text{R}}(y) \right].
\end{aligned} \tag{A.11}$$

The first four terms correspond to diagrams of the kind that is depicted in the top left of Fig. 5.3. As one can see, these diagrams can build a box diagram (Fig. 5.3, top, right) like the one we are looking for when two of them are combined. The remaining two terms are interactions like the one in the bottom left corner of Fig. 5.3, which can build the other two higher order diagrams on the right. Since we are not interested in them, we will therefore focus on the first four terms in Eq. (A.11).

In order to perform the integration over the relativistic fields, we expand S_{R} to second order in $ie^2/2$ such that we *symbolically* get

$$\begin{aligned}
e^{i\left[\psi_{\text{R}}^2 + \frac{ie^2}{2}(\psi_{\text{R}}^4 + \psi_{\text{NR}}^2 \psi_{\text{R}}^2)\right]} \approx e^{i\psi_{\text{R}}^2} \left[1 - \frac{e^2}{2} (\psi_{\text{R}}^4 + \psi_{\text{NR}}^2 \psi_{\text{R}}^2) \right. \\
\left. + \frac{1}{2!} \frac{e^4}{4} (\psi_{\text{R}}^4 + \psi_{\text{NR}}^2 \psi_{\text{R}}^2)^2 + \mathcal{O}(e^6) \right],
\end{aligned} \tag{A.12}$$

where the integration over position space has been left out for simplicity, and ψ_{NR}^2 denotes that the corresponding term contains two ψ_{NR} fields, either with or without bar. Integrating this expression over the relativistic fields, we will end up with something of the form

$$\begin{aligned}
\int \mathcal{D}\psi_{\text{R}} \mathcal{D}\bar{\psi}_{\text{R}} e^{i(S_{0,\text{R}} + S_{\text{int}})} \sim C_{\text{R}} \times \left(1 + \int d^4x d^4y i\beta_2(x,y) \bar{\psi}_{\text{NR}}(x) \psi_{\text{NR}}(y) \right. \\
\left. + \int d^4x d^4y d^4z d^4w i\beta_4(x,y,z,w) \bar{\psi}_{\text{NR}}(x) \psi_{\text{NR}}(y) \bar{\psi}_{\text{NR}}(z) \psi_{\text{NR}}(w) + \dots \right),
\end{aligned} \tag{A.13}$$

where C_{R} represents the constant prefactor from integrating over the purely relativistic part, and β_i denotes the coefficient including all prefactors and coupling constants in front of the i -point correlation function. As explained before, we want to concentrate on the terms containing four non-relativistic fields, corresponding to the box diagrams from 5.3, thus we want to derive

A Calculation of Sommerfeld effect

the form of β_4 . As can be seen from Eq. (A.12), this is given by the term proportional to e^4 containing four relativistic and four non-relativistic fields, i.e., the square product of the first four terms in Eq. (A.11). In total this will give us sixteen terms, many of which will fortunately cancel out or simply disappear.

In order to integrate out the relativistic fields, we use that

$$\overline{\psi_R(x)\psi_R(y)} = \frac{\int \mathcal{D}\bar{\psi}_R \mathcal{D}\psi_R e^{i\bar{\psi}_R(i\partial - m)\psi_R} \psi_R(x)\bar{\psi}_R(y)}{\int \mathcal{D}\bar{\psi}_R \mathcal{D}\psi_R e^{i\bar{\psi}_R(i\partial - m)\psi_R}} = S(x-y), \quad (\text{A.14})$$

which will make sure the factor C_R in Eq. (A.13) can be divided out. The propagator of ψ_R is defined as

$$S(x-y) = \int_R \frac{d^4 p}{(2\pi)^4} \frac{i(\not{p} + m)}{p^2 - m^2 + i\epsilon} e^{-ip(x-y)}, \quad (\text{A.15})$$

and satisfies

$$(i\partial_x - m)S(x-y) = i\delta^4(x-y). \quad (\text{A.16})$$

Furthermore we have that

$$\overline{\psi_R(x)\psi_R(y)} = \overline{\bar{\psi}_R(x)\bar{\psi}_R(y)} = 0, \quad (\text{A.17})$$

due to the anti-commutation relations for fermions, such that only terms including pairs of ψ_R and $\bar{\psi}_R$ will survive.

Four of the remaining six terms are given by

$$\overline{\psi_{NR}(x)\gamma^\mu \psi_R(x)G_{\mu\nu}(x-y)\bar{\psi}_R(y)\gamma^\nu \psi_{NR}(y)} \overline{\psi_{NR}(z)\gamma^\alpha \psi_R(z)G_{\alpha\beta}(z-w)\bar{\psi}_R(w)\gamma^\beta \psi_{NR}(w)} \quad (\text{A.18})$$

$$\overline{\psi_{NR}(x)\gamma^\mu \psi_R(x)G_{\mu\nu}(x-y)\bar{\psi}_R(y)\gamma^\nu \psi_{NR}(y)} \overline{\psi_R(z)\gamma^\alpha \psi_{NR}(z)G_{\alpha\beta}(z-w)\bar{\psi}_{NR}(w)\gamma^\beta \psi_R(w)} \quad (\text{A.19})$$

$$\overline{\psi_R(x)\gamma^\mu \psi_{NR}(x)G_{\mu\nu}(x-y)\bar{\psi}_{NR}(y)\gamma^\nu \psi_R(y)} \overline{\psi_{NR}(z)\gamma^\alpha \psi_R(z)G_{\alpha\beta}(z-w)\bar{\psi}_R(w)\gamma^\beta \psi_{NR}(w)} \quad (\text{A.20})$$

$$\overline{\psi_R(x)\gamma^\mu \psi_{NR}(x)G_{\mu\nu}(x-y)\bar{\psi}_{NR}(y)\gamma^\nu \psi_R(y)} \overline{\psi_R(z)\gamma^\alpha \psi_{NR}(z)G_{\alpha\beta}(z-w)\bar{\psi}_{NR}(w)\gamma^\beta \psi_R(w)}, \quad (\text{A.21})$$

where we have excluded the space integrals and the factor of $e^4/8$ in front of the expressions for the moment being. In fact, the top two and bottom two expressions are the same. For example taking the righthand factor in Eq. (A.19), we can use that

$$\begin{aligned} \overline{\psi_R(z)\gamma^\alpha \psi_{NR}(z)G_{\alpha\beta}(z-w)\bar{\psi}_{NR}(w)\gamma^\beta \psi_R(w)} = \\ \overline{\psi_{NR}(w)\gamma^\beta \psi_R(w)G_{\beta\alpha}(w-z)\bar{\psi}_R(z)\gamma^\alpha \psi_{NR}(z)}, \end{aligned} \quad (\text{A.22})$$

which is equal to the righthand factor in Eq. (A.18) after a redefinition of $\alpha \leftrightarrow \beta$ and $z \leftrightarrow w$

(the only difference is a factor -1 in the momentum q of the virtual photon in the box diagram, which is not important since it is integrated over). Similarly one can derive that Eq. (A.20) and Eq. (A.21) are the same. Therefore these four terms reduce to 2 times Eq. (A.18), shown as the top right diagram in Fig. 5.4, and 2 times Eq. (A.20) (Fig. 5.4, bottom right).

The remaining two terms are given by

$$\overline{\psi}_{\text{NR}}(x)\gamma^\mu \overbrace{\psi_{\text{R}}(x)G_{\mu\nu}(x-y)\overline{\psi}_{\text{NR}}(y)\gamma^\nu\psi_{\text{R}}(y)} \quad \overbrace{\overline{\psi}_{\text{R}}(z)\gamma^\alpha\psi_{\text{NR}}(z)G_{\alpha\beta}(z-w)\overline{\psi}_{\text{R}}(w)\gamma^\beta\psi_{\text{NR}}(w)} \quad (\text{A.23})$$

$$\overbrace{\overline{\psi}_{\text{R}}(x)\gamma^\mu\psi_{\text{NR}}(x)G_{\mu\nu}(x-y)\overline{\psi}_{\text{R}}(y)\gamma^\nu\psi_{\text{NR}}(y)} \quad \overbrace{\overline{\psi}_{\text{NR}}(z)\gamma^\alpha\psi_{\text{R}}(z)G_{\alpha\beta}(z-w)\overline{\psi}_{\text{NR}}(w)\gamma^\beta\psi_{\text{R}}(w)}, \quad (\text{A.24})$$

where each term can have two different contractions as indicated by the upper and lower lines. As in the previous case, the different contractions actually give the the same contribution, such that we can again take 2 times Eq. (A.23) (Fig. 5.4, bottom left) and Eq. (A.24) (Fig. 5.4, top left).

The total therefore comes down to four different terms, each with a factor of $e^4/4$ in front. From Fig. 5.4 it is visible that there are in principle only two different kind of interactions, corresponding to the t- and u-channel (left and right, respectively). The upper diagrams will give the same contribution as the lower ones, such that we only need to consider two terms in the end, with an additional factor of 2. This explains the factor of $e^2/2$ in front of the two terms in Eq. (5.29), where the first term corresponds to the t-channel, and the second term to the u-channel

Non-relativistic expansion of the potential term

Here, we will provide some more details about the non-relativistic expansion of the potential term given in Eq. (5.31):

$$S_p = \frac{ie^2}{2} \int d^4x d^4y \left[\overline{\psi}(x)\gamma^\alpha\psi(x)G_{\alpha\beta}(x-y)\overline{\psi}(y)\gamma^\beta\psi(y) \right], \quad (\text{A.25})$$

Let us now first consider the spatial part of Eq. (A.25), for which $\alpha, \beta = i, j = 1, 2, 3$. The Lorentz vector $\overline{\psi}\gamma^j\psi$ is then given by

$$\overline{\psi}\gamma^j\psi = \psi^\dagger\gamma^0\gamma^j\psi = \psi^\dagger \begin{pmatrix} 0 & \sigma^i \\ \sigma^i & 0 \end{pmatrix} \psi = i\eta^\dagger \left[\frac{\vec{\nabla} \cdot \vec{\sigma}}{2m}, \sigma^i \right] \eta + i\xi^\dagger \left[\sigma^i, \frac{\vec{\nabla} \cdot \vec{\sigma}}{2m} \right] \xi, \quad (\text{A.26})$$

where each term is of order $\mathcal{O}(\frac{\mathbf{p}}{m})$. The spatial part of the potential term contains the product of two of these Lorentz vectors and G_{ij} , such that the resulting terms will all be of order $\mathcal{O}(\frac{\mathbf{p}^2}{m^2})$ or higher and we can neglect all of them.

We therefore focus on the temporal part of the potential term, for which the Lorentz vector

A Calculation of Sommerfeld effect

$\bar{\psi}\gamma^0\psi$ takes the form

$$\bar{\psi}\gamma^0\psi = \psi^\dagger\gamma^0\gamma^0\psi = \psi^\dagger\psi = \eta^\dagger\eta + \xi^\dagger\xi + \mathcal{O}\left(\frac{\mathbf{p}^2}{m^2}\right), \quad (\text{A.27})$$

where we have only written the leading order terms explicitly. The temporal part of the photon propagator is

$$G_{00}(x-y) = -i \int \frac{d^4q}{(2\pi)^4} \frac{1 - (1 - \xi_g) \frac{q_0^2}{q^2}}{q^2 + i\epsilon} e^{-iq \cdot (x-y)}, \quad (\text{A.28})$$

where we have used $g_{00} = 1$. In order to evaluate the potential term, it is convenient to Fourier transform the fields such that we obtain

$$\begin{aligned} & \frac{ie^2}{2} \int d^4x d^4y [\eta^\dagger(x)\eta(x) + \xi^\dagger(x)\xi(x)] G_{00}(x-y) [\eta^\dagger(y)\eta(y) + \xi^\dagger(y)\xi(y)] = \\ & \frac{ie^2}{2} \int \frac{d^4k_1 d^4k_2 d^4k_3 d^4k_4}{(2\pi)^{16}} (2\pi)^4 \delta^{(4)}(k_1 - k_2 + k_3 - k_4) \times \\ & \quad \left[\tilde{\eta}^\dagger(k_2)\tilde{\eta}(k_1) + \tilde{\xi}^\dagger(k_2)\tilde{\xi}(k_1) \right] \tilde{G}_{00}(k_2 - k_1) \left[\tilde{\eta}^\dagger(k_4)\tilde{\eta}(k_3) + \tilde{\xi}^\dagger(k_4)\tilde{\xi}(k_3) \right], \quad (\text{A.29}) \end{aligned}$$

where in the last step we have used that

$$G_{00}(x-y) = \int \frac{d^4k_1}{(2\pi)^4} \frac{d^4k_2}{(2\pi)^4} \tilde{G}_{00}(k_2 - k_1) e^{-i(k_2 - k_1)(x-y)}. \quad (\text{A.30})$$

Comparing this equation to Eq. (A.28) we find that in the non-relativistic limit where $k_i = (m, \mathbf{k}_i)$ and $|\mathbf{k}_i| \ll m$, the Fourier transform of the propagator is given by

$$\begin{aligned} \tilde{G}_{00}(k_2 - k_1) &= -i \left(\frac{1 - (1 - \xi_g) \frac{(k_2^0 - k_1^0)^2}{(k_2 - k_1)^2}}{(k_2 - k_1)^2} \right), \\ &= \frac{-i}{(k_2^0 - k_1^0)^2 - |\mathbf{k}_2 - \mathbf{k}_1|^2} + \frac{i(1 - \xi_g)(k_2^0 - k_1^0)^2}{((k_2^0 - k_1^0)^2 - |\mathbf{k}_2 - \mathbf{k}_1|^2)^2}, \\ &\approx \frac{i}{|\mathbf{k}_2 - \mathbf{k}_1|^2}, \quad (\text{A.31}) \end{aligned}$$

where in the last step we have used that $k_2^0 \simeq k_1^0$. The gauge dependent term therefore disappears since photons and scalars are the same in the non-relativistic limit. Inserting this in Eq. (A.29) and Fourier transforming back, we obtain

$$-\frac{1}{2} \int d^4x d^4y \frac{\alpha \delta(x^0 - y^0)}{|\mathbf{x} - \mathbf{y}|} [\eta^\dagger(x)\eta(x) + \xi^\dagger(x)\xi(x)] [\eta^\dagger(y)\eta(y) + \xi^\dagger(y)\xi(y)], \quad (\text{A.32})$$

as given in Eq. (5.32).

A.1.2 Two-body effective action

Here we will provide the details of the calculation of the two-body wave-function that describes the positronium state. In order to perform the functional integration over the one-particle fields in the two-body action (see Eq. (5.38))

$$S^H \equiv -i \log \left[\int \mathcal{D}\eta \mathcal{D}\eta^\dagger \mathcal{D}\xi \mathcal{D}\xi^\dagger e^{iS_{\text{NR}}} \right], \quad (\text{A.33})$$

we introduce auxiliary fields $\sigma(t, \mathbf{x}, \mathbf{y})$ and $s(t, \mathbf{y}, \mathbf{x})$ that satisfy

$$1 = \int \mathcal{D}\sigma \mathcal{D}s^\dagger \exp \left[\frac{i}{2} \int d(xy) \sigma (s^\dagger - \eta^\dagger \xi) \right] \quad (\text{A.34})$$

$$1 = \int \mathcal{D}\sigma^\dagger \mathcal{D}s \exp \left[\frac{i}{2} \int d(xy) \sigma^\dagger (s - \xi^\dagger \eta) \right], \quad (\text{A.35})$$

which allows us to replace $\eta^\dagger \xi$ with the two-body function s^\dagger , and $\xi^\dagger \eta$ with s . The reason why this is allowed becomes clear when we look at the simple integral

$$\int dx \int dy e^{iy(x-a)} = 2\pi \int dx \delta(x-a) = 2\pi. \quad (\text{A.36})$$

We therefore insert Eq. (A.34) and Eq. (A.35) into Eq. (5.38), and pull out the integration over σ, σ^\dagger

$$\int \mathcal{D}\sigma \mathcal{D}\sigma^\dagger e^{iS^H[\sigma, \sigma^\dagger]} = \int \mathcal{D}\sigma \mathcal{D}\sigma^\dagger \mathcal{D}s \mathcal{D}s^\dagger \mathcal{D}\eta \mathcal{D}\eta^\dagger \mathcal{D}\xi \mathcal{D}\xi^\dagger \exp \left[iS_{\text{NR}} + \frac{i}{2} \int d(xy) [\sigma (s^\dagger - \eta^\dagger \xi) + \sigma^\dagger (s - \xi^\dagger \eta)] \right], \quad (\text{A.37})$$

such that we know we can substitute the two-body wave-functions where necessary, and write everything as

$$\begin{aligned} S^H[\sigma, \sigma^\dagger] = & -i \log \left[\int \mathcal{D}s \mathcal{D}s^\dagger \mathcal{D}\eta \mathcal{D}\eta^\dagger \mathcal{D}\xi \mathcal{D}\xi^\dagger \right. \\ & \exp \left\{ i \int d^4x d^4y (\eta^\dagger(x) \xi^\dagger(x)) K(x, y) \begin{pmatrix} \eta(y) \\ \xi(y) \end{pmatrix} \right. \\ & - \frac{i}{2} \int d(xy) s^\dagger(t, \mathbf{y}, \mathbf{x}) \mathcal{V}(\mathbf{x}, \mathbf{y}) s(t, \mathbf{y}, \mathbf{x}) \\ & \left. \left. + \frac{i}{2} \int d(xy) (\sigma^\dagger(t, \mathbf{x}, \mathbf{y}) s(t, \mathbf{y}, \mathbf{x}) + \sigma(t, \mathbf{x}, \mathbf{y}) s^\dagger(t, \mathbf{y}, \mathbf{x})) \right\} \right], \quad (\text{A.38}) \end{aligned}$$

A Calculation of Sommerfeld effect

where the matrix K consists of two terms

$$K(x, y) = K_0(x, y) + K_\sigma(x, y) \\ = \delta^{(4)}(x - y) \begin{pmatrix} \left(i\partial_{y^0} + \frac{\nabla_y^2}{2m}\right) & 0 \\ 0 & \left(i\partial_{y^0} - \frac{\nabla_y^2}{2m}\right) \end{pmatrix} \quad (\text{A.39})$$

$$- \frac{1}{2} \delta(x^0 - y^0) \begin{pmatrix} 0 & \sigma(y^0, \mathbf{x}, \mathbf{y}) \\ \sigma^\dagger(y^0, \mathbf{y}, \mathbf{x}) & 0 \end{pmatrix}, \quad (\text{A.40})$$

and

$$\mathcal{V}(\mathbf{x}, \mathbf{y}) = -\frac{\alpha}{|\mathbf{x} - \mathbf{y}|} - i\frac{2\pi\alpha^2}{m^2} \delta^{(3)}(\mathbf{x} - \mathbf{y}). \quad (\text{A.41})$$

We can split the functional integration over the fields in Eq. (A.38), since the first term in the exponential only depends on η, η^\dagger, ξ and ξ^\dagger , and the second and third terms depend on s, s^\dagger . The functional integration over the term in the exponential containing the matrix $K(x, y)$ results in $\det iK$. The remaining terms in the exponential we integrate over s and s^\dagger , such that we obtain

$$S^H[\sigma, \sigma^\dagger] = -i\text{Tr}[\log iK] + \frac{1}{2} \int d(xy) \sigma^\dagger(t, \mathbf{y}, \mathbf{x}) \mathcal{V}^{-1}(\mathbf{x}, \mathbf{y}) \sigma(t, \mathbf{y}, \mathbf{x}), \quad (\text{A.42})$$

where we have used that $\det iK = \exp[\text{Tr}[\log iK]]$, and \mathcal{V}^{-1} is the inverse of Eq. (A.41).

Concentrating first on the trace part, we find

$$-i\text{Tr} \log [iK(x, y)] = -i\text{Tr} \log [iK_0 (1 + K_0^{-1} K_\sigma)] \\ = -i\text{Tr} \log [iK_0(x, y)] - i\text{Tr} [K_0^{-1}(x, x_2) K_\sigma(x_2, y)] \\ + \frac{i}{2} \text{Tr} [K_0^{-1}(x, x_2) K_\sigma(x_2, x_3) K_0^{-1}(x_3, x_4) K_\sigma(x_4, y)], \quad (\text{A.43})$$

where in the last step we have Taylor expanded around $K_0^{-1} K_\sigma \ll 1$. The inverse of K_0 is given by

$$K_0^{-1}(x, y) = \begin{pmatrix} S_F(x, y) & 0 \\ 0 & \overline{S}_F(x, y) \end{pmatrix}, \quad (\text{A.44})$$

where

$$S_F(x, y) = \int \frac{d^4 p}{(2\pi)^4} \frac{e^{-ip(x-y)}}{p^0 - \frac{|\mathbf{p}|^2}{2m} + i\epsilon} \quad (\text{A.45})$$

$$\overline{S}_F(x, y) = \int \frac{d^4 p}{(2\pi)^4} \frac{e^{-ip(x-y)}}{p^0 + \frac{|\mathbf{p}|^2}{2m} - i\epsilon}, \quad (\text{A.46})$$

Since the first term in Eq. (A.43) does not depend on σ , and the second term is zero because of

$\text{Tr } \mathbf{K}_\sigma = 0$, only the third term is interesting to us. Therefore we can write the trace part as

$$\begin{aligned} -i\text{Tr}[\log i\mathbf{K}] &\approx \frac{i}{2}\text{Tr}[\mathbf{K}_0^{-1}(x, x_2)\mathbf{K}_\sigma(x_2, x_3)\mathbf{K}_0^{-1}(x_3, x_4)\mathbf{K}_\sigma(x_4, y)] \\ &= \frac{i}{2}\int d^4x d^4x_2 d^4x_3 d^4x_4 \times \\ &\quad S_F(x, x_2)\delta(x_2^0 - x_3^0)\sigma(x_3^0, \mathbf{x}_2, \mathbf{x}_3)\overline{S}_F(x_3, x_4)\delta(x_4^0 - x^0)\sigma^\dagger(x^0, \mathbf{x}_4, \mathbf{x}). \end{aligned} \quad (\text{A.47})$$

Now that we have successfully written the action in two-body states, we introduce new coordinates R and r according to Eq. (5.39)

$$R = \begin{pmatrix} t \\ \frac{\mathbf{x}+\mathbf{y}}{2} \end{pmatrix}, \quad \mathbf{r} = \mathbf{x} - \mathbf{y} \quad (\text{A.48})$$

that separate the motions of the center of mass from the relative motions. In the new variables the two-body state σ is given by

$$\sigma(\mathbf{r}, P) = \int d^4R \sigma(t, \mathbf{x}, \mathbf{y}) e^{iPR}, \quad (\text{A.49})$$

where P is the momentum of the center of mass and furthermore we have $\int d(xy) = d^4R d^3r$. We now consider the potential and annihilation term separately. Obtaining an expression for the potential part (second term in Eq. (A.42)) in the new coordinates does not require much work, and is simply given by

$$-\frac{1}{2}\int \frac{d^4P}{(2\pi)^4} d^3r \sigma(\mathbf{r}, P) \frac{r}{\alpha} \left(1 + i\frac{2\pi r\alpha}{m^2} \delta^{(3)}(\mathbf{r})\right)^{-1} \sigma^\dagger(\mathbf{r}', P). \quad (\text{A.50})$$

Calculating the trace part, however, involves a little more work. We can express Eq. (A.47) in the new coordinates as

$$\begin{aligned} &\frac{i}{2}\int d^4R d^4R' d^4r d^4r' \delta(r^0)\delta(r'^0) \int \frac{d^4P}{(2\pi)^4} \sigma(r, P) e^{-iPR} \int \frac{d^4K}{(2\pi)^4} \sigma^\dagger(r', K) e^{-iKR'} \\ &\int \frac{d^4p}{(2\pi)^4} \frac{e^{-ip(R'+\frac{r'}{2}-R-\frac{r}{2})}}{p^0 - \frac{|\mathbf{p}|^2}{2m} + i\epsilon} \int \frac{d^4k}{(2\pi)^4} \frac{e^{-ik(-R'+\frac{r'}{2}+R-\frac{r}{2})}}{k^0 + \frac{|\mathbf{k}|^2}{2m} - i\epsilon}. \end{aligned} \quad (\text{A.51})$$

After performing the integrals over R', p, R, K , we obtain

$$\begin{aligned} &\frac{i}{2}\int d^4r d^4r' \delta(r^0)\delta(r'^0) \int \frac{d^4P}{(2\pi)^4} \sigma(r, P) \sigma^\dagger(r', P) e^{i(r'-r)P/2} \int \frac{d^3k}{(2\pi)^4} e^{i(\mathbf{r}'-\mathbf{r})\mathbf{k}} \\ &\int dk^0 \frac{e^{-i(r'^0-r^0)k^0}}{(k^0 + P^0 - |\mathbf{k} + \mathbf{P}|^2/2m + i\epsilon)(k^0 + |\mathbf{k}|^2/2m - i\epsilon)}, \end{aligned} \quad (\text{A.52})$$

where the contour integral over k^0 yields $2\pi i (P^0 - |\mathbf{k}|^2/m - |\mathbf{P}|^2/2m - |\mathbf{k}||\mathbf{P}|/m)^{-1}$. Changing variables in momentum space to $\mathbf{q} = \mathbf{P}/2 + \mathbf{k}$ and integrating over r^0, r'^0 , we finally obtain the

A Calculation of Sommerfeld effect

following expression for the trace part

$$\frac{1}{2} \int d^3r d^3r' \int \frac{d^4P}{(2\pi)^4} \sigma(\mathbf{r}, P) \zeta(\mathbf{r} - \mathbf{r}', E) \sigma^\dagger(\mathbf{r}', P), \quad (\text{A.53})$$

where $E = P^0 - |\mathbf{P}|^2/4m$ is the internal energy of the two-body state and ζ is the function as given in Eq. (A.54):

$$\zeta(\mathbf{r}, E) = \int \frac{d^3q}{(2\pi)^3} \frac{me^{-i\mathbf{q}\cdot\mathbf{x}}}{|\mathbf{q}|^2 - mE - i\epsilon}, \quad (\text{A.54})$$

which satisfies

$$\left(-\frac{\nabla^2}{m} - E\right) \zeta(\mathbf{r}, E) = \delta^{(3)}(\mathbf{r}). \quad (\text{A.55})$$

Combining this result with the potential part, we obtain the two-body action cf. Eq. (5.41)

$$\begin{aligned} S^{II}[\sigma, \sigma^\dagger] = & \frac{1}{2} \int \frac{d^4P}{(2\pi)^4} d^3r \left(-\sigma^\dagger(\mathbf{r}, P) \frac{r}{\alpha} \left[1 + i \frac{2\pi r \alpha}{m^2} \delta^{(3)}(\mathbf{r}) \right]^{-1} \sigma(\mathbf{r}, P) \right. \\ & \left. + \int d^3r' \sigma^\dagger(\mathbf{r}', P) \zeta(\mathbf{r}' - \mathbf{r}, E) \sigma(\mathbf{r}, P) \right), \end{aligned} \quad (\text{A.56})$$

From this expression one can derive the Schrödinger equation as explained further in subsection 5.2.3.

A.2 Scalar toy model

Here we will follow the same approach as in the previous Appendix section to calculate the Sommerfeld enhancement for a toy model as defined by Eq. (6.18). First we integrate out the light fields l by shifting the light field

$$l'(x) = l(x) - i \int d^4y D_l(x-y) j(y), \quad (\text{A.57})$$

where the propagator of the light field is given by

$$D_l(x-y) = \int \frac{d^4p}{(2\pi)^4} \frac{i}{p^2 - m_l^2} e^{-ip\cdot(x-y)}, \quad (\text{A.58})$$

such that it satisfies the Klein-Gordon equation

$$(\partial^\mu \partial_\mu + m_l^2) D_l(x-y) = -i\delta^{(4)}(x-y). \quad (\text{A.59})$$

The current is here defined as $j(x) \equiv \frac{A}{2} H^2(x)$. Following the steps as in A.1.1 is straightforward, and we find that the effective Lagrangian is given by

$$S_{\text{eff}}[H] = \int d^4x \left[\frac{1}{2} \partial^\mu H \partial_\mu H + \frac{m_H^2}{2} H^2 \right] + \frac{i}{2} \int d^4x d^4y j(x) D_l(x-y) j(y). \quad (\text{A.60})$$

Integrating out the relativistic parts of the heavy fields is very similar to what we have done in A.1.1. The non-relativistic regime is defined as in Eq. (5.26), and the fields are split up in a non-relativistic and relativistic part in momentum space

$$H = \int_{\text{NR}} \frac{d^4 p}{(2\pi)^4} \tilde{H}(p) e^{-ipx} + \int_{\text{R}} \frac{d^4 p}{(2\pi)^4} \tilde{H}(p) e^{-ipx} = H_{\text{NR}}(x) + H_{\text{R}}(x). \quad (\text{A.61})$$

Considering that Eq. (A.60) contains only an interaction term that is proportional to $j(x)j(y)$, we can expand it in the non-relativistic and relativistic parts. We find that the interaction term with only non-relativistic fields gives the potential term:

$$S_{\text{pot}}[H_{\text{NR}}] = i \frac{A^2}{8} \int d^4 x d^4 y H_{\text{NR}}^2(x) D_I(x-y) H_{\text{NR}}^2(y), \quad (\text{A.62})$$

which corresponds to the diagram on the left in Fig. 6.2.

From the other remaining terms that include both relativistic and non-relativistic fields, we exclude terms that contain odd number of H_{NR} (H_{R}) due to kinematic reasons. In fact, only terms that are proportional to $H_{\text{NR}}(x)H_{\text{R}}(x)H_{\text{NR}}(y)H_{\text{R}}(y)$ interest us since they can build the box diagrams for the annihilation part (see Fig. 6.2 on the right), such that we have

$$S_{\text{int}} = i \frac{A^2}{2} \int d^4 x d^4 y [H_{\text{NR}}(x)H_{\text{R}}(x)D_I(x-y)H_{\text{NR}}(y)H_{\text{R}}(y)]. \quad (\text{A.63})$$

The coefficient is explained by the fact that, since the ordering of the H -fields is unimportant, there are four of such terms. Expanding $\exp iS_{\text{int}} \sim 1 + iS_{\text{int}} + (iS_{\text{int}})^2/2 + \dots$ to second order in the squared coupling A^2 , we find that the relevant term $(iS_{\text{int}})^2/2$ (without prefactors and space integrals) is given by

$$H_{\text{NR}}(x)H_{\text{R}}(x) \overbrace{D_I(x-y)H_{\text{NR}}(y)H_{\text{R}}(y)}^{\text{upper}} \overbrace{H_{\text{NR}}(z)H_{\text{R}}(z)}^{\text{lower}} D_I(z-w)H_{\text{NR}}(w)H_{\text{R}}(w), \quad (\text{A.64})$$

where the two possible contractions of the relativistic fields are indicated by the upper and lower lines, and the pre-factor is given by $A^4/8$. The contractions can be worked out in the same manner as in Eq. (A.14), but now the result is a relativistic propagator of the heavy field D_H^{R} . Since it is a scalar propagator, it has the same form as Eq. (A.58), except the integration is only over the relativistic part of momentum space and the mass in the denominator is exchanged for m_H . Having replaced the contractions by the heavy propagators we obtain

$$S_{\text{ann}}[H_{\text{NR}}] = -i \frac{A^4}{8} \int d^4 x d^4 y d^4 z d^4 w \left[H_{\text{NR}}(x)D_I(x-y)H_{\text{NR}}(y)D_H^{\text{R}}(y-z)H_{\text{NR}}(z)D_I(z-w)H_{\text{NR}}(w)D_H^{\text{R}}(w-x) \right. \\ \left. + H_{\text{NR}}(x)D_I(x-y)H_{\text{NR}}(y)D_H^{\text{R}}(y-w)H_{\text{NR}}(w)D_I(w-z)H_{\text{NR}}(z)D_H^{\text{R}}(z-x) \right], \quad (\text{A.65})$$

where the two different contractions again correspond to t- and u-channel box diagrams.

In order to perform the non-relativistic expansion of the action, we need the correct normaliza-

A Calculation of Sommerfeld effect

tion of the heavy fields, which is obtained from the kinetic term. The non-relativistic momentum space is again defined as in Eq. (5.26), and if we replace it into the propagator of the heavy fields D_H (similar to Eq. (A.58)), we obtain

$$D_H^{\text{NR}}(x) = \langle 0|TH_{\text{NR}}(x)H_{\text{NR}}(0)|0\rangle \simeq \frac{i}{2m_H} \int \frac{d^4k}{(2\pi)^4} \left[\frac{e^{-im_H t}}{k^0 - \frac{\mathbf{k}^2}{2m_H} + i\epsilon} - \frac{e^{im_H t}}{k^0 + \frac{\mathbf{k}^2}{2m_H} - i\epsilon} \right] e^{-ikx}, \quad (\text{A.66})$$

where again $k^\mu \equiv (\delta p^0, \mathbf{p})$. From this we derive that the non-relativistic H -field should look like

$$H_{\text{NR}}(x) = \frac{1}{\sqrt{2m_H}} [\phi(x)e^{-im_H t} + \phi^\dagger(x)e^{im_H t}], \quad (\text{A.67})$$

where the phases are just a convention and not physical. It must be understood that $\phi^\dagger(x)$ creates a heavy field and $\phi(x)$ annihilates one at x . Since the propagator in Eq. (A.66) is equivalent to the time-ordered product of two h -fields, substituting Eq. (6.23) we find that

$$\langle 0|TH_{\text{NR}}(x)H_{\text{NR}}(0)|0\rangle = \frac{1}{2m_H} e^{-im_H t} \langle 0|T\phi(x)\phi^\dagger(0)|0\rangle + \frac{1}{2m_H} e^{im_H t} \langle 0|T\phi^\dagger(x)\phi(0)|0\rangle. \quad (\text{A.68})$$

Matching this with Eq. (A.67), we find that the kinetic term is given by

$$S_{\text{kin}} = \int d^4x \phi^\dagger(x) \left[i\partial_t + \frac{\nabla^2}{2m_H} \right] \phi(x). \quad (\text{A.69})$$

For the potential term we need to consider the non-relativistic expansion of the product $H_{\text{NR}}^2(x)$. Since we are interested in the t-channel diagram, we can ignore the terms proportional to $\phi_x^\dagger \phi_x^\dagger$ (two outgoing heavy fields created at x) and $\phi_x \phi_x$ (two incoming heavy fields annihilated at x). The contributions $\phi_x \phi_x^\dagger$ and $\phi_x^\dagger \phi_x$ are actually the same, since the fields are scalar and the ordering is irrelevant. We therefore obtain

$$S_{\text{pot}} = i \frac{A^2}{8m_H^2} \int \frac{d^4k_1 d^4k_2 d^4k_3 d^4k_4}{(2\pi)^{16}} \int d^4x d^4y (\tilde{\phi}^\dagger(k_2) \tilde{\phi}(k_1)) (\tilde{\phi}^\dagger(k_4) \tilde{\phi}(k_3)) D_l(x-y) e^{-i(k_1-k_2)x - i(k_3-k_4)y}, \quad (\text{A.70})$$

where we have Fourier transformed the fields. Introducing new coordinates that describe the position of the center of mass R and the relative distance between the particles r like in Eq. (5.39), and working out the integral over R , we obtain an expression that includes

$$\int d^4r D_l(r) e^{i(k_2-k_1)r} = \tilde{D}_l(k_2-k_1) \simeq \frac{-i}{|\mathbf{k}_1 - \mathbf{k}_2|^2 + m_l^2}, \quad (\text{A.71})$$

such that we finally arrive at

$$S_{\text{pot}} = \frac{A^2}{8m_H^2} \int d^4x d^4y \frac{\delta(x^0 - y^0) e^{-m_l(x-y)}}{4\pi|\mathbf{x} - \mathbf{y}|} (\phi^\dagger \phi)_x (\phi^\dagger \phi)_y. \quad (\text{A.72})$$

As expected, the action now includes a Yukawa potential since the force carrier l is massive.

The fields should be reshuffled as to correspond to a scalaronium state, $(\phi_x^\dagger \phi_y^\dagger)(\phi_x \phi_y)$, where the right hand annihilates a spin-0 scalaronium state and the left hand creates one.

Finally, we have to do the same for the annihilation term given in Eq. (A.65). We will go through the calculation of the box diagram as depicted in Fig. 6.2 on the right, using the optical theorem to obtain the annihilation cross section of two heavy particles H into two light particles l . The annihilation term in the action reads

$$S_{\text{ann}}[H_{\text{NR}}] = -i \frac{A^4}{8} \int d^4x_1 d^4x_2 d^4x_3 d^4x_4 \left[H_{\text{NR}}(x_1) D_l(x_1 - x_4) H_{\text{NR}}(x_4) D_H^{\text{R}}(x_4 - x_3) H_{\text{NR}}(x_3) D_l(x_3 - x_2) H_{\text{NR}}(x_2) D_H^{\text{R}}(x_2 - x_1) + H_{\text{NR}}(x_1) D_l(x_1 - x_3) H_{\text{NR}}(x_3) D_H^{\text{R}}(x_3 - x_4) H_{\text{NR}}(x_4) D_l(x_4 - x_2) H_{\text{NR}}(x_2) D_H^{\text{R}}(x_2 - x_1) \right] \quad (\text{A.73})$$

where the first term is the ‘usual’ t-channel box diagram, and the second term with crossed l lines (u-channel). Since both diagrams contribute the same amount, the action reduces to one term with a factor 2 included. Going to Fourier space and integrating over position space we obtain

$$S_{\text{ann}} = -i \frac{A^4}{4} \int \frac{d^4p_1 d^4p_2 d^4p_3 d^4p_4}{(2\pi)^{16}} \int d^4k_1 d^4k_2 d^4k_3 d^4k_4 \tilde{H}(p_1) \tilde{H}(p_2) \tilde{H}(p_3) \tilde{H}(p_4) \frac{\delta^{(4)}(k_1 - k_2 + p_1)}{k_1^2 - m_H^2} \frac{\delta^{(4)}(k_2 - k_1 + p_2)}{k_2^2 - m_l^2 + i\epsilon} \frac{\delta^{(4)}(k_3 - k_2 + p_3)}{k_3^2 - m_H^2} \frac{\delta^{(4)}(k_4 - k_3 + p_4)}{k_4^2 - m_l^2 + i\epsilon}, \quad (\text{A.74})$$

where we omitted the NR subscripts for simplicity. Now we evaluate the cut in the diagram, meaning that the two light particles are put on-shell, and we have to use the $i\epsilon$ -prescription to perform the integrals over k_2 and k_4 . Using that $((x - a) \mp i\epsilon)^{-1} = \mathcal{P}[(x - a)^{-1}] \pm i\pi \delta(x - a)$, we get

$$S_{\text{ann}} = \frac{i\pi^2 A^4}{4} \int \frac{d^4p_1 d^4p_2 d^4p_3 d^4p_4}{(2\pi)^{16}} \int d^4k_1 d^4k_2 d^4k_3 d^4k_4 \tilde{H}(p_1) \tilde{H}(p_2) \tilde{H}(p_3) \tilde{H}(p_4) \delta^{(4)}(k_1 - k_2 + p_1) \delta^{(4)}(k_2 - k_1 + p_2) \delta^{(4)}(k_3 - k_2 + p_3) \delta^{(4)}(k_4 - k_3 + p_4) \frac{\delta(k_2^2 - m_l^2)}{k_1^2 - m_H^2} \frac{\delta(k_4^2 - m_l^2)}{k_3^2 - m_H^2}. \quad (\text{A.75})$$

Using the 4D delta-functions to write all loop momenta in the denominators in terms of k_4 , and keeping the integration over k_2 and k_4 , we get

$$S_{\text{ann}} = \frac{i\pi^2 A^4}{4} \int \frac{d^4p_1 d^4p_2 d^4p_3 d^4p_4}{(2\pi)^{16}} \delta^{(4)}(p_1 + p_2 + p_3 + p_4) \tilde{H}(p_1) \tilde{H}(p_2) \tilde{H}(p_3) \tilde{H}(p_4) \int d^4k_2 d^4k_4 \delta^{(4)}(k_4 - k_2 - p_1 - p_2) \frac{\delta(k_2^2 - m_l^2)}{(k_4 - p_1)^2 - m_H^2} \frac{\delta(k_4^2 - m_l^2)}{(k_4 + p_4)^2 - m_H^2}. \quad (\text{A.76})$$

A Calculation of Sommerfeld effect

Using $d^4k\delta(k^2 - m^2)\theta(k^0) = d^3k/2E_k$, where $\theta(k^0)$ is the Heavyside step function, we have

$$S_{\text{ann}} = \frac{i\pi^2 A^4}{4} \int \frac{d^4p_1 d^4p_2 d^4p_3 d^4p_4}{(2\pi)^{16}} \delta^{(4)}(p_1 + p_2 + p_3 + p_4) \tilde{H}(p_1) \tilde{H}(p_2) \tilde{H}(p_3) \tilde{H}(p_4) \\ \int \frac{d^3k'_2}{-2E'_2} \frac{d^3k_4}{2E_4} \delta^{(4)}(k_4 + k'_2 - p_1 - p_2) \frac{1}{(k_4 - p_1)^2 - m_H^2} \frac{1}{(k_4 + p_4)^2 - m_H^2}. \quad (\text{A.77})$$

Here, we have reversed the momentum $k'_2 = -k_2$ to let the light particle with momentum k_2 correspond to an outgoing momentum in the annihilation diagram.

After evaluating the integral over k'_2 , the delta function involving the momenta from the light particles becomes $\delta(E_4 + E'_2 - E_{\text{in}})$, where $E_{\text{in}} \equiv p_1^0 + p_2^0$. We now spend some time to simplify this delta-function. For this we can use that

$$\delta(f(k)) = \frac{\delta(k - k_0)}{\left| \frac{df(k_0)}{dk} \right|}, \quad (\text{A.78})$$

where k_0 is the root of the function $f(k)$. In our case this function is given by $f(|\mathbf{k}_4|) = E_4(|\mathbf{k}_4|) + E'_2(|\mathbf{k}_4|) - E_{\text{in}}$, and one can calculate that the root is given by $|\mathbf{k}_4|_0 = \frac{\sqrt{s}}{2} \sqrt{1 - 4m_l^2/s}$, where $s = E_{\text{in}}^2$ and we evaluated everything in the center of mass frame. The derivative of $f(|\mathbf{k}_4|)$ evaluated at the root can shown to be $2\sqrt{1 - 4m_l^2/s}$, such that the delta function can be substituted by

$$\delta(E_4(|\mathbf{k}_4|) + E'_2(|\mathbf{k}_4|) - E_{\text{in}}) = \frac{\delta\left(|\mathbf{k}_4| - \frac{\sqrt{s}}{2} \sqrt{1 - 4m_l^2/s}\right)}{2\sqrt{1 - 4m_l^2/s}}. \quad (\text{A.79})$$

With this, we can perform the remaining integral over k_4 , where we change to spherical coordinates $d^3k_4 = |\mathbf{k}_4|^2 \sin\theta d\theta d\phi d|\mathbf{k}_4|$ such that we obtain

$$S_{\text{ann}} = -i \frac{\pi^3 A^4}{8} \int \frac{d^4p_1 d^4p_2 d^4p_3 d^4p_4}{(2\pi)^{16}} \delta^{(4)}(p_1 + p_2 + p_3 + p_4) \tilde{H}(p_1) \tilde{H}(p_2) \tilde{H}(p_3) \tilde{H}(p_4) \\ \sqrt{1 - \frac{4m_l^2}{s}} \frac{1}{m_l^2 - \frac{s}{2}} \frac{1}{m_l^2 + \frac{s}{2}}, \quad (\text{A.80})$$

where we have assumed that in the non-relativistic limit, the velocity of the heavy particles disappears: $\beta_h = (2\mathbf{p}_{1,\text{cm}})/\sqrt{s} = (2\mathbf{p}_{2,\text{cm}})/\sqrt{s} \rightarrow 0$. In fact, the center of mass energy squared can be written in terms of the Møller velocity of the heavy particles

$$s \equiv 4m_H^2 \left(1 + \frac{v^2}{4}\right). \quad (\text{A.81})$$

Inserting this into Eq. (A.80) and only keeping the leading order terms in v , we get

$$S_{\text{ann}} = i \frac{\pi^3 A^4}{32 m_H^4} \int \frac{d^4 p_1 d^4 p_2 d^4 p_3 d^4 p_4}{(2\pi)^{16}} \delta^{(4)}(p_1 + p_2 + p_3 + p_4) \tilde{H}(p_1) \tilde{H}(p_2) \tilde{H}(p_3) \tilde{H}(p_4) \frac{\sqrt{1 - \frac{m_l^2}{m_H^2}}}{1 - \frac{m_l^4}{4m_H^4}}. \quad (\text{A.82})$$

Finally, we Fourier transform back, which is easily done since there are no terms depending on momentum any more. Expanding the term $H(x)^4$, we see that there are in total six terms that contain $(\phi_x \phi_x^\dagger)^2$, which gives in total $3/(2m_H^2) (\phi_x \phi_x^\dagger)^2$. The Fourier transform gives a factor of $(2\pi)^{-4}$ such that we get

$$S_{\text{ann}} = i \frac{3A^4}{1024\pi m_H^6} \int d^4 x (\phi(x) \phi^\dagger(x))^2 \frac{\sqrt{1 - \frac{m_l^2}{m_H^2}}}{1 - \frac{m_l^4}{4m_H^4}}. \quad (\text{A.83})$$

To obtain the two-body action, we again introduce auxiliary fields $s(t, \mathbf{x}, \mathbf{y})$ and $\sigma(t, \mathbf{x}, \mathbf{y})$ and their hermitian conjugates, where the former will replace $\phi(t, \mathbf{x}) \phi(t, \mathbf{y})$ (see for comparison Eq. (A.34) and Eq. (A.35)). Integrating over the fields $\sigma, \sigma^\dagger, s, s^\dagger$, we obtain the same equation as in Eq. (A.42), except that $K(x, y) \rightarrow \frac{1}{2} K'(x, y)$ with

$$K'(x, y) = K'_0(x, y) + K'_\sigma(x, y) = \delta^{(4)}(x - y) \begin{pmatrix} \left(i\partial_{y^0} + \frac{\nabla_y^2}{2m_H}\right) & 0 \\ 0 & \left(-i\partial_{y^0} + \frac{\nabla_y^2}{2m_H}\right) \end{pmatrix} \quad (\text{A.84})$$

$$- \delta(x^0 - y^0) \begin{pmatrix} 0 & \sigma(y^0, \mathbf{x}, \mathbf{y}) \\ \sigma^\dagger(y^0, \mathbf{y}, \mathbf{x}) & 0 \end{pmatrix}, \quad (\text{A.85})$$

and \mathcal{V} is now given by

$$\mathcal{V}(\mathbf{x}, \mathbf{y}) = - \frac{A^2}{16\pi m_H^2} \frac{e^{-m_l |\mathbf{x} - \mathbf{y}|}}{|\mathbf{x} - \mathbf{y}|} - i \frac{3}{512\pi} \frac{A^4}{m_H^6} \frac{\sqrt{1 - \frac{m_l^2}{m_H^2}}}{1 - \frac{m_l^4}{4m_H^4}} \delta^{(3)}(\mathbf{x} - \mathbf{y}). \quad (\text{A.86})$$

For the trace part from Eq. (A.42) we can closely follow the calculation as presented in section A.1.2. Carefully noting the minus-signs, we end up with exactly the same expression as in Eq. (A.43). This ensures us that we can directly use the final result from Eq. (5.41) for our toy model here, except replacing \mathcal{V} with the one we defined in Eq. (A.86). This results in a Schrödinger equation exactly as discussed for the Coulomb case, but now with the potential $V(r) = \mathcal{V}(r)$ as in Eq. (A.86), where we have replaced $|\mathbf{x} - \mathbf{y}|$ with r .

A.3 Right-handed sneutrino Dark Matter

A.3.1 Box diagram with Z -boson intermediate states

We start with the effective Lagrangian introduced in Eq. (6.27), and consider the box diagram with two Z -boson intermediate states, which is described by

$$S_{\text{ann}}^Z[\tilde{\nu}, \tilde{\nu}^*] = -i \frac{B^4}{4} \int d^4x_1 d^4x_2 d^4x_3 d^4x_4 \left[\tilde{\nu}(x_1) \overleftrightarrow{\partial}_1^\mu D^\nu(x_1 - x_2) D_{\mu\nu}^Z(x_2 - x_4) \overleftrightarrow{\partial}_2^\nu \tilde{\nu}^*(x_2) \times \tilde{\nu}(x_3) \overleftrightarrow{\partial}_3^\alpha D^\nu(x_4 - x_3) D_{\alpha\beta}^Z(x_3 - x_1) \overleftrightarrow{\partial}_4^\beta \tilde{\nu}^*(x_4) \right], \quad (\text{A.87})$$

where $\overleftrightarrow{\partial}_i^\mu$ is an antisymmetric derivative that works on x_i in both directions. Transforming this equation to Fourier space and working out the derivatives, we obtain

$$S_{\text{ann}}^Z = -i \frac{B^4}{4} \int \frac{d^4p_1 d^4p_2 d^4p_3 d^4p_4}{(2\pi)^{16}} \int d^4k_1 d^4k_2 d^4k_3 d^4k_4 \tilde{N}(p_1) \tilde{N}^*(p_2) \tilde{N}(p_3) \tilde{N}^*(p_4) (p_1 + k_1)^\mu (k_3 - p_3)^\nu (k_1 - p_2)^\alpha (p_4 + k_3)^\beta \left(g_{\mu\nu} - \frac{k_{2,\mu} k_{2,\nu}}{m_Z^2} \right) \left(g_{\alpha\beta} - \frac{k_{2,\alpha} k_{2,\beta}}{m_Z^2} \right) \frac{\delta^{(4)}(k_1 - k_4 - p_1)}{k_1^2 - m_{\tilde{\nu},R,i}^2} \frac{\delta^{(4)}(k_2 - k_1 - p_2)}{k_2^2 - m_Z^2 + i\epsilon} \frac{\delta^{(4)}(k_3 - k_2 - p_4)}{k_3^2 - m_{\tilde{\nu},R,f}^2} \frac{\delta^{(4)}(k_4 - k_3 - p_3)}{k_4^2 - m_Z^2 + i\epsilon}, \quad (\text{A.88})$$

where $\tilde{N}(p) = \int d^4x \tilde{\nu}(x) e^{ipx}$ is the Fourier transform of the sneutrino field. Throughout this calculation we will keep track of the (relativistic (R)) initial (i) and final (f) states where necessary.

First, we focus on simplifying the product with Greek indices. Using the delta functions to simplify the momenta we obtain

$$(p_1 + k_1)^\mu (k_3 - p_3)^\nu (k_1 - p_2)^\alpha (p_4 + k_3)^\beta = (k_4 + 2p_1)^\mu (k_4 - 2p_3)^\nu (k_2 - 2p_2)^\alpha (k_2 + 2p_4)^\beta. \quad (\text{A.89})$$

The whole problem now splits into two separate factors which have a very similar structure:

$$(k_n - 2p_l)^\lambda (k_n + 2p_m)^\rho \left(g_{\lambda\rho} - \frac{k_{n,\lambda} k_{n,\rho}}{m_Z^2} \right), \quad (\text{A.90})$$

where

$$n = \begin{cases} 2, & l = 2, \quad m = 4, \quad \lambda = \alpha, \quad \rho = \beta \\ 4, & l = 3, \quad m = 1, \quad \lambda = \mu, \quad \rho = \nu \end{cases}. \quad (\text{A.91})$$

After some algebra, the expression in Eq. (A.90) simplifies to

$$-4 \left(p_l \cdot p_m - \frac{k_n \cdot p_l k_n \cdot p_m}{m_Z^2} \right). \quad (\text{A.92})$$

Working out this expression in the center-of-mass frame where $p_l^0 = p_m^0 = (\sqrt{s}/2)$ and $\mathbf{p}_l = -\mathbf{p}_m$.

and using the fact that we are in the non-relativistic limit, $p^0 \gg \mathbf{p}$, we obtain the following approximation

$$s \left(\frac{E_n^2}{m_Z^2} - 1 \right), \quad (\text{A.93})$$

where we have neglected all terms proportional to $|\mathbf{p}|^2$ and adopted $k_n^0 = E_n$. The full product in the action can thus be replaced by two of these factors with $n = 2, 4$ in a later stage in the calculation where we perform the non-relativistic expansion and evaluate everything in the center-of-mass frame.

Now we turn back to our long expression for the action. We follow the treatment described in appendix A.2 exactly, first evaluating the 4-dimensional delta functions, then using the optical theorem to obtain

$$\begin{aligned} S_{\text{ann}}^Z &= i4B^4 \pi^2 \int \frac{d^4 p_1 d^4 p_2 d^4 p_3 d^4 p_4}{(2\pi)^{16}} \delta^{(4)}(p_1 + p_2 - p_3 - p_4) \tilde{N}(p_1) \tilde{N}^*(p_2) \tilde{N}(p_3) \tilde{N}^*(p_4) \\ &\quad \int d^4 k_2 d^4 k_4 \frac{\delta(k_2^2 - m_Z^2)}{(k_2 - p_2)^2 - m_{\tilde{\nu},R,i}^2} \frac{\delta(k_4^2 - m_Z^2)}{(k_4 + p_4)^2 - m_{\tilde{\nu},R,f}^2} \\ &\quad \left(p_2 \cdot p_4 - \frac{k_2 \cdot p_2 k_2 \cdot p_4}{m_Z^2} \right) \left(p_1 \cdot p_3 - \frac{k_4 \cdot p_1 k_4 \cdot p_3}{m_Z^2} \right) \end{aligned} \quad (\text{A.94})$$

Apart from the factor on the last line, the problem is exactly the same as described for the toy model. We therefore proceed in the same fashion, substituting $k_4 \rightarrow -k'_4$ and integrating over k'_4 and k_2^0 to get

$$\begin{aligned} S_{\text{ann}}^Z &= i4B^4 \pi^2 \int \frac{d^4 p_1 d^4 p_2 d^4 p_3 d^4 p_4}{(2\pi)^{16}} \delta^{(4)}(p_1 + p_2 - p_3 - p_4) \tilde{N}(p_1) \tilde{N}^*(p_2) \tilde{N}(p_3) \tilde{N}^*(p_4) \\ &\quad \int \frac{d^3 k_2 d^3 k'_4}{2E_2 - 2E'_4} \delta^{(4)}(p_1 + p_2 - k_2 - k'_4) \frac{\delta(k_2^2 - m_Z^2)}{(k_2 - p_2)^2 - m_{\tilde{\nu},R,i}^2} \frac{\delta(k'^2_4 - m_Z^2)}{(k_2 + p_4)^2 - m_{\tilde{\nu},R,f}^2} \\ &\quad \left(p_2 \cdot p_4 - \frac{k_2 \cdot p_2 k_2 \cdot p_4}{m_Z^2} \right) \left(p_1 \cdot p_3 - \frac{k'_4 \cdot p_1 k'_4 \cdot p_3}{m_Z^2} \right). \end{aligned} \quad (\text{A.95})$$

As a next step, we want to evaluate the 3-dimensional integrals over the momenta of the Z-bosons. Integrating over k'_4 will turn the delta function involving k_2, k'_4 into $\delta(E_2 + E'_4 - p_1^0 - p_2^0)$, which we can rewrite in the same manner as described in appendix A.2. We can therefore replace the one-dimensional delta function with

$$\delta(E_2(|\mathbf{k}_2|) + E'_4(|\mathbf{k}_2|) - E_{\text{in}}) = \frac{\delta \left(|\mathbf{k}_2| - \frac{\sqrt{s}}{2} \sqrt{1 - 4m_Z^2/s} \right)}{2\sqrt{1 - 4m_Z^2/s}}, \quad (\text{A.96})$$

which is equivalent to Eq. (A.79). Note that we evaluated this expression in the center-of-mass frame.

We now implement this expression into Eq. (A.95), and perform the 3-dimensional integral

A Calculation of Sommerfeld effect

over k_2 , where we replace $d^3k_2 = |\mathbf{k}_2|^2 \sin \theta d\theta d\phi d|\mathbf{k}_2|$. We only take into account the terms leading order in \mathbf{p}_i such that we can use Eq. (A.93). The full expression becomes

$$S_{\text{ann}}^Z = -i \frac{B^4 \pi^3}{8} \int \frac{d^4 p_1 d^4 p_2 d^4 p_3 d^4 p_4}{(2\pi)^{16}} \delta^{(4)}(p_1 + p_2 - p_3 - p_4) \tilde{N}(p_1) \tilde{N}^*(p_2) \tilde{N}(p_3) \tilde{N}^*(p_4) \frac{\sqrt{1 - 4m_Z^2/s}}{(m_Z^2 - s/2 + \Delta_i)(m_Z^2 + s/2 + \Delta_f)} s^2 \left(1 - \frac{s}{4m_Z^2}\right)^2, \quad (\text{A.97})$$

where we have introduced $\Delta_i = (m_{\tilde{\nu},i}^2 - m_{\tilde{\nu},R,i}^2)$ (and equivalent for f). In comparison with the toy model, the only difference – apart from the mediator mass and the coefficient in front – is the factor $s^2 (1 - s/(4m_Z^2))^2$ due to the Z-boson propagators.

We use now substitution $s = 4m_{\tilde{\nu},i}^2(1 + v^2/4)$, and only keep the leading order terms in v , such that we arrive at

$$S_{\text{ann}}^Z = i \frac{B^4 \pi^3}{2} \int \frac{d^4 p_1 d^4 p_2 d^4 p_3 d^4 p_4}{(2\pi)^{16}} \delta^{(4)}(p_1 + p_2 - p_3 - p_4) \tilde{N}(p_1) \tilde{N}^*(p_2) \tilde{N}(p_3) \tilde{N}^*(p_4) \frac{\sqrt{1 - m_Z^2/m_{\tilde{\nu},i}^2}}{\left(1 - m_Z^2/(2m_{\tilde{\nu},i}^2) - \Delta_i/(2m_{\tilde{\nu},i}^2)\right) \left(1 + m_Z^2/(2m_{\tilde{\nu},i}^2) + \Delta_f/(2m_{\tilde{\nu},i}^2)\right)} \left(1 - \frac{m_{\tilde{\nu},i}^2}{m_Z^2}\right)^2. \quad (\text{A.98})$$

Comparing this expression to Eq. (A.82), we see some resemblance; if the relativistic states are the same as the in- or out-coming ones, i.e., $\Delta_i = \Delta_f = 0$, the expression reduces to the toy model result apart from the extra factor due to the Z-boson field.

We now Fourier transform back the sneutrino fields, which gives a factor of $(2\pi)^{-4}$. The non-relativistic expansion of $(\tilde{\nu} \tilde{\nu}^*)^2$ gives two possible states in the t-channel. Here, we need to be extra careful with the normalization, which gives $(2m_{\tilde{\nu},i})^{-1/2}$ for an initial sneutrino and $(2m_{\tilde{\nu},f})^{-1/2}$ for a final sneutrino, which do not necessarily need to be the same states. Finally we obtain

$$S_{\text{ann}}^Z = i \frac{B^4}{128\pi m_{\tilde{\nu},i} m_{\tilde{\nu},f}} \int d^4x [a_i(x) a_i^*(x) b_f^*(x) b_f(x) + a_f(x) a_f^*(x) b_i^*(x) b_i(x)] \times \frac{\sqrt{1 - m_Z^2/m_{\tilde{\nu},i}^2}}{\left(1 - m_Z^2/(2m_{\tilde{\nu},i}^2) - \Delta_i/(2m_{\tilde{\nu},i}^2)\right) \left(1 + m_Z^2/(2m_{\tilde{\nu},i}^2) + \Delta_f/(2m_{\tilde{\nu},i}^2)\right)} \left(1 - \frac{m_{\tilde{\nu},i}^2}{m_Z^2}\right)^2. \quad (\text{A.99})$$

A.3.2 Annihilation matrix

Here we present the full expressions for the annihilation matrix Γ of the sneutrino model. Due to the lengthy expressions, the results are not given in matrix form but as individual matrix elements.

Annihilation of two sneutrinos into hh is given by the following matrix elements:

$$\Gamma_{11}^h = \frac{A_{\tilde{\nu}}^4 \sqrt{1 - \frac{m_h^2}{m_{\tilde{\nu},1}^2}}}{2048\pi m_{\tilde{\nu},1}^2 (4m_{\tilde{\nu},1}^4 - m_h^4)} \times \frac{(2m_{\tilde{\nu},1}^2 + m_h^2 + 4\text{Sin}[\theta_{\tilde{\nu}}]^2 (-\delta m^2 - 2\delta m m_{\tilde{\nu},1} + 2m_{\tilde{\nu},1}^2 + m_h^2)) \times (2m_{\tilde{\nu},1}^2 - m_h^2 + 4\text{Sin}[\theta_{\tilde{\nu}}]^2 (\delta m^2 + 2\delta m m_{\tilde{\nu},1} + 2m_{\tilde{\nu},1}^2 - m_h^2))}{(-\delta m^4 - 4\delta m^3 m_{\tilde{\nu},1} - 4\delta m^2 m_{\tilde{\nu},1}^2 + 4m_{\tilde{\nu},1}^4 + 2\delta m (\delta m + 2m_{\tilde{\nu},1}) m_h^2 - m_h^4)}, \quad (\text{A.100})$$

$$\Gamma_{12}^h = \frac{A_{\tilde{\nu}}^4 \sqrt{1 - \frac{m_h^2}{m_{\tilde{\nu},1}^2}}}{4096\pi m_{\tilde{\nu},1} (\delta m + m_{\tilde{\nu},1})} \times \frac{(2m_{\tilde{\nu},1}^2 - m_h^2 + 4\text{Sin}[\theta_{\tilde{\nu}}]^2 (\delta m^2 + 2\delta m m_{\tilde{\nu},1} + 2m_{\tilde{\nu},1}^2 - m_h^2))}{(2m_{\tilde{\nu},1}^2 - m_h^2) (\delta m^2 + 2\delta m m_{\tilde{\nu},1} + 2m_{\tilde{\nu},1}^2 - m_h^2) (\delta m^2 + 2\delta m m_{\tilde{\nu},1} + 2m_{\tilde{\nu},1}^2 + m_h^2)}, \quad (\text{A.101})$$

$$\Gamma_{21}^h = \frac{A_{\tilde{\nu}}^4 \sqrt{1 - \frac{m_h^2}{(\delta m + m_{\tilde{\nu},1})^2}}}{4096\pi m_{\tilde{\nu},1} (\delta m + m_{\tilde{\nu},1})} (2(\delta m + m_{\tilde{\nu},1})^2 + m_h^2)^{-1} \times \frac{(2(\delta m + m_{\tilde{\nu},1})^2 + m_h^2 + 4\text{Sin}[\theta_{\tilde{\nu}}]^2 (\delta m^2 + 2\delta m m_{\tilde{\nu},1} + 2m_{\tilde{\nu},1}^2 + m_h^2))}{(\delta m^2 + 2\delta m m_{\tilde{\nu},1} + 2m_{\tilde{\nu},1}^2 - m_h^2) (\delta m^2 + 2\delta m m_{\tilde{\nu},1} + 2m_{\tilde{\nu},1}^2 + m_h^2)}, \quad (\text{A.102})$$

$$\Gamma_{22}^h = \frac{A_{\tilde{\nu}}^4 \sqrt{1 - \frac{m_h^2}{(\delta m + m_{\tilde{\nu},1})^2}}}{2048\pi (\delta m + m_{\tilde{\nu},1})^2} \times (\delta m^2 + 2\delta m m_{\tilde{\nu},1} + 2m_{\tilde{\nu},1}^2 - m_h^2)^{-1} (3\delta m^2 + 6\delta m m_{\tilde{\nu},1} + 2m_{\tilde{\nu},1}^2 + m_h^2)^{-1}. \quad (\text{A.103})$$

A Calculation of Sommerfeld effect

Sneutrinos annihilating into two Z-bosons gives rise to the following matrix elements:

$$\Gamma_{11}^Z = \frac{\pi\alpha^2 \text{Sin}[\theta_{\bar{\nu}}]^4}{16m_Z^4 \text{Sin}[2\theta_W]^4} \frac{m_{\bar{\nu},1}^2 (m_{\bar{\nu},1} - m_Z)^2 (m_{\bar{\nu},1} + m_Z)^2 \sqrt{1 - \frac{m_Z^2}{m_{\bar{\nu},1}^2}}}{(-4m_{\bar{\nu},1}^4 + m_Z^4)} \times$$

$$(\delta m^4 + 4\delta m^3 m_{\bar{\nu},1} + 4\delta m^2 m_{\bar{\nu},1}^2 - 4m_{\bar{\nu},1}^4 - 2\delta m (\delta m + 2m_{\bar{\nu},1}) m_Z^2 + m_Z^4)^{-1} \times$$

$$[-3\delta m^4 - 12\delta m^3 m_{\bar{\nu},1} - 12\delta m^2 m_{\bar{\nu},1}^2 + 32m_{\bar{\nu},1}^4 + 8\delta m (\delta m + 2m_{\bar{\nu},1}) m_Z^2 - 8m_Z^4$$

$$- \delta m (\delta m + 2m_{\bar{\nu},1}) (\delta m \text{Cos}[4\theta_{\bar{\nu}}] (\delta m + 2m_{\bar{\nu},1}) - 4\text{Cos}[2\theta_{\bar{\nu}}] (\delta m^2 + 2\delta m m_{\bar{\nu},1} - 2m_Z^2))], \quad (\text{A.104})$$

$$\Gamma_{12}^Z = \frac{\pi\alpha^2 \text{Sin}[2\theta_{\bar{\nu}}]^2}{128m_Z^4 \text{Sin}[2\theta_W]^4} \frac{m_{\bar{\nu},1}^3 (m_{\bar{\nu},1} - m_Z)^2 (m_{\bar{\nu},1} + m_Z)^2 \sqrt{1 - \frac{m_Z^2}{m_{\bar{\nu},1}^2}}}{(\delta m + m_{\bar{\nu},1}) (4m_{\bar{\nu},1}^4 - m_Z^4)} \times$$

$$(-(\delta m^2 + 2\delta m m_{\bar{\nu},1} + 2m_{\bar{\nu},1}^2)^2 + m_Z^4)^{-1} \times$$

$$[-\delta m^4 - 4\delta m^3 m_{\bar{\nu},1} - 20\delta m^2 m_{\bar{\nu},1}^2 - 32\delta m m_{\bar{\nu},1}^3$$

$$+ \delta m (\delta m + 2m_{\bar{\nu},1}) (\delta m \text{Cos}[4\theta_{\bar{\nu}}] (\delta m + 2m_{\bar{\nu},1}) + 8\text{Cos}[2\theta_{\bar{\nu}}] m_Z^2) + 8(-4m_{\bar{\nu},1}^4 + m_Z^4)], \quad (\text{A.105})$$

$$\Gamma_{21}^Z = \frac{\pi\alpha^2 \text{Sin}[2\theta_{\bar{\nu}}]^2}{128m_Z^4 \text{Sin}[2\theta_W]^4} \frac{(\delta m + m_{\bar{\nu},1})^3 (\delta m + m_{\bar{\nu},1} - m_Z)^2 (\delta m + m_{\bar{\nu},1} + m_Z)^2 \sqrt{1 - \frac{m_Z^2}{(\delta m + m_{\bar{\nu},1})^2}}}{m_{\bar{\nu},1} (\delta m^2 + 2\delta m m_{\bar{\nu},1} + 2m_{\bar{\nu},1}^2 - m_Z^2) (-2(\delta m + m_{\bar{\nu},1})^2 + m_Z^2)} \times$$

$$(\delta m^2 + 2\delta m m_{\bar{\nu},1} + 2m_{\bar{\nu},1}^2 + m_Z^2)^{-1} (2(\delta m + m_{\bar{\nu},1})^2 + m_Z^2)^{-1} \times$$

$$[-17\delta m^4 - 68\delta m^3 m_{\bar{\nu},1} - 116\delta m^2 m_{\bar{\nu},1}^2 - 96\delta m m_{\bar{\nu},1}^3$$

$$+ \delta m (\delta m + 2m_{\bar{\nu},1}) (\delta m \text{Cos}[4\theta_{\bar{\nu}}] (\delta m + 2m_{\bar{\nu},1}) + 8\text{Cos}[2\theta_{\bar{\nu}}] m_Z^2) + 8(-4m_{\bar{\nu},1}^4 + m_Z^4)], \quad (\text{A.106})$$

$$\Gamma_{22}^Z = \frac{\pi\alpha^2 \text{Cos}[\theta_{\bar{\nu}}]^4}{16m_Z^4 \text{Sin}[2\theta_W]^4} \frac{(\delta m + m_{\bar{\nu},1})^2 (\delta m + m_{\bar{\nu},1} - m_Z)^2 (\delta m + m_{\bar{\nu},1} + m_Z)^2 \sqrt{1 - \frac{m_Z^2}{(\delta m + m_{\bar{\nu},1})^2}}}{(-\delta m^2 - 2\delta m m_{\bar{\nu},1} - 2m_{\bar{\nu},1}^2 + m_Z^2) (3\delta m^2 + 6\delta m m_{\bar{\nu},1} + 2m_{\bar{\nu},1}^2 + m_Z^2)} \times$$

$$(-2(\delta m + m_{\bar{\nu},1})^2 + m_Z^2)^{-1} (-2(\delta m + m_{\bar{\nu},1})^2 - m_Z^2)^{-1} \times$$

$$[-29\delta m^4 - 116\delta m^3 m_{\bar{\nu},1} - 180\delta m^2 m_{\bar{\nu},1}^2 - 128\delta m m_{\bar{\nu},1}^3$$

$$- 32m_{\bar{\nu},1}^4 + 8\delta m (\delta m + 2m_{\bar{\nu},1}) m_Z^2 + 8m_Z^4$$

$$+ \delta m (\delta m + 2m_{\bar{\nu},1}) (\delta m \text{Cos}[4\theta_{\bar{\nu}}] (\delta m + 2m_{\bar{\nu},1}) + 4\text{Cos}[2\theta_{\bar{\nu}}] (\delta m^2 + 2\delta m m_{\bar{\nu},1} + 2m_Z^2))]. \quad (\text{A.107})$$

Bibliography

- [1] L. G. van den Aarssen, T. Bringmann, and Y. C. Goedecke, “Thermal decoupling and the smallest subhalo mass in dark matter models with Sommerfeld-enhanced annihilation rates,” *Phys.Rev.* **D85** (2012) 123512, arXiv:1202.5456 [hep-ph].
- [2] L. G. van den Aarssen, T. Bringmann, and C. Pfrommer, “Is Dark Matter with Long-Range Interactions a Solution to All Small-Scale Problems of Λ Cold Dark Matter Cosmology?,” *Phys. Rev. Lett.* **109** (2012) 231301, arXiv:1205.5809 [astro-ph.CO].
- [3] T. van Albada, J. N. Bahcall, K. Begeman, and R. Sancisi, “THE DISTRIBUTION OF DARK MATTER IN THE SPIRAL GALAXY NGC-3198,” *Astrophys.J.* **295** (1985) 305–313.
- [4] D. Clowe, M. Bradač, A. H. Gonzalez, M. Markevitch, S. W. Randall, *et al.*, “A direct empirical proof of the existence of dark matter,” *Astrophys.J.* **648** (2006) L109–L113, arXiv:astro-ph/0608407 [astro-ph].
- [5] D. Kazakov, “Supersymmetry on the Run: LHC and Dark Matter,” *Nucl.Phys.Proc.Suppl.* **203-204** (2010) 118–154, arXiv:1010.5419 [hep-ph].
- [6] M. Boylan-Kolchin, V. Springel, S. D. White, A. Jenkins, and G. Lemson, “Resolving Cosmic Structure Formation with the Millennium-II Simulation,” *Mon.Not.Roy.Astron.Soc.* **398** (2009) 1150, arXiv:0903.3041 [astro-ph.CO].
- [7] A. Kravtsov, “Dark Matter Substructure and Dwarf Galactic Satellites,” *Adv.Astron.* **2010** (2010) 281913, arXiv:0906.3295 [astro-ph.CO].
- [8] W. de Blok, S. S. McGaugh, A. Bosma, and V. C. Rubin, “Mass density profiles of LSB galaxies,” *Astrophys.J.* **552** (2001) L23–L26, arXiv:astro-ph/0103102 [astro-ph].
- [9] M. Boylan-Kolchin, J. S. Bullock, and M. Kaplinghat, “The Milky Way’s bright satellites as an apparent failure of Λ CDM,” *Mon.Not.Roy.Astron.Soc.* **422** (2012) 1203–1218, arXiv:1111.2048 [astro-ph.CO].
- [10] M. R. Buckley and P. J. Fox, “Dark Matter Self-Interactions and Light Force Carriers,” *Phys.Rev.* **D81** (2010) 083522, arXiv:0911.3898 [hep-ph].
- [11] S. A. Khrapak, A. V. Ivlev, G. E. Morfill, and S. K. Zhdanov, “Scattering in the attractive yukawa potential in the limit of strong interaction,” *Phys. Rev. Lett.* **90** (Jun, 2003) 225002.

Bibliography

- [12] S. Khrapak, A. Ivlev, G. Morfill, S. Zhadanov, and H. Thomas, “Scattering in the Attractive Yukawa Potential: application to the ion-drag force in complex plasmas,” *IEEE. Trans. Pl. Sc.* **32** (2004) 555.
- [13] M. Vogelsberger, J. Zavala, and A. Loeb, “Subhaloes in Self-Interacting Galactic Dark Matter Haloes,” *Mon.Not.Roy.Astron.Soc.* **423** (2012) 3740–3752, arXiv:1201.5892 [astro-ph.CO].
- [14] S. Weinberg, *Cosmology*. Oxford University Press, 2008.
- [15] G. Bertone, D. Hooper, and J. Silk, “Particle dark matter: Evidence, candidates and constraints,” *Phys.Rept.* **405** (2005) 279–390, arXiv:hep-ph/0404175 [hep-ph].
- [16] G. Bertone, ed., *Particle Dark Matter: Observations, Models and Searches*. Cambridge University Press, 2010.
- [17] L. Bergström, “Nonbaryonic dark matter: Observational evidence and detection methods,” *Rept.Prog.Phys.* **63** (2000) 793, arXiv:hep-ph/0002126 [hep-ph].
- [18] SDSS Collaboration, K. N. Abazajian *et al.*, “The Seventh Data Release of the Sloan Digital Sky Survey,” *Astrophys.J.Suppl.* **182** (2009) 543–558, arXiv:0812.0649 [astro-ph].
- [19] WMAP Collaboration, E. Komatsu *et al.*, “Seven-Year Wilkinson Microwave Anisotropy Probe (WMAP) Observations: Cosmological Interpretation,” *Astrophys.J.Suppl.* **192** (2011) 18, arXiv:1001.4538 [astro-ph.CO].
- [20] E. Hubble, “A relation between distance and radial velocity among extra-galactic nebulae,” *Proc.Nat.Acad.Sci.* **15** no. 3, (1929) 168–173.
- [21] A. G. Riess, L. Macri, S. Casertano, M. Sosey, H. Lampeitl, *et al.*, “A Redetermination of the Hubble Constant with the Hubble Space Telescope from a Differential Distance Ladder,” *Astrophys.J.* **699** (2009) 539–563, arXiv:0905.0695 [astro-ph.CO].
- [22] Supernova Search Team Collaboration, A. G. Riess *et al.*, “Observational evidence from supernovae for an accelerating universe and a cosmological constant,” *Astron.J.* **116** (1998) 1009–1038, arXiv:astro-ph/9805201 [astro-ph].
- [23] Supernova Cosmology Project Collaboration, S. Perlmutter *et al.*, “Measurements of Ω and Λ from 42 high-redshift supernovae,” *Astrophys.J.* **517** (1999) 565–586, arXiv:astro-ph/9812133 [astro-ph].
- [24] A. Friedmann, “Über die Möglichkeit einer Welt mit konstanter negativer Krümmung des Raumes,” *Z.Phys.* **21** (1924) 326–332.
- [25] A. H. Guth, “The Inflationary Universe: A Possible Solution to the Horizon and Flatness Problems,” *Phys.Rev.* **D23** (1981) 347–356.

- [26] R. Alpher, H. Bethe, and G. Gamow, “The origin of chemical elements,” *Phys.Rev.* **73** (1948) 803–804.
- [27] V. Rubin, N. Thonnard, and J. Ford, W.K., “Rotational properties of 21 SC galaxies with a large range of luminosities and radii, from NGC 4605 /R = 4kpc/ to UGC 2885 /R = 122 kpc/,” *Astrophys.J.* **238** (1980) 471.
- [28] F. Zwicky, “Spectral displacement of extra galactic nebulae,” *Helv.Phys.Acta* **6** (1933) 110–127.
- [29] D. Clowe, A. Gonzalez, and M. Markevitch, “Weak lensing mass reconstruction of the interacting cluster 1E0657-558: Direct evidence for the existence of dark matter,” *Astrophys.J.* **604** (2004) 596–603, arXiv:astro-ph/0312273 [astro-ph].
- [30] A. A. Penzias and R. W. Wilson, “A Measurement of excess antenna temperature at 4080-Mc/s,” *Astrophys.J.* **142** (1965) 419–421.
- [31] P. Peebles and J. Yu, “Primeval adiabatic perturbation in an expanding universe,” *Astrophys.J.* **162** (1970) 815–836.
- [32] SDSS Collaboration, D. J. Eisenstein *et al.*, “Detection of the baryon acoustic peak in the large-scale correlation function of SDSS luminous red galaxies,” *Astrophys.J.* **633** (2005) 560–574, arXiv:astro-ph/0501171 [astro-ph].
- [33] G. F. Smoot, C. Bennett, A. Kogut, E. Wright, J. Aymon, *et al.*, “Structure in the COBE differential microwave radiometer first year maps,” *Astrophys.J.* **396** (1992) L1–L5.
- [34] G. Efstathiou, J. Bond, and S. D. White, “COBE Background radiation anisotropies and large scale structure in the universe,” *Mon.Not.Roy.Astron.Soc.* **258** (1992) 1–6.
- [35] M. Taoso, G. Bertone, and A. Masiero, “Dark Matter Candidates: A Ten-Point Test,” *JCAP* **0803** (2008) 022, arXiv:0711.4996 [astro-ph].
- [36] MACHO Collaboration, C. Alcock *et al.*, “The MACHO project: Microlensing results from 5.7 years of LMC observations,” *Astrophys.J.* **542** (2000) 281–307, arXiv:astro-ph/0001272 [astro-ph].
- [37] Particle Data Group Collaboration, J. Beringer *et al.*, “Review of Particle Physics (RPP),” *Phys.Rev.* **D86** (2012) 010001.
- [38] M. Milgrom, “A Modification of the Newtonian dynamics as a possible alternative to the hidden mass hypothesis,” *Astrophys.J.* **270** (1983) 365–370.
- [39] G. W. Angus, H. Shan, H. Zhao, and B. Famaey, “On the Proof of Dark Matter, the Law of Gravity, and the Mass of Neutrinos,” *Astrophys.J.* **654** (2007) L13–L16, arXiv:astro-ph/0609125 [astro-ph].
- [40] M. Bolz, A. Brandenburg, and W. Buchmüller, “Thermal production of gravitinos,” *Nucl.Phys.* **B606** (2001) 518–544, arXiv:hep-ph/0012052 [hep-ph].

Bibliography

- [41] J. Preskill, M. B. Wise, and F. Wilczek, “Cosmology of the Invisible Axion,” *Phys.Lett.* **B120** (1983) 127–132.
- [42] L. Covi, J. E. Kim, and L. Roszkowski, “Axinos as cold dark matter,” *Phys.Rev.Lett.* **82** (1999) 4180–4183, arXiv:hep-ph/9905212 [hep-ph].
- [43] S. Dodelson and L. M. Widrow, “Sterile-neutrinos as dark matter,” *Phys.Rev.Lett.* **72** (1994) 17–20, arXiv:hep-ph/9303287 [hep-ph].
- [44] J. L. Feng, A. Rajaraman, and F. Takayama, “Superweakly interacting massive particles,” *Phys.Rev.Lett.* **91** (2003) 011302, arXiv:hep-ph/0302215 [hep-ph].
- [45] G. Jungman, M. Kamionkowski, and K. Griest, “Supersymmetric dark matter,” *Phys.Rept.* **267** (1996) 195–373, arXiv:hep-ph/9506380 [hep-ph].
- [46] D. Hooper and S. Profumo, “Dark matter and collider phenomenology of universal extra dimensions,” *Phys.Rept.* **453** (2007) 29–115, arXiv:hep-ph/0701197 [hep-ph].
- [47] A. Birkedal, A. Noble, M. Perelstein, and A. Spray, “Little Higgs dark matter,” *Phys.Rev.* **D74** (2006) 035002, arXiv:hep-ph/0603077 [hep-ph].
- [48] N. Arkani-Hamed, D. P. Finkbeiner, T. R. Slatyer, and N. Weiner, “A Theory of Dark Matter,” *Phys.Rev.* **D79** (2009) 015014, arXiv:0810.0713 [hep-ph].
- [49] Y. Nomura and J. Thaler, “Dark Matter through the Axion Portal,” *Phys.Rev.* **D79** (2009) 075008, arXiv:0810.5397 [hep-ph].
- [50] S. P. Martin, “A Supersymmetry primer,” arXiv:hep-ph/9709356 [hep-ph].
- [51] J. Bernstein, *KINETIC THEORY IN THE EXPANDING UNIVERSE*. Cambridge University Press, 1988.
- [52] E. W. Kolb and M. S. Turner, *THE EARLY UNIVERSE*. Westview Press, 1988.
- [53] J. Edsjö and P. Gondolo, “Neutralino relic density including coannihilations,” *Phys.Rev.* **D56** (1997) 1879–1894, arXiv:hep-ph/9704361 [hep-ph].
- [54] T. Bringmann and S. Hofmann, “Thermal decoupling of WIMPs from first principles,” *JCAP* **0407** (2007) 016, arXiv:hep-ph/0612238 [hep-ph].
- [55] T. Bringmann, “Particle Models and the Small-Scale Structure of Dark Matter,” *New J.Phys.* **11** (2009) 105027, arXiv:0903.0189 [astro-ph.CO].
- [56] L. Bergström, “Dark Matter Evidence, Particle Physics Candidates and Detection Methods,” *Ann.Phys.* **524** (2012) 479–496, arXiv:1205.4882 [astro-ph.HE].
- [57] ATLAS Collaboration, G. Aad *et al.*, “The ATLAS Experiment at the CERN Large Hadron Collider,” *JINST* **3** (2008) S08003.

- [58] **CMS** Collaboration, G. Bayatian *et al.*, “CMS technical design report, volume II: Physics performance,” *J.Phys.G* **G34** (2007) 995–1579.
- [59] **DAMA** Collaboration, R. Bernabei *et al.*, “First results from DAMA/LIBRA and the combined results with DAMA/NaI,” *Eur.Phys.J.* **C56** (2008) 333–355, arXiv:0804.2741 [astro-ph].
- [60] A. Drukier, K. Freese, and D. Spergel, “Detecting Cold Dark Matter Candidates,” *Phys.Rev.* **D33** (1986) 3495–3508.
- [61] M. Fairbairn and T. Schwetz, “Spin-independent elastic WIMP scattering and the DAMA annual modulation signal,” *JCAP* **0901** (2009) 037, arXiv:0808.0704 [hep-ph].
- [62] **CoGeNT** Collaboration, C. Aalseth *et al.*, “Results from a Search for Light-Mass Dark Matter with a P-type Point Contact Germanium Detector,” *Phys.Rev.Lett.* **106** (2011) 131301, arXiv:1002.4703 [astro-ph.CO].
- [63] G. Angloher, M. Bauer, I. Bavykina, A. Bento, C. Bucci, *et al.*, “Results from 730 kg days of the CRESST-II Dark Matter Search,” *Eur.Phys.J.* **C72** (2012) 1971, arXiv:1109.0702 [astro-ph.CO].
- [64] **CDMS-II** Collaboration, Z. Ahmed *et al.*, “Results from a Low-Energy Analysis of the CDMS II Germanium Data,” *Phys.Rev.Lett.* **106** (2011) 131302, arXiv:1011.2482 [astro-ph.CO].
- [65] **XENON100** Collaboration, E. Aprile *et al.*, “Dark Matter Results from 100 Live Days of XENON100 Data,” *Phys.Rev.Lett.* **107** (2011) 131302, arXiv:1104.2549 [astro-ph.CO].
- [66] T. Bringmann, L. Bergström, and J. Edsjö, “New Gamma-Ray Contributions to Supersymmetric Dark Matter Annihilation,” *JHEP* **0801** (2008) 049, arXiv:0710.3169 [hep-ph].
- [67] T. Bringmann, X. Huang, A. Ibarra, S. Vogl, and C. Weniger, “Fermi LAT Search for Internal Bremsstrahlung Signatures from Dark Matter Annihilation,” *JCAP* **1207** (2012) 054, arXiv:1203.1312 [hep-ph].
- [68] C. Weniger, “A Tentative Gamma-Ray Line from Dark Matter Annihilation at the Fermi Large Area Telescope,” *JCAP* **1208** (2012) 007, arXiv:1204.2797 [hep-ph].
- [69] T. Bringmann and C. Weniger, “Gamma Ray Signals from Dark Matter: Concepts, Status and Prospects,” arXiv:1208.5481 [hep-ph].
- [70] J. Silk and A. Stebbins, “Clumpy cold dark matter,” *Astrophys.J.* **411** (1993) 439–449.
- [71] L. Bergström, J. Edsjö, and P. Ullio, “Possible indications of a clumpy dark matter halo,” *Phys.Rev.* **D58** (1998) 083507, arXiv:astro-ph/9804050 [astro-ph].

Bibliography

- [72] J. Diemand, B. Moore, and J. Stadel, “Earth-mass dark-matter haloes as the first structures in the early Universe,” *Nature* **433** (2005) 389–391, arXiv:astro-ph/0501589 [astro-ph].
- [73] S. Profumo and P. Ullio, “Multi-Wavelength Searches for Particle Dark Matter,” in *Particle Dark Matter: Observations, Models and Searches*, G. Bertone, ed., ch. 27. Cambridge University Press, 2010. arXiv:1001.4086 [astro-ph.HE].
- [74] W. H. Press and D. N. Spergel, “Capture by the sun of a galactic population of weakly interacting massive particles,” *Astrophys.J.* **296** (1985) 679–684.
- [75] M. Srednicki, K. A. Olive, and J. Silk, “High-Energy Neutrinos from the Sun and Cold Dark Matter,” *Nucl.Phys.* **B279** (1987) 804.
- [76] **IceCube** Collaboration, J. Ahrens *et al.*, “Icecube - the next generation neutrino telescope at the south pole,” *Nucl.Phys.Proc.Suppl.* **118** (2003) 388–395, arXiv:astro-ph/0209556 [astro-ph].
- [77] **IceCube** Collaboration, R. Abbasi *et al.*, “Limits on a muon flux from neutralino annihilations in the Sun with the IceCube 22-string detector,” *Phys.Rev.Lett.* **102** (2009) 201302, arXiv:0902.2460 [astro-ph.CO].
- [78] **AMANDA** Collaboration, M. Ackermann *et al.*, “Limits to the muon flux from neutralino annihilations in the sun with the amanda detector,” *Astropart.Phys.* **24** (2006) 459–466, arXiv:astro-ph/0508518 [astro-ph].
- [79] **ANTARES** Collaboration, P. Coyle, “The ANTARES Deep-Sea Neutrino Telescope: Status and First Results,” arXiv:1002.0754 [astro-ph.HE].
- [80] F. Donato, N. Fornengo, D. Maurin, P. Salati, and R. Taillet, “Antiprotons in cosmic rays from neutralino annihilation,” *Phys.Rev.* **D69** (2004) 063501, arXiv:astro-ph/0306207 [astro-ph].
- [81] K. Abe, H. Fuke, S. Haino, T. Hams, M. Hasegawa, *et al.*, “Measurement of the cosmic-ray antiproton spectrum at solar minimum with a long-duration balloon flight over Antarctica,” *Phys.Rev.Lett.* **108** (2012) 051102, arXiv:1107.6000 [astro-ph.HE].
- [82] **PAMELA** Collaboration, O. Adriani *et al.*, “PAMELA results on the cosmic-ray antiproton flux from 60 MeV to 180 GeV in kinetic energy,” *Phys.Rev.Lett.* **105** (2010) 121101, arXiv:1007.0821 [astro-ph.HE].
- [83] **AMS** Collaboration, A. Malinin, “Dark matter searches with AMS-02 experiment,” in *Particle Physics on the Eve of LHC*, pp. 207–213. 2007.
- [84] **PAMELA** Collaboration, O. Adriani *et al.*, “An anomalous positron abundance in cosmic rays with energies 1.5-100 GeV,” *Nature* **458** (2009) 607–609, arXiv:0810.4995 [astro-ph].

- [85] **ATIC** Collaboration, J. Chang, J. Adams, H. Ahn, G. Bashindzhagyan, M. Christl, *et al.*, “An excess of cosmic ray electrons at energies of 300-800 GeV,” *Nature* **456** (2008) 362–365.
- [86] **Fermi LAT** Collaboration, A. A. Abdo *et al.*, “Measurement of the Cosmic Ray e^+ plus e^- spectrum from 20 GeV to 1 TeV with the Fermi Large Area Telescope,” *Phys.Rev.Lett.* **102** (2009) 181101, arXiv:0905.0025 [astro-ph.HE].
- [87] **H.E.S.S.** Collaboration, F. Aharonian *et al.*, “Probing the ATIC peak in the cosmic-ray electron spectrum with H.E.S.S.,” *Astron.Astrophys.* **508** (2009) 561, arXiv:0905.0105 [astro-ph.HE].
- [88] M. Pospelov and A. Ritz, “Astrophysical Signatures of Secluded Dark Matter,” *Phys.Lett.* **B671** (2009) 391–397, arXiv:0810.1502 [hep-ph].
- [89] I. Cholis, D. P. Finkbeiner, L. Goodenough, and N. Weiner, “The PAMELA Positron Excess from Annihilations into a Light Boson,” *JCAP* **0912** (2009) 007, arXiv:0810.5344 [astro-ph].
- [90] P. J. Fox and E. Poppitz, “Leptophilic Dark Matter,” *Phys.Rev.* **D79** (2009) 083528, arXiv:0811.0399 [hep-ph].
- [91] D. Hooper, P. Blasi, and P. D. Serpico, “Pulsars as the Sources of High Energy Cosmic Ray Positrons,” *JCAP* **0901** (2009) 025, arXiv:0810.1527 [astro-ph].
- [92] D. Malyshev, I. Cholis, and J. Gelfand, “Pulsars versus Dark Matter Interpretation of ATIC/PAMELA,” *Phys.Rev.* **D80** (2009) 063005, arXiv:0903.1310 [astro-ph.HE].
- [93] P. D. Serpico, “Astrophysical models for the origin of the positron ‘excess’,” *Astropart.Phys.* **39-40** (2012) 2–11, arXiv:1108.4827 [astro-ph.HE].
- [94] J. Binney and S. Tremaine, *Galactic Dynamics*. Princeton University Press, 2008.
- [95] J. A. Peacock, *Cosmological physics*. Cambridge University Press, 1999.
- [96] J. Silk, “Cosmic black body radiation and galaxy formation,” *Astrophys.J.* **151** (1968) 459–471.
- [97] S. Weinberg, “Entropy generation and the survival of protogalaxies in an expanding universe,” *Astrophys.J.* **168** (1971) 175.
- [98] S. Hofmann, D. J. Schwarz, and H. Stöcker, “Damping scales of neutralino cold dark matter,” *Phys.Rev.* **D64** (2001) 083507, arXiv:astro-ph/0104173 [astro-ph].
- [99] A. M. Green, S. Hofmann, and D. J. Schwarz, “The power spectrum of SUSY - CDM on sub-galactic scales,” *Mon.Not.Roy.Astron.Soc.* **353** (2004) L23, arXiv:astro-ph/0309621 [astro-ph].

Bibliography

- [100] A. M. Green, S. Hofmann, and D. J. Schwarz, “The First wimpy halos,” *JCAP* **0508** (2005) 003, arXiv:astro-ph/0503387 [astro-ph].
- [101] A. Loeb and M. Zaldarriaga, “The Small-scale power spectrum of cold dark matter,” *Phys.Rev.* **D71** (2005) 103520, arXiv:astro-ph/0504112 [astro-ph].
- [102] E. Bertschinger, “The Effects of Cold Dark Matter Decoupling and Pair Annihilation on Cosmological Perturbations,” *Phys.Rev.* **D74** (2006) 063509, arXiv:astro-ph/0607319 [astro-ph].
- [103] J. Sommer-Larsen and A. Dolgov, “Formation of disk galaxies: warm dark matter and the angular momentum problem,” *Astrophys.J.* **551** (2001) 608–623, arXiv:astro-ph/9912166 [astro-ph].
- [104] A. M. Green and S. P. Goodwin, “On mini-halo encounters with stars,” *Mon.Not.Roy.Astron.Soc.* **375** (2007) 1111–1120, arXiv:astro-ph/0604142 [astro-ph].
- [105] T. Goerdt, O. Y. Gnedin, B. Moore, J. Diemand, and J. Stadel, “The survival and disruption of CDM micro-haloes: Implications for direct and indirect detection experiments,” *Mon.Not.Roy.Astron.Soc.* **375** (2007) 191–198, arXiv:astro-ph/0608495 [astro-ph].
- [106] L. Pieri, E. Branchini, and S. Hofmann, “Difficulty of detecting minihalos via γ Rays from dark matter annihilation,” *Phys.Rev.Lett.* **95** (2005) 211301, arXiv:astro-ph/0505356 [astro-ph].
- [107] S. K. Lee, S. Ando, and M. Kamionkowski, “The Gamma-Ray-Flux Probability Distribution Function from Galactic Halo Substructure,” *JCAP* **0907** (2009) 007, arXiv:0810.1284 [astro-ph].
- [108] S. Ando and E. Komatsu, “Anisotropy of the cosmic gamma-ray background from dark matter annihilation,” *Phys.Rev.* **D73** (2006) 023521, arXiv:astro-ph/0512217 [astro-ph].
- [109] S. Ando, E. Komatsu, T. Narumoto, and T. Totani, “Dark matter annihilation or unresolved astrophysical sources? Anisotropy probe of the origin of cosmic gamma-ray background,” *Phys.Rev.* **D75** (2007) 063519, arXiv:astro-ph/0612467 [astro-ph].
- [110] M. Fornasa, L. Pieri, G. Bertone, and E. Branchini, “Anisotropy probe of galactic and extra-galactic Dark Matter annihilations,” *Phys.Rev.* **D80** (2009) 023518, arXiv:0901.2921 [astro-ph].
- [111] F. Li, A. L. Erickcek, and N. M. Law, “A new probe of the small-scale primordial power spectrum: astrometric microlensing by ultracompact minihalos,” *Phys.Rev.* **D86** (2012) 043519, arXiv:1202.1284 [astro-ph.CO].

- [112] L. A. Moustakas, K. Abazajian, A. Benson, A. S. Bolton, J. S. Bullock, *et al.*, “Strong gravitational lensing probes of the particle nature of dark matter,” in *astro2010: The Astronomy and Astrophysics Decadal Survey*, vol. 2010 of *Astronomy*, p. 214. 2009. arXiv:0902.3219 [astro-ph.CO].
- [113] J. Chen and S. M. Koushiappas, “Gravitational Nanolensing from Subsolar Mass Dark Matter Halos,” *Astrophys.J.* **724** (2010) 400–410, arXiv:1008.2385 [astro-ph.CO].
- [114] S. M. Koushiappas, “The detection of sub-solar mass dark matter halos,” *New J.Phys.* **11** (2009) 105012, arXiv:0905.1998 [astro-ph.CO].
- [115] A. Pinzke, C. Pfrommer, and L. Bergström, “Gamma-rays from dark matter annihilations strongly constrain the substructure in halos,” *Phys.Rev.Lett.* **103** (2009) 181302, arXiv:0905.1948 [astro-ph.HE].
- [116] A. Pinzke, C. Pfrommer, and L. Bergström, “Prospects of detecting gamma-ray emission from galaxy clusters: cosmic rays and dark matter annihilations,” *Phys.Rev.* **D84** (2011) 123509, arXiv:1105.3240 [astro-ph.HE].
- [117] M. Lattanzi and J. I. Silk, “Can the WIMP annihilation boost factor be boosted by the Sommerfeld enhancement?,” *Phys.Rev.* **D79** (2009) 083523, arXiv:0812.0360 [astro-ph].
- [118] Q. Yuan, X.-J. Bi, J. Liu, P.-F. Yin, J. Zhang, *et al.*, “Clumpiness enhancement of charged cosmic rays from dark matter annihilation with Sommerfeld effect,” *JCAP* **0912** (2009) 011, arXiv:0905.2736 [astro-ph.HE].
- [119] T. R. Slatyer, N. Toro, and N. Weiner, “Sommerfeld-enhanced annihilation in dark matter substructure: Consequences for constraints on cosmic-ray excesses,” *Phys.Rev.* **D86** (2012) 083534, arXiv:1107.3546 [hep-ph].
- [120] J. Bovy, “Substructure Boosts to Dark Matter Annihilation from Sommerfeld Enhancement,” *Phys.Rev.* **D79** (2009) 083539, arXiv:0903.0413 [astro-ph.HE].
- [121] J. M. Cornell and S. Profumo, “Earthly probes of the smallest dark matter halos,” *JCAP* **1206** (2012) 011, arXiv:1203.1100 [hep-ph].
- [122] M. Kuhlen, M. Vogelsberger, and R. Angulo, “Numerical Simulations of the Dark Universe: State of the Art and the Next Decade,” *Phys.Dark Univ.* **1** (2012) 50–93, arXiv:1209.5745 [astro-ph.CO].
- [123] W. Dehnen, “Towards optimal softening in 3-D n-body codes: I. minimizing the force error,” *Mon.Not.Roy.Astron.Soc.* **324** (2001) 273, arXiv:astro-ph/0011568 [astro-ph].

Bibliography

- [124] R. Angulo, V. Springel, S. White, A. Jenkins, C. Baugh, *et al.*, “Scaling relations for galaxy clusters in the Millennium-XXL simulation,” *Mon.Not.Roy.Astron.Soc.* **426** (2012) 2046–2062, arXiv:1203.3216 [astro-ph.CO].
- [125] W. H. Press and P. Schechter, “Formation of galaxies and clusters of galaxies by selfsimilar gravitational condensation,” *Astrophys.J.* **187** (1974) 425–438.
- [126] A. Jenkins, C. Frenk, S. D. White, J. Colberg, S. Cole, *et al.*, “The Mass function of dark matter halos,” *Mon.Not.Roy.Astron.Soc.* **321** (2001) 372, arXiv:astro-ph/0005260 [astro-ph].
- [127] J. F. Navarro, C. S. Frenk, and S. D. White, “A Universal density profile from hierarchical clustering,” *Astrophys.J.* **490** (1997) 493–508, arXiv:astro-ph/9611107 [astro-ph].
- [128] A. F. Neto, L. Gao, P. Bett, S. Cole, J. F. Navarro, *et al.*, “The statistics of Λ CDM Halo Concentrations,” *Mon.Not.Roy.Astron.Soc.* **381** (2007) 1450–1462, arXiv:0706.2919 [astro-ph].
- [129] J. Einasto, “On the Construction of a Composite Model for the Galaxy and on the Determination of the System of Galactic Parameters,” *Trudy Astrof. Inst. Alma-Ata* **5** (1965) 87–100.
- [130] J. F. Navarro, E. Hayashi, C. Power, A. Jenkins, C. S. Frenk, *et al.*, “The Inner structure of Λ CDM halos - III. Universality and asymptotic slopes,” *Mon.Not.Roy.Astron.Soc.* **349** (2004) 1039, arXiv:astro-ph/0311231 [astro-ph].
- [131] V. Springel, J. Wang, M. Vogelsberger, A. Ludlow, A. Jenkins, *et al.*, “The Aquarius Project: the subhalos of galactic halos,” *Mon.Not.Roy.Astron.Soc.* **391** (2008) 1685–1711, arXiv:0809.0898 [astro-ph].
- [132] J. E. Gunn and J. R. Gott III, “On the Infall of Matter into Clusters of Galaxies and Some Effects on Their Evolution,” *Astrophys.J.* **176** (1972) 1–19.
- [133] A. A. Klypin, A. V. Kravtsov, O. Valenzuela, and F. Prada, “Where are the missing Galactic satellites?,” *Astrophys.J.* **522** (1999) 82–92, arXiv:astro-ph/9901240 [astro-ph].
- [134] SDSS Collaboration, V. Belokurov *et al.*, “Cats and Dogs, Hair and A Hero: A Quintet of New Milky Way Companions,” *Astrophys.J.* **654** (2007) 897–906, arXiv:astro-ph/0608448 [astro-ph].
- [135] M. Mateo, “Dwarf galaxies of the Local Group,” *Ann.Rev.Astron.Astrophys.* **36** (1998) 435–506, arXiv:astro-ph/9810070 [astro-ph].
- [136] S. Koposov, V. Belokurov, N. Evans, P. Hewett, M. Irwin, *et al.*, “The Luminosity Function of the Milky Way Satellites,” *Astrophys.J.* **686** (2008) 279–291, arXiv:0706.2687 [astro-ph].

- [137] E. J. Tollerud, J. S. Bullock, L. E. Strigari, and B. Willman, “Hundreds of Milky Way Satellites? Luminosity Bias in the Satellite Luminosity Function,” *Astrophys. J.* **688** (2008) 277–289, arXiv:0806.4381 [astro-ph].
- [138] A. A. Thoul and D. H. Weinberg, “Hydrodynamic Simulations of Galaxy Formation. II. Photoionization and the Formation of Low-Mass Galaxies,” *Astrophys. J.* **465** (1996) 608, arXiv:astro-ph/9510154.
- [139] R. S. Somerville, “Can Photoionization Squelching Resolve the Substructure Crisis?” *Astrophys. J.* **572** (June, 2002) L23–L26, arXiv:astro-ph/0107507.
- [140] E. Scannapieco, R. J. Thacker, and M. Davis, “High-Redshift Galaxy Outflows and the Formation of Dwarf Galaxies,” *Astrophys. J.* **557** (Aug., 2001) 605–615, arXiv:astro-ph/0011258.
- [141] A. V. Kravtsov, O. Y. Gnedin, and A. A. Klypin, “The Tumultuous Lives of Galactic Dwarfs and the Missing Satellites Problem,” *Astrophys. J.* **609** (July, 2004) 482–497, arXiv:astro-ph/0401088.
- [142] M. Hoeft, G. Yepes, S. Gottlöber, and V. Springel, “Dwarf galaxies in voids: suppressing star formation with photoheating,” *Mon.Not.Roy.Astron.Soc.* **371** (Sept., 2006) 401–414, arXiv:astro-ph/0501304.
- [143] C. Pfrommer, P. Chang, and A. E. Broderick, “The Cosmological Impact of Luminous TeV Blazars III: Implications for Galaxy Clusters and the Formation of Dwarf Galaxies,” *Astrophys. J.* **752** (2012) 24, arXiv:1106.5505 [astro-ph.CO].
- [144] K. Tassis, A. V. Kravtsov, and N. Y. Gnedin, “Scaling Relations of Dwarf Galaxies without Supernova-driven Winds,” *Astrophys. J.* **672** (Jan., 2008) 888–903, arXiv:astro-ph/0609763.
- [145] Z. Haiman, M. J. Rees, and A. Loeb, “Destruction of Molecular Hydrogen during Cosmological Reionization,” *Astrophys. J.* **476** (Feb., 1997) 458, arXiv:astro-ph/9608130.
- [146] R. Barkana and A. Loeb, “The Photoevaporation of Dwarf Galaxies during Reionization,” *Astrophys. J.* **523** (Sept., 1999) 54–65, arXiv:astro-ph/9901114.
- [147] P. R. Shapiro, I. T. Iliev, and A. C. Raga, “Photoevaporation of cosmological minihaloes during reionization,” *Mon.Not.Roy.Astron.Soc.* **348** (Mar., 2004) 753–782, arXiv:astro-ph/0307266.
- [148] M.-M. Mac Low and A. Ferrara, “Starburst-driven Mass Loss from Dwarf Galaxies: Efficiency and Metal Ejection,” *Astrophys. J.* **513** (Mar., 1999) 142–155, arXiv:astro-ph/9801237.
- [149] P. F. Hopkins, E. Quataert, and N. Murray, “Stellar Feedback in Galaxies and the Origin of Galaxy-scale Winds,” *Mon.Not.Roy.Astron.Soc.* **421** (2012) 3522–3537, arXiv:1110.4638 [astro-ph.CO].

Bibliography

- [150] M. Uhlig, C. Pfrommer, M. Sharma, B. Nath, T. Enßlin, *et al.*, “Galactic winds driven by cosmic-ray streaming,” *Mon.Not.Roy.Astron.Soc.* **423** no. 3, (2012) 2374–2396, arXiv:1203.1038 [astro-ph.CO].
- [151] M. A. Zwaan, M. J. Meyer, and L. Staveley-Smith, “The velocity function of gas-rich galaxies,” *Mon.Not.Roy.Astron.Soc.* **403** (Apr., 2010) 1969–1977, arXiv:0912.1754 [astro-ph.CO].
- [152] D. N. Spergel and P. J. Steinhardt, “Observational Evidence for Self-Interacting Cold Dark Matter,” *Phys.Rev.Lett.* **84** (Apr., 2000) 3760–3763, arXiv:astro-ph/9909386.
- [153] P. Bode, J. P. Ostriker, and N. Turok, “Halo formation in warm dark matter models,” *Astrophys.J.* **556** (2001) 93–107, arXiv:astro-ph/0010389 [astro-ph].
- [154] J. J. Dalcanton and C. J. Hogan, “Halo cores and phase space densities: Observational constraints on dark matter physics and structure formation,” *Astrophys.J.* **561** (2001) 35–45, arXiv:astro-ph/0004381 [astro-ph].
- [155] A. R. Zentner and J. S. Bullock, “Halo substructure and the power spectrum,” *Astrophys.J.* **598** (2003) 49, arXiv:astro-ph/0304292 [astro-ph].
- [156] R. E. Smith and K. Markovic, “Testing the Warm Dark Matter paradigm with large-scale structures,” *Phys.Rev.* **D84** (2011) 063507, arXiv:1103.2134 [astro-ph.CO].
- [157] M. Viel, J. Lesgourgues, M. G. Haehnelt, S. Matarrese, and A. Riotto, “Can sterile neutrinos be ruled out as warm dark matter candidates?,” *Phys.Rev.Lett.* **97** (2006) 071301, arXiv:astro-ph/0605706 [astro-ph].
- [158] U. Seljak, A. Makarov, P. McDonald, and H. Trac, “Can Sterile Neutrinos Be the Dark Matter?,” *Phys.Rev.Lett.* **97** no. 19, (Nov., 2006) 191303, arXiv:astro-ph/0602430.
- [159] A. Boyarsky, J. Lesgourgues, O. Ruchayskiy, and M. Viel, “Lyman-alpha constraints on warm and on warm-plus-cold dark matter models,” *JCAP* **0905** (2009) 012, arXiv:0812.0010 [astro-ph].
- [160] A. Burkert, “The Structure of Dark Matter Halos in Dwarf Galaxies,” *Astrophys. J.* **447** (July, 1995) L25, arXiv:astro-ph/9504041.
- [161] M. Persic, P. Salucci, and F. Stel, “The Universal rotation curve of spiral galaxies: 1. The Dark matter connection,” *Mon.Not.Roy.Astron.Soc.* **281** (1996) 27, arXiv:astro-ph/9506004 [astro-ph].
- [162] S. Blais-Ouellette, P. Amram, and C. Carignan, “Accurate Determination of the Mass Distribution in Spiral Galaxies: II. Testing the Shape of Dark Halos,” *Astron.J.* **121** no. 4, (2001) 1952, astro-ph/0006449.

- [163] J. D. Simon, A. D. Bolatto, A. Leroy, L. Blitz, and E. L. Gates, “High-resolution measurements of the halos of four dark matter-dominated galaxies: Deviations from a universal density profile,” *Astrophys.J.* **621** (2005) 757–776, arXiv:astro-ph/0412035 [astro-ph].
- [164] W. de Blok, “The Core-Cusp Problem,” *Adv.Astron.* **2010** (2010) 789293, arXiv:0910.3538 [astro-ph.CO].
- [165] G. Gilmore, M. I. Wilkinson, R. F. Wyse, J. T. Kleyna, A. Koch, *et al.*, “The Observed properties of Dark Matter on small spatial scales,” *Astrophys.J.* **663** (2007) 948–959, arXiv:astro-ph/0703308 [ASTRO-PH].
- [166] L. E. Strigari, C. S. Frenk, and S. D. White, “Kinematics of Milky Way Satellites in a Lambda Cold Dark Matter Universe,” *Mon.Not.Roy.Astron.Soc.* **408** (2010) 2364–2372, arXiv:1003.4268 [astro-ph.CO].
- [167] N. Evans, J. An, and M. Walker, “Cores and Cusps in the Dwarf Spheroidals,” *Mon.Not.Roy.Astron.Soc.Lett.* **393** no. 1, (2009) L50–L54, arXiv:0811.1488 [astro-ph].
- [168] M. G. Walker, M. Mateo, E. W. Olszewski, J. Penarrubia, N. W. Evans, *et al.*, “A Universal Mass Profile for Dwarf Spheroidal Galaxies,” *Astrophys.J.* **704** (2009) 1274–1287, arXiv:0906.0341 [astro-ph.CO].
- [169] G. Battaglia, A. Helmi, E. Tolstoy, M. Irwin, V. Hill, and P. Jablonka, “The Kinematic Status and Mass Content of the Sculptor Dwarf Spheroidal Galaxy,” *Astrophys. J.* **681** (July, 2008) L13–L16, arXiv:0802.4220.
- [170] N. Amorisco and N. Evans, “Dark Matter Cores and Cusps: The Case of Multiple Stellar Populations in Dwarf Spheroidals,” *Mon.Not.Roy.Astron.Soc.* **419** no. 1, (2012) 184–196, arXiv:1106.1062 [astro-ph.CO].
- [171] M. G. Walker and J. Penarrubia, “A Method for Measuring (Slopes of) the Mass Profiles of Dwarf Spheroidal Galaxies,” *Astrophys.J.* **742** (2011) 20, arXiv:1108.2404 [astro-ph.CO].
- [172] M. A. Breddels, A. Helmi, R. C. E. van den Bosch, G. van de Ven, and G. Battaglia, “Schwarzschild models of the Sculptor dSph galaxy,” *EPJ Web of Conferences* **19** (Feb., 2012) 03009, arXiv:1110.4808 [astro-ph.CO].
- [173] A. Pontzen and F. Governato, “How supernova feedback turns dark matter cusps into cores,” *Mon.Not.Roy.Astron.Soc.* **421** no. 4, (2012) 3464–3471, arXiv:1106.0499 [astro-ph.CO].
- [174] R. K. de Naray and K. Spekkens, “Do Baryons Alter the Halos of Low Surface Brightness Galaxies?,” *Astrophys.J.* **741** (2011) L29, arXiv:1109.1288 [astro-ph.CO].

Bibliography

- [175] T. Sawala, C. Scannapieco, U. Maio, and S. D. White, “Formation of isolated dwarf galaxies with feedback,” *Mon.Not.Roy.Astron.Soc.* **402** (Mar., 2010) 1599–1613, arXiv:0902.1754 [astro-ph.GA].
- [176] A. V. Macciò, S. Paduroiu, D. Anderhalden, A. Schneider, and B. Moore, “Cores in warm dark matter haloes: a Catch 22 problem,” *Mon.Not.Roy.Astron.Soc.* **424** (Aug., 2012) 1105–1112, arXiv:1202.1282 [astro-ph.CO].
- [177] N. Yoshida, V. Springel, S. D. White, and G. Tormen, “Collisional dark matter and the structure of dark halos,” *Astrophys.J.* **535** (2000) L103, arXiv:astro-ph/0002362 [astro-ph].
- [178] J. Miralda-Escude, “A test of the collisional dark matter hypothesis from cluster lensing,” *Astrophys.J.* **564** no. 1, (2002) 60, arXiv:astro-ph/0002050 [astro-ph].
- [179] S. Balberg, S. L. Shapiro, and S. Inagaki, “Selfinteracting dark matter halos and the gravothermal catastrophe,” *Astrophys.J.* **568** (2002) 475–487, arXiv:astro-ph/0110561 [astro-ph].
- [180] O. Y. Gnedin and J. P. Ostriker, “Limits on collisional dark matter from elliptical galaxies in clusters,” *Astrophys.J.* **561** (2001) 61–68, arXiv:astro-ph/0010436 [astro-ph].
- [181] A. Loeb and N. Weiner, “Cores in Dwarf Galaxies from Dark Matter with a Yukawa Potential,” *Phys.Rev.Lett.* **106** (2011) 171302, arXiv:1011.6374 [astro-ph.CO].
- [182] M. Boylan-Kolchin, J. S. Bullock, and M. Kaplinghat, “Too big to fail? The puzzling darkness of massive Milky Way subhaloes,” *Mon.Not.Roy.Astron.Soc.* **415** (July, 2011) L40–L44, arXiv:1103.0007 [astro-ph.CO].
- [183] C. A. Vera-Ciro, A. Helmi, E. Starkeburg, and M. A. Breddels, “Not too big, not too small: the dark halos of the dwarf spheroidals in the Milky Way,” *Mon.Not.Roy.Astron.Soc.* **428** no. 2, (2013) 1696–1703, arXiv:1202.6061 [astro-ph.CO].
- [184] J. Wang, C. S. Frenk, J. F. Navarro, L. Gao, and T. Sawala, “The missing massive satellites of the Milky Way,” *Mon.Not.Roy.Astron.Soc.* **424** (Aug., 2012) 2715–2721, arXiv:1203.4097 [astro-ph.GA].
- [185] M. Boylan-Kolchin, V. Springel, S. D. M. White, and A. Jenkins, “There’s no place like home? Statistics of Milky Way-mass dark matter haloes,” *Mon.Not.Roy.Astron.Soc.* **406** (Aug., 2010) 896–912, arXiv:0911.4484 [astro-ph.CO].
- [186] M. T. Busha, R. H. Wechsler, P. S. Behroozi, B. F. Gerke, A. A. Klypin, and J. R. Primack, “Statistics of Satellite Galaxies around Milky-Way-like Hosts,” *Astrophys. J.* **743** (Dec., 2011) 117, arXiv:1011.6373 [astro-ph.CO].

- [187] Q. Guo, S. Cole, V. Eke, and C. Frenk, “The satellite luminosity functions of galaxies in Sloan Digital Sky Survey,” *Mon.Not.Roy.Astron.Soc.* **417** (Oct., 2011) 370–381, arXiv:1101.2674 [astro-ph.CO].
- [188] L. Liu, B. F. Gerke, R. H. Wechsler, P. S. Behroozi, and M. T. Busha, “How Common are the Magellanic Clouds?,” *Astrophys. J.* **733** (May, 2011) 62, arXiv:1011.2255 [astro-ph.CO].
- [189] L. E. Strigari and R. H. Wechsler, “The Cosmic Abundance of Classical Milky Way Satellites,” *Astrophys. J.* **749** (Apr., 2012) 75, arXiv:1111.2611 [astro-ph.CO].
- [190] Y.-S. Li and S. D. M. White, “Masses for the Local Group and the Milky Way,” *Mon.Not.Roy.Astron.Soc.* **384** (Mar., 2008) 1459–1468, arXiv:0710.3740.
- [191] Q. Guo, S. White, C. Li, and M. Boylan-Kolchin, “How do galaxies populate dark matter haloes?,” *Mon.Not.Roy.Astron.Soc.* **404** (May, 2010) 1111–1120, arXiv:0909.4305 [astro-ph.CO].
- [192] M. R. Lovell, V. Eke, C. S. Frenk, L. Gao, A. Jenkins, T. Theuns, J. Wang, S. D. M. White, A. Boyarsky, and O. Ruchayskiy, “The haloes of bright satellite galaxies in a warm dark matter universe,” *Mon.Not.Roy.Astron.Soc.* **420** (Mar., 2012) 2318–2324, arXiv:1104.2929 [astro-ph.CO].
- [193] A. Sommerfeld, “Über die Beugung und Bremsung der Elektronen,” *Ann.Phys.* **403** no. 3, (1931) 257–330.
- [194] J. Hisano, S. Matsumoto, and M. M. Nojiri, “Unitarity and higher order corrections in neutralino dark matter annihilation into two photons,” *Phys.Rev.* **D67** (2003) 075014, arXiv:hep-ph/0212022 [hep-ph].
- [195] J. Hisano, S. Matsumoto, and M. M. Nojiri, “Explosive dark matter annihilation,” *Phys.Rev.Lett.* **92** (2004) 031303, arXiv:hep-ph/0307216 [hep-ph].
- [196] J. Hisano, S. Matsumoto, M. M. Nojiri, and O. Saito, “Non-perturbative effect on dark matter annihilation and gamma ray signature from galactic center,” *Phys.Rev.* **D71** (2005) 063528, arXiv:hep-ph/0412403 [hep-ph].
- [197] J. Hisano, S. Matsumoto, M. Nagai, O. Saito, and M. Senami, “Non-perturbative effect on thermal relic abundance of dark matter,” *Phys.Lett.* **B646** (2007) 34–38, arXiv:hep-ph/0610249 [hep-ph].
- [198] M. Cirelli, A. Strumia, and M. Tamburini, “Cosmology and Astrophysics of Minimal Dark Matter,” *Nucl.Phys.* **B787** (2007) 152–175, arXiv:0706.4071 [hep-ph].
- [199] **HEAT** Collaboration, S. Barwick *et al.*, “Measurements of the cosmic ray positron fraction from 1-GeV to 50-GeV,” *Astrophys.J.* **482** (1997) L191–L194, arXiv:astro-ph/9703192 [astro-ph].

Bibliography

- [200] **AMS-01** Collaboration, M. Aguilar *et al.*, “Cosmic-ray positron fraction measurement from 1 to 30-GeV with AMS-01,” *Phys.Lett.* **B646** (2007) 145–154, arXiv:astro-ph/0703154 [astro-ph].
- [201] **H.E.S.S.** Collaboration, F. Aharonian *et al.*, “The energy spectrum of cosmic-ray electrons at TeV energies,” *Phys.Rev.Lett.* **101** (2008) 261104, arXiv:0811.3894 [astro-ph].
- [202] **FERMI-LAT** Collaboration, D. Grasso *et al.*, “On possible interpretations of the high energy electron-positron spectrum measured by the Fermi Large Area Telescope,” *Astropart.Phys.* **32** (2009) 140–151, arXiv:0905.0636 [astro-ph.HE].
- [203] E. A. Baltz, J. Edsjö, K. Freese, and P. Gondolo, “The Cosmic ray positron excess and neutralino dark matter,” *Phys.Rev.* **D65** (2002) 063511, arXiv:astro-ph/0109318 [astro-ph].
- [204] G. L. Kane, L.-T. Wang, and T. T. Wang, “Supersymmetry and the cosmic ray positron excess,” *Phys.Lett.* **B536** (2002) 263–269, arXiv:hep-ph/0202156 [hep-ph].
- [205] D. Hooper, J. E. Taylor, and J. Silk, “Can supersymmetry naturally explain the positron excess?,” *Phys.Rev.* **D69** (2004) 103509, arXiv:hep-ph/0312076 [hep-ph].
- [206] I. Cholis, L. Goodenough, D. Hooper, M. Simet, and N. Weiner, “High Energy Positrons From Annihilating Dark Matter,” *Phys.Rev.* **D80** (2009) 123511, arXiv:0809.1683 [hep-ph].
- [207] M. Cirelli, M. Kadastik, M. Raidal, and A. Strumia, “Model-independent implications of the e^+ , anti-proton cosmic ray spectra on properties of Dark Matter,” *Nucl.Phys.* **B813** (2009) 1–21, arXiv:0809.2409 [hep-ph].
- [208] L. Bergström, J. Edsjö, and G. Zaharijas, “Dark matter interpretation of recent electron and positron data,” *Phys.Rev.Lett.* **103** (2009) 031103, arXiv:0905.0333 [astro-ph.HE].
- [209] M. Cirelli and A. Strumia, “Minimal Dark Matter predictions and the PAMELA positron excess,” *PoS IDM2008* (2008) 089, arXiv:0808.3867 [astro-ph].
- [210] S. Profumo, “Dissecting cosmic-ray electron-positron data with Occam’s Razor: the role of known Pulsars,” *Central Eur.J.Phys.* **10** (2012) 1–31, arXiv:0812.4457 [astro-ph].
- [211] F. Donato, D. Maurin, P. Brun, T. Delahaye, and P. Salati, “Constraints on WIMP Dark Matter from the High Energy PAMELA \bar{p}/p data,” *Phys.Rev.Lett.* **102** (2009) 071301, arXiv:0810.5292 [astro-ph].
- [212] L. Bergström, G. Bertone, T. Bringmann, J. Edsjö, and M. Taoso, “Gamma-ray and Radio Constraints of High Positron Rate Dark Matter Models Annihilating into New Light Particles,” *Phys.Rev.* **D79** (2009) 081303, arXiv:0812.3895 [astro-ph].

- [213] P. Meade, M. Papucci, A. Strumia, and T. Volansky, “Dark Matter Interpretations of the e^+e^- Excesses after FERMI,” *Nucl.Phys.* **B831** (2010) 178–203, arXiv:0905.0480 [hep-ph].
- [214] J. Zavala, M. Vogelsberger, and S. D. White, “Relic density and CMB constraints on dark matter annihilation with Sommerfeld enhancement,” *Phys.Rev.* **D81** (2010) 083502, arXiv:0910.5221 [astro-ph.CO].
- [215] S. Hannestad and T. Tram, “Sommerfeld Enhancement of DM Annihilation: Resonance Structure, Freeze-Out and CMB Spectral Bound,” *JCAP* **1101** (2011) 016, arXiv:1008.1511 [astro-ph.CO].
- [216] S. Galli, F. Iocco, G. Bertone, and A. Melchiorri, “CMB constraints on Dark Matter models with large annihilation cross-section,” *Phys.Rev.* **D80** (2009) 023505, arXiv:0905.0003 [astro-ph.CO].
- [217] T. R. Slatyer, N. Padmanabhan, and D. P. Finkbeiner, “CMB Constraints on WIMP Annihilation: Energy Absorption During the Recombination Epoch,” *Phys.Rev.* **D80** (2009) 043526, arXiv:0906.1197 [astro-ph.CO].
- [218] J. Hisano, M. Kawasaki, K. Kohri, T. Moroi, K. Nakayama, *et al.*, “Cosmological constraints on dark matter models with velocity-dependent annihilation cross section,” *Phys.Rev.* **D83** (2011) 123511, arXiv:1102.4658 [hep-ph].
- [219] A. Hryczuk, R. Iengo, and P. Ullio, “Relic densities including Sommerfeld enhancements in the MSSM,” *JHEP* **1103** (2011) 069, arXiv:1010.2172 [hep-ph].
- [220] A. Hryczuk, “The Sommerfeld enhancement for scalar particles and application to sfermion co-annihilation regions,” *Phys.Lett.* **B699** (2011) 271–275, arXiv:1102.4295 [hep-ph].
- [221] A. Hryczuk and R. Iengo, “The one-loop and Sommerfeld electroweak corrections to the Wino dark matter annihilation,” *JHEP* **1201** (2012) 163, arXiv:1111.2916 [hep-ph].
- [222] G. T. Bodwin, E. Braaten, and G. P. Lepage, “Rigorous QCD analysis of inclusive annihilation and production of heavy quarkonium,” *Phys.Rev.* **D51** (1995) 1125–1171, arXiv:hep-ph/9407339 [hep-ph].
- [223] L. Rosenström, “Sommerfeld enhancement for neutralino dark matter,” Master’s thesis, Stockholm University, June, 2011.
- [224] S. Matsumoto, “Derivation of schroedinger equation from quantum field theory.” Private communication, 2004.
- [225] R. Iengo, “Sommerfeld enhancement: General results from field theory diagrams,” *JHEP* **0905** (2009) 024, arXiv:0902.0688 [hep-ph].

Bibliography

- [226] R. Iengo, “Sommerfeld enhancement for a Yukawa potential,” arXiv:0903.0317 [hep-ph].
- [227] M. E. Peskin and V. Schroeder, Daniel, *An introduction to Quantum Field Theory*. Westview Press, 1995.
- [228] S. Cassel, “Sommerfeld factor for arbitrary partial wave processes,” *J.Phys.G* **G37** (2010) 105009, arXiv:0903.5307 [hep-ph].
- [229] T. R. Slatyer, “The Sommerfeld enhancement for dark matter with an excited state,” *JCAP* **1002** (2010) 028, arXiv:0910.5713 [hep-ph].
- [230] J. L. Feng, M. Kaplinghat, and H.-B. Yu, “Sommerfeld Enhancements for Thermal Relic Dark Matter,” *Phys.Rev.* **D82** (2010) 083525, arXiv:1005.4678 [hep-ph].
- [231] L. Landau and E. Lifshitz, *Quantum Mechanics (Non-relativistic Theory)*, vol. 3 of *Course of Theoretical Physics*. Butterworth-Heinemann, third edition ed., 1977.
- [232] C. Ramsauer, “Über den Wirkungsquerschnitt der Gasmoleküle gegenüber langsamen Elektronen,” *Ann.Phys.* **369** no. 6, (1921) 513–540.
- [233] L. E. Ibanez, “The Scalar Neutrinos as the Lightest Supersymmetric Particles and Cosmology,” *Phys.Lett.* **B137** (1984) 160.
- [234] T. Falk, K. A. Olive, and M. Srednicki, “Heavy sneutrinos as dark matter,” *Phys.Lett.* **B339** (1994) 248–251, arXiv:hep-ph/9409270 [hep-ph].
- [235] C. Arina and N. Fornengo, “Sneutrino cold dark matter, a new analysis: Relic abundance and detection rates,” *JHEP* **0711** (2007) 029, arXiv:0709.4477 [hep-ph].
- [236] M. W. Goodman and E. Witten, “Detectability of Certain Dark Matter Candidates,” *Phys.Rev.* **D31** (1985) 3059.
- [237] B. Pontecorvo, “Inverse beta processes and nonconservation of lepton charge,” *Sov.Phys.JETP* **7** (1958) 172–173.
- [238] **Super-Kamiokande** Collaboration, Y. Fukuda *et al.*, “Evidence for oscillation of atmospheric neutrinos,” *Phys.Rev.Lett.* **81** (1998) 1562–1567, arXiv:hep-ex/9807003 [hep-ex].
- [239] S. King, “Neutrino mass models,” *Rept.Prog.Phys.* **67** (2004) 107–158, arXiv:hep-ph/0310204 [hep-ph].
- [240] R. N. Mohapatra and G. Senjanović, “Neutrino Mass and Spontaneous Parity Nonconservation,” *Phys.Rev.Lett.* **44** (1980) 912.
- [241] N. Arkani-Hamed, L. J. Hall, H. Murayama, D. Smith, and N. Weiner, “Small neutrino masses from supersymmetry breaking,” *Phys.Rev.* **D64** (2001) 115011, arXiv:hep-ph/0006312 [hep-ph].

- [242] Y. Grossman and H. E. Haber, “Sneutrino mixing phenomena,” *Phys.Rev.Lett.* **78** (1997) 3438–3441, arXiv:hep-ph/9702421 [hep-ph].
- [243] D. Smith and N. Weiner, “Inelastic dark matter,” *Phys.Rev.* **D64** (2001) 043502, arXiv:hep-ph/0101138 [hep-ph].
- [244] G. Belanger, M. Kakizaki, E. Park, S. Kraml, and A. Pukhov, “Light mixed sneutrinos as thermal dark matter,” *JCAP* **1011** (2010) 017, arXiv:1008.0580 [hep-ph].
- [245] **CDMS-II** Collaboration, Z. Ahmed *et al.*, “Dark Matter Search Results from the CDMS II Experiment,” *Science* **327** (2010) 1619–1621, arXiv:0912.3592 [astro-ph.CO].
- [246] M. Kakizaki. Private communication, 2010.
- [247] M. Hindmarsh and O. Philipsen, “Dark Matter of weakly interacting massive particles and the QCD equation of state,” *Phys.Rev.* **D71** (2005) 087302, arXiv:hep-ph/0501232 [hep-ph].
- [248] J. B. Dent, S. Dutta, and R. J. Scherrer, “Thermal Relic Abundances of Particles with Velocity-Dependent Interactions,” *Phys.Lett.* **B687** (2010) 275–279, arXiv:0909.4128 [astro-ph.CO].
- [249] J. L. Feng, M. Kaplinghat, and H.-B. Yu, “Halo Shape and Relic Density Exclusions of Sommerfeld-Enhanced Dark Matter Explanations of Cosmic Ray Excesses,” *Phys.Rev.Lett.* **104** (2010) 151301, arXiv:0911.0422 [hep-ph].
- [250] J. Bjorken, S. Ecklund, W. Nelson, A. Abashian, C. Church, *et al.*, “Search for Neutral Metastable Penetrating Particles Produced in the SLAC Beam Dump,” *Phys.Rev.* **D38** (1988) 3375.
- [251] Z. Fodor and S. Katz, “Critical point of QCD at finite T and μ , lattice results for physical quark masses,” *JHEP* **0404** (2004) 050, arXiv:hep-lat/0402006 [hep-lat].
- [252] **MILC** Collaboration, C. Bernard *et al.*, “QCD thermodynamics with three flavors of improved staggered quarks,” *Phys.Rev.* **D71** (2005) 034504, arXiv:hep-lat/0405029 [hep-lat].
- [253] D. P. Finkbeiner, L. Goodenough, T. R. Slatyer, M. Vogelsberger, and N. Weiner, “Consistent Scenarios for Cosmic-Ray Excesses from Sommerfeld-Enhanced Dark Matter Annihilation,” *JCAP* **1105** (2011) 002, arXiv:1011.3082 [hep-ph].
- [254] J. D. March-Russell and S. M. West, “WIMPonium and Boost Factors for Indirect Dark Matter Detection,” *Phys.Lett.* **B676** (2009) 133–139, arXiv:0812.0559 [astro-ph].
- [255] D. Feldman, Z. Liu, and P. Nath, “PAMELA Positron Excess as a Signal from the Hidden Sector,” *Phys.Rev.* **D79** (2009) 063509, arXiv:0810.5762 [hep-ph].

Bibliography

- [256] M. Ibe, H. Murayama, and T. Yanagida, “Breit-Wigner Enhancement of Dark Matter Annihilation,” *Phys.Rev.* **D79** (2009) 095009, arXiv:0812.0072 [hep-ph].
- [257] W.-L. Guo and Y.-L. Wu, “Enhancement of Dark Matter Annihilation via Breit-Wigner Resonance,” *Phys.Rev.* **D79** (2009) 055012, arXiv:0901.1450 [hep-ph].
- [258] X.-J. Bi, P.-F. Yin, and Q. Yuan, “Breit-Wigner Enhancement Considering the Dark Matter Kinetic Decoupling,” *Phys.Rev.* **D85** (2012) 043526, arXiv:1106.6027 [hep-ph].
- [259] S. Profumo, K. Sigurdson, and M. Kamionkowski, “What mass are the smallest protohalos?,” *Phys.Rev.Lett.* **97** (2006) 031301, arXiv:astro-ph/0603373 [astro-ph].
- [260] C. Boehm, P. Fayet, and R. Schaeffer, “Constraining dark matter candidates from structure formation,” *Phys.Lett.* **B518** (2001) 8–14, arXiv:astro-ph/0012504 [astro-ph].
- [261] X.-l. Chen, M. Kamionkowski, and X.-m. Zhang, “Kinetic decoupling of neutralino dark matter,” *Phys.Rev.* **D64** (2001) 021302, arXiv:astro-ph/0103452 [astro-ph].
- [262] P. Gondolo, J. Hisano, and K. Kadota, “The Effect of quark interactions on dark matter kinetic decoupling and the mass of the smallest dark halos,” *Phys.Rev.* **D86** (2012) 083523, arXiv:1205.1914 [hep-ph].
- [263] E. R. Tittley and H. Couchman, “Hierarchical clustering, the universal density profile, and the mass-temperature scaling law of galaxy clusters,” arXiv:astro-ph/9911365 [astro-ph].
- [264] V. Avila-Reese, P. Colin, O. Valenzuela, E. D’Onghia, and C. Firmani, “Formation and structure of halos in a warm dark matter cosmology,” *Astrophys.J.* **559** (2001) 516–530, arXiv:astro-ph/0010525 [astro-ph].
- [265] J. Zavala, Y. P. Jing, A. Faltenbacher, G. Yepes, Y. Hoffman, S. Gottlöber, and B. Catinella, “The Velocity Function in the Local Environment from Λ CDM and Λ WDM Constrained Simulations,” *Astrophys. J.* **700** (Aug., 2009) 1779–1793, arXiv:0906.0585 [astro-ph.CO].
- [266] A. Boyarsky, O. Ruchayskiy, and D. Iakubovskyi, “A Lower bound on the mass of Dark Matter particles,” *JCAP* **0903** (2009) 005, arXiv:0808.3902 [hep-ph].
- [267] E. Puchwein, C. Pfrommer, V. Springel, A. E. Broderick, and P. Chang, “The Lyman α forest in a blazar-heated Universe,” *Mon.Not.Roy.Astron.Soc.* **423** (June, 2012) 149–164, arXiv:1107.3837 [astro-ph.CO].
- [268] A. V. Macciò and F. Fontanot, “How cold is dark matter? Constraints from Milky Way satellites,” *Mon.Not.Roy.Astron.Soc.* **404** (May, 2010) L16–L20, arXiv:0910.2460 [astro-ph.CO].

- [269] N. Menci, F. Fiore, and A. Lamastra, “Galaxy formation in warm dark matter cosmology,” *Mon.Not.Roy.Astron.Soc.* **421** (Apr., 2012) 2384–2394, arXiv:1201.1617 [astro-ph.CO].
- [270] J. Redondo, “Bounds on Very Weakly Interacting Sub-eV Particles (WISPs) from Cosmology and Astrophysics,” in *Proceedings of the 4th Patras Workshop on Axions, WIMPs and WISPs*, pp. 23–26. 2008. arXiv:0810.3200 [hep-ph].
- [271] J. Jaeckel and A. Ringwald, “The Low-Energy Frontier of Particle Physics,” *Ann.Rev.Nucl.Part.Sci.* **60** (2010) 405–437, arXiv:1002.0329 [hep-ph].
- [272] J. P. Leveille, “The Second Order Weak Correction to $(G-2)$ of the Muon in Arbitrary Gauge Models,” *Nucl.Phys.* **B137** (1978) 63.
- [273] **LSND** Collaboration, L. Auerbach *et al.*, “Measurement of electron-neutrino electron elastic scattering,” *Phys.Rev.* **D63** (2001) 112001, arXiv:hep-ex/0101039 [hep-ex].
- [274] C.-W. Chiang, G. Faisel, Y.-F. Lin, and J. Tandean, “Constraining Nonstandard Neutrino-Electron Interactions due to a New Light Spin-1 Boson,” arXiv:1204.6296 [hep-ph].
- [275] M. Archidiacono, E. Calabrese, and A. Melchiorri, “The Case for Dark Radiation,” *Phys.Rev.* **D84** (2011) 123008, arXiv:1109.2767 [astro-ph.CO].
- [276] R. Harnik, J. Kopp, and P. A. Machado, “Exploring ν Signals in Dark Matter Detectors,” *JCAP* **1207** (2012) 026, arXiv:1202.6073 [hep-ph].
- [277] **IceCube** Collaboration, R. Abbasi *et al.*, “The IceCube Neutrino Observatory IV: Searches for Dark Matter and Exotic Particles,” arXiv:1111.2738 [astro-ph.HE].
- [278] **IceCube** Collaboration, R. Abbasi *et al.*, “Search for Dark Matter from the Galactic Halo with the IceCube Neutrino Telescope,” *Phys.Rev.* **D84** (2011) 022004, arXiv:1101.3349 [astro-ph.HE].
- [279] A. B. Newman, T. Treu, R. S. Ellis, and D. J. Sand, “The Dark Matter Distribution in Abell 383: Evidence for a Shallow Density Cusp from Improved Lensing, Stellar Kinematic and X-ray Data,” *Astrophys. J. Lett.* **728** (Feb., 2011) L39, arXiv:1101.3553 [astro-ph.CO].

Acknowledgements

This work would not have been possible without the support of many people.

First of all, I would like to thank my supervisor Torsten Bringmann, for giving me the opportunity to do my PhD at such an interesting and intellectual place as Hamburg. It was very educational and inspirational to work with him, and I learned a lot during this time. He taught me to be independent, critical and meticulous, and most of all to use my brains. It was a great experience, and I am thankful for his guidance and confidence.

I had the pleasure of working together with some very nice colleagues. I thank Christoph Pfrommer, for the very fruitful and enjoyable collaboration. I also want to express my gratitude towards Yaşar Goedecke, for the many helpful and pleasant discussions. Not to forget Mitsuru Kakizaki, for letting me use his helpful notes.

Furthermore I am thankful that I got to work in such a nice group, which I am proud to have been a part of. A warm thanks to Masaki Asano, Enrico Borriello, Sovan Chakraborty, Carmelo Evoli, Alessandro Mirizzi, Peter Schiffer, Günter Sigl, and former members and guests, for the interesting, useful, and pleasant discussions.

I also want to express my gratitude towards the (former) PhD students of this group – Rafael Alves Batista, Francesca Calore, Jörg Kulbartz, Ninetta Saviano, Andrey Saveliev, Arjen van Vliet, Martin Vollmann, and Le Zhang – many of which became good friends to me. Their support, companionship, help and friendship have been essential to me, and I have enjoyed our conversations very much. I am also grateful for the Movie Club and its members for the many nice relaxing evenings after a stressful day of work. I thank Andrey in particular, for helping me with the German translation of the abstract of this thesis.

During my PhD I also obtained a lot of support from my friends and family in the Netherlands. A big thanks to Marilyn, Babs, Sascha, Silvia, Carolien, Jan, Ina, Leo, Mark, Dennis, Marjolijn, Isa, Lode, Lies and Geert, for taking the effort of visiting me here, and of course all others who stayed in contact with me.

I would not have been able to finish my PhD without my wonderful parents Piet and Rina. They have always been there for me with their advice, support and compassion when I needed it the most. I am grateful for everything they have done for me, and I hope I have made them proud of me.

Last but not least, I want to express my deepest gratitude towards my boyfriend Jeroen Kurvink. I am very thankful that he has stood by me all this time, and I would not know what I would have done without him.

Selbstständigkeitserklärung

Ich erkläre, dass ich die vorliegende Arbeit selbstständig und nur unter Verwendung der angegebenen Literatur und Hilfsmittel angefertigt habe.

Hamburg, den 25. April 2013

Laura Gusta van den Aarssen